Theory of carrier transport in III-N based heterostructures

Michael John Oliver O'Donovan
BSc
114383406

NATIONAL UNIVERSITY OF IRELAND, CORK

SCHOOL OF SCIENCE

DEPARTMENT OF PHYSICS

Thesis submitted for the degree of Doctor of Philosophy

1 May 2023

Head of Department: Prof. John McInerney

Supervisors: Dr. Stefan Schulz
Prof. Eoin P. O'Reilly

Research supported by the Sustainable Energy Authority of Ireland and Science Foundation Ireland

Contents

List of Figures

List of Tables

I, Michael John Oliver O'Donovan, certify that this thesis is my own work and I have not obtained a degree in this university or elsewhere on the basis of the work submitted in this thesis.

Michael John Oliver O'Donovan

For my family.

`Cross postgraduate begins early, making mess of test.`

12 across - The Irish Times Crossword, 18/06/22 [1]

List of acronyms

1-D	One-dimensional
2-D	Two-dimensional
3-D	Three-dimensional
AlN	Aluminium nitride
BTE	Boltzmann transport equation
CBE	Conduction band edge
DD	Drift-diffusion
DFT	Density functional theory
EL	Electroluminescence
EMA	Effective mass approximation
FDM	Finite difference method
FEM	Finite element method
FVM	Finite volume method
GaAs	Gallium arsenide
GaN	Gallium nitride
HSE	Heyd-Scuseri-Ernzerhof
InN	Indium nitride
I-V	Current-voltage
LED	Light emitting diode
LLT	Localization landscape theory
MQW	Multi-quantum well
NEGF	Non-equilibrium Green's function
QCSE	Quantum confined Stark effect
QW	Quantum Well
RA	Random alloy
SRH	Shockley-Read-Hall
SQW	Single quantum well
TB	Tight-binding
VBE	Valence band edge
VCA	Virtual Crystal Approximation
VFF	Valence force field

[1] The solution is *Exam*.

Publication list

Journal publications

[1] "Impact of random alloy fluctuations on the carrier distribution in multi-color (In,Ga)N/GaN quantum well systems", Michael O'Donovan, Patricio Farrell, Julien Moatti, Timo Streckenbach, Thomas Koprucki and Stefan Schulz, *submitted, Preprint available at* `arxiv.org/abs/2209.11657`

[2] "Multiscale simulations of uni-polar hole transport in (In,Ga)N quantum wells systems", Michael O'Donovan, Patricio Farrell, Timo Streckenbach, Thomas Koprucki and Stefan Schulz, *Optical and Quantum Electronics* **54**, 405 (2022)

[3] "From atomistic tight-binding theory to macroscale drift diffusion: multiscale modeling and numerical simulation of uni-polar charge transport in (In,Ga)N devices with random fluctuations", Michael O'Donovan, Debapriya Chaudhuri, Timo Streckenbach, Patricio Farrell, Stefan Schulz and Thomas Koprucki, *Journal of Applied Physics* **130**, 065702 (2021)

[4] "Multiscale simulations of the electronic structure of III-nitride quantum wells with varied indium content: Connecting atomistic and continuum-based models", Debapriya Chaudhuri, Michael O'Donovan, Timo Streckenbach, Oliver Marquardt, Patricio Farrell, Saroj K. Patra, Thomas Koprucki and Stefan Schulz, *Journal of Applied Physics* **129**, 073104 (2021)

[5] "Impact of Random Alloy Fluctuations on inter-well transport in InGaN/GaN multi-quantum well systems: An atomistic non-equilibrium Green's function study", Michael O'Donovan, Mathieu Luisier, Eoin P. O'Reilly and Stefan Schulz, *Journal of Physics: Condensed Matter*, **33** 045302 (2020)

Conference talks

"Vertical charge transport in (In,Ga)N quantum well systems: Connecting atomistic electronic structure theory with macroscale drift-diffusion",
Michael O'Donovan, Patricio Farrell, Timo Streckenbach, Thomas Koprucki and Stefan Schulz, at *the International Workshop on Nitride Semiconductors* – Berlin, October 2022

"Carrier transport in (In,Ga)N quantum well systems: Connecting atomistic tight-binding electronic structure theory to drift-diffusion simulations",
Michael O'Donovan, Patricio Farrell, Timo Streckenbach, Thomas Koprucki and Stefan Schulz, at *Numerical Simulation of Optoelectronic Devices* – Online (`www.nusod.org/2022/`), September 2022

"Impact of random alloy fluctuations on carrier transport in (In,Ga)N quantum well systems: Linking atomistic tight-binding models to drift-diffusion",

Michael O'Donovan, Patricio Farrell, Timo Streckenbach, Thomas Koprucki and Stefan Schulz, at *the International Conference on Simulation of Semiconductor Processes and Devices* – Granada, September 2022

"Uni-polar transport in (In,Ga)N quantum well systems: Connecting atomistic electronic structure theory with macroscale drift-diffusion", Michael O'Donovan, Patricio Farrell, Timo Streckenbach, Thomas Koprucki and Stefan Schulz, at *UK Nitride Consortium* – Online (`www.uknc.org/meetings/`), January 2022

"Uni-polar transport in InGaN quantum well systems: From alloy fluctuations to quantum corrected drift-diffusion calculations", Michael O'Donovan, Patricio Farrell, Timo Streckenbach, Debapriya Chaudhuri, Thomas Koprucki and Stefan Schulz at *Semiconductor and Integrated Opto-Electronics Conference* – Online (`www.cardiff.ac.uk/conferences/sioe-conference/`), April 2021

"Impact of random alloy fluctuations on inter-well transport in InGaN/GaN multi-quantum well systems", Michael O'Donovan, Mathieu Luisier, Eoin P. O'Reilly and Stefan Schulz at *UK Nitride Consortium* – Online (`www.uknc.org/meetings/`), January 2021

"Atomic analysis if transport properties of InGaN/GaN multi-quantum wells", Michael O'Donovan, Mathieu Luisier, Eoin P. O'Reilly and Stefan Schulz at *Numerical Simulation of Optoelectronic Devices* – Ottawa, July 2019

Conference posters

"Impact of alloy fluctuations on uni-polar charge transport in (In,Ga)N quantum wells: Connecting atomistic electronic structure theory with macroscale drift-diffusion", Michael O'Donovan, Patricio Farrell, Timo Streckenbach, Thomas Koprucki and Stefan Schulz, poster presented at *Simon Collaboration on Localization of waves: Workshop on Semiconductors, Perovskites and 2D materials* – Paris, December 2021

"Unipolar transport in InGaN quantum well systems - Connecting alloy fluctuations to a quantum corrected drift-diffusion model". Michael O'Donovan, Patricio Farrell, Timo Streckenbach, Debapritya Chaudhuri, Thomas Koprucki and Stefan Schulz, poster presented at *Photonics Ireland* – Online (`www.ipic.ie/photonics-ireland-conference-2021/`), June 2021

Contributions to invited talks

"Connecting atomistic and continuum models for (In,Ga)N quantum wells: From tight-binding energy landscapes to electronic structure and carrier transport" presented by Dr. Stefan Schulz at *Numerical Simulation of Optoelectronic Devices* – Online (`www.nusod.org/2021/`), September 2021

"Carrier transport, radiative and non-radiative recombination in (In,Ga)N heterostructures: Insights from atomistic and multi-scale simulations" presented by Dr. Stefan Schulz at *Applied Mathematics and Simulation for Semiconductors and Electrochemical Systems* – Berlin, September 2021

Acknowledgements

There are so many people that have supported me over the last number of years I must thank. First, thanks to my supervisor, Dr. Stefan Schulz, for offering me the opportunity to pursue a PhD with him. I've learned a lot from him over the course of this degree, not limited to semiconductor physics: I appreciate how he has helped me navigate the world of research, and has offered advice on broader aspects of life. He has been extremely understanding if at any point I was going through a difficult time, for which I am ever grateful. To add to this, our meetings have always had a good atmosphere, which has made my time here in Tyndall very enjoyable.

I also thank my co-supervisor, Prof. Eoin O'Reilly for the sharp and valuable insights he offered into my work, and for having led such a wonderful group which I am fortunate to have been a part of. I wish him the best as he moves on to a new stage of his life.

Thank you to my monitor, Dr. Philip Murphy Armando. At my review meetings he always offered great advice looking at the bigger picture of my career, while engaging in interesting scientific discussions also.

The nature of a research group means that most of the personnel have changed since I joined in 2018; I reached 18 names before I gave up counting. At every moment the team was a pleasure to be around with a kind atmosphere. When life ground to a halt for several months and we were only able to meet outside we still had some very enjoyable coffees in Fitzgerald park. I wish everyone the best of luck in their future endeavours.

There are more people without whom I could not have carried out the research contained within this thesis. Thank you to my funders, the Sustainable Energy Authority of Ireland and Science Foundation Ireland, for their financial support, and to my collaborators at ETH Zürich and WIAS Berlin for providing both tools enabling my work and insights into my results.

Of course there's more to life than work, and the last few years would not have been the same without my friends. I've been lucky to be surrounded by people that are up for any excursion, make me laugh, and have offered me great friendship and support. For fear of forgetting anyone I've grouped them into three broad categories:

- Anyone who has spent a disproportionate amount of time hanging out in Deerpark (even for if you live there).
- Everyone who strolled up and down the railway walk with me.
- Anybody who picked up the phone to catch up from a different country.

I have a family which I can trust and rely on. Thank you to my sisters, Grace and Mary, and my parents, Naomi and Mick. They're always ready with a cupán tae to chat about everything and anything that is going on. My family has always been encouraging in everything I have undertaken, and their confidence in me during this PhD has been no different.

My last word of thanks goes to Louise. She has shown remarkable patience with me as I got wound up with stress these last few months; I can only hope I am half as supporting to her. As always, I am looking forward to our next adventure.

Abstract

Wurtzite III-nitride materials and their alloys have attracted significant interest for solid state lighting applications. This is due to the direct band gaps of InN, GaN, and AlN crystals, which span a wide range of emission wavelengths. Due to the importance of these systems, the goal of optimising device performance has been an extremely active field of research. An important aspect of this is the development of improved modeling techniques. More recently, an emphasis has been put on understanding the impact the disordered alloy microstructure has on the electronic structure, however models focusing on transport properties are less mature. This is in part due to the challenges of connecting a random alloy description of the underlying microstructure with transport models.

This thesis addresses this difficult problem by developing and utilizing different simulation frameworks, focusing on transport properties of (In,Ga)N/GaN quantum well systems. More specifically, the non-equilibrium Green's function (NEGF) formalism has been employed to study ballistic transport in a fully quantum mechanical setting. This builds on a tight-binding description of the electronic structure which ensures an atomistic description of the alloy is achieved. Our results indicate that while the alloy microstructure is of secondary importance for electrons, the transmission of holes is strongly perturbed by the presence of disorder. This is attributed to the breakdown of the translational symmetry of the system, which opens up new channels not present when fluctuations in local alloy content are neglected (using a virtual crystal approximation).

Moreover, we have developed a new semi-classical multi-scale drift-diffusion model. This allows simulation of full devices due to a reduced computational demand compared to the NEGF formalism, while still keeping a microscopic resolution and accounting for important quantum corrections. The starting point is again the tight-binding model, which is used as a foundation to describe the alloy microstructure: A 3-dimensional energy landscape is extracted which includes an atomistic description of alloy fluctuations, local strain, and local polarization. This can be used as a confining potential for electrons and holes, and quantum corrections can be included in a numerically efficient manner via the recently developed localization landscape theory.

This landscape, including or excluding quantum corrections, is used to study both unipolar electron and hole transport. Our results show that, when quantum corrections are accounted for, the virtual crystal approximation is again a good approximation for *electron* transport, whereas *hole* transport is reduced due to carrier localization effects in the quantum well region.

Finally this framework is extended to a *p-i-n* junction, where carrier (and thus recombination) distribution across a multi-quantum well system is studied. This system allows

for a comparison between our in-house model and a commercial software package. Without including disorder in the alloy microstructure both schemes fail to reproduce literature experimental results. However, the situation changes when the random alloy microstructure is accounted for using our newly developed approach: The predicted behaviour is consistent with literature experimental results, without changing any other simulation parameters. These results highlight the importance of the treatment of the alloy microstructure in simulations, and indicate that our developed framework is an ideal starting point for modeling III-N systems to understand fundamental properties and guide device design.

Part I

Background

Chapter 1

Prologue: From the origins of the LED to current research challenges

The invention of the light emitting diode (LED) was a many step process which took decades, and the technology is still being improved today. The first key revelation in the path towards developing an LED is credited to Henry J. Round for the discovery of electroluminescence (EL). In 1907, while working on silicon carbide (SiC) rectifiers, he reported that "the crystal gave out a yellowish light" when a bias of 10 V was applied to it [6], although this short publication was largely unnoticed until 1969 [7]. In the 1920s, Oleg Lossev independently discovered EL while driving a current through rectifiers based on zinc oxide (ZnO) and SiC [8]. During his work he studied the threshold current at which light emission is observed. He also noted that this light was not incandescence (as is found in, for example, tungsten filament light bulbs [9]) as the device was not heating, and instead associated the emission with the inverse process of Einstein's photoelectric effect; an overview of Lossev's achievements is described in Ref. [10].

Both Round and Lossev worked primarily with Schottky diodes, a connection between a metal and a semiconductor, whereas the modern LED is based on a so-called *p*-*n* junction [11]. Russell Ohl of Bell Laboratories who was studying photocells is reported to have discovered the first *p*-*n* junction in 1939 [12]. A *p*-*n* junction contains two regions, one which has been "*n*-doped" and one which has been "*p*-doped" (there is also a *p*-*i*-*n* junction which contains an undoped (intrinsic) region sandwiched between the *p*- and *n*-doped regions). *n*-doping a material "donates" free electrons which can be used to carry electric current. In contrast, *p*-doping "accepts" free electrons. Having "accepted" electrons is equivalent to the presence of *holes*, positively charged quasiparticles corresponding to the absence of an electron [13]. Like electrons, holes can also be used to carry current. The description of electron and hole injection across the *p*-*n* junction was described by Lehovec *et al.* in 1951, along with proposing a description of

the valence band and conduction band [14]. This is qualitatively the same description used today.

The efficiency of the discussed SiC light-emitting devices is limited due to the fundamental properties of the material, namely SiC has an indirect[1] bandgap [15]. Recombination in indirect-gap materials is fundamentally less efficient than direct-gap materials and, in order to improve the efficiency of LEDs, direct-gap materials e.g. III-V materials such as gallium arsenide (GaAs) [16] or II-VI materials such as zinc selenide (ZnSe) [17] are used.

Another significant improvement into the efficiency of these devices was the invention of the double heterostructure[2] and quantum well (QW). These both consist of a (lower band gap) material being sandwiched between layers of a different material. This allows the emitted light to have energy lower than the bandgap of the surrounding material, which means it can not be reabsorbed by the barrier and light can escape the device more easily (this will be revisited in Section 2.1.2). Double heterostructures and QWs differ in their width: QWs are narrower such that quantum mechanical effects play a role [18]. QWs have become a common feature of LED structures being researched (see Fig. 1.1) and will be discussed extensively in this thesis.

Semiconductor materials composed of group III and group V elements (III-V semiconductors) which contain arsenide and phosphide as the group V element have proved successful in infrared and red wavelengths [19]. The band gap of a selection of these binary materials and ternary alloys is shown in Fig. 1.2 (a). For some applications shorter wavelengths provide technological benefits. For example, when storing data a shorter wavelengths of light allow for a larger amount of information to be contained on the same physical size of disk (e.g. Bluray which is read using a blue laser can hold more data than a DVD which is read with a red laser [20]). Not only this, but in many displays red, green and blue (rgb) lights are used to form pixels, which can be used to effectively appear any colour across the visible spectrum. In order to implement this, efficient red, green and blue emitters are all required. A shorter wavelength corresponds to a higher band gap, and (as can be seen in Fig. 1.2 (a)) the conventional III-V materials at these band gaps are indirect (for example gallium phosphide (GaP) and aluminium arsenide (AlAs)). The quaternary alloy aluminium gallium indium phosphide (AlGaInP) has been used to extend the wavelength of III-V emitters from red into orange wavelengths, however this also becomes inefficient if the emission is pushed into green wavelengths [21].

At the other end of the visible spectrum, in the 1980s there was a competition between II-VI materials and III-N materials to become the standard for blue lighting; ZnSe had

[1] In an indirect gap material, unlike a direct gap material, the conduction band minimum and valence band maximum have differing crystal momenta, which is detrimental for light-emission.

[2] The "significant improvement" of a double heterostructure won the won Zhores Alferov and Herbert Kroemer the Nobel Prize in physics in 2000 [18].

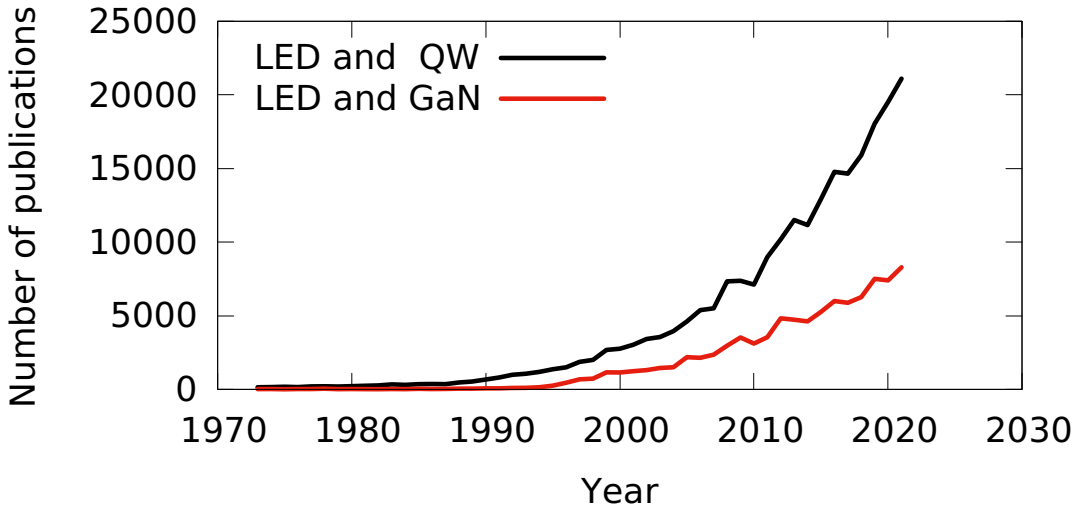

Figure 1.1: Number of publications per year including the phrases "light emitting diode" and "quantum well" (LED and QW, black) and including the phrases "light emitting diode" and "GaN" (LED and GaN, red) from 1973 to 2022. This figure was generated using data obtained on 15/11/22, from Digital Science's Dimensions platform, available at https://app.dimensions.ai.

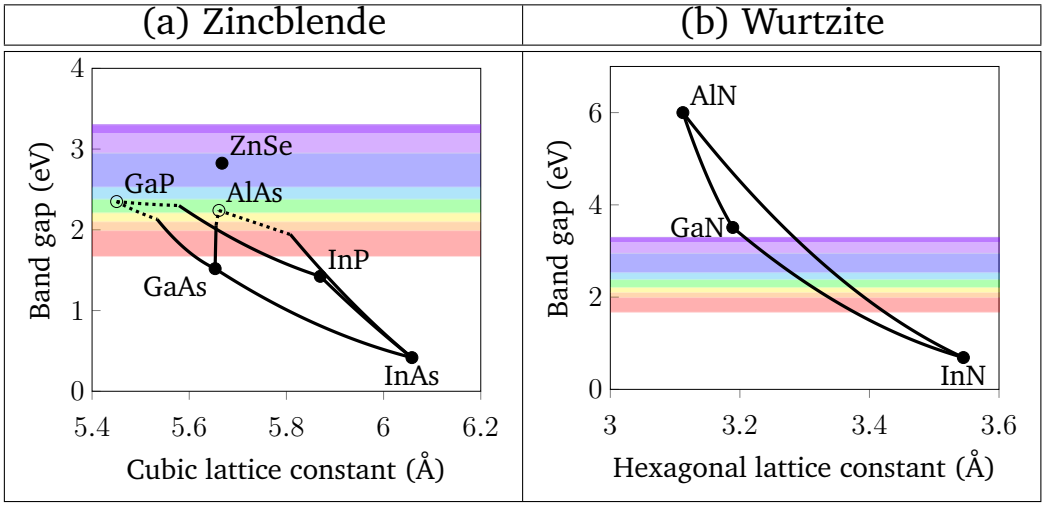

Figure 1.2: In-plane lattice constant vs band gap for a selection of (a) zincblende materials and (b) wurtzite materials. Filled (unfilled) dots indicate direct (indirect) gap binary materials. Solid (dashed) lines indicate direct (indirect) gap ternary alloys. Presented data are the minimum band gap of $\{E_g^\Gamma, E_g^X, E_g^L\}$ for each material. The visible part of the spectrum is shown via colors. Band gap parameters for wurtzite III-N materials are from Refs. [22, 23] with bowing parameters taken from Ref. [24], parameters for zincblende III-V materials are from Ref. [25] and ZnSe from Refs. [26, 27].

much higher crystal quality than gallium nitride (GaN), and was therefore regarded as the front-runner for blue light emitters [28]. However, the III-N material system has become the more frequently used. In particular, GaN-based systems are the topic of our next discussion.

1.1 GaN-based LEDs

The interest in III-N material systems stems from the wide band gap range (c.f. Fig 1.2 (b)) between InN in the infrared (0.69 eV [22]), GaN (3.51 eV [22]) in the near ultraviolet (UV) and AlN (6.0 eV [23]) in the UV C part of the spectrum [29]. In particular, as InN and GaN are either side of the visible spectrum, the alloy (In,Ga)N could emit, in principle, across the entire visible spectrum, depending on its composition. As a result, (In,Ga)N devices have been developed targeting myriad applications, including road signage [30, 31], displays [32, 33], and photovoltaics [34, 35].

III-N materials suffered from a high defect density and poor p-doping. Amano *et al.*, under the supervision of Akasaki, discovered that a low-energy electron beam irradiation could activate magnesium dopants, thus solving the p-doping issue [36]. Later Nakamura *et al.* found that an annealing could be used for the same purpose [37]. Since these breakthroughs interest in GaN-based LEDs has risen (see clear increase in Fig 1.1 (red) from 1990s onwards). Isamu Akasaki, Hiroshi Amano, and Shuji Nakamura won the 2014 Nobel prize in physics "for the invention of efficient blue light-emitting diodes which has enabled bright and energy-saving white light source" [38]. The white light could be generated by exciting a phosphor with blue light; the output light, a mixture of blue and yellow, appears white to the human eye [28].

As mentioned, GaN crystals have high dislocation densities. If this density of defects was present in other III-V materials their efficiency would drastically decrease (see, for example, Fig. 13 in Ref. [28]). In spite of this, reasonably high efficiency can be achieved with GaN. This can be explained by the localization of carriers, which allows carriers to recombine radiatively without diffusing to defects [39]. We shall discuss localization, along with some other characteristics of III-N devices in the next section.

1.1.1 Localization, Droop and the "Green Gap"

III-N alloys such as (In,Ga)N and (Al,Ga)N have been shown to exhibit strong localization effects due to alloy disorder [40–43]. Localization is the confining of electronic states to small regions of the alloy. In (In,Ga)N alloys this is particularly strong for holes, which can have a localization length on the order of 1 nm [44]. Apart from explaining the high efficiency of III-N devices, localization is also the explanation behind a number of physical phenomena associated with III-N alloys and heterostructures including inhomogeneous broadening of emission peaks [45] and the temperature dependence of the photoluminescence peak energy [46, 47].

Thanks to localization effects, LEDs made from III-N materials can have quite high efficiency at blue and violet wavelengths. We have already mentioned that other III-V materials emit efficiently in the red wavelengths. Unfortunately, both AlGaInP and (In,Ga)N devices get less efficient as the bandgap is pushed towards green wave-

lengths [48]. This is known as the *green gap* problem. Some properties which may cause a reduction of efficiency in III-N alloys and heterostructures are the formation of defects [49, 50], and an increase in the quantum confined Stark effect (QCSE) with composition (caused by spontaneous and piezoelectric polarization, discussed in Sections 2.1.2 and 3.3.2) [50].

On top of the green gap, and also important for III-N devices operating at shorter wavelengths, III-N LEDs also suffer from the so-called efficiency droop: As the current density increases, the internal quantum efficiency (the ratio of radiative current density to total current density) decreases [51]. Auger recombination is often cited as the cause of this efficiency droop [51–53] though other contributions such as electron leakage have also been suggested [52, 54].

1.2 Current state of modeling techniques

To tackle these challenges associated with III-N alloys, reliable modeling techniques are key to increasing understanding and guiding the design of future devices. Carrier localization has been considered extensively in the modeling of the electronic and optical properties of III-N based heterostructures [4, 55–58].

On the other hand, when studying transport in a device a common approach is a one-dimensional (1-D) model which neglects carrier localization effects originating from the underlying alloy microstructure [59–64]. 1-D simulations can lead to an overestimate of the turn-on voltage of an LED, and an often used approach is to reduce the intrinsic polarization fields in the simulations (by a factor of 2) in order to fit current-voltage (I-V) curves to experimental data [65, 66]. The underlying physical origin however is not clear for such a drastic assumption. Studies by Li *et al.* have shown that the alloy microstructure, namely random alloy fluctuations, significantly affect the I-V curves of a device [67]. Such approaches often require three-dimensional (3-D) transport models to achieve an improved description of device characteristics, although modified 1-D models have also been employed [68, 69]. These calculations often build on modified continuum-based models for the electronic structure of the active region [70].

On top of this, the standard semi-classical description of transport neglects quantum mechanical effects [63, 71]. To account for quantum mechanical effects, the standard model can be coupled with the Schrödinger equation in a self-consistent process to describe carrier densities [64–66, 69]. The numerical demand of this approaches means that it is generally only treated in 1-D, and quantum mechanical transport through a 3-D disordered III-N alloy has not been addressed. Our first goal in this thesis is to describe a multi-QW (MQW) system, which is at the heart of modern III-N LEDs, in a fully atomistic and quantum mechanical setting, and to study the impact that the alloy

microstructure has on quantum mechanical transport properties.

As previously mentioned, 3-D semi-classical transport models have been employed to study the impact of the alloy microstructure, which is built on top of a (spatially varying) continuum description of an alloy [67]. In III-N alloys atomistic effects are important for describing the electronic properties, and it is unclear if the continuum approach captures local effects correctly. Instead, a transport model should be built on top of an atomistic description of the system which can accurately describe the electronic structure. Our second goal in this thesis is to develop a 3-D multi-scale framework to study carrier transport in a semi-classical description which still captures atomistic features and quantum corrections in the QW region of a device.

1.3 Thesis overview

In Chapter 2 we present general information about the wurtzite crystal structure, and the properties of III-N-based heterostructures and LEDs in more detail. We build on this in Chapter 3 and introduce $\mathbf{k}\cdot\mathbf{p}$ and tight-binding models which describe the electronic structure of single-particle states in a continuum and atomistic setting respectively. Continuum and atomistic descriptions of strain and polarization in QW systems are also introduced here. This chapter ends by presenting a method for approximating the ground state in a given region which can be used as a numerically inexpensive substitute for solving the Schrödinger equation, namely localization landscape theory.

Chapter 4 extends the electronic structure methods to introduce theories describing carrier transport in a quantum mechanical non-equilibrium Green's function (NEGF) and semi-classical drift-diffusion (DD) description. For the DD model we develop a framework which uses an energy landscape extracted from atomistic tight-binding to include alloy fluctuations in a multi-scale simulations.

We investigate the impact that the description of the alloy microstructure has on ballistic transport through (In,Ga)N/GaN MQWs in Chapter 5. These MQWs might form, for example, the active region of an LED. Our results using the NEGF formalism show that in the case of electrons, the specific treatment of the underlying alloy is of secondary importance for describing carrier transport between wells. The same is not true for holes, where the symmetry-breaking effect of an alloy is crucial for developing an accurate picture of hole transport. Here we also investigate the impact that polarization fields and a potential from a *p-i-n* junction have on transmission properties.

Due to the numerical demand of the NEGF formalism we move away from the *full* quantum mechanical description towards a modified DD approach in Chapter 6. In this case we use the multi-scale DD framework building on tight-binding electronic structure theory to investigate the properties of uni-polar transport for both electrons and holes. This allows us to disentangle the transport effects from other contributions

such as recombination processes. In the case of electrons, both quantum corrections and alloy fluctuations result in an increased electron current. Conversely, in the case of uni-polar hole transport, alloy fluctuations are detrimental to carrier transport due to the localization of carriers.

Having learned about the behaviour of electron and hole transport from the uni-polar study, we investigate a *p-i-n* junction using the DD framework in Chapter 7. Here we target previous literature experimental results which describe the carrier distribution across a MQW. Including the effects of the fluctuating alloy microstructure has a significant impact of results. Experimental findings could be reproduced where a standard modeling approach utilizing a commercial software package failed without changing any other modeling parameters.

Finally, a summary of conclusions and an outlook of future topics of research are presented in Chapters 8 and 9.

Chapter 2

Introduction

We highlighted in the prologue the current state of simulations of III-N materials and devices. The basis of any transport simulator will be the electronic structure. In order to build an electronic structure theory we must first start with a good description of the underlying crystal structure of III-N materials.

2.1 Crystal structures

To start our analysis of semiconductor materials we shall assume that we are dealing with a perfect crystalline material, which does not contain any defects. There are a number of different crystal lattices which are formed by III-V materials with various symmetries [11]. For example, III-Arsenide materials such as GaAs preferentially form in the zincblende phase [72]. On the other hand, III-Nitride materials such as GaN and InN are thermodynamically stable in the wurtzite phase [11]. The wurtzite lattice is shown in Fig 2.1.

The ideal wurtzite crystal consists of two hexagonal, close-packed sub-lattices which are offset along the growth (c) direction by 5/8 c, where c is the lattice constant along this direction [73]. The III-N crystals contain alternating layers of cations (group III atoms such as indium or gallium) and anions (nitrogen). Each atom has 4 tetrahedrally bonded nearest-neighbours. The primitive unit cell is a four atom basis which has 6-fold rotational symmetry in the c-plane[1].

[1]Without translation the crystal has 3-fold rotational symmetry, however the structure is non-symmorphic, and contains 6-fold rotational symmetry when paired with a non-primitive translation [74].

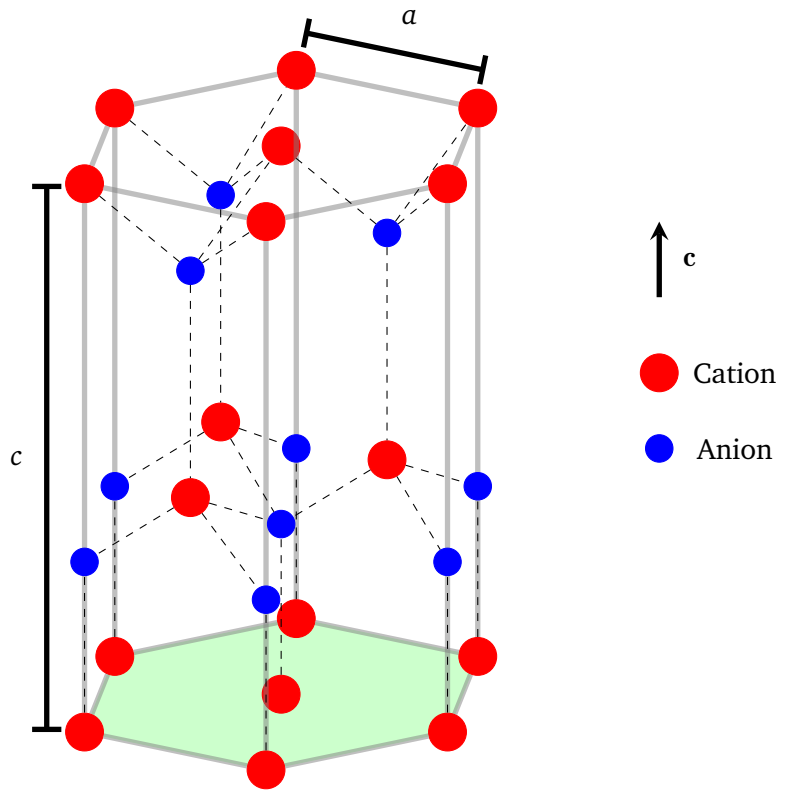

Figure 2.1: Hexagonal cell of the wurtzite crystal structure. Cations are shown in red and anions in blue. Each anion (cation) has 4 cation (anion) nearest-neighbours. The bonds between these atoms are shown with grey dashed lines. The c-plane is shown in green, which has a normal vector along the c-direction, $[0001]$-direction[2]of the crystal. The lattice constants a (in-plane) and c (out-of-plane) are shown.

In an ideal wurtzite lattice the positions within the unit cell are [75]

$$\begin{aligned}\mathbf{\Delta}_1 &= (0,0,0)\ ,\\ \mathbf{\Delta}_2 &= (0,a/\sqrt{3},c/8)\ ,\\ \mathbf{\Delta}_3 &= (0,a/\sqrt{3},c/2)\ ,\\ \mathbf{\Delta}_4 &= (0,0,5c/8)\ .\end{aligned}$$

This basis exists at every point in the hexagonal Bravais lattice whose lattice vectors are

$$\begin{aligned}\mathbf{r}_1 &= (a,0,0)\ ,\\ \mathbf{r}_2 &= (-a/2,\sqrt{3}a/2,0)\ ,\\ \mathbf{r}_3 &= (0,0,c)\ ,\end{aligned}$$

[2]The planes and directions in a wurtzite crystal can be denoted using Miller-Bravais indices, $(hkil)$ and $[hkil]$ respectively [76]. The indices h, k and l correspond to lattice vectors $\mathbf{r}_{1-3}$, and are equivalent to the Miller indices used in other crystal phases such as zincblende. The extra index, $i = -h - k$, allows for the easy identification of equivalent directions in a wurtzite crystal. The $[hkil]$-direction is perpendicular to the $(hkil)$-plane.

so that an atom with index i is located at

$$\mathbf{\Delta}_i^{\text{replica}} = \mathbf{\Delta}_i + n_1\mathbf{r}_1 + n_2\mathbf{r}_2 + n_3\mathbf{r}_3$$

where n_1, n_2 and n_3 are integers; in real space the lattice is also referred to as the *direct* lattice.

III-N materials can be grown along different crystallographic planes. GaN is often grown along the [0001] (*c*-) direction (perpendicular to the c-plane, (0001), which is shown in green in Fig. 2.1) due to difficulties associated with growing high-quality structures along other planes such as the $(11\bar{2}0)$ or $(1\bar{1}00)$ (a- and m-) planes [77–79]. In this thesis we focus on c-plane materials, and discuss their electronic and transport properties.

To gain insight into the fundamental material properties, such as lattice constants, information about the crystal planes is required. This can be obtained experimentally by using diffraction measurements (e.g. Ref. [80]). Diffraction is related to the so-called *reciprocal* lattice, which describes the spatial frequency of points in the direct lattice. Reciprocal lattice vectors, $\mathbf{G}$, are vectors which describe waves with the same periodicity as the direct lattice, and therefore satisfy the equation [13]

$$\exp\left(i\mathbf{G}\cdot\mathbf{R}\right) = 1 \quad \therefore \quad \mathbf{G}_j \cdot \mathbf{r}_j = 2\pi m_j \ , \tag{2.1}$$

where $\mathbf{R} = n_1\mathbf{r}_1 + n_2\mathbf{r}_2 + n_3\mathbf{r}_3$ and n_i and m_j are integers. This can be expressed in terms of primitive reciprocal lattice vectors,

$$\mathbf{G} = m_1\mathbf{k}_1 + m_2\mathbf{k}_2 + m_3\mathbf{k}_3 \ ,$$

which (in 3-D) are determined via [13]

$$\mathbf{k}_i = 2\pi\frac{\mathbf{r}_j \times \mathbf{r}_k}{\mathbf{r}_i \cdot (\mathbf{r}_j \times \mathbf{r}_k)} \ .$$

Like the direct lattice, the reciprocal lattice can be divided into primitive cells which are defined by the primitive vectors; this is referred to as the first Brillouin zone [13]. For a wurtzite crystal this results in a hexagonal Brillouin zone, with primitive reciprocal lattice vectors of [75]

$$\begin{aligned}
\mathbf{k_1} &= \frac{2\pi}{a}(1, 1/\sqrt{3}, 0) \ , \\
\mathbf{k_2} &= \frac{4\pi}{\sqrt{3}a}(0, 1, 0) \ , \\
\mathbf{k_3} &= \frac{2\pi}{c}(0, 0, 1) \ .
\end{aligned}$$

The electron wave functions in a lattice, and thus the electronic structure, is affected

by the reciprocal lattice, as we shall see in the next section.

2.1.1 Electronic band structure

To study the electronic structure of pure crystals in principle the many-body Schrödinger equation needs to be solved, where the time-independent Hamiltonian is described in Eq. (2.2) [81].

$$\begin{aligned}\hat{\mathcal{H}} = &-\overbrace{\frac{\hbar^2}{2m}\sum_{i=1}^{n}\nabla_i^2}^{\hat{T}_e} - \overbrace{\frac{\hbar^2}{2M}\sum_{I=1}^{N}\nabla_I^2}^{\hat{T}_n} - \overbrace{\frac{1}{4\pi\epsilon_0}\sum_{i=1}^{n}\sum_{I=1}^{N}\frac{Z_I e^2}{|r_i - R_I|}}^{\hat{V}_{e-n}} \\ &+ \underbrace{\frac{1}{8\pi\epsilon_0}\sum_{i}^{n}\sum_{j\neq i}^{n}\frac{e^2}{|r_i - r_j|}}_{\hat{V}_{e-e}} + \underbrace{\frac{1}{8\pi\epsilon_0}\sum_{I}\sum_{J\neq I}^{N}\frac{Z_I Z_J e^2}{|R_I - R_J|}}_{\hat{V}_{n-n}}\end{aligned} \tag{2.2}$$

$\hat{T}_n$ and $\hat{T}_e$ are the kinetic energy terms for all the nuclei and electrons in the system which depend on m and M, the masses of the electron and nucleus respectively. $\hat{V}_{e-n}$, $\hat{V}_{e-e}$ and $\hat{V}_{n-n}$ are the potential terms including the (attractive) electron-nucleus interaction, (repulsive) electron-electron interaction and (repulsive) nucleus-nucleus interaction. Here, Z_I is the proton number of the nucleus I. As we are interested in the electronic structure, and not in the nuclear behaviour, we use the Born-Oppenheimer approximation; as the nuclear mass is much greater than that of the electron ($m \ll M$) the kinetic energy of the nuclei is negligible compared to that of the electrons [82]. The Schrödinger equation therefore reduces to

$$\hat{\mathcal{H}} = \hat{T}_e + \hat{V}_{e-n} + \hat{V}_{e-e} + \hat{V}_{n-n} \ .$$

This is still a very complex problem to solve, in particular due to $\hat{V}_{e-e}$, as the energy of an electron depends on the positions of all other electrons in the system via Coulomb interactions. In order to make this problem tractable we use the single-particle approximation where we assume that the particle is moving through an effective potential generated by all the other electrons and nuclei in the system [83]. Now the Hamiltonian can be written in terms of the electron kinetic energy operator and an effective potential:

$$\hat{\mathcal{H}} = \sum_{i=1}^{n}\left(\frac{-\hbar^2}{2m}\nabla_i^2 + \hat{V}_{\text{eff}}\right) = \sum_{i=1}^{n}\hat{H}_i \ .$$

The Hamiltonian for the full system is simply the sum of the single-particle Hamiltonians describing all the electrons in the system individually, which is to say, the total energy of the many-body system is the sum of the energies of the single-particles. The interaction of the single-particle state with the other electrons is taken into account only through the effective potential, so we are left with the single-particle time-independent

Schrödinger equation,

$$\hat{H}\psi(\mathbf{r}) = \frac{-\hbar^2}{2m}\nabla^2\psi(\mathbf{r}) + V_{\text{eff}}(\mathbf{r})\psi(\mathbf{r}) = E\psi(\mathbf{r}) \tag{2.3}$$

where ψ is the single-particle wave function.

In a pure crystal the potential, $V_{\text{eff}}(\mathbf{r})$, has translational symmetry (due to the underlying symmetry of the material):

$$V_{\text{eff}}(\mathbf{r}) = V_{\text{eff}}(\mathbf{r} + n_1\mathbf{r}_1 + n_2\mathbf{r}_2 + n_3\mathbf{r}_3) \ ,$$

where $\mathbf{r}_i$ are the primitive lattice vectors of the crystal and n_i are integers, $i \in \{1, 2, 3\}$. For example in a wurtzite material $\mathbf{r}_i$ would be the primitive lattice vectors outlined in Section 2.1.

In a potential with translational symmetry, the electronic wave function can be expressed as a Bloch function, where the solution is divided into a product of a periodic ($u_{\mathbf{k}}(\mathbf{r})$) and a plane-wave ($e^{i\mathbf{k}\cdot\mathbf{r}}$) contribution [84]:

$$\psi_{\mathbf{k}}(\mathbf{r}) = e^{i\mathbf{k}\cdot\mathbf{r}}u_{\mathbf{k}}(\mathbf{r}) \ .$$

The periodic contribution, $u_{\mathbf{k}}(\mathbf{r})$, has the same periodicity as the potential profile of the crystal, so determining the solution of $u_{\mathbf{k}}(\mathbf{r})$ over the crystals unit cell corresponds to knowing the solution anywhere in space up to a phase factor which depends on the quantum number $\mathbf{k}$:

$$\psi_{\mathbf{k}}(\mathbf{r}+\mathbf{R}) = e^{i\mathbf{k}\cdot(\mathbf{r}+\mathbf{R})}u_{\mathbf{k}}(\mathbf{r}+\mathbf{R}) \equiv e^{i\mathbf{k}\cdot\mathbf{R}}(e^{i\mathbf{k}\cdot\mathbf{r}}u_{\mathbf{k}}(\mathbf{r})) = e^{i\mathbf{k}\cdot\mathbf{R}}\psi_{\mathbf{k}}(\mathbf{r}) \ .$$

In the above equation $\mathbf{R}$ is a vector composed of an integer number of the primitive lattice vectors, $\mathbf{R} = n_1\mathbf{r}_1 + n_2\mathbf{r}_2 + n_3\mathbf{r}_3$, and $\mathbf{k}$ is known as the wavevector which is related to the crystal momentum, $\mathbf{p} \equiv \hbar\mathbf{k}$.

For each $\mathbf{k}$ there is a discrete set of eigenstates and corresponding eigenvalues. We label these states with the index j so now our set of eigenstates are denoted

$$\psi_{j\mathbf{k}}(\mathbf{r}) = e^{i\mathbf{k}\cdot\mathbf{r}}u_{j\mathbf{k}}(\mathbf{r}) \ . \tag{2.4}$$

The discrete set of eigenstates vary continuously with $\mathbf{k}$ [13]. This results in *bands* of energies corresponding to eigenvalues of the Schrödinger equation.

In the next paragraph we aim to restrict the values of $\mathbf{k}$ which are needed to gather complete information about the crystal. To do this we follow the example of Ref. [85] and consider (for simplicity) a 1-D system which is periodic along x with a lattice

constant of a. The wave function can be written as

$$\psi_{j\mathbf{k}}(x) = e^{ikx} u_{j\mathbf{k}}(x) \ .$$

Here we introduce the reciprocal lattice vector, $G_m = 2\pi m/a$ (this can be found directly from Eq. (2.1)) where m is an integer, and a is the lattice constant defining the periodicity along the x-direction. Multiplying our expression with a plane wave with wavevector G_m and its complex conjugate our wave function becomes

$$\psi_{j\mathbf{k}}(x) = e^{ikx} e^{iG_m x} e^{-iG_m x} u_{j\mathbf{k}}(x) = e^{i(k+G_m)x} \left(e^{-iG_m x} u_{j\mathbf{k}}(x) \right) \ .$$

Our manipulated equation still has the form of a plane wave term, $e^{i(k+G_m)x}$, and a periodic term with a period of the lattice constant, $e^{-iG_m x} u_{j\mathbf{k}}(x)$. This indicates that k is not uniquely defined, as $k + G_m$ is equivalent to k. This allows us to restrict calculations to the interval $\left[0, \frac{2\pi}{a}\right]$ which is the first Brillouin zone. This is known as the reduced zone scheme which drastically reduces the numerical effort required to determine the electronic states in a crystal, as once they are known in this interval then they are known for any wavevector k up to a phase [85]. This can be generalized to higher dimensions.

The band structure for GaN is shown in Fig. 2.2. The conduction band maximum and valence band minimum of the binaries GaN and InN are all located at the center of the Brilloin zone, $\mathbf{k} = (0, 0, 0) = \Gamma$. This means these materials have a direct band gap, and are therefore good candidates for light emitting applications, as was highlighted in the prologue. As was also mentioned, the band gaps of bulk InN (0.69 eV [22]), GaN (3.51 eV [22]) and AlN (6.0 eV [23]) span from the red to near UV to deep UV part of the spectra. Therefore, in principle, alloys of these materials could emit across the entire visible spectrum as well as UV wavelengths [29].

For heterostructures, the alignment of the bands with respect to each other is important. This can be calculated, and the resulting band alignment relative to GaN means that InN will form a well for both electrons and holes (valence band offset $\approx$ 0.62 eV [86]), whereas AlN will form a barrier for electrons and holes (valence band offset $\approx$ -0.2 eV [24]). These materials could therefore be used to manipulate electronic properties of devices by introducing heterostructures.

2.1.2 Heterostructures

In the prologue we discussed how QWs are important for LEDs in terms of efficiency, and targeting specific wavelength emission. In GaN-based structures, heterostructures are often generated by embedding an alloy within the barrier material, although they can also be comprised of binaries, for example in the form of a so-called digital alloy [87, 88]. A heterostructure of particular interest in this thesis is a QW, which uses

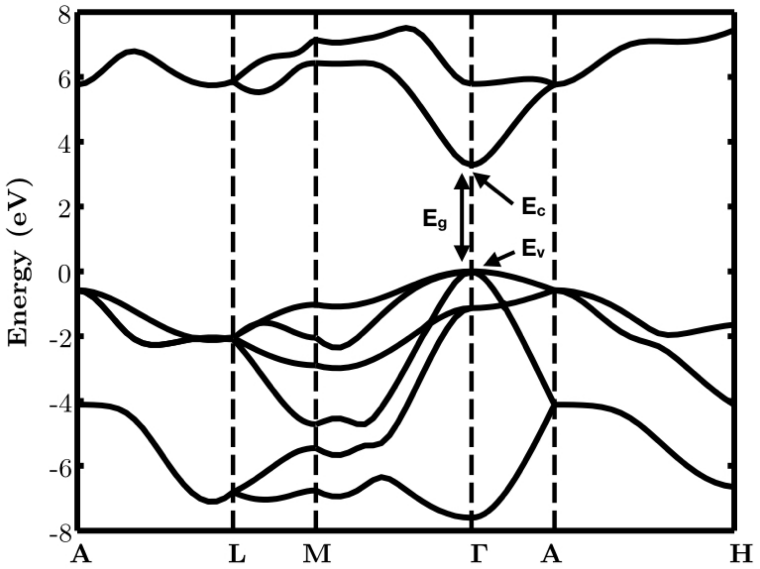

Figure 2.2: Band structure of bulk GaN calculated with Heyd-Scuseri-Ernzerhof density functional theory. The conduction band minimum (E_c) and valence band maximum (E_v) are located at Γ resulting in a direct gap material with a band gap of E_g.

differences in the band structure (such as the valence band and conduction band alignment mentioned in Section 2.1.1) of the well material and the barrier material to confine carriers in one direction, e.g. along the wurtzite c-axis.

Heterostructures can be classified by their band alignment, namely type I or type II alignment [11]. A double heterostructure with type I band alignment is shown in Fig. 2.3 (a). In this case the band gap of the material B sits entirely within the band gap of the material A. As a result, when embedded within material A a confining well for both electrons and holes is formed. If only one carrier is confined by the embedded material a type II heterostructure is formed, which is shown in Fig 2.3 (b). In the shown case only electrons will be confined by material C due to the different conduction and valence band alignments. As radiative recombination is dependent on the overlap of electron and hole wavefunctions, in LED devices normally a type I band offset is targeted.

Not only can these heterostructures aid the confining of carriers, they can also allow the tuning of the emission wavelength. For example, QWs will have a reduced (composition dependent) band gap, and this could be engineered in order to target specific colour emission wavelength. In the simplest case, the QW corresponds to a 1-D particle in a box problem. As such, the eigenenergies will also depend on the width of the box and this can be used to tailor the confined energy levels [89]. As mentioned in the prologue, the smaller QW bandgap also means the light emitted will not be reabsorbed by the barrier material before escaping the device. As such, introducing QWs reduces photon recycling [90]. A schematic of the impact of including a QW in a structure is shown in Fig. 2.4.

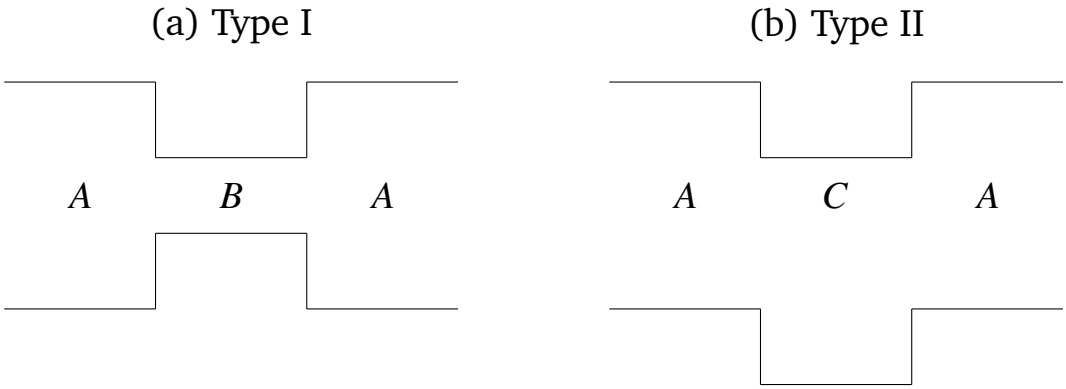

Figure 2.3: Schematic of double heterostructure formed using (a) a type I band alignment where the conduction and valence band both form a well in the region composed of material B, and (b) a type II band offset where only one band confines carriers in the region composed of material C (in this case, the conduction band).

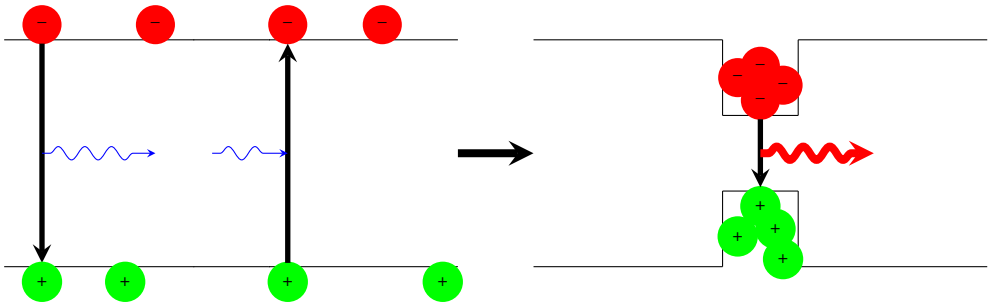

Figure 2.4: Schematic of the impact a quantum well has on electrons (red circles) and holes (green circles). When a quantum well is included the lowest energy states are confined to the low bandgap region resulting in an increased overlap of the electrons and holes and a decrease in the emission energy. The high energy photons (blue arrow) can be reabsorbed by the material and produce another electron-hole pair, while the lower energy photon (red arrow) emitted by the quantum well cannot excite carriers in the wide-bandgap material allowing it to escape the device.

The inclusion of heterostructures may be beneficial for confining carriers and manipulating emission wavelengths, however the incorporation of an alloy also leads to further effects which must be considered. For example, the a lattice constants of InN and GaN differ by approximately 11%. The lattice mismatch will lead to strain effects in the active region of (In,Ga)N/GaN-based LEDs [91].

In a bulk system or a heterostrucutre strain effects modify the electronic structure by changing material properties such as the energy band maxima and minima [92] and the effective masses [93]. In III-V materials compressive hydrostatic strain increases the band gap which is often attributed to an increase in the conduction band energy along with a decrease in the valence band energy [25]. In a heterostrucutre this will also impact the confinement of states by changing the relative energies of the conduction and valence band positions between materials comprising a heterostructure.

Strain is described by a second rank tensor,

$$\varepsilon = \begin{pmatrix} \varepsilon_{xx} & \varepsilon_{xy} & \varepsilon_{xz} \\ \varepsilon_{yx} & \varepsilon_{yy} & \varepsilon_{yz} \\ \varepsilon_{zx} & \varepsilon_{zy} & \varepsilon_{zz} \end{pmatrix} ,$$

whose ij^{th} component describes the relative change in position along the i-direction due to a deformation along the j-direction.

This can also be written in Voigt notation,

$$\varepsilon = \begin{pmatrix} \varepsilon_1 & \varepsilon_2 & \varepsilon_3 & \varepsilon_4 & \varepsilon_5 & \varepsilon_6 \end{pmatrix}^{\dagger} ,$$

where $\varepsilon_{xx} = \varepsilon_1$, $\varepsilon_{yy} = \varepsilon_2$, $\varepsilon_{zz} = \varepsilon_3$, $2\varepsilon_{yz} = \varepsilon_4$, $2\varepsilon_{xz} = \varepsilon_5$, and $2\varepsilon_{xy} = \varepsilon_6$. A more detailed description of the strain tensor and how to determine the associated strain components in a QW is presented in Section 3.3.

On top of strain effects, due to the wurtzite crystal structure these materials exhibit strong spontaneous polarization fields [94]. In a crystal consisting of more than one atomic species (whose electronegativies differ), each bond will have a certain dipole moment associated with it. In zincblende materials these dipole contributions cancel each other out, and the net dipole moment per volume, and thus the net polarization, is zero [95]. However, in wurtzite crystals, due to the lack of an inversion center along the c-direction, these contributions do not cancel and a permanent dipole per volume exists within the material along the c-direction. This is the so-called spontaneous polarization, $\mathbf{P}_{\text{sp}}$. The polarization is normally defined in terms of the distance from the anion to cation along the [0001] direction. This results in a spontaneous polarization vector pointing in the $-c$ direction for GaN and InN [96].

When a crystal is strained, deformations of the crystal lattice also lead to a polarization. This is referred to as a piezoelectric polarization and is exhibited by wurtzite crystals. This is also found in III-V zincblende materials although the polarization is generally weaker than in wurtzite III-N materials due to the more ionic nature of the III-N bonds [95].

Using Voigt notation the first-order piezoelectric polarization, $\mathbf{P}_{\text{pz}}$, in the i direction is described by [96]

$$P_{\text{pz},i} = \sum_{j=1}^{6} e_{ij}\varepsilon_j \ .$$

Elements of the strain tensor are denoted ε_j and the piezoelectric coefficients are de-

noted by e_{ij} such that the piezoelectric tensor in Voigt notation is

$$e = \begin{pmatrix} e_{11} & e_{12} & e_{13} & e_{14} & e_{15} & e_{16} \\ e_{21} & e_{22} & e_{23} & e_{24} & e_{25} & e_{26} \\ e_{31} & e_{32} & e_{33} & e_{34} & e_{35} & e_{36} \end{pmatrix} . \tag{2.5}$$

Second order polarization has also been investigated in III-N systems [97], although often this is neglected and only first order piezoelectricity is considered.

The total polarization is therefore given by the sum of the spontaneous and piezoelectric contributions,

$$\mathbf{P}_{\text{total}} = \mathbf{P}_{\text{sp}} + \mathbf{P}_{\text{pz}} .$$

If the total polarization is constant across a crystal, for example in an unstrained bulk material, the polarization will not impact the electronic structure. To demonstrate this, we consider the total charge density to be the sum of free charges and bound charges:

$$\rho_{\text{total}} = \rho_{\text{free}} + \rho_{\text{bound}} .$$

The bound charge is given by the (negative) divergence of the polarization vector [98]:

$$\rho_{\text{bound}} = -\nabla \cdot \mathbf{P} .$$

If there is no change in the polarization the bound charge is zero. On the other hand, if there is an interface between two materials of differing polarization a charge will be induced. We take for example a QW system where the well has a different polarization to the barrier, and assume that the free charge is zero; this is indicated in the schematic in Fig. 2.5. As the polarization differs across the interface a charge is induced at either side of the QW. This has a capacitor-like profile, with a large 2-dimensional (2-D) negative charge on one side and positive charge on the other. The sheet charges in turn introduces a capacitor-like potential profile, called the built-in polarization potential, which will influence the electronic and optical properties of the system.

In a III-N-based QW this leads to a potential drop across the heterostructure. This can lead to the spatial separation of electrons and holes leading to a reduction in recombination rate and a red shift in the emission wavelength, known as the quantum confined stark effect (QCSE) [99], which is illustrated in Fig. 2.6. A detailed discussion around how to calculate the profile of this field in a continuum and atomistic picture is presented in Section 3.3.

Here we have presented some general aspects of crystal structures with attention directed towards wurtzite III-N heterostructures. We are interested in device behaviour, for example in a light emitting diode. Therefore, we turn our attention to the background of *p*-*n* junctions in the next section, which are a key element in LEDs.

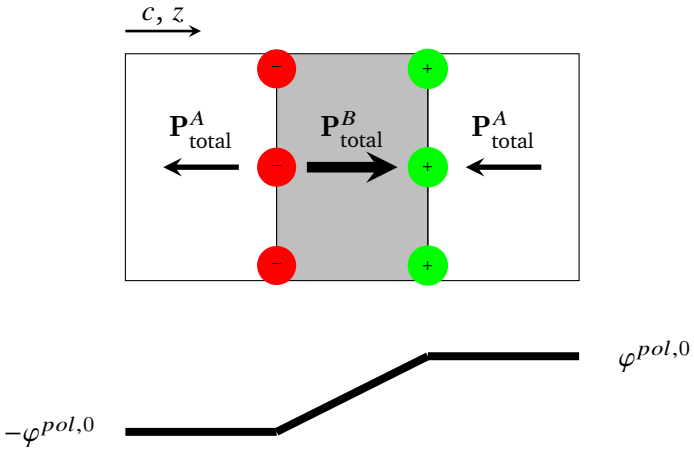

Figure 2.5: A change in the total polarization vector results in a bound charge being formed between regions of material A (white) and material B (grey); material B has a different polarization than material A. At the left (right) interface a negative (positive) sheet charge is formed similar to that of a capacitor. The form of the potential profile is shown below the figure.

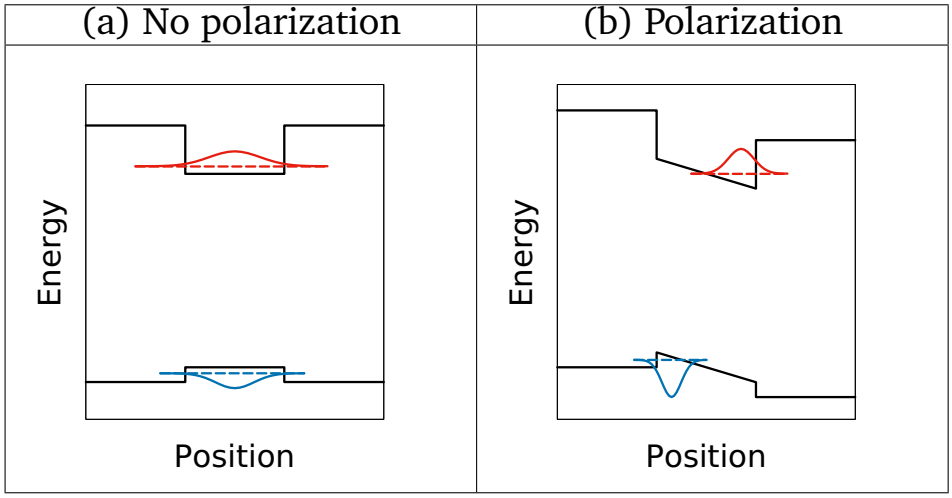

Figure 2.6: Schematic of the conduction and valence band edges are shown in black, and the electron (hole) profile in red (blue). The energy of the state is denoted using a dashed line of the same colour. The behaviour is indicated (a) excluding and (b) including the polarization potential which results in the spatial separation of the electron and hole, and a decrease in the band gap.

2.2 Light-emitting diodes

We have already seen in the prologue that LEDs are semiconductor optoelectronic devices which are used to produce light when a bias voltage is applied. This generally consists of a so-called p-n junction; a connection of two materials which have been p- and n-doped in order to generate free carriers which can be used to produce light through a radiative recombination process of these carriers. Materials can be p-doped by 'acceptor' atoms, in order to produce loosely bound holes which are free to more within the material, or n-doped by 'donor' atoms to similarly produce loosely bound

electrons. The energy level of these dopants is shown in the schematic in Fig. 2.7. To excite the electrons or holes to the conduction or valence band requires ideally a small amount of energy. This is referred to as the dopant activation energy for donors, ΔE_D and acceptors, ΔE_A.

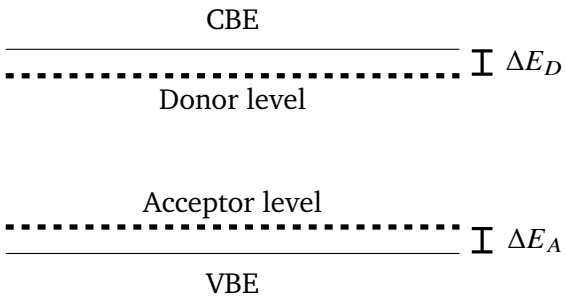

Figure 2.7: Schematic illustrating the conduction and valence band edges (CBE and VBE) in a semiconductor (solid lines). The acceptor and donor levels sit within the band gap close to the band edges such that it ideally takes a small amount of (thermal) energy, ΔE_A or ΔE_D, to excite carriers to the band edges.

The amount of free carriers at a point is described via the Fermi level. Introducing dopants moves the Fermi level either towards the valence band edge (VBE) in the case of p-doping, or towards the conduction band edge (CBE) in the case of n-doping [100].

Bringing n- and p-doped materials into contact with each other therefore would lead to a jump in the Fermi level across the p-n junction even at equilibrium. As we will see in later discussions, a change in the Fermi level indicates that current is flowing, which is not the case in equilibrium.

Fick's law tells us that particles will tend to move from regions of high concentration to low concentration [101]. Therefore when the two doped regions are brought into contact electrons and holes *diffuse* into the opposite region due to the large concentration difference across the junction. This creates regions at the interface of the n- and p-doped sections which are not charge neutral, introducing an electric field between the doped regions. The electric field causes the *drift* of carriers, opposing the diffusion of the electrons and holes at equilibrium. Carrier drift can be increased by applying an external electric field through an applied bias, V_A, causing a net current through the junction.

The electric field can be described as the negative gradient of the electric potential, which can be calculated via Poisson's equation:

$$-\nabla \cdot \big(\epsilon(\mathbf{r})\nabla\psi(\mathbf{r})\big) = \rho(\mathbf{r}) \ . \tag{2.6}$$

The potential is given by ψ and depends on the (position dependent) dielectric constant ϵ and charge density ρ. This potential causes a band bending, modifying the conduction and valence band edges which are given by $\mathrm{CBE}(\mathbf{r}) = E_c(\mathbf{r}) - q\psi(\mathbf{r})$ and $\mathrm{VBE}(\mathbf{r}) =$

$E_v(\mathbf{r}) - q\psi(\mathbf{r})$ where $E_{c,v}$ is the band edge energies of the intrinsic material when not impacted by the potential ψ; q is the elementary charge. A schematic of the band edges in a p-n junction in the absence of any applied bias ($V_A = 0$) is shown in Fig. 2.8. The potential drop from the n-doped to the p-doped region without applying a bias is called the built-in voltage, V_{BI}.

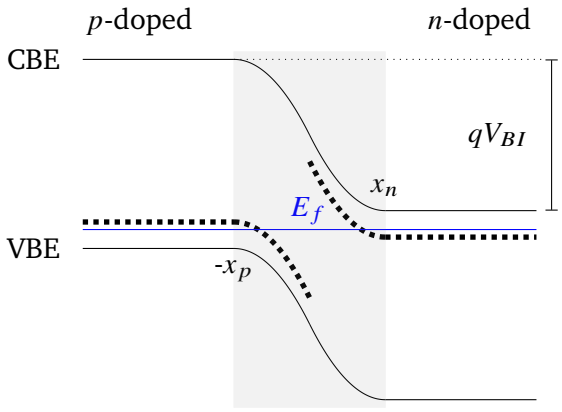

Figure 2.8: Schematic of the conduction and valence band edge profile in a p-n junction. The Fermi level (blue) is constant in equilibrium resulting in a potential drop across the junction with energy qV_{BI}. A region with low free carrier density (depletion region) is formed between $-x_p$ and x_n (shaded in grey). The donor levels are indicated with dashed black lines.

Now we have a structure whose Fermi level at equilibrium is flat (as physically is required). When, for example, electrons diffuse to the p-doped region there are many holes for them to recombine with, either radiatively or non-radiatively (the same goes for holes which diffuse to the n-doped region). When these carriers recombine there are less free carriers available for transport processes. This region with a low density of free carriers is called the *depletion region* and is shown in grey shading in Fig. 2.8. Using the approximation that the free charge density profile is piecewise-constant (see Fig. 2.9) the width of this depletion region can be estimated via [102]

$$W_D = x_n + x_p = \sqrt{\frac{2\epsilon(V_{BI} - V_A)}{q}\frac{N_D + N_A}{N_D N_A}}$$

where V_{BI}, V_A, N_A and N_D are the built-in voltage, applied voltage, acceptor doping density and donor doping density respectively.

A more accurate treatment of the junction would self-consistently calculate the device potential and free charge densities when the Fermi level is constant [103], however the assumption of piece-wise constant densities offers a good starting point which we can use to gain insight into the behaviour of these junctions.

The size of the depletion region depends on the doping densities used, and varies with applied bias. If a bias is applied so that the field pulls the electrons and holes away

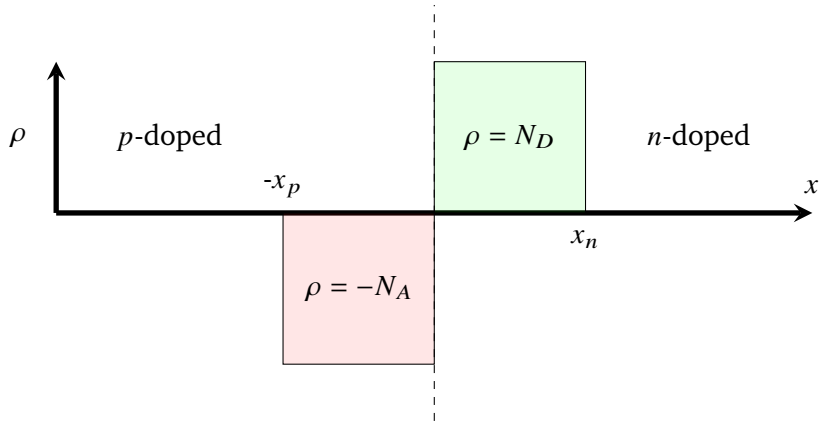

Figure 2.9: Charge density profile of a p-n junction (p-doping on the left, n-doping on the right) assuming that carriers diffuse across the interface (dashed line) and completely recombine with the majority carrier up until a point ($x_{p,n}$) causing a non-zero charge density. Beyond this point the charge density is 0.

from the depletion layer (reverse bias) the width of the depletion layer is increased. Conversely, if the voltage applies a field that pushes electrons and holes towards the depletion region (forward bias) the depletion width decreases. As the applied bias approached the built-in potential the depletion width goes to zero.

In order to extract light from these devices the junction is normally operated with forward voltage, allowing current to flow and carriers to recombine. It would be beneficial to maximize the recombination rate from devices by encouraging electrons and holes to be located in the same region in space. This can be achieved by adding confining structures to the junction, such as a QW (as discussed in Section 2.1.2); QW structures are a common addition to LEDs (c.f. Fig. 1.1).

We saw in this section that describing a III-N based LED requires an understanding of crystal structures, alloys, heterostructures, electronic structure and device behaviour. In the next part we shall consider the theoretical models used to study transport in (In,Ga)N QW systems. In order to understand carrier transport we require a description of the electronic structure. To construct this we shall follow a similar format and start our discussion with a description of the electronic structure of a bulk crystal. Then we shall add the necessary ingredients we need to describe alloys and heterostructures, including strain and polarization effects found in III-N QW systems. In Chapter 4 we shall discuss the theory of quantum transport as well as full device modeling in a semi-classical framework.

Part II

Theory

Chapter 3

Electronic structure theory

The behaviour of optoelectronic devices will be strongly dependent on the electronic structure of the device. The spatial and energetic distribution of electron and hole states will have a significant impact on transport and optical properties of a system. Therefore an accurate description of the underlying electronic structure is a key ingredient for our description of the transport properties of a device.

There are two broad categories for both electronic structure calculations and transport models: (i) *ab initio* calculations which do not need (at least in principle) any input parameters, and (ii) semi-empirical models which require extra information from experiment or first principle calculations. In the first category, from an electronic structure point of view falls density functional theory (DFT), whereas transport might be studied from first principles using the NEGF formalism.

DFT starts from the many-body Hamiltonian (using the Born-Oppenheimer approximation [104]) introduced in Section 2.1.1 to determine the many-body ground state charge density. To solve this problem, the system is often mapped to a system where the kinetic energy contribution is described by a non-interacting system and exchange and correlation effects between the carriers are described by exchange-correlation functionals. For the latter, several different approximations can be used, starting from the well know local density approximation up to newly developed hybrid functional schemes [104]. Once such an equation is established, the variational principle can be used to find the many-body density which minimizes the energy of the ground state [105]. This is ideally suited to a periodic system, which, as we discussed, can be completely described through the primitive unit cell. While DFT has been applied to alloys [86], and nanostructures such as quantum dots [106, 107], many density functional theories (such as the Kohn-Sham formalism [108]) scale with the number of atoms cubed, making DFT calculations of larger systems unattainable.

On top of this, extending parameter-free first principle calculations to study transport in fully quantum mechanical framework using a DFT-NEGF approach is a numerically

extremely demanding task and thus limited to small systems [109–111]. In order to model a heterostructure including the effects of alloy disorder in a (multi) QW system, the system size is typically on the order of at least $\approx 10^5$ atoms, much larger than those previously studies using DFT-NEGF frameworks.

One available option is to implement our second category of electronic structure theory. Semi-empirical methods can be designed in order to reproduce the highly accurate results from DFT, while simultaneously being capable of modeling larger systems. This could then be coupled to an *ab initio* transport solver to accurately model quantum transport, or connected to semi-classical frameworks; both of these options will be discussed in Chapter 4. Therefore we proceed by introducing such theories which can reproduce DFT band structures (at least in specific regions of the Brillouin zone), namely $\mathbf{k}\cdot\mathbf{p}$ theory and atomistic tight-binding.

3.1 $\mathbf{k}\cdot\mathbf{p}$ and effective mass approximation

$\mathbf{k}\cdot\mathbf{p}$ theory is based on time-independent perturbation theory. This model is used to accurately describe the electronic structure of a material close to a selected $\mathbf{k}$-point in the first Brillouin zone at which the energy and wave functions are known [112]. This be used to treat different crystal structures (e.g. zincblende, wurtzite) [113,114] with various levels of refinement. For example, the number of basis states (bands) can be varied (e.g. single-band, 8-band) [4, 113], with or without including the impact that spin has on the results [112]. This can be applied to bulk systems, but also to nanostructures and larger device structures due to the reduced numerical demand compared to DFT. We shall first consider the model applied to a bulk crystal, before briefly discussing the modifications needed to apply it to an alloy.

Following the formalism of Kane, the $\mathbf{k}\cdot\mathbf{p}$ Hamiltonian is derived by plugging the Bloch wave function (Eq. (2.4)) into the single particle Hamiltonian (Eq. (2.3)) [112]. The $\mathbf{k}\cdot\mathbf{p}$ Hamiltonian is

$$\hat{H} = \frac{\hat{p}^2}{2m} + \frac{\hbar^2}{2m}k^2 + \frac{\hbar}{m}\mathbf{k}\cdot\mathbf{p} + \hat{V} \ . \tag{3.1}$$

Here we are neglecting spin-orbit coupling, which is much smaller than in other III-V materials (e.g. splitting due to spin-orbit coupling is approximately 0.017 eV in GaN [24] vs 0.341 in GaAs [25]). Details of how to include this in a $\mathbf{k}\cdot\mathbf{p}$ formalism are discussed in Ref. [112]. The second last term (linear in $\mathbf{k}$) gives the Hamiltonian it's name. Defining $\hat{H}_{\mathbf{k_0}}$ to be the Hamiltonian at $\mathbf{k} = \mathbf{k_0}$ (a k-point of particular interest, at which the energy and wave functions are known),

$$\hat{H}_{\mathbf{k_0}} = \frac{\hat{p}^2}{2m} + \frac{\hbar^2}{2m}k_0^2 + \frac{\hbar}{m}\mathbf{k_0}\cdot\mathbf{p} + \hat{V} \ ,$$

then Eq. (3.1) can be expressed as

$$\hat{H} = \hat{H}_{\mathbf{k_0}} + \frac{\hbar^2}{2m}(k^2 - k_0^2) + \frac{\hbar}{m}(\mathbf{k} - \mathbf{k_0})\cdot\mathbf{p} \ .$$

In Chapter 2 we saw that in the case of III-N materials, the conduction band minimum and valence band maximum occur at the Γ-point, so here we will only describe equations expanding around $\mathbf{k_0} = \mathbf{0}$. While the expression in Eq. (3.1) is exact, the final two terms can be treated as a perturbation to the system around $\mathbf{k_0}$, and properties of the system can be approximated using perturbation theory [115].

The energy of the n^{th} non-degenerate band as a function of $\mathbf{k}$, approximated by second order perturbation theory, is [85]

$$E_n(\mathbf{k}) = E_n(\mathbf{0}) + \frac{\hbar}{m}\mathbf{k}\cdot\mathbf{p}_{nn} + \frac{\hbar^2 k^2}{2m} + \frac{\hbar^2}{m^2}\sum_{n'\neq n}\frac{|\mathbf{k}\cdot\mathbf{p}_{\mathbf{nn'}}|^2}{E_n(\mathbf{0}) - E_{n'}(\mathbf{0})} \ , \tag{3.2}$$

where

$$\mathbf{p}_{\mathbf{nn'}} = \langle u_{n\mathbf{k_0}}|\,\mathbf{p}\,|u_{n'\mathbf{k_0}}\rangle \ .$$

In diamond crystals structures, due to symmetry considerations the term linear in $\mathbf{k}$ ($\mathbf{k}\cdot\mathbf{p}_{nn}$) is identically zero [85,112]; in III-N semiconductor materials this term is small compared to the quadratic contribution [85, 116]. We follow the widely employed approximation and neglect this term going forward leaving only terms independent of $\mathbf{k}$ or quadratic in $\mathbf{k}$.

When employing a $\mathbf{k}\cdot\mathbf{p}$ model generally there is an energy scale which is of particular interest for the study (for example, close to the conduction and valence band edges). Bands in this energy range will interact with each other, but will also be impacted (to a lesser extent) by bands which are farther away in energy. Following the approach of Löwdin, these bands can be divided into two distinct categories; A-bands which will be treated explicitly, and B-bands which will not be treated explicitly, although the coupling which they have with the A-bands will be considered implicitly [117]. This allows the restriction of basis states to only a small subset of the total bands, which significantly decreases the numerical demand and the complexity of the model, while still providing an accurate description of the band structure in the energy range of interest.

In this case Eq. (3.2) becomes

$$E_n(\mathbf{k}) = E_n(\mathbf{0}) + \frac{\hbar^2 k^2}{2m} + \frac{\hbar^2}{m^2}\sum_{n'\in A\neq n}\frac{|\mathbf{k}\cdot\mathbf{p}_{\mathbf{nn'}}|^2}{E_n(\mathbf{0}) - E'_n(\mathbf{0})} + \frac{\hbar^2}{m^2}\sum_{n'\in B}\frac{|\mathbf{k}\cdot\mathbf{p}_{\mathbf{nn'}}|^2}{E_n(\mathbf{0}) - E'_n(\mathbf{0})} \ . \tag{3.3}$$

The simplest case is a single band model. Here only one band is treated explicitly, e.g. the conduction band. This is the only A-class band, so the sum over A in Eq. (3.3) does not contain any terms. The B-class bands modify the band via the effective mass

chosen in the Hamiltonian, which impacts the parabolicity of the band in question:

$$E^{\mathrm{EMA}} = E(\mathbf{0}) + \frac{\hbar^2}{2m_x^*}k_x^2 + \frac{\hbar^2}{2m_y^*}k_y^2 + \frac{\hbar^2}{2m_z^*}k_z^2 \ ,$$

where

$$m_l^* = \left(\frac{1}{m} + \frac{2}{m^2}\sum_{n'\in B}\frac{|\hat{\mathbf{l}}\cdot\mathbf{p}_{\mathbf{nn'}}^{\mathbf{2}}|}{E_n(\mathbf{0}) - E_{n'}(\mathbf{0})}\right)^{-1}$$

is the effective mass along the l-direction, $\hat{\mathbf{l}}$ is the unit vector in this $\mathbf{k}$-direction [112]. $E(\mathbf{0})$ describes the band energy at the Γ-point, therefore this can give a good approximation of states close to the Γ-point where the band is approximately parabolic, however will break down for $\mathbf{k}$-vectors farther away from this point.

So far we have only considered the case of a non-degenerate band. If $E_n(\mathbf{0})$ is degenerate then the denominator of some terms will be zero. The theory can be modified to include degenerate bands using, for instance, the Luttinger-Kohn model; more details can be found in Ref. [118].

Due to the small number of bands needed to implement $\mathbf{k}\cdot\mathbf{p}$ models, they can be applied to quantum confining structures such as dots, wires and wells of realistic size and geometry, providing a significant benefit over *ab initio* frameworks in terms of numerical expense. However they also require a large number of input parameters which are (in principle) not required in *ab initio* models. This may be a drawback, as it can involve complex fitting procedures in order to try and obtain parameters. On the other hand, it may be beneficial as it can offer control over aspects which are not well described in some *ab initio* frameworks, e.g. the band gap of many materials predicted using a local density approximation [105]. The single band EMA only requires two free parameters, the effective mass and the energy at $\mathbf{k_0}$. However the number of parameters increases with the number of A-class bands considered. If multiple bands are implemented in a wurtzite crystal the effective mass is replaced by Luttinger-like parameters to describe the impact of the class B bands [114].

3.1.1 Extending the model beyond bulk crystal structures

Our discussion until now has centered on describing the electronic properties of a pure bulk crystal, where the infinite crystal can be modeled by considering only a single unit cell (recall discussion in Section 2.1.1). This can be modified in order to extend the model to an alloy by considering a virtual material.

The "bandstructure" of an alloy can be calculated using the $\mathbf{k}\cdot\mathbf{p}$ method using the so-called virtual crystal approximation (VCA). In this case an effective unit cell is constructed whose properties are assumed to be an interpolation of the properties of the constituent bulk materials. For example, in an $In_xGa_{1-x}N$ virtual crystal the material

parameter A might be assumed to be

$$A^{\mathrm{InGaN}}(x) = x \cdot A^{\mathrm{InN}} + (1-x) \cdot A^{\mathrm{GaN}} + x(1-x) \cdot B^{\mathrm{InGaN}} \ ,$$

where the superscript denotes the given bulk material parameter, B^{InGaN} is the bowing parameter associated with non-linear changes in the parameter with alloy composition, and x is the fractional InN content of the alloy [24].

If the electronic structure is only weakly perturbed by including an alloy then this approach may provide good results (e.g. InGaAs/GaAs QW systems [119]). However, if the underlying microstructure is important for describing these effects the $\mathbf{k}\cdot\mathbf{p}$ method may not provide the required resolution of the crystal. An atomistic model may be required which resolves the individual atoms within the unit cells. In the next section we proceed to introduce the tight-binding model which can provide such a resolution.

3.2 Tight-binding model

The tight-binding (TB) model is an atomistic description of a lattice which uses a small number of strongly localized atomic-like orbitals as basis states. TB is a flexible method and can be applied to a variety of problems, and adjusted to suit the needs of each problem being addressed. As is the case with $\mathbf{k}\cdot\mathbf{p}$ theory, it can be used to model different crystal structures (cubic, zincblende, wurtzite) [75, 120, 121] and be treated with varying levels of complexity. For example, the number of basis states used (sp^3, $sp^3d^5s^\star$) [122,123], the cut-off distance where orbital interactions are considered (nearest-neighbour, next-nearest-neighbour) [124, 125], and the inclusion or omission of spin-orbit coupling [126] can all be considered. Here we discuss the construction of a single-particle TB Hamiltonian using a nearest-neighbour model which neglects spin-orbit coupling.

TB models assume atomic-like basis states which are tightly bound to the atoms that they are located on, and as such the interaction that this state has with states on surrounding atoms decreases quickly as separation is increased [74,75]. The potential due to the lattice acts as a perturbation to the state. We follow the derivation in Ref. [74] and start with the energy of an isolated ν orbital sitting at the atom of species α in the $\mathbf{R_n}^{\mathrm{th}}$ unit cell. The Schrödinger equation is given in Eq. (3.4).

$$\hat{H}^{\mathrm{atomic}} \left|\mathbf{R_n}, \alpha, \nu\right\rangle = \left(\frac{\hat{\mathbf{p}}^2}{2m} + \hat{V}^{\mathrm{atomic}}\right) \left|\mathbf{R_n}, \alpha, \nu\right\rangle = E^{\mathrm{atomic}}_{\alpha,\nu} \left|\mathbf{R_n}, \alpha, \nu\right\rangle \ . \tag{3.4}$$

Given that we know the properties of the isolated atom, we are interested in modeling how this changes when the atoms interacts with other nearby atoms. In the case of a

crystal we are interested in the modification due to all the other atoms in the lattice:

$$\hat{H}^{\text{bulk}} = \hat{H}^{\text{atomic}} + \hat{V}^{\text{lattice}} = \hat{H}^{\text{atomic}}_{\alpha,\nu} + \sum_{m}\sum_{\alpha'} V(\mathbf{R_m}, \alpha')(1 - \delta_{n,m}\delta_{\alpha,\alpha'}) \ . \tag{3.5}$$

$\hat{V}^{\text{lattice}}$ is the potential at the atom under consideration due to all atoms in the crystal, neglecting the α atom in the unit cell $\mathbf{R_n}$ itself, which is already accounted for in the atomic term, $\hat{H}^{\text{atomic}}$, of the full Hamiltonian, $\hat{H}^{\text{bulk}}$. This potential is periodic in a bulk crystal, and therefore this is satisfied by Bloch states. The basis states can be written in reciprocal space as

$$|\mathbf{k}, \alpha, \nu\rangle = \frac{1}{\sqrt{N}} \sum_{n} e^{i\mathbf{k}\cdot(\mathbf{R_n}+\mathbf{\Delta}_\alpha)} \, |\mathbf{R_n}, \alpha, \nu\rangle \ . \tag{3.6}$$

Here the atom α is located at position $\mathbf{\Delta}_\alpha$ within the unit cell at $\mathbf{R_n}$, and N is the number of unit cells in considered in the system. We can have more than one atom in the basis, as seen in Section 2.1 the wurtzite crystal consists of a four atom basis on a hexagonal lattice; $\{\mathbf{\Delta}_\alpha\}$ forms the basis of the crystal and $\mathbf{R_n}$ denotes the location of the unit cell in the lattice.

We are now able to construct a wave function as a linear combination of our basis states by summing over all orbitals and atomic sites considered:

$$|\mathbf{k}\rangle = \sum_{\alpha,'\nu'} c_{\alpha',\nu'}(\mathbf{k}) \, |\mathbf{k}, \alpha', \nu'\rangle = \sum_{\alpha',\nu'} c_{\alpha',\nu'}(\mathbf{k}) \left(\frac{1}{\sqrt{N}} \sum_{n'} e^{i\mathbf{k}\cdot(\mathbf{R_{n'}}+\mathbf{\Delta}_{\alpha'})} \, |\mathbf{R_{n'}}, \alpha', \nu'\rangle \right) . \tag{3.7}$$

The coefficients of the wave function, $c_{\alpha',\nu'}(\mathbf{k})$, can be determined by solving the Schrödinger equation,

$$\hat{H}^{\text{bulk}} \, |\mathbf{k}\rangle = E(\mathbf{k}) \, |\mathbf{k}\rangle \ .$$

By applying $\langle \mathbf{k}, \alpha, \nu|$ from the left we arrive at the matrix equation:

$$\sum_{\alpha',\nu'} [\langle \mathbf{k}, \alpha, \nu|\hat{H}^{\text{bulk}} c_{\alpha',\nu'} |\mathbf{k}, \alpha', \nu'\rangle - E(\mathbf{k}) c_{\alpha',\nu'} \langle \mathbf{k}, \alpha, \nu|\mathbf{k}, \alpha', \nu'\rangle] = 0 \ .$$

The tightly-bound orbitals on different lattice sites which are used as basis states are not generally orthogonal. They can, however be transformed using a Löwdin transform which orthogonalizes these states while also maintaining the symmetry of the original orbitals [127]. As such, we can use the identity $\langle \mathbf{k}, \alpha, \nu|\mathbf{k}, \alpha', \nu'\rangle = \delta_{\alpha,\alpha'}\delta_{\nu,\nu'}$ to arrive at the expression:

$$\sum_{\alpha',\nu'} \langle \mathbf{k}, \alpha, \nu|\hat{H}^{\text{bulk}}|\mathbf{k}, \alpha', \nu'\rangle \, c_{\alpha',\nu'} = E(\mathbf{k}) c_{\alpha,\nu} \ . \tag{3.8}$$

For the sake of simplified discussion we shall now assume that there is only one atom per unit cell, α, which contains only one orbital as a basis state, ν. In this case Eq. (3.8) is simplified to

$$\langle \mathbf{k}, \alpha, \nu|\hat{H}^{\text{bulk}}|\mathbf{k}, \alpha, \nu\rangle = E(\mathbf{k}) \ .$$

Applying our ansatz for $|\mathbf{k}, \alpha, \nu\rangle$ from Eq. (3.6) results in

$$\frac{1}{N}\sum_{n,n'} e^{i\mathbf{k}\cdot(\mathbf{R}_{\mathbf{n}'}+\boldsymbol{\Delta}_{\alpha'}-\mathbf{R}_{\mathbf{n}}-\boldsymbol{\Delta}_{\alpha})} \langle \mathbf{R}_{\mathbf{n}}, \alpha, \nu|\hat{H}^{\text{bulk}}|\mathbf{R}_{\mathbf{n}'}, \alpha', \nu'\rangle = E(\mathbf{k}) \,.$$

The translational invariance of the crystal allows us to remove one of the sums over the unit cells and the divisor of N, as the result for each unit cell is the same and we end up adding this result N times and dividing by N, so instead we can focus on one cell located at a fixed position, $\mathbf{R_0}$.

$$\sum_{n'} e^{i\mathbf{k}\cdot(\mathbf{R}_{\mathbf{n}'}+\boldsymbol{\Delta}_{\alpha'}-\mathbf{R_0}-\boldsymbol{\Delta}_{\alpha})} \langle \mathbf{R_0}, \alpha, \nu|\hat{H}^{\text{bulk}}|\mathbf{R}_{\mathbf{n}'}, \alpha', \nu'\rangle = E(\mathbf{k}) \,. \tag{3.9}$$

Considering just the $\langle \mathbf{R_0}, \alpha, \nu|\, \hat{H}^{\text{bulk}}\, |\mathbf{R}_{\mathbf{n}'}, \alpha', \nu'\rangle$ term for now, and recalling the expression for the bulk Hamiltonian from Eq. (3.5):

$$\begin{aligned}\langle \mathbf{R_0}, \alpha, \nu|\, \hat{H}^{\text{bulk}}\, |\mathbf{R}_{\mathbf{n}'}, \alpha', \nu'\rangle &= E^{\text{atomic}}_{\alpha',\nu'}\delta_{0,n'}\delta_{\alpha,\alpha'}\delta_{\nu,\nu'} \\ &\quad + \sum_m \sum_\alpha \langle \mathbf{R_0}, \alpha, \nu|\, V(\mathbf{R}_{\mathbf{m}}, \alpha)\, |\mathbf{R}_{\mathbf{n}'}, \alpha', \nu'\rangle\, (1 - \delta_{n',m}\delta_{\alpha,\alpha'}) \,.\end{aligned} \tag{3.10}$$

Since we are considering only one atom species and orbital type $\alpha' = \alpha$ and $\nu' = \nu$. The sum including the potential from the lattice can now be expanded according to the proximity of the neighbouring atoms to the atom which we are focusing on. The same principle can be applied with multiple atoms in the cell, however the added complexity is not rewarded with deeper insight.

Dividing this up into groups depending on the proximity of the unit cells $\mathbf{R_0}$ to $\mathbf{R}_{\mathbf{n}'}$, Eq. (3.10) becomes

$$\begin{aligned}\langle \mathbf{R_0}, \alpha, \nu|\, \hat{H}^{\text{bulk}}\, |\mathbf{R}_{\mathbf{n}'}, \alpha, \nu\rangle = &\left[E^{\text{atomic}}_{\alpha,\nu} + \sum_{m\neq n'} \langle \mathbf{R_0}, \alpha, \nu|\, V(\mathbf{R}_{\mathbf{m}}, \alpha)\, |\mathbf{R}_{\mathbf{n}'}, \alpha, \nu\rangle\right]\delta_{0,n'} \\ &+ \left[\sum_m \langle \mathbf{R_0}, \alpha, \nu|\, V(\mathbf{R}_{\mathbf{m}}, \alpha)\, |\mathbf{R}_{\mathbf{n}'}, \alpha, \nu\rangle\right]\delta_{0\pm1,n'} \\ &+ \left[\sum_m \langle \mathbf{R_0}, \alpha, \nu|\, V(\mathbf{R}_{\mathbf{m}}, \alpha)\, |\mathbf{R}_{\mathbf{n}'}, \alpha, \nu\rangle\right]\delta_{0\pm2,n'} \\ &+ \ldots\end{aligned} \tag{3.11}$$

As the basis states are assumed to be strongly bound to their lattice site the overlaps decrease quickly as the separation between atomic sites is increased [74, 75]. As such, the sum in Eq. (3.11) can be truncated appropriately (nearest-neighbour model: truncate after $\delta_{0\pm1,n'}$, next-nearest-neighbour model: truncate after $\delta_{0\pm2,n'}$, etc.). The first bracket in the expression above is called the *on-site energy*,

$$E^{\text{on-site}}_{\alpha,\nu} = E^{\text{atomic}}_{\alpha,\nu} + \sum_{m\neq 0} \langle \mathbf{R_0}, \alpha, \nu|\, V(\mathbf{R}_{\mathbf{m}}, \alpha)\, |\mathbf{R_0}, \alpha, \nu\rangle \,. \tag{3.12}$$

This is the energy of an orbital sitting on the lattice site being considered ($\mathbf{R_0}$ in this case) which has been modified by the presence of the other atoms in the crystal. The other terms (which constitute the off-diagonal terms in the TB Hamiltonian matrix, when including a phase term as seen in Eq. (3.9)) are hopping terms which describe the coupling between orbitals on separate atomic sites.

The evaluation of the quantities in this expression requires solving two-center integrals involving the potential at position $\mathbf{R_0}$ due to the atom at $\mathbf{R_m}$ as well as three-center integrals which include for example an orbital sitting at $\mathbf{R_0}$, an orbital sitting at $\mathbf{R_{n'}}$ and the potential due to an atom $\mathbf{R_m}$, where $0 \neq n' \neq m$. One approach proposed by Slater and Koster is to neglect these three-center integrals, as these terms are significantly smaller than the two-center integral contributions [120]. In this approximation the sum over the entire crystal is reduced to considering two spherical potentials located (in the case of Eq. (3.11)) at $\mathbf{R_0}$ and $\mathbf{R_{n'}}$. Slater and Koster determine expressions for the hopping terms of a TB Hamiltonian based on the orbital (and bond) type, and direction cosines which indicate the angle between the atoms being considered [120].

The matrix elements needed in the TB model could be calculated from *ab initio* approaches in, for example, DFT-based TB methods [128–130]. An alternate approach is to take the TB matrix elements and use them as free parameters to fit results to band structure data. The number of free parameters will depend on the number of orbitals included at each atomic site and the number of neighbours which are considered to have non-zero hopping terms. This semi-empirical approach is widely employed [121, 131, 132]. The TB model used throughout this thesis is a semi-empirical sp^3, nearest-neighbour model which has been benchmarked against Heyd-Scuseri-Ernzerhof (HSE) hybrid functional DFT [96].

3.2.1 Extending the model beyond bulk crystal structures

We saw in the $\mathbf{k}\cdot\mathbf{p}$ theory that an alloy could be modeled in the form of a virtual crystal. The same principle can be applied to the TB model, where the onsite energies and hopping terms can be described as interpolated values of the bulk materials constituting the alloy. This provides a continuum approximation for the description of an alloy.

A drawback of the $\mathbf{k}\cdot\mathbf{p}$ model is that it is defined only down to the unit cell, and individual atoms (such as anion and cation species) are not resolved. This limitation is not present in the case of TB where the individual atoms are modeled explicitly. This allows for the treatment of an alloy without generating an effective material composed of virtual atoms.

Here we consider the example of an (In,Ga)N alloy which is treated using a nearest-neighbour TB model. The parameters for bulk InN and GaN can be determined from bulk band structure as discussed, providing the on-site energies and hopping terms of gallium and nitrogen atoms in GaN and of indium and nitrogen atoms in InN. Due

to the crystal structure, the neighbours of all cation sites (indium or gallium) will be nitrogen. Therefore the nearest-neighbour environment is the same as in a bulk crystal, so the on-site energy and hopping terms will also be the same as the bulk material (if strain effects are neglected). At the anion sites the situation is not so straightforward, as the neighbours could be either gallium or indium. The on-site energy of a given atomic species may differ between the bulk binaries, as is the case between InN and GaN [96]. A common approach is to assign the on-site energy as a weighted average which is dependent on the local environment of the atom in the system [133–135]. For example, a nitrogen atom with three gallium neighbours and one indium neighbour would be assigned on-site energies which are a combination of the on-site energies of GaN and of InN in a ratio of 3:1. In future calculations we assume that in regions of (In,Ga)N the indium atoms are distributed randomly (random alloy), without including any clustering. This is in line with experimental observations [40].

We have described two methods for describing an alloy with TB: a virtual crystal and a random alloy. A comparison of the results from these two approaches for a given alloy composition allows us to investigate the impact that alloy fluctuations have on various properties.

The second approach requires the construction of a supercell containing many unit cells to generate a distribution of indium and gallium atoms. This breaks the translational symmetry which was originally present in the system. The assumption that $\mathbf{k}$ is a good quantum number is no longer valid, and therefore we do not consider a dispersion relation when discussing an alloy, instead taking $\mathbf{k} = \mathbf{0}$.

As already indicated above, so far we have discussed an alloy without mentioning strain or polarization effects which may impact (for example) the energies of orbitals at a given lattice site. We saw in Chapter 2 that these can have an impact on electronic properties of a material. In the next section we extend our discussion to a heterostructure to include these effects, as well as other points of consideration for modeling an alloy.

3.3 Heterostructures

The TB and $\mathbf{k}\cdot\mathbf{p}$ models have been introduced for both binary and alloy III-N materials. In order to extend the models to heterostructures one important aspect, which was mentioned in Section 2.1.1, is the relative band offset values of different materials.

In Chapter 2 we introduced heterostructures, and discussed how a type I band alignment could be used to (e.g.) confine electrons and holes. Two aspects are important. First, the band gap of the confining material should be smaller than the barrier material. Second, the natural valence band edge offset (which does not include modifications from strain or polarization effect) will impact characteristics.

Determining the (composition dependent) direct band gap of a material can be achieved via spectroscopic techniques [136, 137]. However the band alignment between unstrained systems cannot be determined so straightforwardly. The question was targeted for (In,Ga)N alloys theoretically by Moses and Van de Walle who used (non-polar) surface calculations to align the conduction and valence band edges relative to the vacuum level with hybrid functional DFT [86]. As already mentioned, results showed that the InN natural valence band edge offset is 0.62 eV above the GaN band edge.

The relative band alignment is included in both the $\mathbf{k}\cdot\mathbf{p}$ and TB models through the matrix elements used to describe a unit cell of the bulk materials. When this has been considered, a description of an alloy or a heterostructure can be constructed. Beyond this, strain and polarization will also play a role. In this thesis we are primarily concerned with alloys in the context of a c-plane QW structure, embedded within a binary material. Our discussion around the description of strain and polarization will focus on these heterostructures, which simplifies their profiles somewhat compared to, for example, a quantum dot [138].

3.3.1 Strain

We start with a description of strain in an alloy. We have seen already in Chapter 2 that strain effects can impact the electronic structure of a material. The strain in an alloy can be divided into two categories: macroscopic effects, which occur on the length scale of a unit cell or larger, and microscopic effects which occur on the atomic scale (e.g. embedding an indium atom in a GaN crystal would result in a local strain around the indium atom). Though we are ultimately interested in modeling an alloy in an atomistic framework we shall start in the continuum picture, which is the implementation used to include effects in a VCA. Here the microscopic effects are in general not included, only capturing the macroscopic description.

3.3.1.1 Continuum elasticity

In a continuum description of strain we do not consider any local strain effects within the unit cell. In this case we assume the lattice constant of the virtual material is a (linear) combination of the constituent bulk materials.

Assuming that the strained material can be formed via a small deformation of the unstrained material, the initial strain is determined by the relative difference between the lattice constant of the alloy and the material to which it is being strained (the host material). The initial strain tensor is [139]

$$\varepsilon = \begin{pmatrix} \frac{a^0-a}{a} & 0 & 0 \\ 0 & \frac{b^0-b}{b} & 0 \\ 0 & 0 & \frac{c^0-c}{c} \end{pmatrix}$$

where a, b and c are the lattice constants of the strained material and a^0, b^0 and c^0 are the lattice constants of the host material. In the case of wurtzite III-N materials $a = b \neq c$. Here there has been no relaxation of the strained material.

Turning our attention to a QW system we make the assumption that the barrier material is unstrained, and the QW is strained to match the in-plane (a) lattice constant of the barrier; the QW material is allowed to relax along the c-direction (out-of-plane) This is usually a well justified approach (compare, for example, Fig. 1 in Ref. [41] and Fig 2 in Ref. [138]).

The in-plane strain is given by the fractional change in the a-lattice constant as before, and the strain along the c-direction minimizes the elastic energy of the system. This depends on the elastic properties of the alloy and is given by [138]

$$\varepsilon_{33} = -2\frac{C_{13}}{C_{33}}\varepsilon_{11} \ . \tag{3.13}$$

C_{ij} are the elastic constants of the well material which in a continuum description of an alloy are assumed to be interpolated values of the elastic constants of the constituent materials.

The continuum description of strain is suitable for application to a virtual crystal description of an alloy, for example $\mathbf{k} \cdot \mathbf{p}$ or TB implementing a VCA. However, as our goal is to be able to model alloy fluctuations atomistically we require a model which accounts for the internal relaxation of the atoms in the alloy.

3.3.1.2 Atomistic strain

An atomistic description of strain allows for the change of position of atoms within a strained unit cell. There are several options for modeling the interactions between atoms in a crystal. These include the methods of Stillinger and Weber [140], Lennard-Jones [141], Musgrave and Pople [142] and Keating [143]. The last two are so-called valence force field (VFF) models which are frequently employed in semiconductor heterostructures [144–146].

In the VFF model the interatomic potential between each atom is modeled to include the impact in the change in bond length, bond angle, as well as cross terms, e.g. bond-bending and stretching terms. In this work relaxed atomic positions are calculated using Martin's potential [147] which has been discussed in detail in Ref. [91]. With

this potential the energy at the i^{th} atom, V_i, is given by

$$V_i = \frac{1}{2}\sum_{i\neq j}\overbrace{\frac{1}{2}k_r(r_{ij}-r_{ij}^0)^2}^{\text{Bond stretching}} + \sum_{j\neq i}\sum_{k\neq i,k>j}\left\{\overbrace{\frac{1}{2}k_\theta^i r_{ij}^0 r_{ik}^0(\theta_{ijk}-\theta_{ijk}^0)^2}^{\text{Bond bending}}\right.$$
$$\left. + \overbrace{k_{r\theta}^i\left[r_{ij}^0(r_{ij}-r_{ij}^0)+r_{ik}^0(r_{ik}-r_{ik}^0)\right](\theta_{ijk}-\theta_{ijk}^0)}^{\text{Bond-angle}} + \overbrace{k_{rr}^i(r_{ij}-r_{ij}^0)(r_{ik}-r_{ik}^0)}^{\text{Bond-bond}}\right\}$$
$$+ {\sum_{j\neq i}}' \underbrace{\frac{Z_i^* Z_j^* q^2}{4\pi\epsilon_0\epsilon_r r_{ij}}}_{\text{Coulomb}} - \frac{1}{2}\sum_{j\neq i}\underbrace{\frac{1}{4}\alpha_M\frac{Z_i^* Z_j^* q^2}{4\pi\epsilon_0\epsilon_r r_{ij}^2}(r_{ij}-r_{ij}^0)}_{\text{Coulomb Screening}} \quad .$$

In this expression k_r, k_θ^i $k_{r\theta}^i$, k_{rr}^i are the force constants corresponding to bond stretching, bond bending, bond-angle and bond-bond interactions respectively, r_{ij}^0 and r_{ij} are the bond lengths between atom i and j in the unstrained and strained structures, and θ_{ijk}^0 and θ_{ijk} are the angles formed at atom i by the bonds connecting it to atoms j and k in the unstrained and strained structures respectively. In a wurtzite structure each atom has 4 bonds and 6 angles within the local tetrahedron formed by its nearest-neighbour environment.

The bond stretching term describes the increase in energy due to the change in bond length between atoms i and j away from the unstrained bond length. The bond bending term accounts for the change in energy due change in angle formed with neighbours when moved away from equilibrium. If the angle θ_{ijk} decreases the bond lengths connecting atom i to atoms j and k would tend to increase; this is captured in the bond-angle term which describes the impact of the bond angle on the bond lengths. The bond-bond term includes forces which occur on a bond when a nearby bond changes length, e.g. shortening one bond extends another. All these terms only consider the neighbouring atoms, the Coulomb term however takes into account the potential due to every atom in the lattice and runs over the (infinite) crystal; this is denoted by the $'$ symbol in the sum. In the Coulomb term Z_i^* is the effective charge of the atom i, q is the elementary charge, ϵ_0 and ϵ_r are the free-space and relative dielectric constants. The final term is a repulsion term which corrects for the screening of charge within the nearest neighbour environment where α_M is the Madelung constant. This contribution is required to keep the crystal stable [147].

We follow a similar approach for determining the force constants to that which we saw for determining the on-site energy at an anion site in TB. If only one binary material is involved then the constants can be assumed to correspond to that material. However, where a combination of In-N and Ga-N bonds are involved averaged parameters are used. The material parameters for the bulk materials are determined through fitting results from HSE DFT [148]. This potential is calculated for each atom in the system

under consideration, implemented with the highly efficient and parallelized software, LAMMPS [149]. The atomic positions are moved via the conjugate gradient method in order to find the relaxed atomic positions which minimize the potential energy of the supercell being relaxed.

Once the relaxed positions have been determined it is also possible to calculate the local strain tensor by finding the solution to [150]

$$\varepsilon = \begin{pmatrix} R_{12,x} & R_{23,x} & R_{34,x} \\ R_{12,y} & R_{23,y} & R_{34,y} \\ R_{12,z} & R_{23,z} & R_{34,z} \end{pmatrix} \times \begin{pmatrix} R^0_{12,x} & R^0_{23,x} & R^0_{34,x} \\ R^0_{12,y} & R^0_{23,y} & R^0_{34,y} \\ R^0_{12,z} & R^0_{23,z} & R^0_{34,z} \end{pmatrix}^{-1} - \mathbb{1} \, .$$

Here $\mathbf{R^0_{ij}} = (R^0_{ij,x}, R^0_{ij,y}, R^0_{ij,z})^T$ is the edge of the ideal tetrahedron connecting vertices i and j as shown in Fig. 3.1, $\mathbf{R_{ij}} = (R_{ij,x}, R_{ij,y}, R_{ij,z})^T$ is the corresponding edge of the relaxed tetrahedron and $\mathbb{1}$ is the identity matrix; a polar decomposition is also employed to ensure the local strain matrix is symmetric [151]. Now the off-diagonal elements of the strain tensor ε_{12}, ε_{23}, ε_{13}, ε_{21}, ε_{32} and ε_{31}, are no longer necessarily zero, even in a QW system.

We discussed in Section 2.1.2 how strain effects could influence the electronic structure. So far, while we have described the steps needed to calculate the strain in both a continuum and atomistic framework, we have not detailed how the strain will be included in electronic structure calculations; this shall be the focus of our next discussion.

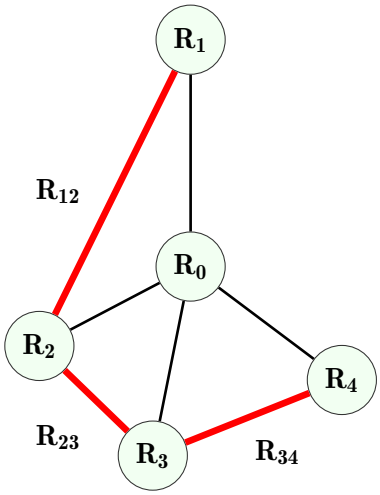

Figure 3.1: Schematic of local tetrahedron surrounding atom at $\mathbf{R_0}$ showing relevant edges needed to compute strain. Black lines indicate inter-atomic bonds between the central atom and its 4 nearest neighbours ($\mathbf{R_{1-4}}$), red lines indicate tetrahedron edges used to compute the strain tensor.

3.3.1.3 Including strain effects in electronic structure calculations

In both the $\mathbf{k}\cdot\mathbf{p}$ and TB methods the strain can be incorporated as a correction to the Hamiltonian,

$$\hat{H} = \hat{H}_0 + \hat{H}_{\text{strain}} \ ,$$

where $\hat{H}_0$ is the unstrained Hamiltonian and $\hat{H}_{\text{strain}}$ is the correction due to strain [114]. The number of components in $\hat{H}_{\text{strain}}$ will depend on the number of basis states included in the model. Here we shall consider an sp^3 model for TB, but first a single band EMA.

3.3.1.3.1 Continuum strain effects

The single band EMA can be a good description of the conduction band close to the center of the Brillouin zone. When a material is strained, modifications to this state can be described by the Pikus-Bir Hamiltonian. For example the conduction band edge would evolve as follows: [114]

$$H_{\text{strain}} = S_c = a_2(\varepsilon_{xx} + \varepsilon_{yy}) + a_1\varepsilon_{zz} \tag{3.14}$$

where S_s is the change in energy of the conduction band edge state, $a_{1,2}$ are the deformation potentials associated with strain out-of-plane and in-plane, and ε_{ij} are elements of the strain tensor as described in Section 2.1.2. This has the effect of moving the absolute scale of the band structure, and does not impact the effective mass in the single band description. Similarly, the valence band is modified by strain as

$$H_{\text{strain}} = S_v = v_2(\varepsilon_{xx} + \varepsilon_{yy}) + v_1(\varepsilon_{zz}) \ , \tag{3.15}$$

where $v_{1,2}$ are the valence band deformation potentials. Here, effects due to shear strain (ε_{ij} with $i \neq j$) have been neglected. This is sufficient in a 1-D description of a QW system, as we have already seen that these contributions are zero. Strain will also impact different valence bands differently (see, for example Ref. [118]) and in some situations a single band may not suffice. Multi-band descriptions of strain can also be constructed, for example a 6-band $\mathbf{k}\cdot\mathbf{p}$ model could be used to describe strained valence band states [114].

3.3.1.3.2 Atomistic tight-binding model

In the continuum description the strain was applied to the unit cell, and deformation potential was simply the change in the band energy due to this. In an atomistic model the cause for these changes becomes more intuitive. Considering this in the TB formalism, variation in the bond length will modify the hopping terms between neighbouring atoms. Not only this, but the on-site energy will also be adjusted due to a changes in the potential from the surrounding lattice (c.f. Eq. (3.11)). A natural method of including strain might be a modification to the hopping terms depending on the strain state (e.g.

Refs. [152] and [153]). This approach introduces a large number of adjustable parameters which need to be determined, for example through a fitting procedure. Here we take a different approach and include strain as a correction to the on-site energies using the Pikus-Bir Hamiltonian [96]. This provides a straightforward approach to include strain with a small number of parameters which can be extracted directly from DFT; no fitting procedure is required. The strain correction at the i^{th} atomic site is given by

$$H^i_{\text{strain}} = \begin{pmatrix} S_s & 0 & 0 & 0 \\ 0 & S_{xx} & S_{xy} & S_{xz} \\ 0 & S_{xy} & S_{yy} & S_{yz} \\ 0 & S_{xz} & S_{yz} & S_{zz} \end{pmatrix},$$

where

$$\begin{aligned} S_s &= a_2(\varepsilon_{xx} + \varepsilon_{yy}) + a_1\varepsilon_{zz} \ , \\ S_{xx} &= l_1\varepsilon_{xx} + m_1\varepsilon_{yy} + m_2\varepsilon_{zz} \ , \\ S_{yy} &= m_1\varepsilon_{xx} + l_1\varepsilon_{yy} + m_2\varepsilon_{zz} \ , \\ S_{zz} &= m_3\varepsilon_{xx} + m_3\varepsilon_{yy} + l_2\varepsilon_{zz} \ , \\ S_{xy} &= n_1\varepsilon_{xy} \ , \\ S_{xz} &= n_2\varepsilon_{xz} \ , \\ S_{yz} &= n_2\varepsilon_{yz} \end{aligned}$$

are the changes in energy of the s, p_x, p_y and p_z orbitals due to strain. The material parameters are related to the deformation potentials, D_i, of the material via [154]

$$\begin{aligned} l_1 &= D_2 + D_4 + D_5 \ , \\ l_2 &= D_1 \ , \\ m_1 &= D_2 + D_4 - D_5 \ , \\ m_2 &= D_1 + D_3 \ , \\ m_3 &= D_2 \ , \\ n_1 &= 2D_5 \ , \\ n_2 &= \sqrt{2}D_6 \ . \end{aligned}$$

For the TB model discussed in this thesis, deformation potentials were extracted from HSE DFT [155]. As is the case with the TB parameters for the on-site energies and interaction terms, parameters at nitrogen sites are treated as a linear combination of the parameters corresponding to InN or GaN depending on the number of neighbours of each are present as before. It is worth noting that these parameters are fitted at $\mathbf{k} = \mathbf{0}$. This approach may not provide accurate results over the full Brillouin zone. However, as we are focusing on an alloy we are primarily interested in the behaviour

at the Γ-point, and therefore this is not a major limitation in this case.

3.3.2 Polarization potential

As discussed in Section 2.1.2, III-N materials grown in the wurtzite phase exhibit a spontaneous polarization vector field within the crystal. On top of this, when strained they also produce piezoelectric fields which impact the polarization in the material. We saw in the case of strain that there are macroscale and atomic scale effects. Polarization effects can also be categorized in this way, where a continuum model does not show the full picture. Here we discuss the description of these effects in more detail starting with a continuum model.

3.3.2.1 Continuum polarization

In Section 2.1.2 we discussed how the change in polarization due to a QW structure can lead to a capacitor-like accumulation of charge resulting in a built-in polarization. We revisit this here in more detail and focus on a single strained c-plane QW of width h, where the spontaneous polarization also differs between the well and barrier materials. The total polarization, as described in Section 2.1.2, is $\mathbf{P}(\mathbf{r}) = \mathbf{P}_{\text{sp}}(\mathbf{r}) + \mathbf{P}_{\text{pz}}(\mathbf{r})$. Due to the absence of shear strain in a continuum description of a c-plane QW the piezoelectric contribution is

$$\mathbf{P}_{\text{pz}} = (\varepsilon_1 e_{31} + \varepsilon_2 e_{32} + \varepsilon_3 e_{33})\hat{\mathbf{z}}$$

where ε_i are elements of the strain tensor and e_{ij} are elements of the piezoelectric tensor. Using Voigt notation, the piezoelectric tensor of a wurtzite c-plane QW is given by [96]

$$e = \begin{pmatrix} 0 & 0 & 0 & 0 & e_{15} & 0 \\ 0 & 0 & 0 & e_{15} & 0 & 0 \\ e_{31} & e_{31} & e_{33} & 0 & 0 & 0 \end{pmatrix} .$$

This describes the macroscopic polarization field generated while in the presence of strain.

Using this tensor and the relation between strain and the elastic constants given in Eq. (3.13), the expression for the polarization field within a single QW is given by

$$\mathbf{P}_{\text{pz}} = P_{\text{pz}}^{W}\hat{\mathbf{z}} = 2\varepsilon_1\left(e_{31} - e_{33}\frac{C_{13}}{C_{33}}\right)\hat{\mathbf{z}} .$$

The potential profile can be found by solving Poisson's equation:

$$-\nabla\cdot\left(\epsilon(\mathbf{r})\nabla\varphi^{\text{pol}}(\mathbf{r})\right) = \rho^{\text{pol}}(\mathbf{r}) = -\nabla\cdot\mathbf{P}(\mathbf{r}) .$$

In the single quantum well with unstrained barriers being treated as a 1-D system this is straightforward, and by applying suitable boundary conditions (for example, zero

field in the barrier as $z \to \pm\infty$) the final solution can be written concisely as [138]

$$\varphi^{pol}(z) = \left(\frac{P^W_{\text{sp}} - P^B_{\text{sp}} + P^W_{\text{pz}}}{2\epsilon^W} \right) (|z| - |z-h|) \ .$$

Here we are assuming that the well begins at $z = 0$, has a width of h, and a dielectric constant of ϵ^W; there is no dependence on the in-plane coordinates (x and y).

3.3.2.2 Atomistic polarization

The previously described framework is applicable to a continuum model, and also an atomistic framework using a VCA. If we use an atomistic description of strain we get local strain effects. We require a theory which can turn these into local polarization effects. Extending the above approach to an atomistic model, due to the internal relaxation of atomic positions is not simple. However it is important to capture the effects due to the large lattice mismatch present in (In,Ga)N alloys.

Instead, a different approach is used; the polarization model used is described in detail in Ref. [156]. In an atomistic framework there will be fluctuations in the polarization due to changes in local composition and strain. The i^{th} component of the *local* polarization vector at a given lattice site is given by [96]

$$P^{\text{pz}}_i = \underbrace{\sum_{j=1}^{6} e^{(0)}_{ij} \varepsilon_j}_{\text{Macroscopic}} + \underbrace{P^{\text{sp}}_i - \frac{e}{V_0} \frac{\mathcal{Z}^0_i}{N_N} \left(\sum_{\alpha=1}^{N_N} l^\alpha_i - \sum_{j=1}^{3} (\delta_{ij} + \varepsilon_{ij}) \sum_{\alpha=1}^{N_N} l^\alpha_{j,0} \right)}_{\text{local}} \tag{3.16}$$

where $e^{(0)}_{ij}$ are the piezoelectric coefficients obtained from a clamped-ion calculation where the ionic coordinates are not allowed to relax internally, ε_j is the macroscopic strain in Voigt notation, P^{sp}_i is the i^{th} component spontaneous polarization, $\mathcal{Z}^0_i$ is the Born effective charge, N_N is the number of nearest neighbours (4 in wurtzite structures), $l^\alpha_{j,0}$ and l^α_j are the bond vectors pointing from the j^{th} neighbour towards the central atom before and after strain respectively. The sum of l^α_i over the local tetrahedron around an atom represents the bond asymmetry, and would be 0 if the i^{th} atom was in the center of a perfect tetrahedron.

If this is evaluated at every atomic site determining values for $\mathcal{Z}$ would be an extensive task, as at a nitrogen site there are multiple nearest-neighbour environments which need to be considered. Instead, we treat only the cation sites whose nearest neighbour sites will always be nitrogen atoms, reducing the number of effective charges needed to two (one for GaN and one for InN).

When the polarization vector is calculated it is possible in principle to evaluate the potential via Poisson's equation, as was done in the continuum calculation. In an atomistic framework this presents technical challenges due to the irregular grid formed by

the relaxed atomic positions. Instead we implement a point-dipole method, where the potential at an atomic site $\mathbf{R_0}$ is determined to be the sum of the contribution of all the dipoles which are present in the lattice [156].

The quantity calculated using Eq. (3.16) is the polarization, which can be described as the dipole density. Therefore the dipole moment in a given volume is

$$\mathbf{p}_i = \mathbf{P}_i V_i \ .$$

The effective volume of each dipole generated in our wurtzite crystal structure is

$$V_i = (\mathbf{r_1} - \mathbf{r_4}) \cdot [(\mathbf{r_2} - \mathbf{r_4}) \times (\mathbf{r_3} - \mathbf{r_4})]$$

where $\mathbf{r_i}$ are the atomic positions of the atoms forming the tetrahedral environment around the i^{th} lattice site [156]. Therefore the point-dipole at each cation site can be evaluated. A point-dipole at position $\mathbf{R}_i$ will generate a potential at position $\mathbf{r}$ of

$$\phi^i_{\mathbf{p}}(\mathbf{r}) = \frac{1}{4\pi\epsilon_r\epsilon_0} \frac{\mathbf{p}_i \cdot (\mathbf{r} - \mathbf{R}_i)}{|\mathbf{r} - \mathbf{R}_i|^3} \ .$$

The total potential therefore at the i^{th} atomic site is the sum of the point-dipole potentials due to all other atoms:

$$\varphi^i_{\text{pol}} = \sum_{j \neq i} \phi^j_{\mathbf{p}}(\mathbf{r}_i) \ .$$

3.3.2.3 Including polarization effects in electronic structure calculations

Once the potential has been evaluated, either using a continuum or atomistic approach, it can be incorporated to the electronic structure theories previously discussed as a site-diagonal correction to the Hamiltonian being used. This approach is the same for $\mathbf{k} \cdot \mathbf{p}$ and TB models. Taking an sp^3 TB model as an example, the correction due to the polarization potential at the i^{th} lattice site is

$$H^i_{\text{pol}} = \begin{pmatrix} \varphi^i_{\text{pol}} & 0 & 0 & 0 \\ 0 & \varphi^i_{\text{pol}} & 0 & 0 \\ 0 & 0 & \varphi^i_{\text{pol}} & 0 \\ 0 & 0 & 0 & \varphi^i_{\text{pol}} \end{pmatrix}$$

where φ^i_{pol} is the polarization potential at the atomic site in question.

The Hamiltonian including strain and polarization effects can now be constructed as

$$\hat{H} = \hat{H}_0 + \hat{H}_{\text{strain}} - q\hat{H}_{\text{pol}} \ .$$

Single particle states and energies can be calculated by finding the eigenvectors and

eigenvalues of the full Hamiltonian $\hat{H}$.

Eigenvalue problems are a numerically challenging task, particularly for systems with a large number of basis states. On top of this, in transport calculations the Schrödinger equation may be needed to be solved self-consistently with the Poisson and current equations.

As a result, in order to capture a quantum description of particles in very large systems (self-consistently) while maintaining a fine resolution of the alloy microstructure, approximations of the Schrödinger equation may be needed. In the next section we introduce one such technique called localization landscape theory.

3.4 Localization Landscape Theory

In previous sections we have considered how to describe single particle states of a system in order to learn about electronic states and energies. Even if we are only interested in a small number of states close to the band edges solving an eigenvalue problem is a numerically expensive task. Here we consider a different approach which allows for the estimation of a local ground state *without* solving an eigenvalue problem, the so-called localization landscape theory (LLT). This approach was first presented by Filoche and Mayboroda in 2012 studying a *localization landscape* in a disordered medium [157]. This existed simply as a mathematical tool until 2017, when the model was first applied to semiconductors to introduce modeling of devices [158], study Urbach tails [159] and investigate transport properties [67] in (In,Ga)N-based devices.

Localization landscape theory is a general method which can be applied to any random landscape in order to estimate the (local) ground state energy and wave function in any localization region in a single band description. Here we derive the expression, following the procedure from Ref. [157] (supplementary material), although we consider here a discrete basis set.

The states in the system are determined by the single band Hamiltonian, $\hat{H}$, with eigenstates

$$\hat{H}\left|\psi^n\right\rangle = E_n\left|\psi^n\right\rangle \quad .$$

We are aiming to approximate the ground state wave function, $|\psi^0\rangle$ which has an energy E_0. The ground state wave function can be expressed of a vector of the complex coefficients, ϕ_i^0, which describe the state:

$$\left|\psi^0\right\rangle = \begin{pmatrix} \phi_0^0 & \phi_1^0 & \dots & \phi_j^0 & \dots & \phi_{N-1}^0 & \phi_N^0 \end{pmatrix}^\dagger \quad . \tag{3.17}$$

In the case of the single band EMA there is only one basis state at each position in the system, so ϕ_i^0 is the coefficient describing the ground state wave function at the position $\mathbf{x}_i$.

3.4.1 Green's function

In order to derive LLT (and later the NEGF formalism) we introduce the Green's function of the Hamiltonian operator. The Green's function for the time-independent, single particle Schrödinger equation is defined via [160]

$$[E - \hat{H}(\mathbf{r})]\hat{G}(\mathbf{r}, \mathbf{r}'; E) = \delta(\mathbf{r} - \mathbf{r}') \ , \tag{3.18}$$

or in matrix form

$$[E\mathbb{1} - H]G(E) = \mathbb{1} \ , \tag{3.19}$$

where E is the energy, H is the Hamiltonian, G is the Green's function, $\delta(\mathbf{r} - \mathbf{r}')$ is the δ-function and $\mathbb{1}$ is the identity matrix. The δ-function has the property

$$f(\mathbf{r}) = \int f(\mathbf{r}')\delta(\mathbf{r} - \mathbf{r}')\mathrm{d}\mathbf{r}' \ ,$$

or in the matrix case,

$$f_i = \sum_j f_j \delta_{i,j} \ , \tag{3.20}$$

so that

$$\delta_{i,j} = \begin{cases} 0 & i \neq j \\ 1 & i = j \end{cases} \ ,$$

which for the full system becomes the identity matrix (only non-zero entries along the diagonal when $i = j$). The Green's function describes the response of a system at position $\mathbf{r}$ due to an impulse in the form of a δ-function at position $\mathbf{r}'$.

3.4.2 Deriving localization landscape theory

From Eq. (3.19) it can be seen that varying E has the effect of varying the absolute energy scale of the Hamiltonian. In the case the of Schrödinger equation this can be freely done with the only effect being a shift in the eigenenergies of the Hamiltonain, as the potential is only defined up to a constant. That is to say

$$(\hat{H} - E\mathbb{1})\,|\psi^n\rangle = \hat{T}\,|\psi^n\rangle + (\hat{V} - E\mathbb{1})\,|\psi^n\rangle = (E_n - E)\,|\psi^n\rangle$$

where the eigenfunction $|\psi^n\rangle$ is independent of E, and has an eigenvalue $E_n - E$. For the derivation of LLT we shall refer to E as the reference energy, also denoted E_{ref}. We shall assume that this is zero for now, though as we shall see later the choice of E_{ref} can impact results after the Green's function has been considered, and it should be chosen to minimize the absolute value of the ground state energy (while keeping it positive). We also modify the definition of the Green's function slightly by changing the sign, in

line with the approach taken in Ref. [157]:

$$HG = \mathbb{1} \ .$$

Considering this matrix multiplication element by element, the i^{th} row of H and the j^{th} column of G multiply to produce the equation

$$\sum_{k \in \Omega} H_{i,k} G_{k,j} = \delta_{i,j} \ . \tag{3.21}$$

Using our identity in Eq. (3.20) the elements of the ground state can be described as

$$\phi^0_j = \sum_{i \in \Omega} \phi^0_i \delta_{i,j} \ .$$

Replacing the δ-function with our expression from Eq. (3.21) the j^{th} the component of $|\psi^0\rangle$ can be written in terms of the Hamiltonian and the Green's function:

$$\phi^0_j = \sum_{i \in \Omega} \phi^0_i \sum_{k \in \Omega} H_{i,k} G_{k,j} = \sum_{k \in \Omega} \Big(\sum_{i \in \Omega} \phi^0_i H_{i,k} \Big) G_{k,j} \ . \tag{3.22}$$

As $|\psi^0\rangle$ is an eigenstate with energy E_0,

$$\sum_{i \in \Omega} \phi^0_i H_{i,k} = E_0 \phi^0_k \ .$$

This allows us to rewrite Eq. (3.22) as

$$\phi^0_j = E_0 \sum_{k \in \Omega} \phi^0_k G_{k,j} \ .$$

The amplitude of ϕ^0_j has an upper bound:

$$|\phi^0_j| = \left| E_0 \sum_{k \in \Omega} \phi^0_k G_{k,j} \right| \leq E_0 \sum_{k \in \Omega} |\phi^0_k| |G_{k,j}| \ . \tag{3.23}$$

In the above equation we have assumed that E_0 is positive. This can always be achieved by shifting the absolute energy scale of the Hamiltonian.

The right hand side of Eq. (3.23) includes in the sum the magnitude of the elements of $|\psi^0\rangle$. We now endeavour to find an upper bound for this term to simplify our upper bound of $|\phi^0_j|$. To do so we introduce the concept of a p-norm. The p-norm of a vector $|v\rangle$ (whose elements are $\{v_i\}$) is defined as [161]

$$\|\mathbf{v}\|_p = \left(\sum_i |v_i|^p \right)^{\frac{1}{p}} \ .$$

If p is 2 this corresponds to the Euclidean norm ($\|\mathbf{v}\|_2 \equiv \|\mathbf{v}\|$). Increasing the value of p results in an increased contribution to the norm from the larger values of v_i and a suppression of the smaller values. As $p \to \infty$ only the maximum value of v_i will contribute to the norm, so this is equivalent to the amplitude of the maximum value of v_i:

$$\|\mathbf{v}\|_\infty \equiv \text{Max}\{|v_i|\} \ .$$

This is the so-called *infinity norm* (sometimes called the supremum norm or the max norm) of the vector. As $|\phi_k^0| \leq \|\psi^0\|_\infty$ the following inequality holds:

$$\sum_{k \in \Omega} |\phi_k^0||G_{k,j}| \leq \|\psi^0\|_\infty \sum_{k \in \Omega} |G_{k,j}| \ .$$

Therefore dividing Eq. (3.23) by $E_0\|\psi^0\|_\infty$ results in the expression

$$\frac{|\phi_j^0|}{E_0||\psi^0||_\infty} \leq \sum_{k \in \Omega} |G_{k,j}| \ .$$

If all the entries of G are positive[1] then the absolute value of the Green's function in the sum over k can be ignored, and the inequality can be expressed as

$$\frac{|\phi_j^0|}{E_0||\psi^0||_\infty} \leq \sum_{k \in \Omega} G_{k,j} \times 1 \equiv u_j \ , \tag{3.24}$$

where u_j is the upper bound which we are trying to evaluate. Recalling the properties of the δ-function (Eq. (3.20)), we rewrite u_j as

$$u_j = \sum_{i \in \Omega} \delta_{i,j} u_i \ .$$

Replacing the δ-function with the product of the Hamiltonian and Green's function (Eq. (3.21)) we are left with

$$u_j = \sum_{i \in \Omega} \left(\sum_{k \in \Omega} H_{i,k} G_{k,j} \right) u_i = \sum_{k \in \Omega} G_{k,j} \sum_{i \in \Omega} H_{i,k} u_i \ . \tag{3.25}$$

Comparing the expressions for u_j in Eq. (3.24) and Eq. (3.25) it is clear that the following expression must hold:

$$\sum_{i \in \Omega} H_{i,k} u_i = 1 \quad \forall \quad k \in \Omega \ ,$$

[1] The Green's function of the Hamiltonian is positive if the Hamiltonian is positive definite [162]. This was already assumed to be the case in Eq. (3.23) where the ground state was declared to be positive, $E_0 > 0$ and thus $E_n > 0 \ \forall \ n$.

or, written in matrix form

$$H\,|u\rangle = 1\ . \tag{3.26}$$

This is the so-called *landscape equation*, whose solution, u bounds the amplitude of the ground state wave function (normalized in some way by the energy and the norm of the wave function). Therefore to calculate the localization landscape, *only a linear system of equations needs to be solved.* This provides a significant benefit in terms of numerical demand when compared to solving an eigenvalue problem which is required in order to calculate the ground state from the Schrödinger equation.

The object u can be used to approximate the ground state wave function [158, 163]. This is illustrated for a test system in Fig. 3.2 (i) (a) where a square QW with periodic boundary conditions is considered. The normalized wave function amplitude calculated via the Schrödinger equation is compared to the localization landscape function, u (normalized over the same region such that the Euclidean norms are 1); the profiles are comparable inside the well region, although the landscape function is non-zero outside the well region whereas the wave function decays quickly due to the potential energy of the barrier being greater than the energy of the state. An energy landscape

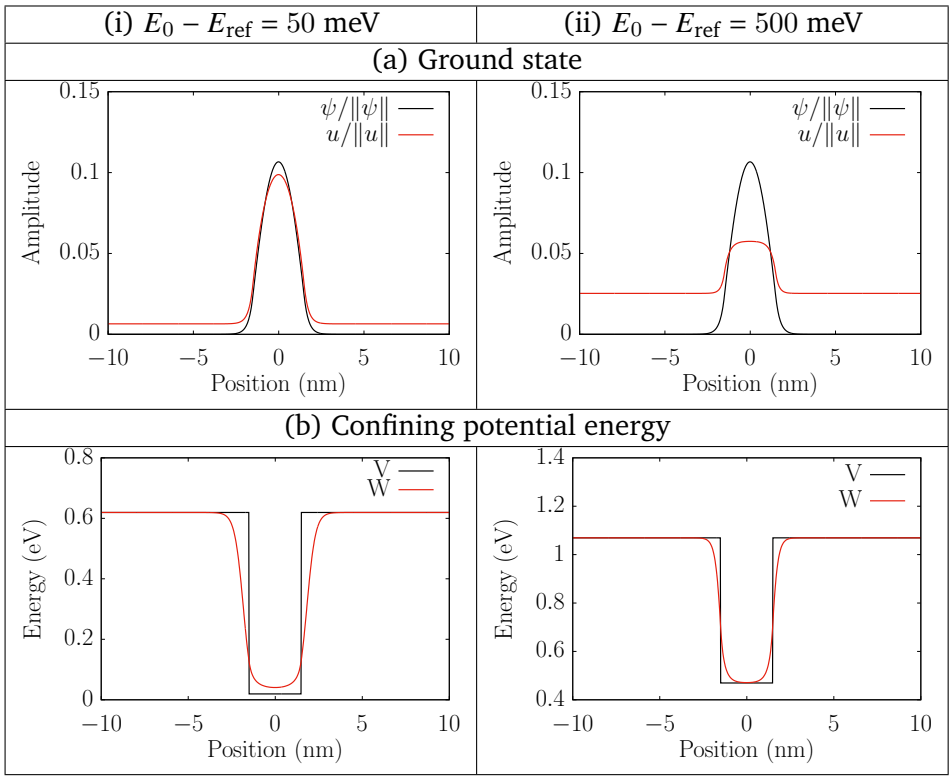

Figure 3.2: (a) A comparison of the normalized ground state charge density calculated by the Schrödinger equation (black) and the normalized landscape function squared (red). (b) The confining potential energy profile input to the Schrödinger equation (black) and the effective potential calculated from localization landscape theory, $W = 1/u$ (red). Results are shown for systems where the ground state sits 50 meV and (ii) 500 meV above the reference energy.

can also be extracted from u. To do so the inverse of u at each point is taken [158]:

$$W_j = \frac{1}{u_j} \ . \tag{3.27}$$

This can be treated as an *effective* confining potential which can be used to include quantum corrections in a classical description of a system [158]. Figure 3.2 (i) (b) shows the confining potential energy used in the original Schrödinger equation (black) and the effective confining potential energy (red) extracted using LLT. Two features are of note. Firstly, the effective confining potential energy is less deep, and the lowest point sits slightly above the bottom of the QW. This is capturing the effect of the confinement energy which causes the ground state to sit above the bottom of the QW. Secondly, the effective potential energy profile of the well is broader than the original potential energy. This captures the quantum effect of the wave function leaking into the barrier material, which is not included in a classical description where this region is forbidden for carriers at energies less than the confining energy.

LLT could be used, for example, in drift-diffusion calculations where the conduction and valence band edges are used as input without solving the Schrödinger equation, and the carriers are treated as point like charges; an effective landscape could be used in this case to include some quantum effects as mentioned above. This will impact the barriers that carriers encounter, and impact the position of the Fermi energy.

3.4.3 Drawbacks of the method

Although LLT is a numerically efficient way to include quantum corrections without having to solve an eigenvalue problem there are some drawbacks from not using the full Schrödinger equation. As we saw above, the wave function resulting from the time-independent Schrödinger equation is independent of the zero-point of the potential. This is not the case for Eq. (3.26), where the reference energy of the potential plays a role in the resulting effective landscape. This is shown clearly by Chaudhuri *et al.* where a modified landscape approach is suggested, motivated by expanding the landscape in the basis of eigenstates of H:

$$H\,|u\rangle = H \sum_n \alpha_n \,|\psi^n\rangle = \sum_n \alpha_n E_n \,|\psi^n\rangle$$

where n runs over the eigenstates $|\psi^n\rangle$ of H which have eigenvalue E_n [163]. The coefficients, α_n, can be extracted by using the orthogonality of the eigenstates:

$$\langle\psi^i|\,H\,|u\rangle = \sum_n \alpha_n E_n \,\langle\psi^i|\psi^n\rangle = \alpha_i E_i \ .$$

Recalling from Eq. (3.26) that $H|u\rangle = 1$ the coefficients can be expressed as

$$\alpha_i = \frac{\langle \psi^i | 1 \rangle}{E_i}$$

so the expansion of $|u\rangle$ is

$$|u\rangle = \sum_n \frac{\langle \psi^n | 1 \rangle}{E_n} |\psi_n\rangle \quad . \tag{3.28}$$

From Eq. (3.28) it can be seen that the resulting form of the landscape $|u\rangle$ will depend on the absolute values of E_n, and will not remain fixed as the reference energy is changed. In particular, we are interested in describing the ground state in the region of interest, so we require the 0^{th} term to dominate the expansion: $\alpha_j \ll \alpha_0 \ \ \forall \ \ j \neq 0$. To satisfy this, the reference energy of the Hamiltonian can be picked so that the ground state is very close to 0, while still retaining the positive definiteness of the Hamiltonian (as was required in the derivation for LLT).

For Fig. 3.2 (i) the reference energy of the system was chosen such that the ground state energy was 50 meV above the reference energy. Figure 3.2 (ii) shows the results of the same system such that this difference is 500 meV. With such a large separation between the reference energy and the ground state energy the results from LLT become significantly worse for the form of the ground state wave function (c.f. Fig. 3.2 (i) (a) and Fig. 3.2 (ii) (a)). The resulting energy landscape, W, also has a less smoothed out well-barrier interface. On top of this, the effect of carriers sitting above the bottom of the well (due to confinement) which was present when $E_0 - E_{\text{ref}} = 50$ meV is no longer visible (c.f. Fig. 3.2 (ii) (a) and Fig. 3.2 (ii) (b)). As the reference energy becomes infinitely far away from the ground state energy the effective confining potential energy approaches the profile of the original confining potential energy landscape used in the Schrödinger equation.

So far LLT has been applied to a range of topics using effective mass [158, 164] and TB Hamiltonians [165, 166]. However, in all these frameworks only a single band was considered, and the model is yet to be extended to a multi-band model. In the applications discussed in this thesis this is not a significant issue, as the lowest conduction band of InN and GaN are both s-like in character, and the highest valence band states both have $p_{x,y}$-character. In this case a single band Hamiltonian is sufficient to capture the key physics. The same may not necessarily be the case for other systems, such as AlGaN- or AlInN-based structures (due to the significant differences in AlN band structure compared to InN and GaN [167]). In the case of AlN the highest valence band state has p_z character [168]. The character of the highest valence band state is important for describing the optical polarization of the emitted light [169, 170]. Therefore a single band model may not be sufficient, and LLT may not be so simply applied, particularly when studying systems as a function of aluminium content.

In this chapter we have described electronic structure theories which can be used in a

variety of settings, including continuum frameworks, atomistic models and a numerically efficient approximation of a particle ground state. In the next chapter we shall introduce different approaches to describe transport in a system, which build on the here-presented electronic structure theories. We shall continue our discussion starting with a quantum description to model ballistic transmission, before moving towards a semi-classical framework which is capable of modeling a full device while still maintaining an atomistic description of an alloy.

Chapter 4

Carrier Transport Theory

As we saw in Chapter 3 there are many ways of describing energy states in a semiconductor or semiconductor heterostructure. Equally there are many flavours of models describing transport through such systems. The most fundamental approaches start with a quantum mechanical framework, and evaluates the probability of transmission between states. In this chapter we introduce the non-equilibrium Green's function formalism which treats the system in this way. This is numerically very demanding, and other models which take a more classical approach are often used used when describing full devices. One such model is drift-diffusion, which we will discuss in greater detail in Section 4.2.

4.1 Non-equilibrium Green's function formalism

The NEGF is a quantum mechanical approach used for describing transport in a device. The formalism was built on work carried out in the 1960's by Schwinger [171], Fujita [172], Keldysh [173] and others describing carrier dynamics. We consider this framework to describe a device which is connected to two leads (which act as a source and drain for charge carriers) which extend infinitely far. As we shall see, this approach reduces the infinitely large system into a finite dimensional problem. In this chapter we follow methods found in Ref. [174] to introduce the framework.

We start with the Hamiltonian describing the full system, $\hat{H}$: we are dealing here with three regions, one *device* region (which may contain, for example quantum wells), and two semi-infinite *leads*, which form the contacts of the system. This is indicated in schematic form in Fig. 4.1. The time-independent Schrödinger equation indicates the energy of charge carriers in the system is given by

$$\hat{H} |\psi\rangle = E |\psi\rangle \ .$$

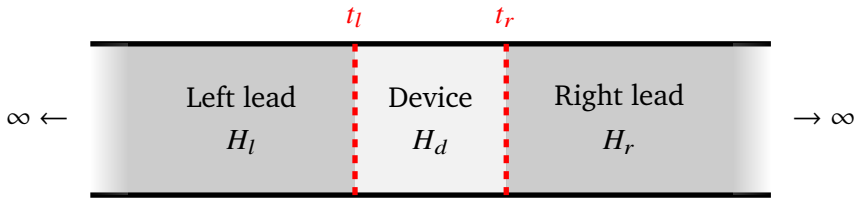

Figure 4.1: Structure of device considered while deriving non-equilibrium Green's function formalism. The device region when isolated is described by the Hamiltonian H_d, and the semi-infinite left and right leads are described by H_l and H_r respectively. The coupling between the device region and the leads takes place in the regions shown by red dashed lines, and the submatrices are denoted t_l and t_r.

The full Hamiltonian of the device and leads is

$$\hat{H} = \begin{pmatrix} H_l & t_l & 0 \\ t_l^\dagger & H_d & t_r \\ 0 & t_r^\dagger & H_r \end{pmatrix}$$

where subscript l, r and d denotes properties in the left lead, right lead and device regions respectively. H_i are the Hamiltonians of each isolated region (with $i \in \{l, d, r\}$) and t_i are the coupling terms between the i^{th} lead and the device region (with $i \in \{l, r\}$). Here we assume there is no interaction between the two leads. We saw in Section 3.4.1 that the Green's function for the single-particle, time independent Schrödinger equation is defined by[1]

$$(E\mathbb{1} - \hat{H})\hat{G} = \mathbb{1}\,, \tag{4.1}$$

where E is the energy, $\mathbb{1}$ is the identity matrix and $\hat{G}$ is the Green's function. We also write $\hat{G}$ in terms of block matrices,

$$\hat{G} = \begin{pmatrix} G_l & G_{ld} & G_{lr} \\ G_{dl} & G_d & G_{dr} \\ G_{rl} & G_{rd} & G_r \end{pmatrix}.$$

Applying the matrix multiplication in Eq. (4.1) results in nine equations. As we are interested in the device region we focus on the expressions which contain G_d:

$$(E\mathbb{1} - H_l)G_{ld} + t_l G_d = 0\,, \tag{4.2a}$$

$$(E\mathbb{1} - H_d)G_d + t_l^\dagger G_{ld} + t_r G_{rd} = \mathbb{1}\,, \tag{4.2b}$$

$$(E\mathbb{1} - H_l)G_{rd} + t_R G_{dr} = 0\,. \tag{4.2c}$$

From Eq. (4.2a) and Eq. (4.2c) expressions for G_{ld} and G_{rd} can be derived in terms of

[1] As in Section 3.4, the Green's functions and subsequent derived quantities will depend on energy, $\hat{G} \rightarrow \hat{G}(E)$. For compact notation we neglect this for the majority of the section, and only re-introduce it later when it becomes more relevant to the discussion.

G_d:

$$G_{ld} = -g_l t_l G_d \ ,$$

$$G_{rd} = -g_r t_r^\dagger G_d \ ,$$

where $g_{l,r} = (E\mathbb{1} - H_{l,r})^{-1}$ are the Green's functions of the isolated leads.

Using this information and Eq. (4.2b) the Green's function of the device can be expressed as

$$G_d = [E\mathbb{1} - H_d - \Sigma_l - \Sigma_r]^{-1} \ , \tag{4.4}$$

where $\Sigma_{l,r}$ are the scattering self energies which act as a correction to the system to account for the coupling of the device region with the semi-infinite leads. These are given by

$$\Sigma_l = t_l^\dagger g_l t_l \ ,$$
$$\Sigma_r = t_r g_r t_r^\dagger \ .$$

Now we are able to describe the response in the device using a finite-dimentional matrix. This however requires us to know the Green's function of an isolated semi-infinite lead. These are also known as surface Green's functions, and could be derived analytically [175] or calculated numerically [176].

The Green's function of the device in general admits two solutions, one corresponding to outward propagating waves, away from the excitation, and one to formed by waves coming in and disappearing at the point of excitation. Physically, we are interested in the waves which are propagating out from a point of excitation. To distinguish between these solutions a infinitesimal complex energy, $i\eta^+ (\eta^+ > 0)$ is often added to Eq. (4.4) which causes waves propagating in one direction to become unphysical, as the (complex) wavevector will cause the wave function to balloon as the position goes to infinity [175]. This is the retarded Green's function, G^R. Similarly subtracting this complex energy results in the advanced Green's function, G^A.

$$G^R = [(E + i\eta^+)\mathbb{1} - H_d - \Sigma]^{-1} \ ,$$
$$G^A = [(E - i\eta^+)\mathbb{1} - H_d - \Sigma^\dagger]^{-1} \ .$$

Σ is the total self-energy associated with the leads, and in the case of multiple leads it is the sum of each contribution so that in our case it is $\Sigma_l + \Sigma_r$. In general we will concern ourselves with the retarded Green's function which is associated with the outward propagating waves, though the advanced Green's function is related to this via $G^R = [G^A]^\dagger$.

We have defined Σ to be the self-energy associated with all of the leads, however extra self-energy terms are often included to account for scattering within the device. These

are so-called *Bütticker probes*, which are included in a similar manner to the leads, however they do not act as a source or drain for the carriers, they only change their energy and momentum [177]. One such scattering mechanism is electron-phonon scattering, where charge carriers lose their energy to lattice excitations. This can be included in the NEGF formalism via the self-consistent Born approximation [178–180].

In the work carried out in this thesis we consider *ballistic* transport. In this case we neglect these scattering mechanisms, and consider only the interaction single-particle states have with the material through which they are transmitting (e.g. changes in the conduction or valence band energy will cause a scattering of carriers). The time-independent Schrödinger equation for the device in the presence of an incoming source, $|s\rangle$ is given by [174]

$$E\,|\psi\rangle = H_d\,|\psi\rangle + \Sigma\,|\psi\rangle + |s\rangle \ , \tag{4.5}$$

which indicates that the energy in the device depends on not only the device Hamiltonian, but also the coupling to the leads (via Σ) and the injection of states through a source term.

Writing this in terms of the retarded Green's function the wave function within the device due to an incoming source, $|s\rangle$, is

$$|\psi\rangle = G^R\,|s\rangle \ .$$

The density matrix of $|\psi\rangle$ is given by $2\pi\,|\psi\rangle\langle\psi|$, which we shall denote G^n, following the notation used by Datta [175]. We can write this in terms of the Green's function and the source term:

$$G^n = 2\pi G^R\,|s\rangle\langle s|\,G^A = G^R\Sigma^{\text{in}}G^A \ , \tag{4.6}$$

where we have labeled the density matrix of the source term as Σ^{in} which describes the electrons entering the device region (in-scattering). Similarly the density matrix of electrons leaving the system can be described by Σ^{out}. As the out-scattering of electrons is equivalent to the in-scattering of holes, the hole density matrix is analogously

$$G^p = G^R\Sigma^{\text{out}}G^A \ , \tag{4.7}$$

The total number of available states is given by the spectral density, A. This is the total electron states and the total hole states combines, and is thus given by the expression

$$A = G^n + G^p = G^R\Gamma G^A = G^A\Gamma G^R \ , \tag{4.8}$$

where for the last two terms we have introduced the broadening term, Γ, which takes into account the change in energy of the system due to interaction with the leads [175]:

$$\Gamma = i([G^A]^{-1} - [G^R]^{-1}) = i(\Sigma - \Sigma^\dagger) = \Sigma^{\text{in}} + \Sigma^{\text{out}} \ . \tag{4.9}$$

By multiplying Γ by G^R and G^A from the left and right (right and left) respectively we find an alternate expression for A:

$$A = i(G^R - G^A) \ . \tag{4.10}$$

The spectral density is the matrix analogy to the density of states, and the trace of this matrix gives the number of available states at a given energy (remembering that the Green's function is energy dependent). In the same way the carrier density at a given energy can be determined by the product of the carrier distribution function (Fermi-Dirac function $f(E)$) and the density of states, the electron and hole density matrices can be determined via

$$\begin{aligned} G^n &= f(E)A \ , \\ G^p &= (1 - f(E))A \ . \end{aligned}$$

Using our expression for A from Eq. (4.8) these can be written in terms of the broadening function, Γ:

$$\begin{aligned} G^n &= f(E)G^R\Gamma G^A \ , \\ G^p &= (1 - f(E))G^R\Gamma G^A \ . \end{aligned}$$

By comparing these expressions with our original terms of the carrier density functions (Eq. (4.6) and Eq. (4.7)) the following expressions for the in-scattering and out-scattering rates can be found:

$$\Sigma^{\text{in}} = f(E)\Gamma \ , \tag{4.11}$$

$$\Sigma^{\text{out}} = (1 - f(E))\Gamma \ . \tag{4.12}$$

A table listing useful quantities and their physical meaning is given in table 4.1.

Table 4.1: A table connecting quantities used in NEGF formalism to a classical equivalent.

Symbol	Classical equivalent
G^n	Electron density
G^p	Hole density
A	Density of states
Σ^{in}	In-scattering
Σ^{out}	Out-scattering
Γ	Total scattering

4.1.1 Probability Current Density

Up until now we have considered the Hamiltonian of a system connected to contacts in the form of two semi-infinite leads, and introduced some useful identities which will be of interest going forward. Ultimately our goal is to investigate ballistic transmission (related to ballistic current as we will see later). In order to do this we shall look at the *probability current density*, $I(E)$.

The trace of G^n (Eq. (4.6)) represents the number of electrons in the system, N. We are interested in the current, therefore the time derivative of $|\psi\rangle\langle\psi|$ is of interest to us, as

$$I(E) = q\frac{\partial N}{\partial t} = q\frac{\partial}{\partial t}Tr\big(2\pi\,|\psi\rangle\langle\psi|\,\big)\ , \tag{4.13}$$

where $I(E)$ is the energy resolved current and $Tr(M)$ is the trace operator, which sums the diagonal elements of the matrix M. The time evolution of $|\psi\rangle$ is described via the Schrödinger equation,

$$i\hbar\frac{\partial}{\partial t}|\psi\rangle = \hat{H}\,|\psi\rangle\ ,$$
$$-i\hbar\frac{\partial}{\partial t}\langle\psi| = \langle\psi|\,\hat{H}\ .$$

Expanding the derivative of $|\psi\rangle\langle\psi|$ via the product rule for differentiation, and applying the Schrödinger equation and its complex conjugate results in the following expression:

$$\frac{\partial}{\partial t}|\psi\rangle\langle\psi| = \frac{i}{\hbar}\Big[\,|\psi\rangle\left(\langle\psi|\,(H_d+\Sigma^\dagger)+\langle s|\,\right)-\left((H_d+\Sigma)\,|\psi\rangle+|s\rangle\,\right)\langle\psi|\,\Big]\ .$$

Using the identities already described ($|\psi\rangle = G^R\,|s\rangle$, $\langle\psi| = \langle s|\,G^A$, $G^n = 2\pi\,|\psi\rangle\langle\psi|$, and $\Sigma^{\text{in}} = 2\pi\,|s\rangle\langle s|$) this expression can be simplified to

$$\frac{\partial N}{\partial t} = \frac{i}{2\pi\hbar}Tr\Big[G^nH_d - H_dG^n + G^n\Sigma^\dagger - \Sigma G^n + G^R\Sigma^{\text{in}} - \Sigma^{\text{in}}G^A\Big]\ .$$

As $Tr[AB] = Tr[BA]$ and $Tr[A+B] = Tr[A]+Tr[B]$ we can write this as

$$\frac{\partial N}{\partial t} = \frac{1}{2\pi\hbar}Tr\big[A\Sigma^{\text{in}} - \Gamma G^n\big]\ ,$$

where we have used Eq. (4.9) and Eq. (4.10). This gives us a neat expression for the current,

$$I(E) = \frac{q}{2\pi\hbar}Tr\big[A\Sigma^{\text{in}} - \Gamma G^n\big] = \frac{q}{2\pi\hbar}Tr\big[\Sigma^{\text{in}}G^p - \Sigma^{\text{out}}G^n\big]\ .$$

We are interested in a device in steady-state. In this case the number of electrons in the device is not changing, and the time-derivative of the carrier density (Eq. (4.13)) is zero. On the other hand, the total current $I(E)$ is made up of current contributions between different leads. These are not necessarily individually 0, however their sum will be in order to conserve the number of electrons in the system.

The current at contact m will therefore be [174]

$$I_m(E) = \frac{q}{2\pi\hbar} Tr\left[\Sigma_m^{\text{in}} G^p - \Sigma_m^{\text{out}} G^n\right] .$$

The expression for the current can be manipulated using equations (4.6)–(4.9) to reach the expression

$$I_m(E) = \frac{q}{2\pi\hbar} Tr[\Sigma_m^{\text{in}} G^R \Gamma - \Gamma_m G^R \Sigma^{\text{in}} G^A] ,$$

where Σ_m^{in} and Γ_m are the in-scattering and total scattering at the m^{th} contact only. The other scattering terms, Σ^{in} and Γ correspond to the full device, and can be described as the sum the contributions associated with each contact:

$$\Gamma = \sum_c \Gamma_c ,$$
$$\Sigma^{\text{in}} = \sum_c \Sigma_c^{\text{in}} ,$$

where c denotes each contact (in the case introduced there $c \in \{l, r\}$). The current at the m^{th} contact is now

$$I_m(E) = \frac{q}{2\pi\hbar} \sum_c Tr[\Sigma_m^{\text{in}} G^R \Gamma_c G^A - \Gamma_m G^R \Sigma_c^{\text{in}} G^A] .$$

Recalling from Eq. (4.11) the in-scattering rate can be written in terms of Γ and the Fermi function, the current at the m^{th} contact can finally be described as

$$I_m(E) = \frac{q}{2\pi\hbar} \sum_c Tr[\Gamma_m G^R \Gamma_c G^A](f_m(E) - f_c(E)) ,$$

where $f_m(E)$ Fermi function at the m^{th} contact, and an individual term in the sum is the current between contacts m and c. In the structure with two contacts, l and r, the current at r arriving from l is therefore given by

$$I_r(E) = \frac{q}{2\pi\hbar} T(E)(f_r(E) - f_l(E)) , \tag{4.14}$$

where the transmission is

$$T(E) = Tr[\Gamma_r G^R \Gamma_l G^A] . \tag{4.15}$$

This expression for the transmission is physically quite opaque, however we now have an expression which can be calculated providing we know the Green's function of the system coupled to the semi-infinite leads, and the broadening function associated with each lead. This can be achieved by carrying out the required matrix inversions and multiplications, or by implementing a recursive Green's function algorithm [181].

Equation (4.14) shows that the current between the contacts r and l is proportional to the difference between the probability of the initial and final state being occupied. If

the Fermi level is equal at both points current will not flow, which is the same result we shall see in the classical approximation implementing drift-diffusion. On top of this, it is straightforward to see in this case that the current at l from r is simply $-I_r$. The total current at r is the integral of I_r over all energy:

$$\mathcal{I}_r = \frac{q}{2\pi\hbar}\int T(E)(f_r(E) - f_l(E))\mathrm{d}E \ .$$

In this work we focus solely on the transmission function, and study the impact that different treatments of an alloy will have on transmission of both electrons and holes. We also study only ballistic tunnelling, where no scattering events take place. In this case the transport can be described equivalently using the so-called wave function formalism (or quantum transmitting boundary method), which numerically is much less demanding than the NEGF equations [123].

Even though it appears obvious to think of T as the probability of an electron leaving the left lead has of reaching the right lead it is worth noting that $T(E)$ can actually exceed 1. As this quantity is energy resolved, and not state resolved, if there are degenerate states T tells us the sum of the probabilities of each state transmitting. This is evidenced for example in Ref. [123] where the band structures and transmission profiles for various nanowires are shown; there is a step-change in the transmission profile (as a function of energy) whenever the number of bands at each energy changes.

So far we have made no assumptions about the Hamiltonian being used to describe the electronic structure of the system under consideration. The NEGF formalism has been coupled successfully with a range of Hamiltonians including DFT [109–111], TB [123, 182], and effective mass [183–185] models. In this work we couple a TB Hamiltonian (described in detail in Chapter 3) to study systems in an atomistic setting including alloy fluctuations, as well as strain and polarization profiles calculated with atomistic theories.

When considering a 3-D device structure the NEGF formalism is limited in its application to small devices due to the high numerical demand, even in the ballistic case. In order to model a full device, approximations must be made in order to extend modeling to a full device-size domain. To this end we introduce the DD framework in the next section.

4.2 Drift-diffusion

Due to the reduced numerical demand of DD compared to fully quantum mechanical approaches, the framework has been widely applied to studying transport in devices. DD, or modified DD frameworks are frequently employed in the study of a range of devices such as LEDs [67, 182, 186], transistors [187, 188] and solar cells [34, 35]. As the name suggests, DD models the motion of particles due to an external force causing

the carriers to drift (e.g. a field moving electrons via Lorentz Force), as well as due to changes in the particle concentration (Fick's Law of diffusion). In this section we derive the model starting from the Boltzmann transport equation, and introduce the ingredients required to implement the model.

4.2.1 Deriving drift-diffusion from Boltzmann transport

The Boltzmann transport equation (BTE) is a statistical model describing the behaviour of a thermodynamical system, and can be used to describe for example the motion of fluids or of charged particles subject to an electromagnetic field [189]. The BTE is a semi-classical analogy to the NEGF formalism in the sense that NEGF couples quantum dynamics to scattering processes, while the BTE uses semi-classical dynamics while also introducing scattering mechanisms. Therefore the BTE is a suitable formalism for describing carrier dynamics in a device as long as quantum mechanics does not play an important role, as the formalism considers the carriers to be point-like particles. On the other hand the BTE is still a computationally expensive method if information about the full carrier distribution function is required [190]. This limits its usefulness for device applications, and therefore we focus on trying to determine average properties of the carrier distribution via the method of moments. Here we derive the DD equations from the statistical BTE following the procedure in Ref. [191], with further insights provided in Ref. [192].

The BTE is:

$$\frac{d}{dt}f(\mathbf{r},\mathbf{k},t) = \Big[\frac{\partial}{\partial t} + \underbrace{\mathbf{v}\cdot\nabla}_{\text{position}} + \underbrace{\frac{1}{\hbar}\mathbf{F}\cdot\nabla_k}_{\text{momentum}}\Big] f(\mathbf{r},\mathbf{k},t) = \Big(\frac{\partial f}{\partial t}\Big)_{\text{coll}} . \tag{4.16}$$

A phenomenological derivation of this equation is described in Ref. [13]. In the above equation, $f(\mathbf{r},\mathbf{k},t)$ describes the probability of finding a particle in the phase space $(\mathbf{r},\mathbf{k})$ at time t. These particles are considered to be point-like with position $\mathbf{r}$ and momentum $\hbar\mathbf{k}$. The velocity, $\mathbf{v}$, can be related to the band structure via the relation $\mathbf{v} = \nabla_{\mathbf{k}}E(\mathbf{k})/\hbar$, where $E(\mathbf{k})$ is the energy dispersion of the system.

The *position* term refers to the change in position of particles due to their group velocity, $\mathbf{v}$, while the *momentum* term refers to the change in momentum due to the force $\mathbf{F}$ (e.g. an electric field). In Eq. (4.16), and in subsequent equations, ∇ denotes the gradient operator with respect to position, whereas $\nabla_{\mathbf{k}}$ is the gradient with respect to the wavevector $\mathbf{k}$.

Scattering events are assumed to impact the momentum of particles, but not their position. Therefore the right-hand term can be described by the sum of all the scattering

events:

$$\left(\frac{\partial f}{\partial t}\right)_{\text{coll}} = \overbrace{\sum_{\mathbf{k}'} f(\mathbf{r},\mathbf{k}',t)[1-f(\mathbf{r},\mathbf{k},t)]W(\mathbf{k}',\mathbf{k},\mathbf{r})\mathrm{d}\mathbf{k}'}^{\text{scattering in}} \underbrace{-\sum_{\mathbf{k}'} f(\mathbf{r},\mathbf{k},t)[1-f(\mathbf{r},\mathbf{k}',t)]W(\mathbf{k},\mathbf{k}',\mathbf{r})\mathrm{d}\mathbf{k}'}_{\text{scattering out}}$$

where $W(\mathbf{k},\mathbf{k}',\mathbf{r})$ is the rate of scattering from a state at position $\mathbf{r}$ with wavevector $\mathbf{k}$ into a state with wavevector $\mathbf{k}'$. The first term describes the rate at which states are scattered into the state $f(\mathbf{r},\mathbf{k},t)$ while the second term describes the scattering out of the state.

In the BTE several assumptions are made [192]:

1. The carriers can be assigned a position and momentum as if they are classical particles. This requires that the size of the system being considered is much greater than the mean-free path between collisions (greater than the particle wave packet), and that the potential varies slowly compared to the particle wave function. The energy scales being considered must also be much greater than the uncertainty due to the spread of the particle momentum.

2. Carrier motion between scattering events is assumed to be well governed by Newton's laws of motion.

3. All scattering processes are independent, instantaneous, do not cause a change in particle position (only momentum) and are perturbations which can be described using Fermi's golden rule to estimate their probability per unit time. This is the so-called "molecular chaos" assumption, or *Stoßzahlansatz* [193].

The Boltzmann transport equation can be solved using, for example, Monte Carlo methods [194]. Alternatively the method of moments can be used to try and gain information about some ensemble averages such as the average particle density and flux at each position and time.

4.2.1.1 The method of moments

We are interested in finding the average properties of our system described by the BTE. Therefore we proceed by multiplying the BTE by some function which depends on $\mathbf{k}$. We shall call this $\Psi(\mathbf{k})$ which later we will take to be different orders of polynomial of $\mathbf{k}$. We then integrate this over all $\mathbf{k}$-space, while keeping the position- and time-dependence. Multiplying Eq. (4.16) by $\Psi(\mathbf{k})$ and integrating it over all $\mathbf{k}$-space results in

$$\int_{\mathbf{k}} \Psi \frac{\partial f}{\partial t}\mathrm{d}\mathbf{k} + \int_{\mathbf{k}} \Psi \mathbf{v}\cdot\nabla f \mathrm{d}\mathbf{k} + \int_{\mathbf{k}} \Psi \frac{1}{\hbar}\mathbf{F}\cdot\nabla_{\mathbf{k}} f \mathrm{d}\mathbf{k} = \int_{\mathbf{k}} \Psi\left(\frac{\partial f}{\partial t}\right)_{\text{coll}}\mathrm{d}\mathbf{k}\ . \tag{4.17}$$

The quantities Ψ and $\mathbf{v}$ do not depend on time or position [192] so we can write

$$\int_{\mathbf{k}} \Psi \frac{\partial f}{\partial t} \mathrm{d}\mathbf{k} = \frac{\partial}{\partial t} \int_{\mathbf{k}} \Psi f \mathrm{d}\mathbf{k} \ ,$$

and

$$\int_{\mathbf{k}} \Psi \mathbf{v} \cdot \nabla f \mathrm{d}\mathbf{k} = \nabla \cdot \int_{\mathbf{k}} \Psi \mathbf{v} f \mathrm{d}\mathbf{k} \ .$$

Using the relation $\nabla_{\mathbf{k}}(\Psi f) = f\nabla_{\mathbf{k}}\Psi + \Psi\nabla_{\mathbf{k}} f$ we can also rewrite the third term in Eq. (4.17) as

$$\int_{\mathbf{k}} \Psi \frac{1}{\hbar}\mathbf{F} \cdot \nabla_{\mathbf{k}} f \mathrm{d}\mathbf{k} = \frac{1}{\hbar}\mathbf{F} \cdot \int_{\mathbf{k}} \nabla_{\mathbf{k}}(\Psi f) \mathrm{d}\mathbf{k} - \frac{1}{\hbar}\mathbf{F} \cdot \int_{\mathbf{k}} f \nabla_{\mathbf{k}} \Psi \mathrm{d}\mathbf{k} \ .$$

Using integration by parts we can eliminate one of the terms in the above expression:

$$\frac{1}{\hbar}\mathbf{F} \cdot \int_{\mathbf{k}} \nabla_{\mathbf{k}}(\Psi f) \mathrm{d}\mathbf{k} = \frac{1}{\hbar}\mathbf{F} \cdot \oint_{\partial\Omega} \Psi f \hat{\boldsymbol{\nu}} \mathrm{d}\sigma \ - \frac{1}{\hbar}\mathbf{F} \cdot \int_{\mathbf{k}} \Psi f \nabla_{\mathbf{k}} 1 \mathrm{d}\mathbf{k} \ = 0,$$

where $\hat{\boldsymbol{\nu}}$ is the outward pointing normal of the surface in $\mathbf{k}$-space, $\partial\Omega$. The second term is clearly zero, as it involves the gradient of a constant function. Assuming that $f(\mathbf{k}, \mathbf{t}, t) \to 0$ as $|\mathbf{k}| \to \infty$ such that $\Psi f \to \mathbf{0}$ this surface integral will also evaluate to 0. As we will later choose Ψ to be polynomial in $\mathbf{k}$ this will be the case if the particle distribution decays exponentially as $|\mathbf{k}| \to \infty$. Assuming this to be true, we are left with

$$\frac{\partial}{\partial t} \int_{\mathbf{k}} \Psi f \mathrm{d}\mathbf{k} + \nabla \cdot \int_{\mathbf{k}} \mathbf{v} \Psi f \mathrm{d}\mathbf{k} - \frac{1}{\hbar}\mathbf{F} \cdot \int_{\mathbf{k}} f \nabla_{\mathbf{k}} \Psi \mathrm{d}\mathbf{k} = \int_{\mathbf{k}} \left(\frac{\partial(\Psi f)}{\partial t} \right)_{\mathrm{coll}} \mathrm{d}\mathbf{k} \tag{4.18}$$

which is a functional of our test function Ψ. By choosing this function to be integer powers of $\mathbf{k}$ the Boltzmann transport equation can be replaced with a series of partial differential equations.

4.2.1.1.1 Zeroth order moment: Carrier conservation

Setting $\Psi = 1$, Eq. (4.18) becomes

$$\frac{\partial}{\partial t} \int_{\mathbf{k}} f(\mathbf{k}, \mathbf{r}, t) \mathrm{d}\mathbf{k} + \nabla \cdot \int_{\mathbf{k}} \mathbf{v}(\mathbf{k}) f(\mathbf{k}, \mathbf{r}, t) \mathrm{d}\mathbf{k} = \int_{\mathbf{k}} \left(\frac{\partial f}{\partial t} \right)_{\mathrm{coll}} \mathrm{d}\mathbf{k} \ . \tag{4.19}$$

Note the momentum term has vanished as it includes the derivative of a constant function. The integral of the probability distribution function over all $\mathbf{k}$ is simply the particle density at position $\mathbf{r}$ at time t:

$$n(\mathbf{r}, t) = \int_{\mathbf{k}} f(\mathbf{k}, \mathbf{r}, t) \mathrm{d}\mathbf{k} \ . \tag{4.20}$$

Turning our attention to the second term of Eq. (4.19), at a position $\mathbf{r}$ at time t the average particle velocity is the sum of the velocities of all particles at position $\mathbf{r}$ and

time t, divided by the corresponding particle density (Eq. (4.20)):

$$\overline{\mathbf{v}}(\mathbf{r},t) = \frac{\int_{\mathbf{k}} \mathbf{v}(\mathbf{k}) f(\mathbf{k},\mathbf{r},t)\mathrm{d}\mathbf{k}}{\int_{\mathbf{k}} f(\mathbf{k},\mathbf{r},t)\mathrm{d}\mathbf{k}} \ .$$

The average particle current density is $\mathbf{J}(\mathbf{r},t) = n(\mathbf{r},t)\overline{\mathbf{v}}(\mathbf{r},t)$:

$$\mathbf{J}(\mathbf{r},t) = \int_{\mathbf{k}} \mathbf{v}(\mathbf{k}) f(\mathbf{r},\mathbf{k},t)\mathrm{d}\mathbf{k} \ . \tag{4.21}$$

Using the derived expressions for carrier density (Eq. (4.20)), and current density (Eq. (4.21)), equation (4.19) now becomes a continuity equation for carriers:

$$\frac{\partial n}{\partial t} + \nabla \cdot \mathbf{J} = \left(\frac{\partial n}{\partial t}\right)_{\mathrm{coll}} \ . \tag{4.22}$$

Different populations, such as electrons and holes, can be coupled together via the collision term which could include recombination and generation.

4.2.1.1.2 First order moment: Momentum conservation

For the first-order moment of the BTE we choose $\Psi(\mathbf{k})$ to be the carrier momentum, $\hbar\mathbf{k}$. The first-order moment equation becomes

$$\frac{\partial}{\partial t}\int_{\mathbf{k}} \hbar\mathbf{k} f \mathrm{d}\mathbf{k} + \nabla \cdot \int_{\mathbf{k}} \hbar\mathbf{v}\mathbf{k} f \mathrm{d}\mathbf{k} - \mathbf{F} \cdot \int_{\mathbf{k}} f \nabla_{\mathbf{k}} \mathbf{k} \mathrm{d}\mathbf{k} = \int_{\mathbf{k}} \left(\frac{\partial(\hbar\mathbf{k} f)}{\partial t}\right)_{\mathrm{coll}} \mathrm{d}\mathbf{k} \ . \tag{4.23}$$

The average momentum is given by

$$\overline{\mathbf{p}}(\mathbf{r},t) = \frac{\int_{\mathbf{k}} \hbar\mathbf{k} f(\mathbf{r},\mathbf{k},t)\mathrm{d}\mathbf{k}}{\int_{\mathbf{k}} f(\mathbf{r},\mathbf{k},t)\mathrm{d}\mathbf{k}} \ . \tag{4.24}$$

We start with the third term of Eq. (4.23), associated with the change in momentum due to an external force. This can be evaluated as:

$$\mathbf{F} \cdot \int_{\mathbf{k}} f \nabla_{\mathbf{k}} \mathbf{k} \mathrm{d}\mathbf{k} = \mathbf{F} \int_{\mathbf{k}} f \mathrm{d}\mathbf{k} = \mathbf{F} n(\mathbf{r},t) \ .$$

Now considering the other terms of Eq. (4.18) individually

$$\frac{\partial}{\partial t}\int_{\mathbf{k}} \hbar\mathbf{k} f \mathrm{d}\mathbf{k} = \frac{\partial(n\overline{\mathbf{p}})}{\partial t}$$

and

$$\nabla \cdot \int_{\mathbf{k}} \hbar\mathbf{v}\mathbf{k} f \mathrm{d}\mathbf{k} = \frac{\hbar^2}{m^*} \nabla \cdot \int_{\mathbf{k}} \mathbf{k}\,\mathbf{k} f \mathrm{d}\mathbf{k} \tag{4.25}$$

where in the last equation we have assumed parabolic energy bands $\left(E(\mathbf{k}) = \frac{\hbar^2 k^2}{2m^*}\right)$, so

that

$$\mathbf{v} = \frac{1}{\hbar}\nabla_{\mathbf{k}} E(\mathbf{k}) \rightarrow \frac{\hbar\mathbf{k}}{m^*} \tag{4.26}$$

with m^* being the effective mass of the band associated with the particle species n.

$\mathbf{kk}$ can be rewritten in terms of $\overline{\mathbf{k}}$ (where $\overline{\mathbf{k}} = \overline{\mathbf{p}}/\hbar$) as

$$\mathbf{k}\,\mathbf{k} = (\mathbf{k}-\overline{\mathbf{k}})(\mathbf{k}-\overline{\mathbf{k}}) + 2\overline{\mathbf{k}}\,\mathbf{k} - \overline{\mathbf{k}}\,\overline{\mathbf{k}} \ ,$$

where the juxtapose multiplication of two vectors is the outer (tensor) product ($\mathbf{kk} \implies \mathbf{k}\otimes\mathbf{k}$) [195]. Integrating this over all $\mathbf{k}$-space, weighted by the probability distribution function f results in

$$\int_{\mathbf{k}} \mathbf{k}\,\mathbf{k} f \mathrm{d}\mathbf{k} = \int_{\mathbf{k}} (\mathbf{k}-\overline{\mathbf{k}})(\mathbf{k}-\overline{\mathbf{k}}) f \mathrm{d}\mathbf{k} + \int_{\mathbf{k}} 2\overline{\mathbf{k}}\,\mathbf{k} f \mathrm{d}\mathbf{k} - \int_{\mathbf{k}} \overline{\mathbf{k}}\,\overline{\mathbf{k}} f \mathrm{d}\mathbf{k} \ .$$

As $\overline{\mathbf{k}}$ is the result of a definite integral over all $\mathbf{k}$, it is independent of $\mathbf{k}$. As a result it can be taken outside the integrals in all cases. Recalling equations (4.20) and (4.24) this now can be rewritten as

$$\int_{\mathbf{k}} \mathbf{k}\,\mathbf{k} f \mathrm{d}\mathbf{k} = \int_{\mathbf{k}} (\mathbf{k}-\overline{\mathbf{k}})(\mathbf{k}-\overline{\mathbf{k}}) f \mathrm{d}\mathbf{k} + n\overline{\mathbf{k}}\,\overline{\mathbf{k}} \ . \tag{4.27}$$

We will introduce in the following the *covariance matrix* [196], with more details in Appendix A. The covariance between particle momenta at position $\mathbf{r}$ at time t is [192]

$$\mathbf{C}[\mathbf{k};\mathbf{r},t] = \frac{\int_{\mathbf{k}} (\mathbf{k}-\overline{\mathbf{k}})(\mathbf{k}-\overline{\mathbf{k}}) f(\mathbf{k},\mathbf{r},t)\mathrm{d}\mathbf{k}}{\int_{\mathbf{k}} f(\mathbf{k},\mathbf{r},t)\mathrm{d}\mathbf{k}} = \frac{\int_{\mathbf{k}} (\mathbf{k}-\overline{\mathbf{k}})(\mathbf{k}-\overline{\mathbf{k}}) f(\mathbf{k},\mathbf{r},t)\mathrm{d}\mathbf{k}}{n(\mathbf{r},t)} \ ,$$

The covariance describes how scattered the distribution of $\mathbf{k}$-values are when described by the function f; higher covariance describes a more spread out distribution [196]. Here we associate the distribution of momenta around the average value with the *random* particle motion, so the temperature tensor can be written in terms of the covariance of $\mathbf{k}$ as [192]

$$\mathbf{T}[\mathbf{r},t] = \frac{\hbar^2}{m^* k_B}\mathbf{C}[\mathbf{k};\mathbf{r},t] \ . \tag{4.28}$$

The diagonal elements of $\mathbf{T}$, T_{ii} represents the random motion in the i-direction, while the off-diagonal elements, T_{ij}, represent the correlation between motion in the i and j directions. A further discussion on the connection between covariance and temperature is presented in Appendix A.

Motivated by this expression for the temperature we multiply Eq. (4.27) by $\frac{\hbar^2}{m^*}$:

$$\frac{\hbar^2}{m^*}\int_{\mathbf{k}} \mathbf{k}\,\mathbf{k} f \mathrm{d}\mathbf{k} = n k_B \mathbf{T} + \frac{1}{m^*} n\overline{\mathbf{p}}\,\overline{\mathbf{p}} \ . \tag{4.29}$$

To continue evaluating the first-order moment we take the divergence of Eq. (4.29) to

evaluate Eq. (4.25):

$$\nabla \cdot \int_{\mathbf{k}} \hbar \mathbf{k} \mathbf{v} f \, \mathrm{d}\mathbf{k} = \nabla \cdot \left(n k_B \mathbf{T} + \frac{1}{m^*} n \overline{\mathbf{p}}\,\overline{\mathbf{p}} \right) = \nabla \cdot (n k_B \mathbf{T}) + \frac{1}{m^*} \nabla \cdot (n \overline{\mathbf{p}}\,\overline{\mathbf{p}}) \ .$$

Using the identity

$$\nabla \cdot (n \overline{\mathbf{p}}\,\overline{\mathbf{p}}) = (n \overline{\mathbf{p}} \cdot \nabla) \overline{\mathbf{p}} + \overline{\mathbf{p}} \nabla \cdot (n \overline{\mathbf{p}})$$

and collecting all the terms together, the first-order continuity equation is

$$\frac{\partial (n \overline{\mathbf{p}})}{\partial t} + \nabla \cdot (n k_B \mathbf{T}) + \frac{1}{m^*} [(n \overline{\mathbf{p}} \cdot \nabla) \overline{\mathbf{p}} + \overline{\mathbf{p}} \nabla \cdot (n \overline{\mathbf{p}})] - n \mathbf{F} = \left(\frac{\partial (n \overline{\mathbf{p}})}{\partial t} \right)_{\text{coll}} \ .$$

Finally, using the Newtonian definition for momentum, recalling that the particle current density is given by $\mathbf{J} = n \overline{\mathbf{v}}$, and dividing by the effective mass the momentum conservation can be written in terms of the current density:

$$\frac{\partial \mathbf{J}}{\partial t} + (\mathbf{J} \cdot \nabla) \overline{\mathbf{v}} + \overline{\mathbf{v}} \nabla \cdot \mathbf{J} + \frac{1}{m^*} \nabla \cdot (n k_B \mathbf{T}) - \frac{n}{m^*} \mathbf{F} = \left(\frac{\partial \mathbf{J}}{\partial t} \right)_{\text{coll}} \ . \tag{4.30}$$

Higher order moments can be derived which give further continuity equations (second order moment gives energy continuity, with third order giving the energy flux continuity). These can be used to derive the DD model via energy balancing [192]. Instead we truncate the expansion here, and follow the method in Ref. [191] to derive the DD formalism by focusing on the collision term.

4.2.1.1.3 Collision term

The collision term in the BTE describes the change in state occupation via scattering into or out of available states. In an optoelectronic device such as an LED this is done via generation, G, or recombination, R, of electrons and holes. The generation term describes the production of free carriers in the device. Physically this could be describing for example photo-generation. Generation would be important to consider if we were applying the DD model to, for example, optically pumped devices where the main source of excited carriers is from photon absorption, in order to study the diffusion length of minority carriers [197], or solar cells [34, 35]. In this thesis we are focusing our study on electrically pumped devices, and therefore generation is of secondary importance, compared to the recombination rate, R.

If generation and recombination events occur at the same rate then the rate of change of particle density is zero:

$$\left(\frac{\partial n}{\partial t} \right)_{\text{coll}} = G - R \ .$$

Now we consider the rate of change of the current density due to collisions,

$$\left(\frac{\partial \mathbf{J}}{\partial t} \right)_{\text{coll}} = \left(\frac{\partial (n \overline{\mathbf{v}})}{\partial t} \right)_{\text{coll}} \ .$$

Using the product rule for differentiation the RHS becomes

$$\left(\frac{\partial \mathbf{J}}{\partial t}\right)_{\text{coll}} = \left(n\frac{\partial \overline{\mathbf{v}}}{\partial t}\right)_{\text{coll}} + \left(\frac{\partial n}{\partial t}\right)_{\text{coll}} \overline{\mathbf{v}} \ .$$

A *relaxation time approximation* is used to describe the scattering between bands [198]. Scattering between bands corresponds to a change in the average velocity (Eq. (4.26)).

$$\left(n\frac{\partial \overline{\mathbf{v}}}{\partial t}\right)_{\text{coll}} = -n\frac{\overline{\mathbf{v}} - \overline{\mathbf{v}^{\mathbf{eq}}}}{\tau}$$

where $\overline{\mathbf{v}^{\mathbf{eq}}}$ is the ultimate average velocity of the distribution if there is no external force acting on the particles (here, $\overline{\mathbf{v}^{\text{eq}}} = \mathbf{0}$), and τ is the relaxation time to return to this state. Using the relaxation time approximation the collision terms in the carrier and momentum conservation equations, Eq. (4.22) and Eq. (4.30), can be written as

$$\begin{aligned}\left(\frac{\partial n}{\partial t}\right)_{\text{coll}} &= G - R \ , \\ \left(\frac{\partial \mathbf{J}}{\partial t}\right)_{\text{coll}} &= -n\frac{\overline{\mathbf{v}}}{\tau} + (G-R)\overline{\mathbf{v}} \ .\end{aligned}$$

Again using the product rule to expand the derivative of the current density (and current density collision term) in Eq. (4.30), and using the carrier continuity equation in Eq. (4.22) to replace the divergence of $\mathbf{J}$ leads to

$$n\frac{\partial \overline{\mathbf{v}}}{\partial t} + (\mathbf{J}\cdot\nabla)\overline{\mathbf{v}} + \frac{1}{m^*}\nabla\cdot(nk_B\mathbf{T}) - \frac{n}{m^*}\mathbf{F} = \left(n\frac{\partial \overline{\mathbf{v}}}{\partial t}\right)_{\text{coll}}$$

Using the relaxation time approximation for the remaining collision term we arrive at the equation

$$n\frac{\partial \overline{\mathbf{v}}}{\partial t} + (\mathbf{J}\cdot\nabla)\overline{\mathbf{v}} + \frac{1}{m^*}\nabla\cdot(nk_B\mathbf{T}) - \frac{n}{m^*}\mathbf{F} = -n\frac{\overline{\mathbf{v}}}{\tau} \ .$$

Multiplying this expression by the relaxation time, and re-ordering results in

$$n\overline{\mathbf{v}} + n\left(\tau\frac{\partial \overline{\mathbf{v}}}{\partial t}\right) + \tau(\mathbf{J}\cdot\nabla)\overline{\mathbf{v}} + \frac{\tau}{m^*}\nabla\cdot(nk_B\mathbf{T}) = \frac{n\tau}{m^*}\mathbf{F} \ . \tag{4.31}$$

In order to proceed we make the following assumption about our system [191]:

1. $\tau\left|\frac{\partial \overline{\mathbf{v}}}{\partial t}\right| \ll |\overline{\mathbf{v}}| \rightarrow$ Relaxation time is much shorter than the rate of change of the average velocity due to external influences. As a results the second term in Eq. (4.31) will be negligible compared to the first term.
2. $\tau\left|\nabla\overline{\mathbf{v}}\right| \ll 1 \rightarrow$ Spatial variations in velocity are small compared to the scattering rate. In this case the third term in Eq. (4.31) will be negligible compared to the first term (as $\mathbf{J} = n\overline{\mathbf{v}}$, so third term equivalent to $\tau(n\overline{\mathbf{v}}\cdot\nabla)\overline{\mathbf{v}}$).

Using these assumptions, and recasting Eq. (4.31) in terms of $\mathbf{J} = n\overline{\mathbf{v}}$ the current can

be written as

$$\mathbf{J} + \frac{\tau n \nabla \cdot (k_B \mathbf{T})}{m^*} + \frac{\tau k_B \mathbf{T} \cdot \nabla n}{m^*} = \frac{n\tau}{m^*}\mathbf{F}$$

where we have also expanded the divergence term using the identity[2]

$$\nabla \cdot (n\mathbf{T}) = n\nabla \cdot \mathbf{T} + \mathbf{T}^\dagger \nabla n = n\nabla \cdot \mathbf{T} + \mathbf{T}\nabla n \ .$$

Up until now we have considered particles moving under some arbitrary force, and looked at the current in terms of particle number. We are particularly interested in charge carrier transport in the presence of an electric field; in an LED the electric field is generated by applying a bias across the device. The force on an *electron* can be written in terms of the electric potential, ψ:

$$\mathbf{F}(\mathbf{r}) = -q\mathcal{E}(\mathbf{r}) = q\nabla\psi(\mathbf{r}) \ .$$

where q is the elementary charge. This leaves us with an expression for the electron current density, $\mathbf{J}_n$, of

$$\mathbf{J}_n = -\frac{\tau_n n \nabla \cdot (k_B \mathbf{T})}{m_n^*} - \frac{\tau_n k_B \mathbf{T} \cdot \nabla n}{m_n^*} - \frac{q\tau_n n}{m_n^*}\nabla\psi \ . \tag{4.32}$$

We have now got an expression for the particle current density. The temperature $\mathbf{T}$ here refers to the carrier temperature; however, if we assume that the particle species is in thermal equilibrium everywhere in the device (no "hot" carriers) this is equivalent to the device temperature. We shall also make the commonly used assumption that the device temperature is constant across the device [192].

$$\mathbf{J}_n = -\frac{\tau_n k_B T \nabla n}{m_n^*} - \frac{q\tau_n n}{m_n^*}\nabla\psi \ .$$

One can now define mobility and diffusion constants, $\mu_{n,p}$ and $D_{n,p}$, according to

$$\mu_{n,p} = \frac{q\tau_{n,p}}{m_{n,p}^*} \ ,$$
$$D_{n,p} = \frac{\tau_{n,p}}{m_{n,p}^*} k_B T \ ,$$

where the subscript n denotes properties associated with electrons and subscript p denotes denotes properties associated with holes. The mobility, $\mu_{n,p}$, determines the response particles have in to an applied electric field; higher mobility results in higher current for a given applied field. Similarly the diffusion constant $D_{n,p}$ determines the

[2] As we already discussed, the temperature tensor, $\mathbf{T}$, is related to the covariance of $\mathbf{k}$. We assume that this is a diagonal tensor (see Appendix A) so any off-diagonal terms of $\mathbf{T}$ are 0. Not only this, but the ij off-diagonal term describes the correlation between k_i and k_j, which must be the same as the correlation between k_j and k_i, so even without the diagonal assumption $\mathbf{T} = \mathbf{T}^\dagger$.

tendency particles have to diffuse; higher diffusion constant results at higher diffusive current at a given carrier concentration gradient.

The DD equations for electrons can therefore be written as

$$\frac{\partial n}{\partial t} + \nabla \cdot \mathbf{J}_n = G - R \ , \tag{4.33}$$

$$\mathbf{J}_n = -D_n \nabla n + \mu_n n \nabla \psi \ . \tag{4.34}$$

In summary these two equations tell us that (i) the rate of change of carrier density depends on the rate of carriers flowing into and out of a given volume, and the difference between the generation and recombination rates (Eq. (4.33)), and (ii) the current is driven by the diffusion of carriers due to a change in their concentration (governed by the diffusion constant, D) and by the drift of carriers due to a field (governed by the mobility, μ) (Eq. (4.34)). Similar expressions can be derived for holes, accounting for the fact that an electric field exerts a force in the opposite direction compared to electrons:

$$\frac{\partial p}{\partial t} + \nabla \cdot \mathbf{J}_p = G - R \ , \tag{4.35}$$

$$\mathbf{J}_p = -D_p \nabla p - \mu_p p \nabla \psi \ . \tag{4.36}$$

The mobility and diffusion constants are related to each other through the Einstein relation [13]:

$$\mu_{n,p} = \frac{q}{k_B T} D_{n,p} \ . \tag{4.37}$$

This relationship can be seen readily by treating equilibrium carrier densities with Boltzmann statistics (more details in Section 4.2.1.2) and requiring that the current at equilibrium is $\mathbf{0}$. This demands that the drift and diffusion terms in the current equation exactly cancel each other resulting in the Einstein relation.

While we have so far determined expressions for the carrier continuity and current density, these depend on the electrostatic potential, ψ, which has not yet been considered. The potential will depend on the spatial distribution of charges, therefore in order to correctly model device behaviour Eq. (4.33) and Eq. (4.34) should be solved coupled with Poisson's equation (Eq. (2.6)):

$$-\nabla \cdot \left(\epsilon(\mathbf{r}) \nabla \psi(\mathbf{r})\right) = \rho(\mathbf{r}) \ . \tag{2.6 revisited}$$

4.2.1.2 Coupling the current equations with Poisson's equation

The carrier density of electrons, n, and holes, p, in a semiconductor can be written in terms of a statistical function [103]:

$$n = N_c \mathcal{F}\left(\frac{q\psi - q\varphi_n - E_c}{k_B T}\right) , \tag{4.38a}$$

$$p = N_v \mathcal{F}\left(\frac{E_v - q\psi + q\varphi_p}{k_B T}\right) , \tag{4.38b}$$

Here $N_{c,v}$ is the effective density of states, $E_{c,v}$ is the band edge energy of the undoped material (without any added potential), $\varphi_{n,p}$ is the quasi-Fermi potential and ψ is the electrostatic potential. As discussed in Section 2.2 this potential is generated by the doping profile, as well as by the free charges in the device. In a 3-D system the effective density of states is given by

$$N_{c,v} = 2\left(\frac{m^*_{n,p} k_B T}{2\pi\hbar^2}\right)^{3/2} \tag{4.39}$$

where $m^*_{n,p}$ is the effective mass of the particle, k_B is the Boltzmann constant and T is the temperature [103]. $\mathcal{F}$ is a statistical function describing the carriers energetic distribution and can be described using a Boltzmann approximation, where

$$\mathcal{F}(\eta) \rightarrow \exp(\eta) ,$$

or with Fermi-Dirac statistics where $\mathcal{F}(\eta)$ is the Fermi integral of order $1/2$:

$$\mathcal{F}(\eta) \rightarrow \frac{1}{\sqrt{\pi}} \int_0^\infty \frac{\xi^{1/2}}{1 + \exp(\xi - \eta)} d\xi .$$

The change in sign of the arguments of the distribution function, $\mathcal{F}$, in Eq. (4.38) is due to the holes being described in the *valence band picture*, rather than the *hole picture*; in the valence band picture the least energetic hole state has the highest energy in the valence band, and excited states have lower energies, whereas in the hole picture this is reversed, and the hole ground state has the highest energy on an absolute scale.

Using the expressions for the densities (Eq. (4.38)), as well as the Einstein relation (Eq. (4.37)), the current density can be written neatly in terms of the gradient of the quasi-Fermi potentials [103]:

$$\mathbf{J}_n = \mu_n n \nabla \varphi_n , \tag{4.40}$$

$$\mathbf{J}_p = -\mu_p p \nabla \varphi_p . \tag{4.41}$$

This indicates that the gradient of the quasi-Fermi potential is the driver for carrier current in the DD framework. Up until this point we have considered the density of the carriers, and their current. To convert this to charge current we define the flow of charge due to electrons as $\mathbf{j}_n = -q\mathbf{J}_n$ and holes as $\mathbf{j}_p = +q\mathbf{J}_p$. Therefore the charge

currents due to electrons and holes are given by [103]

$$\mathbf{j}_n(\mathbf{r}) = -q\mu_n(\mathbf{r})n(\mathbf{r})\nabla\varphi_n(\mathbf{r}) \ ,$$

$$\mathbf{j}_p(\mathbf{r}) = -q\mu_p(\mathbf{r})p(\mathbf{r})\nabla\varphi_p(\mathbf{r}) \ .$$

The potential ψ will depend on the position of charges in the system, so this is often coupled with the Poisson equation (Eq. (2.6)) to determine the potential self-consistently with the DD equations.

In a system with only electrons, the charge density ρ is replaced by the total free electron charge density: $q(N_D - n)$, where N_D is the ionized donor density introduced in Section 2.2. Similarly for a system with only excess holes this is given by $\rho = q(p - N_A)$ where N_A is the ionized acceptor density. A bi-polar system has a charge density comprising of both of these, so Poisson's equation would include both species. Also the DD equations of both charges should be considered resulting in a system of equations which needs to be solved self-consistently:

$$-\nabla(\epsilon\nabla\psi(\mathbf{r})) = q(p(\mathbf{r}) - N_A(\mathbf{r}) - n(\mathbf{r}) + N_D(\mathbf{r})) \ , \tag{4.42a}$$

$$q\frac{\partial n(\mathbf{r})}{\partial t} - \nabla\cdot\mathbf{j}_n(\mathbf{r}) = q(G(\mathbf{r}) - R(\mathbf{r})) \ , \tag{4.42b}$$

$$q\frac{\partial p(\mathbf{r})}{\partial t} + \nabla\cdot\mathbf{j}_p(\mathbf{r}) = q(G(\mathbf{r}) - R(\mathbf{r})) \ , \tag{4.42c}$$

$$\mathbf{j}_n(\mathbf{r}) = -q\mu_n n(\mathbf{r})\nabla\varphi_n(\mathbf{r}) \ , \tag{4.42d}$$

$$\mathbf{j}_p(\mathbf{r}) = -q\mu_p p(\mathbf{r})\nabla\varphi_p(\mathbf{r}) \tag{4.42e}$$

where the carrier densities are described as in Eq. (4.38)

This system of equations is known as the van Roosbroeck system [199] and is the central result of this derivation. The DD system of equations is the workhorse of many commercially available software packages, e.g. Refs. [200, 201]. An applied bias can be introduced via the boundary conditions of the quasi-Fermi potentials. For our purposes we shall only be interested in steady-state current, so the time-derivatives of the electron and hole densities can be neglected. On top of this, if only one carrier species needs to be considered, for example if the device under investigation is uni-polar, and only doped to produce one carrier species, the system of equations can be reduced to accordingly (e.g. no need to consider hole current in only electrons are present in the system).

4.2.1.3 Recombination model

The implementation of Eq. (4.42) requires information about the band edge profile, E_c and E_v, as well as expressions describing the generation and recombination of carriers, G and R. As previously discussed, generation is key in optically pumped devices. How-

ever, as this thesis is focused on electrically pumped devices we assume G is negligible.

To describe the recombination rate, R^{α}, we employ the so-called ABC model [202,203]. This takes into account three recombination processes: (defect related) Shockley-Read-Hall (SRH) ($\propto n$, where n is the carrier density), radiative ($\propto n^2$) and (non-radiative) Auger (also called Auger-Meitner [204], $\propto n^3$) recombination. The total recombination is then the sum of these three components.

The SRH rate is related to defect densities, and it is obtained from:

$$R^{\mathrm{SRH}}(\mathbf{r}) = A_0(n,p)r(n,p) \ , \tag{4.43}$$

where $A_0(n,p)$ is given by

$$A_0(n,p) = \frac{1}{\tau_p\big(n(\mathbf{r}) + n_i(\mathbf{r})\big) + \tau_n\big(p(\mathbf{r}) + n_i(\mathbf{r})\big)} \ .$$

τ_n and τ_p are the electron and hole lifetimes. The *excess carrier density* $r(n,p)$ is given by

$$r(n,p) = n(\mathbf{r})p(\mathbf{r}) - n_i^2(\mathbf{r})$$

where the intrinsic carrier density is [103]

$$n_i^2(\mathbf{r}) = n(\mathbf{r})p(\mathbf{r}) \exp\left(\frac{q\varphi_n - q\varphi_p}{k_B T}\right)$$

where $\varphi_{n,p}$ are the electron and hole quasi-Fermi potentials. The radiative recombination rate is a two carrier process which is calculated via

$$R^{\mathrm{RAD}}(\mathbf{r}) = B_0 r(n,p) \ , \tag{4.44}$$

where B_0 is the radiative recombination coefficient. Finally the Auger rate is a non-radiative, three-carrier, process which, instead of emitting a photon when carriers recombine, excites a third carrier to a higher-energy state. Its rate is

$$R^{\mathrm{AUG}}(\mathbf{r}) = (C_n n(\mathbf{r}) + C_p p(\mathbf{r}))r(n,p) \ , \tag{4.45}$$

where C_n and C_p are the electron-electron-hole and hole-hole-electron Auger coefficients respectively. All these parameters will in principle carry a composition dependence [205–207]. Furthermore, B_0, C_p and C_n will also be carrier density dependent [58, 208, 209]. A widely made assumption is to treat these as constant values across the device region [67, 210].

4.2.1.4 Discretization of van Roosbroeck system of equations

To solve the van Roosbroeck system of equations numerically an approximation of Eq. (4.42) is required. There are a few options in this case:

1. Finite difference method (FDM), e.g. Ref. [211]. Here derivatives are approximated by (usually) linearly discretized functions. This has the advantage of being straightforward to implement, however can result in non-physical descriptions of the current density [103]. On top of this, finite difference approaches can give poor results in the presence of discontinuities [212]. In a system with many interfaces (as in a fluctuating energy landscape in an (In,Ga)N QW) good treatment of discontinuities will be important.

2. Finite element method (FEM), e.g. Ref. [67]. Here the differential equations are multiplied by a test function, and converted into an integral form which is discretized on the mesh. The integral form provides a better treatment of discontinuities than the differential form (as in FDM) [212]. The FEM is also more easily applied to more general mesh shapes than finite difference than finite difference methods. A discretization of the DD equations using the FEM can be found in Ref. [191].

3. Finite volume method (FVM), e.g. Ref. [3]. Like the FEM this treats the system in integral form, and therefore is also good at treating interfaces. On top of this, the flux of, for instance, charges entering a given volume is exactly the flux charges leaving the neighbour along their joining surface, so this method conserves currents making it a particularly suitable method for discretizing the DD equations.

We discretize Eq. (4.42) via the FVM on Voronoi cells [103]. In a distribution of points the Voronoi cell corresponding to point i is the volume which is closer to i than any other point in the set. The construction of such a mesh from a boundary conforming Delaunay triangulation (no other points in the set lie within the circumcircle of a constructed triangle, and any triangle sharing an edge with the domain has an opposite angle less than or equal to $90°$ [103, 214]) is illustrated in Fig. 4.2.

Equation (4.42) is integrated over a test volume ω_k and Gauss's divergence theorem is applied, resulting in the integral equations

$$
\begin{aligned}
-\int_{\partial\omega_k} \varepsilon_s \nabla\psi \cdot \hat{\boldsymbol{\nu}} ds &= q \int_{\omega_k} \left(C - n\left(\psi, \varphi_n\right) + p(\psi, \varphi_p)\right) d\mathbf{r} \ , \\
\int_{\partial\omega_k} \mathbf{j}_n \cdot \hat{\boldsymbol{\nu}} ds &= q \int_{\omega_k} R d\mathbf{r}, \\
\int_{\partial\omega_k} \mathbf{j}_p \cdot \hat{\boldsymbol{\nu}} ds &= -q \int_{\omega_k} R d\mathbf{r},
\end{aligned}
$$

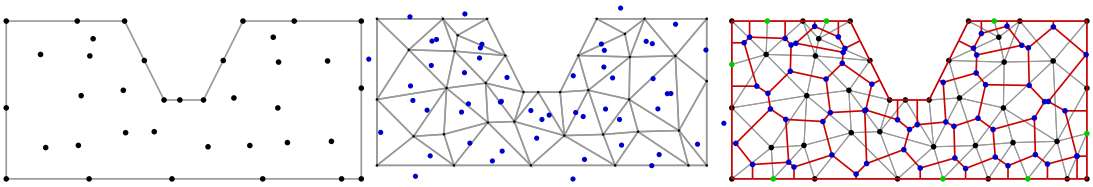

Figure 4.2: Left: Piecewise linear description of computational domain with given point cloud (black dots). Center: Delaunay triangulation of domain (gray edges) and triangle circumcenters (blue dots). As some boundary triangles have angles larger than $90°$ opposite to the boundary, their circumcenters lie outside of the domain. Right: Boundary conforming Delaunay triangulation with automatically inserted additional points at the boundary (green dots) by projecting the circumcenters outside onto the boundary of the computational domain. The boundary conforming Delaunay triangulation is created from the original point cloud (black dots) plus the projected circumcenters (green dots). Now all circumcenters (blue dots) lie within the computational domain. The boundaries of the (restricted) Voronoi cells are shown as well (red edges). Since the Voronoi cells are constructed from a boundary conforming Delaunay triangulation, the edge between any two neighbouring boundary cells is perpendicular to both boundary nodes. This is by construction also true for interior nodes and the edge separating them. The images were created with `triangle` [213].

for $k = 1, \ldots, N$, where N corresponds to the number of cells. C is the doping density given by $C(\mathbf{r}) = N_A(\mathbf{r}) - N_D(\mathbf{r})$. Here, $\hat{\boldsymbol{\nu}}$ is the outward-pointing unit normal to the control volume ω_k. These equations represent an integral form of the van Roosbroeck system on every control volume. In particular, the first equation is Gauss' law of electrodynamics. The second (third) equation constitutes a balance law for the electrons (holes).

Next, the surface integrals are split into the sum of integrals over the planar interfaces between the control volume ω_k and its neighbours. Employing one point quadrature rules for the surface and volume integrals, we deduce the finite volume scheme:

$$\sum_{\omega_\ell \in \mathcal{N}(\omega_k)} |\partial\omega_k \cap \partial\omega_\ell| D_{k,\ell} = q|\omega_k| \left(C_k - n\left(\psi_k, \varphi_{n;k}\right) + p\left(\psi_k, \varphi_{p;k}\right)\right) , \tag{4.46a}$$

$$\sum_{\omega_\ell \in \mathcal{N}(\omega_k)} |\partial\omega_k \cap \partial\omega_\ell| j_{n;k,\ell} = q|\omega_k| R_k , \tag{4.46b}$$

$$\sum_{\omega_\ell \in \mathcal{N}(\omega_k)} |\partial\omega_k \cap \partial\omega_\ell| j_{p;k,\ell} = -q|\omega_k| R_k . \tag{4.46c}$$

In the above formulae, $\mathcal{N}(\omega_k)$ denotes the set of all control volumes neighbouring ω_k. In 2-D, the measure $|\partial\omega_k \cap \partial\omega_\ell|$ corresponds to the length of the boundary line segment and in 3-D to the area of the intersection of the boundary surfaces. The measure $|\omega_k|$ is in 2-D given by the area and in 3-D by the volume of the control volume ω_k. The unknowns ψ_k and $\varphi_{n;k}$ and $\varphi_{p;k}$ are approximations of the electric potential as well as the quasi Fermi potentials for electrons and holes evaluated at node $\mathbf{x}_k$ (black dots in

Fig. 4.2, left). Accordingly, R_k is defined as

$$R_k = R\big(n\left(\psi_k, \varphi_{n;k}\right), p\left(\psi_k, \varphi_{p;k}\right)\big)$$

which is calculated using the ABC model as described previously. The doping is defined by the integral average

$$C_k = \frac{1}{\omega_k}\int_{\omega_k} C(\mathbf{r})d\mathbf{r}\ ,$$

which can be approximated by its nodal value $C(\mathbf{x}_k)$. The numerical fluxes $D_{k,\ell}$, $j_{n;k,\ell}$ and $j_{p;k,\ell}$ in Eq. (4.46) approximate the fluxes $-\epsilon\nabla\psi\cdot\hat{\boldsymbol{\nu}}_{k\ell}$, $\mathbf{j}_n\cdot\hat{\boldsymbol{\nu}}_{k\ell}$ and $\mathbf{j}_p\cdot\hat{\boldsymbol{\nu}}_{k\ell}$ in Eq. (4.42), respectively, on the interfaces between two adjacent control volumes ω_k and ω_ℓ. The electric displacement flux is approximated by

$$D_{k,\ell} = -\epsilon_s\frac{\psi_\ell - \psi_k}{h_{k,\ell}},$$

where

$$h_{k,\ell} = \|\mathbf{x}_\ell - \mathbf{x}_k\|$$

is the edge length and ϵ_s is the dielectric constant.

In the case of Boltzmann statistics the carrier flux can be numerically approximated using, for example, the Scharfetter-Gummel scheme [215]. In this case the flux in a system with varying band edges is (when extended to treat fluctuating band edge energies) [103]

$$\begin{aligned} j_i = -z_i q\mu_n U_T N_i\frac{1}{h}\Bigg\{ & B\left(-z_i\frac{\delta\psi - \delta E_i/q}{U_T}\right)\exp(\eta_{i,L}) \\ & - B\left(z\frac{\delta\psi - \delta E_i/q}{U_T}\right)\exp(\eta_{i,K})\Bigg\}\ , \end{aligned} \tag{4.47}$$

where i represents the carrier species for electrons or holes; in general $i\in\{n,p\}$ however for the band edge energies and effective density of states $i\in\{c,v\}$. The parameter z_i is the charge number for the carrier being considered ($z_i=-1$ for electrons and $z_i=+1$ for holes), $B(x) = x/(\exp(x)-1)$ denotes the Bernoulli function, $U_T = \frac{k_B T}{q}$ the thermal voltage, $\delta\psi = \psi_L - \psi_K$ and $\delta E_i = E_{i,L} - E_{i,K}$ and

$$\eta_{i,P} = z_i\frac{E_{i,P} - q(\psi_P - \varphi_{i,P})}{k_B T},\quad P\in\{K,L\}.$$

The subindices K and L refer to the nodes $\mathbf{x}_K$ and $\mathbf{x}_L$ associated to the corresponding cells.

For more general statistics, such as Fermi-Dirac statistics, other fluxes must be applied. For Fermi-Dirac and Boltzmann statistics the excess chemical potential (SEDAN) flux

can be applied: [216]

$$j_i = -z_i q \mu_n U_T N_i \frac{1}{h} \left\{ B\left(-\delta\nu(\eta_i) - z_i \frac{\delta\psi - \delta E_i/q}{U_T} \right) \mathcal{F}(\eta_{i,L}) - B\left(\delta\nu(\eta_i) + z_i \frac{\delta\psi - \delta E_i/q}{U_T} \right) \mathcal{F}(\eta_{i,K}) \right\} . \tag{4.48}$$

In this case the symbols are consistent with the Scharfetter-Gummel equation with the additional definition that $\nu(\eta_i) = \eta_i - \log(\mathcal{F}(\eta_i))$, and $\delta\nu(\eta_i) = \nu(\eta_L) - \nu(\eta_K)$; in the case of Boltzmann statistics $\nu(\eta)$ is 0 and the scheme reduces to the Scharfetter-Gummel equation. A numerical analysis of the SEDAN scheme as well as other flux approximations in a finite volume discretization is given in Ref. [217].

4.2.2 Drift-diffusion energy landscape

In the last section we also saw that transport in a DD description relies on an energy landscape which is comprised of (conduction and valence) band edge energies, E_i. For an alloy the choice of E_i is often taken to be a virtual material with a linear or quadratic interpolation of the band edge energies of the constituent materials (this is the approach taken by many commercial software packages, such as next**nano** [200]). Strain and polarization effects are then included via deformation potentials and by solving Poisson's equation for the polarization charges respectively. This approach is taken not only in 1-D calculations, but also 2- and 3-D calculations which generate a "local" alloy composition [67, 218]. These methods require generation of an alloy map which is then averaged over a sampling volume to obtain the "local" alloy content. The volume used is somewhat arbitrary, and the resulting conduction and valence band edges can depend strongly on the volumes used. Here we present a different technique, which extracts the band edge energies directly from TB on an atomistic mesh.

4.2.2.1 Extracting a confining landscape from Tight-binding

In Chapter 3 we saw how an alloy is treated in an atomistic framework using TB, including strain and polarization effects. So far this has been considered in the framework of electronic structure calculations, as well as quantum transport. It would be beneficial to combine the TB framework with DD by using TB to generate an atomistic description of the (local) band edge values instead of local alloy contents, E_i. This would have the advantage of treating the system in an atomistic framework for the description of the alloy microstructure, strain effects and polarization fields while being coupled to a transport solver capable of simulating large devices than fully atomistic and quantum mechanical approached. At our starting point, we assume we have already generated a TB Hamiltonian, $\hat{H}$ including an alloy, atomistic strain and polarization potential. From here we endeavour to extract an energy landscape.

In a nearest-neighbour model, the energy at a given lattice site is determined completely by the onsite energy, and the interaction with the nearest neighbours. As such, we aim to construct a framework which considers only this environment. The atoms in question are shown in schematic form in Fig. 4.3, where $|i\rangle$ is the atom at which we are determining the local energy.

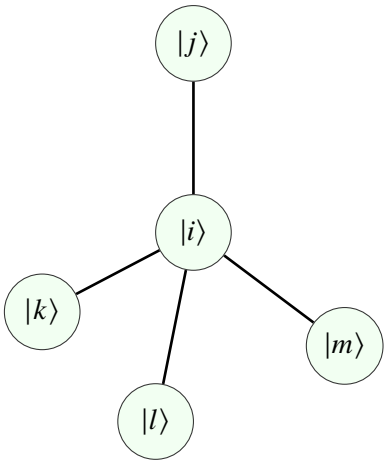

Figure 4.3: Tetrahedron surrounding a central atom, $|i\rangle$, consisting of the four nearest neighbours accounted for in the tight-binding Hamiltonian interactions, $|j\rangle$, $|k\rangle$, $|l\rangle$ and $|m\rangle$. Here all basis states (in our case s, p_x, p_y, p_z) are represented in a given ket.

The states at the i^{th} atom can be described as a linear combination of atomic-like orbitals, which we saw for the TB model in Section 3.2; $\mathbf{R_i}$ denotes the unit cell which contains the atom, α_i denotes the atom within that unit cell and ν denotes the orbitals comprising the basis states at each atom:

$$|i\rangle = \sum_{\nu} |\mathbf{R_i}, \alpha_i, \nu\rangle \ .$$

We proceed by constructing a local Hamiltonian, H^{local}, which is dependent only on the local tetrahedron:

$$H^{\text{local}} = \begin{pmatrix} \langle i|\hat{H}|i\rangle & \sum_N \langle i|\hat{H}|N\rangle \\ \sum_N \langle N|\hat{H}|i\rangle & \frac{1}{4}\sum_N \langle N|\hat{H}|N\rangle \end{pmatrix} \equiv \begin{pmatrix} E^0 & H_{int}^{1-4} \\ H_{int}^{1-4\dagger} & E^{1-4} \end{pmatrix} ,$$

where the sums over N run over the four nearest neighbour atoms, $N \in \{j,k,l,m\}$ including also the different orbital contributions. If an sp^3 basis is being used each entry is a 4×4 submatrix (or more generally, $n\times n$ where n is the number of basis orbitals are used) populated by entries of the full TB Hamiltonian. E^0 is the on-site energies at the lattice site in question. The interaction this atom has with the neighbouring atoms, H_{int}^{1-4}, is simply the sum of the interactions the atom i has with each neighbour. However, the onsite term, E^{1-4}, is the average energy of the carrier sitting on the neighbours. This is similar to the procedure used to generate a Hamiltonian for a

primitive unit cell (e.g. in Ref. [121] and Ref. [75]).

In order to extract a local conduction and valence band edge this local Hamiltonian is diagonalized at each lattice site. Thus a 3-D confining energy landscape can be extracted from the full Hamiltonian. A 2-D slice of the valence and conduction band edge energy extracted in this way is shown in Fig. 4.4 for a system containing an $In_{0.1}Ga_{0.9}N$ QW within a GaN barrier including polarization fields. The fluctuations in the band edge energies due to alloy fluctuations are clearly visible in both the valence and conduction band edges. When the local Hamiltonian is applied to a pure crystal (e.g. bulk GaN) the resulting conduction and valence band energies give the expected energy gap (in GaN ≈ 3.45 eV).

As the entries for the local Hamiltonian have been taken from the full TB Hamiltonian, atomistic strain and polarization effects are automatically included in the energy landscape produced. This provides an advantage as it avoids the need to solve for these using a continuum approach. A continuum treatment would involve an interpolation of material parameters and possibly the introduction of bowing parameters which are not required using this method.

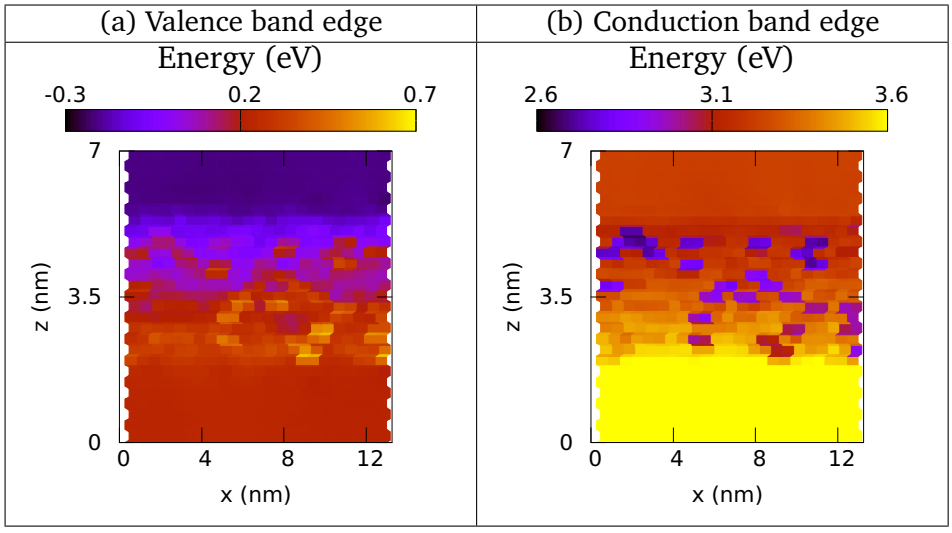

Figure 4.4: 2-D slice of the (a) valence band edge and (b) conduction band edge of an $In_{0.1}Ga_{0.9}N$ quantum well embedded in GaN barriers. The well is located between 2 nm and 5 nm along z and the resulting landscape fluctuates strongly within this region. The energy landscape was extracted from tight-binding using the local Hamiltonian.

The confining energy landscape has been used to calculate the electronic structure of various (In,Ga)N/GaN quantum well systems using a single band EMA [4]. As the calculations were based on the same underlying alloy microstructure as the TB method a direct comparison between the electronic structures could be made. We have performed such an analysis, which revealed that in order to get good agreement between TB and EMA (in terms of absolute energy, and the separation between excited states) a composition dependent band offset is required in both the valence and conduction

band edge within the QW region [4].

4.2.2.2 Including alloy fluctuations in a drift-diffusion model

The DD framework treats charges as point-like particles, however a quantum mechanical treatment would describe the carrier as a wavefunction which has a larger spatial extent. It has already been discussed in the literature that for transport properties, the spatial length scale of the potential fluctuations is effectively determined by the de Broglie wavelength [67]. While in VCA this may be of secondary importance, in a strongly fluctuating energy landscape it is important to account for this, since it may lead to percolation paths in such a landscape. The question has been discussed in detail in Ref. [67] and the authors applied a Gaussian averaging procedure to determine the local alloy content. The same ad-hoc procedure has been employed by Di Vito *et al.* [219]. We can follow a similar approach here and employ a Gaussian averaging, however we apply this to the original *band edge profile* $E_{c,v}^{\mathrm{TB}}$ from TB

$$E_{c,v}^{\sigma}(\mathbf{x}_i) = \frac{\sum_j E_{c,v}^{\mathrm{TB}}(\mathbf{x}_j) \exp\left(-\frac{(|\mathbf{x}_i - \mathbf{x}_j|)^2}{2\sigma^2}\right)}{\sum_j \exp\left(-\frac{(|\mathbf{x}_i - \mathbf{x}_j|)^2}{2\sigma^2}\right)} \tag{4.49}$$

but *not* to the alloy content. Here, $E_{c,v}^{\sigma}(\mathbf{x}_i)$ is the CBE or VBE energy at the (lattice) site $\mathbf{x}_i$; σ denotes the Gaussian width and acts as a smoothing parameter. This averaging procedure is only relevant in (or near) regions where the band edge energies fluctuate. For (In,Ga)N-based LEDs, which are of interest for this present study, this approach has been applied to the active region of the device. We stress again, in Refs. [67,219] the In content at each point is computed from a Gaussian average, and then the strain, built-in field and ultimately the CBE and VBE is computed in a purely continuum framework. We go beyond this by calculating the CBE and VBE (the confining potential) at each (lattice) site from the atomistic TB approach, with no need to calculate local strain or built-in potentials in a continuum-based framework, before applying a Gaussian function to the confining potential. Thus, in comparison to Refs. [67, 219] we have here a posteriori broadening and transfer the atomistic effects on band offset, strain and built-in field due to alloy fluctuations directly into the confining energy landscape before averaging.

4.2.2.3 Including quantum corrections in a drift-diffusion model

Many commercial software packages have the option to include quantum corrections by solving the Schrödinger equation self-consistently with the Poisson and DD equations [200, 201]. This is a numerically demanding task even in 1-D, and is numerically unfeasible in a 3-D calculation which is needed to include a description of alloy fluctuations. However, as we saw in Section 3.4, LLT can be used to extract an effective confining potential describing carrier wave functions in a numerically efficient manner.

The local band edges extracted from TB can be used to describe the confining potential energy in the Hamiltonian. An effective confining energy landscape, $W(\mathbf{r})$, can be determined as described in Eq. (3.27). The resulting landscape will have a softened potential at interfaces, which in some ways mimics tunneling processes allowing carriers to pass barriers at lower energies than is allowed classically. The effective potential will also include confinement energy, which will have a knock-on effect on the position of the quasi Fermi level. The effective confining potential energy landscape was described in more detail in Section 3.4.2. In this way we have a method which can include quantum corrections in a DD calculation in a numerically efficient manner.

In our comparison between TB and the EMA a rigid band offset was required in the QW region of the extracted energy landscape in order to reproduce the correct ground state energies. As LLT is also based on a single band model this energy shift should also be included to provide an appropriate description of the effective confining potential.

The effective confining potential also smooths out the strong fluctuations in the TB landscape, which makes it a useful tool when coupling the TB model with DD. This approach can be applied both the a random alloy, as well as a VCA.

Both of these methods are carried out on the (wurtzite) lattice on which the TB model is based; this results in an atomistic mesh resolution being used. To carry out a full device transport simulation with such a fine discretization would be a huge numerical challenge, and is basically unfeasible for targeting LED structures. Therefore we require a multi-scale framework where a coarser mesh can be employed where fluctuations on small length scales are of secondary importance.

4.2.2.4 Device mesh generation for transport calculations

The local band edges need to be transferred to a mesh that allows us to perform the transport calculations. Two aspects are important here. First, the mesh needs to be fine enough to capture alloy fluctuations in the active region; we call this region in the following the *atomistic mesh*, which forms the so-called *atomistic region*. Second, in regions where no alloy fluctuations are present, the band edge energies can be obtained from the literature or directly from TB (e.g. n-doped GaN contacts). In this contact region the mesh can also be chosen much coarser when compared to the atomistic region; this helps to keep the computational cost low. The latter part is very important to make self-consistent 3-D DD simulations feasible. A schematic illustration of our approach to address this challenge is shown in Fig. 4.5, which describes also the level of atomistic and or quantum correction contributions in the carrier transport calculations. We start from an atomistic TB energy landscape as discussed above and ultimately construct a larger mesh for the DD simulations.

Next, we discuss the post-processing within the atomistic region before we explain the embedding into the larger mesh. Using the atom lattice sites as nodes, we construct

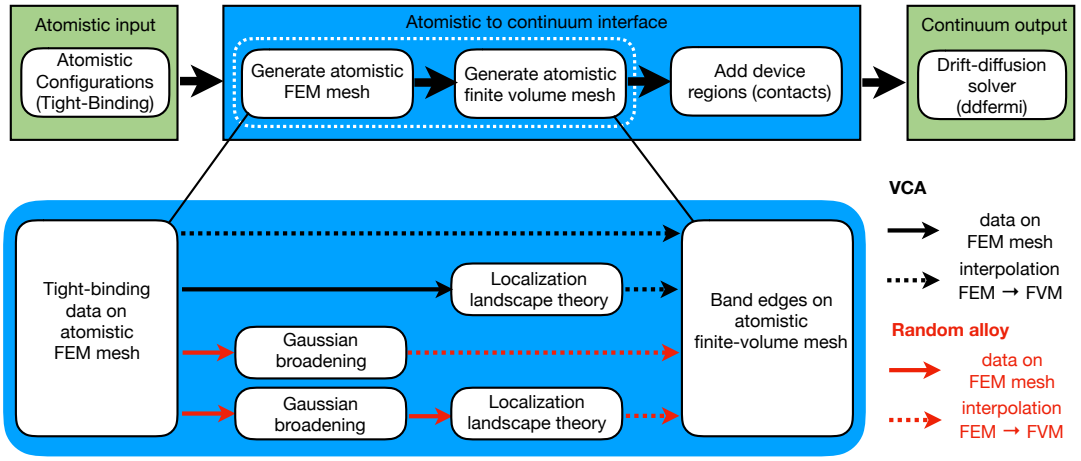

Figure 4.5: Schematic workflow to connect an atomistic tight-binding model to a continuum-based drift-diffusion solver (here `ddfermi`). The connection between the atomistic and continuum-based grid is achieved in three steps. First we generate an atomistic finite element method (FEM) mesh with as many nodes as atomic sites. The data on the FEM mesh is then interpolated on a Voronoi finite volume method (FVM) mesh needed for stable drift-diffusion simulations. Finally, the FVM mesh is enlarged by adding coarser contact and intrinsic regions. The inset details four different ways atomistic band-edge data are transferred to the FVM mesh. Whereas the data paths indicated in black refer to VCA type of data, the data paths in red refer to random alloy data. Solid arrows indicate an operation (stated in the box) on the FEM mesh and dashed arrows indicate interpolation to the FVM mesh. The meshes are shown visually in Fig. 4.6.

a FEM mesh via `TetGen` [220, 221]. The TB energy landscape determines the energy values at the nodes. Figure 4.6 (a) depicts the TB model data for a 3.1 nm thick $In_{0.1}Ga_{0.9}N$ SQW in the x-z-plane, where the z-axis is parallel to the wurtzite c-axis. The depicted test structure has 38,150 atoms and the corresponding FEM mesh has 38,150 nodes and 280,816 tetrahedra, see Fig. 4.6 (b); this mesh represents the atomistic region discussed above.

In order to perform full-device calculations, contact regions (as an example we shall consider an n-i-n junction which contains two n-doped GaN contacts) have to be attached to the atomistic region of the simulation. Our specific approach which we described in detail in Section 4.2.1.4 requires a mesh which ensures that the numerical fluxes are perpendicular to the cell interfaces and allows us to employ a FVM. Therefore, the next step is the generation of such a FVM mesh from the atomistic mesh which satisfies this additional requirement. Again via `TetGen` we produce a so-called boundary-conforming Delaunay-tetrahedral mesh (for details see Section 4.2.1.4) which includes the original FEM lattice sites and interpolate the atomistic data onto it, see Fig. 4.6 (b) to (c). The FVM mesh has 47,248 nodes and 305,272 tetrahedra. Finally, we attach coarser intrinsic meshes as well as doped GaN contact regions to both sides of the atomistic region, again using `TetGen`. Thus, a complete n-i-n junction has

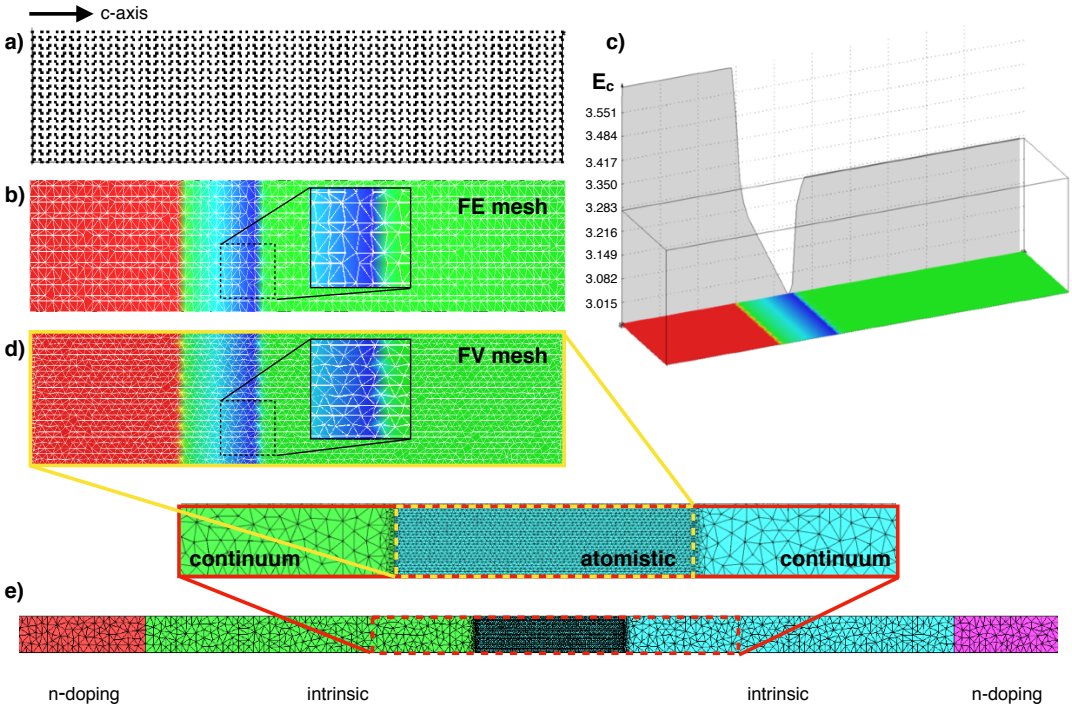

Figure 4.6: Transfer of atomistic data to a larger finite volume mesh for continuum-based drift-diffusion simulations. We start with a point set (a) defined by the atomistic lattice sites as provided by tight-binding. Using `TetGen`, a tetrahedral finite-element mesh (b) is generated, which has exactly the same number of nodes as there are atoms in (a). In doing so, the tight-binding input is exactly represented on the nodes of the atomistic finite element method mesh. The colors in (b) represent the values of the conduction band edge E_c and (c) depicts the E_c profile of an $In_{0.1}Ga_{0.9}N$ single quantum well in virtual crystal approximation. The data from the atomistic finite element method mesh are then interpolated to a finite volume mesh (d), namely a boundary-conforming Delaunay-triangulation generated by `TetGen` [220, 221]. After attaching intrinsic device regions and doped contact regions to the atomistic region, the full 3-D device mesh (e) for drift-diffusion simulations is established.

been created, see Fig. 4.6 (d), which contains the atomistic region (box with yellow-dashed lines), the coarse grained intrinsic GaN (light blue and green) and n-doped GaN (red and purple) regions. As already said, we have used here an n-i-n structure as an example, however the approach can now be easily adapted for a p-i-p setup, p-i-n setup or other material systems. The resulting boundary-conforming finite-volume mesh of the complete uni- and bi-polar structures can be used for DD simulations with `ddfermi` [222]. The tool chain for creating the combined meshes and transferring TB data has been implemented with `WIAS-pdelib` [223] and `TetGen` [220, 221].

Overall in the last two chapters we have presented theories to describe the electronic structure (such as an EMA, TB, and LLT) and transport properties (using NEGF and DD) of materials and heterostructures. This has provided us with tools to target transport properties in (a) a quantum-mechanical approach and (b) a multiscale semi-classical description. In the next chapter we will present results obtained using the described

models. We begin by focusing on ballistic quantum transport through a multi-quantum well system, before proceeding to target larger device-like systems with the DD model.

Part III

Results

Chapter 5

Impact of alloy fluctuations on ballistic transport through InGaN/GaN multi quantum well systems

As we saw in the prologue, (In,Ga)N-based devices have attracted strong interest for lighting applications in the visible spectral range. Fluctuations in the alloy microstructure play an important role in the properties of these devices. Throughout Chapters 3 and 4 we have introduced theoretical models of the electronic structure and transport with the goal of investigating how alloy fluctuations can impact device behaviour.

Not only will alloy fluctuations have an impact on carrier transport properties, quantum effects have also been shown to be important in (In,Ga)N-based LEDs. For example, experimental studies observe significant ballistic hole transport through (In,Ga)N MQWs [224]. Ballistic transport includes tunneling processes which are not captured in a classical description of particles. Previous simulation studies have considered quantum transport using NEGF [185] or the Wentzel-Kramers-Brillouin (WKB) approximation [60, 225] through (In,Ga)N QWs. However, these approaches described the system in the frame of a 1-D model, and thus neglected the impact that alloy fluctuations have on the system. Other studies have included alloy fluctuations in a semi-classical description of transport, without including a quantum mechanical description of tunnelling [67]. Both of these approaches are missing a key aspect, as the theoretical description of (In,Ga)N/GaN MQW systems asks for a full 3-D model that captures both atomistic alloy induced effects as well as quantum mechanical contributions such as tunneling.

In this work we address transport through (In,Ga)N/GaN QWs in a fully 3-D atom-

istic and quantum mechanical frame. On the electronic structure side, an atomistic TB model is applied to capture carrier localization effects on a microscopic level. To achieve a quantum mechanical description of ballistic transport properties we employ the NEGF approach, implemented in OMEN [123].

This is used to determine the transmission spectra of electrons and holes through (In,Ga)N/GaN MQW systems, and investigate the impact including alloy fluctuations has compared to treating the system in VCA. The influence of the energy alignment of states in neighbouring wells is studied in detail by varying the level of disorder between QWs, and by the inclusion and omission of fields due to polarization and a *p-i-n* junction.

The chapter is organized as follows: Section 5.1 gives a brief overview of the NEGF framework which was introduced in Section 4.1. The details and features of the model MQW systems used in our study are outlined in Section 5.2. The results of our calculations are presented in Section 5.3. Finally, Section 5.4 summarizes the results of this study.

5.1 Theoretical Framework

The NEGF formalism builds on top of the TB model introduced in Section 3.2. *This is the foundation for all theoretical frameworks, and here we summarize once the main components:* To capture the effects of alloy fluctuations on a microscopic level, and its impact on ballistic transport properties, our electronic structure model is an atomistic nearest neighbor sp^3 TB model. To include (local) strain and polarization effects found in c-plane InGaN/GaN QW systems the VFF and local polarization theories discussed in Section 3.3 are used.

To calculate transport properties in an atomistic and quantum mechanical framework, we use the TB model as the starting point for NEGF based calculations, as discussed in Section 4.1. More specifically, the TB Hamiltonian is connected to the NEGF solver OMEN which takes input of the TB Hamiltonian, and modifies it to include for open boundary conditions. As electron-phonon scattering is not considered in ballistic transport, the transport is computed using the wave function formalism, as implemented in OMEN [123].

We discussed in Chapter 2 that an LED structure also exhibits an electrostatic built-in field due to *n*- and *p*-doped regions of the device, which modifies the CBE and VBE of the MQWs further. Therefore, to simulate and analyze transport properties of an LED-relevant active region using (In,Ga)N MQW systems the potential profile from a *p-i-n* junction is calculated using next**nano** [200] with a mesh size of 0.1 nm. The potential profile is calculated in 1-D using GaN material parameters from Ref. [24] and dielectric constants from Ref. [226]. (In,Ga)N QWs are not included at this step of the

calculation. Instead, the potential profile from the *p-i-n* junction is mapped onto the TB mesh, and included as a correction to the QW region in addition to the built-in field from local polarization theory.

Overall, the aim of this study is to gain insight into the impact of alloy fluctuations on inter-well electron and hole transport properties. Therefore, we are interested in how carriers tunnel/transmit through an (In,Ga)N/GaN MQW with different barrier widths and with different "levels of randomness" in the wells (see below for details). To do so, we are focussing on ballistic transport calculations. To this end we start and end the simulation cell with (In,Ga)N regions. A schematic illustration of a typical simulation cell is given in Fig. 5.1. The left and right contacts are treated the same way as the MQWs being considered for transport calculations. This means, in a VCA the contacts are described by a virtual crystal; if random alloy fluctuations are being considered in the well regions, the contacts are set up as a random alloy. We note that left and right contact exhibit always the same alloy configuration. In doing so, this approach ensures that the carriers populate the wells and that transmission properties can be studied efficiently, without having to include numerically expensive electron-phonon coupling effects. We note that similar approaches have been used in the literature to study the ballistic transport properties in (In,Ga)N MQWs, however, without considering the impact of alloy fluctuations and thus connected carrier localization effects [60, 225, 227].

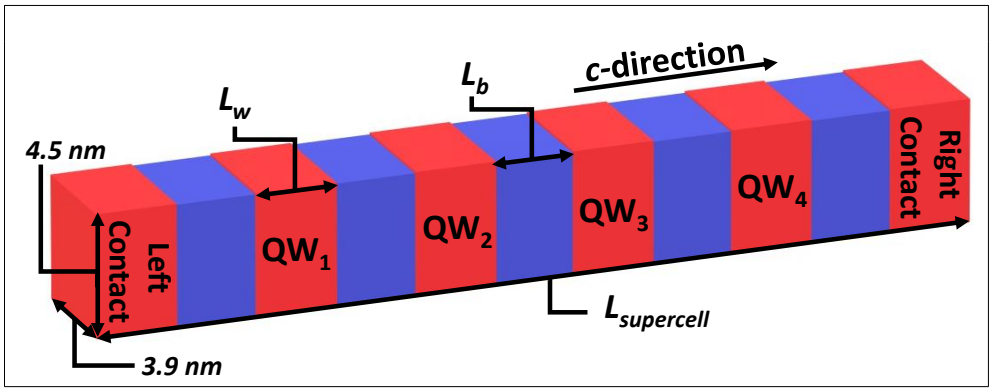

Figure 5.1: Schematic illustration of the supercell used in our ballistic transport calculations. Red indicates regions of $In_{0.12}Ga_{0.88}N$ and blue indicates regions of GaN.

To address the question of the impact of (random) alloy fluctuations on the ballistic transport properties of (In,Ga)N MQWs in detail, we proceed in the following way. As a starting point we describe the MQW system within VCA. The results from the VCA calculations are then compared to an equivalent structure (e.g. same In content, same barrier width etc.) in which random alloy fluctuations are taken into account on a microscopic level.

We note that both VCA and calculations accounting for alloy fluctuations are performed on three-dimensional supercells. Such a set up leads to band folding effects. In the fol-

lowing we focus our attention on $\mathbf{K}_{\parallel} = \mathbf{0}$ states, where $\mathbf{K}_{\parallel}$ is the supercell in-plane $\mathbf{k}$-vector. In the case of our VCA calculations where $\mathbf{k}_{\parallel}$, the in-plane wave function of the primitive cell, is a good quantum number, several states with different in-plane wavevectors are folded back to $\mathbf{K}_{\parallel} = \mathbf{0}$. In the (random) alloy case, due to the breaking of the translational invariance, the states can no longer be classified with a unique $\mathbf{k}_{\parallel}$. In principle band structures as a function of $\mathbf{K}_{\parallel}$ can be derived, but alloy fluctuations will again affect the band structure and thus the transport properties. By band unfolding methods, effective band structures for the "primitive" cell can be obtained. Previous theoretical studies on SiGe and AlGaAs systems have used effective band structures for random alloy supercells and compared the calculated transmission properties of these systems with VCA results [228, 229]. These data show that random alloy fluctuations affect the transmission properties, but that this is a general feature and applicable to all considered $\mathbf{K}_{\parallel}$- or $\mathbf{k}_{\parallel}$-states in a similar fashion. Therefore, to study the impact of alloy fluctuations on electron and hole ballistic transport in c-plane (In,Ga)N/GaN MQWs in general, we consider in the following the situation of $\mathbf{K}_{\parallel} = \mathbf{0}$. To flesh out the influence of alloy fluctuations in detail, we vary also the "level of randomness" in the wells. How this is done is described in the following section, where the MQW model systems are introduced.

5.2 Model Systems

To study the impact of alloy fluctuations on electron and hole ballistic transport properties, we investigate different structures. First we focus our attention on fundamental aspects such as how the "level of randomness" in an (In,Ga)N MQW system affects the results. The supercells that underlie these studies are described in Section 5.2.1. In a second step, Section 5.2.2, we turn our attention to systems that in terms of the number of QWs, well width and the presence of a *p-i-n* junction induced electrostatic built-in field better resemble a device structure. Here, structures with different barrier widths L_b are considered, allowing us to analyze the impact of L_b on the ballistic carrier properties.

5.2.1 Varying levels of disorder in (In,Ga)N multi quantum well systems

We will first look at an $In_{0.12}Ga_{0.88}N$/GaN MQW system with two wells. The well width L_w and barrier width L_b are $L_w = L_b = 2.6$ nm. Similar well widths and alloy contents have been used in other studies, e.g. Ref. [230]. For our full 3-D calculation, a supercell with an in-plane area A of $A \approx 3.2 \times 2.8$ nm^2 and a height of $h \approx 18.1$ nm along the c-direction is generated; the cell contains 14,000 atoms. The (in-plane) hole localization length in (In,Ga)N QWs with 10% is of the order of 2 nm [44]. Thus, the chosen in-plane dimensions are large enough to capture the (in-plane) localization length of holes; the out-of plane (along the c-axis) hole localization lengths are of similar length

but are mainly determined by the built-in polarization field along the growth direction, which is taken into account in our calculations.

In order to investigate the impact of (random) alloy fluctuations on inter-well transport in general, three different situations, in terms of how the QW region is described in the TB model, will be discussed. The aim is to compare results from calculations in which the "level of disorder" within the QWs varies. More specifically, the $In_{0.12}Ga_{0.88}N$ QWs will be described by

1. a VCA - Any variation in local alloy composition is neglected.
2. a random distribution of In atoms in the (In,Ga)N well, but *both QWs* exhibit the *same In atom distributions* (same microscopic configuration). This system is labeled as "Random I".
3. a random distribution of In atoms in the (In,Ga)N well, but the QWs exhibit *different In atom distributions* (different microscopic configurations). This system is labeled as "Random II".

5.2.2 Interplay of barrier width and *p-i-n* junction field

While the supercells discussed above are designed to shed light on the impact of alloy disorder on ballistic transport properties in general, it is also important to analyze the impact of the barrier width and the electrostatic built-in field due to the presence of a *p-i-n* junction on the results. Here, we consider an $In_{0.12}Ga_{0.88}N$ MQW system, embedded in a *p-i-n* junction, with well widths of $L_w = 2.6$ nm. As already mentioned above, the field due to a *p-i-n* junction is calculated within next**nano** [200]. To do so, in next**nano** the intrinsic region is set to a width of 55 nm and *n*- and *p*-contacts are modeled with constant doping density profiles of 5×10^{18} cm^{-3} and 2×10^{19} cm^{-3} respectively; similar doping concentrations have for instance been used in Ref. [231]. In the following we focus our attention on the equilibrium solution, meaning that no bias is applied. This set up is sufficient for our aim to gain first insight into the interplay of alloy fluctuations, barrier width and combined electrostatic field originating from intrinsic spontaneous, piezoelectric and *p-i-n*-junction induced fields.

Building on this framework, the transport calculations are performed on supercells with an in-plane area A of $A = 4.5 \times 3.9$ nm^2, which again is large enough to capture hole localization effects; the increased in-plane area will allow for more localized hole states within the supercell. To study the impact of the barrier width L_b on the results, MQWs with two different barrier widths have been studied, namely $L_b = 3.1$ nm and $L_b = 5.2$ nm. The overall system size is therefore $4.5\times3.9\times28.8$ nm^3 (43,904 atoms) and $4.5\times3.9\times34.6$ nm^3 (59,584 atoms), respectively. While the approximation Random I is useful to establish general aspects, we do not study this situation here, since it is unlikely to be found in structures grown epitaxially. Thus we consider a VCA

description of the wells and different random microscopic configurations in the wells (Random II, see above). To analyze the impact of the alloy microstructure in more detail, the calculations have been repeated five times, thus five different microscopic alloy configurations have been generated.

5.3 Results

Having discussed the theoretical framework and the model systems under consideration, we present here the results of our calculations. Before turning to transport results, in Section 5.3.1, we initially discuss general aspects of the electronic structure of (In,Ga)N/GaN MQWs and how it is affected by alloy fluctuations and electrostatic built-in fields. This information is important for understanding the observed transmission spectra of the different model systems. In Section 5.3.2 we present results on the impact of different levels of disorder on electron and hole ballistic transport. The impact of barrier width, alloy fluctuations and built-in field due to a *p-i-n* junction on electron and hole transmission spectra are discussed in Section 5.3.3.

5.3.1 Electronic structure of an (In,Ga)N/GaN MQW: VCA vs Random Alloy

To establish general aspects of the impact of alloy fluctuations on the electronic structure in MQW systems, we study in the following the structures discussed in Section 5.2.1. To highlight the impact of symmetry breaking, e.g. induced by polarization fields, we treat the polarization field of the two QW system as a linear combination of two single QWs embedded in an infinite host matrix. The CBE and VBE profiles within VCA in the absence and the presence of the built-in field are shown in Fig. 5.2 (a) and (b) respectively. Comparing Fig. 5.2 (a) and (b) clearly shows that the built-in field breaks the symmetry of the otherwise identical wells. In the following, to disentangle effects stemming from the electrostatic built-in potentials (due to the spontaneous and piezoelectric polarization fields) and effects originating from the alloy microstructure, we first analyze results in the absence of the built-in field.

Figure 5.3 shows isosurfaces of the electron (blue) and hole (red) ground state charge densities for (i) VCA, (ii) Random I and (iii) Random II systems viewed along the *c*-axis. This "top view" gives information about the charge density distribution within the *c*-plane. The isosurface corresponds to 40% of the respective maximum charge density values. Figure 5.3 also shows the planar-integrated charge density, $P(z_\alpha^k)$, which is defined by

$$P(z_\alpha^k) = \sum_{i,j} \sum_{\nu} |c_{\alpha,\nu}^{ijk}|^2 \ , \tag{5.1}$$

given that the TB (electron or hole) wave function, $|\psi\rangle$, following the notation of Sec-

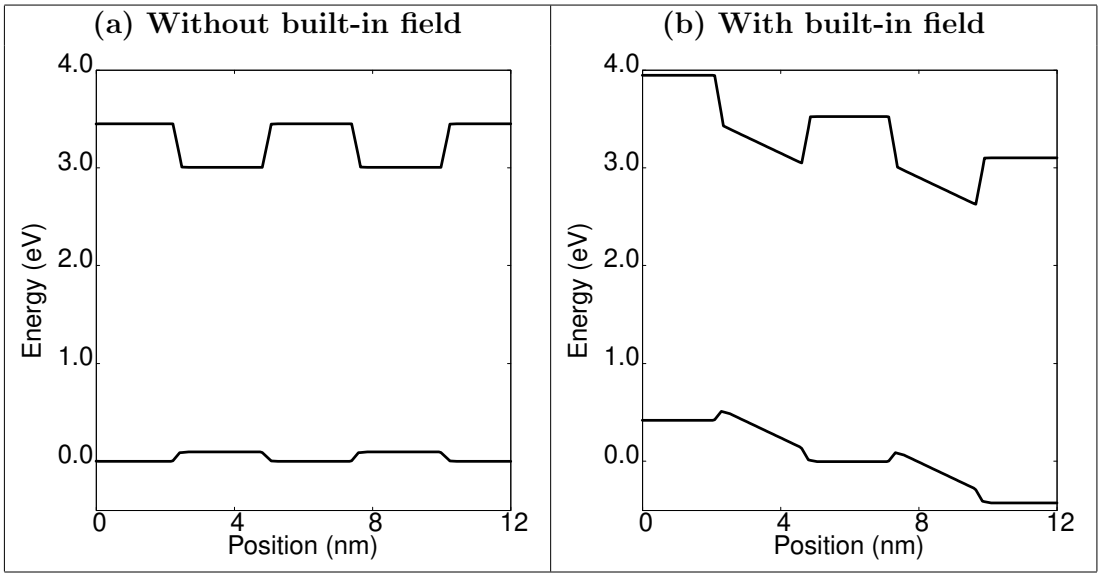

Figure 5.2: Conduction and valence band edges for a two $In_{0.12}Ga_{0.88}N$/GaN quantum well system described in a virtual crystal approximation. (a) Band edges in the absence of spontaneous and piezoelectric polarization induced built-in potentials. (b) Band edges in the presence of these built-in potentials.

tion 3.2, is expressed as:

$$|\psi\rangle = \sum_{i,j,k} \sum_{\alpha,\nu} c^{ijk}_{\alpha,\nu} \; |\mathbf{R}^{ijk}, \alpha, \nu\rangle \quad . \tag{5.2}$$

Here, i, j and k denote the x, y and z coordinates of the unit cell, $\mathbf{R}^{ijk}$, α denotes the atom within the unit cell (the four atom wurtzite basis) and ν is the orbital located on this atom ($\nu \in \{s, p_x, p_y, p_z\}$). Thus, z^k_α is the z-coordinate of the plane perpendicular to the c-direction running though the α atom in the k^{th} unit cell along this direction. The basis states of the sp^3 TB model are denoted by $|\mathbf{R}^{ijk}, \alpha, \nu\rangle$ with expansion coefficients at each lattice site given by $c^{ijk}_{\alpha,\nu}$. These are obtained by solving the eigenvalue problem for the Hamiltonian describing the MQW system, $\hat{H}\,|\psi\rangle = E\,|\psi\rangle$.

While the isosurface plots of the charge densities viewed along the c-axis provide insight into in-plane carrier localization effects, the planar-integrated probability density $P(z^k_\alpha)$, Eq. (5.1), gives insight into carrier localization along the c-axis, e.g., in which QW the carriers are localized.

In a first step we turn our attention to the VCA results. Since in this case alloy fluctuations within the QW region are not captured, the electron and hole charge densities are distributed across the entire two QWs. This is clearly reflected in $P(z^k_\alpha)$ shown in Fig. 5.3 (i). Turning to the system labeled as Random I, Fig. 5.3 (ii), in which case the alloy fluctuations are identical in both wells, the electron charge density is still well distributed across the two QWs, as $P(z^k_\alpha)$ shows. However, some alloy fluctuation

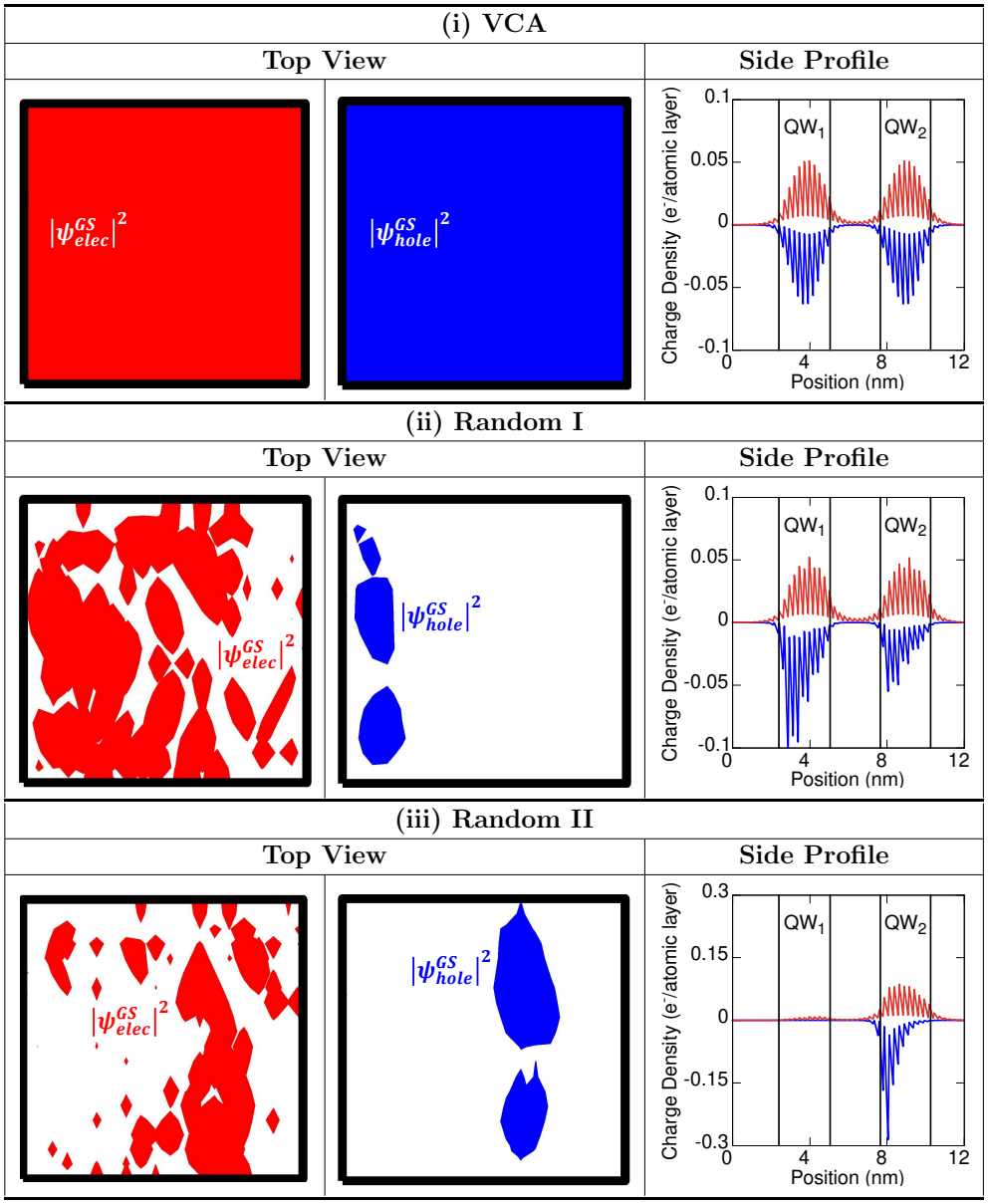

Figure 5.3: Top view (along the *c*-axis) of isosurface plots of (left) electron and (middle) hole charge densities for a (i) VCA, (ii) Random I and (iii) Random II system without the inclusion of the built-in polarization field. The isosurfaces correspond to 40% of the respective maximum charge density values. The right panel of the figure shows the planar integrated charge density, $P(z^k_\alpha)$, along the supercell for both electrons and holes.

induced localization effects are visible in the different plots. Looking at the electron ground state first, we find an almost equal distribution of charge density in both wells. Due to the low effective electron mass, at least when compared to the holes, the electron wave functions of the two wells couple similar to the bonding and anti-bonding states in a homonuclear molecule. We find that this is also reflected in the calculated energy spectrum (not shown) where the first two electron states are energetically split and that this splitting is reduced with increasing barrier width between wells. Turning

to the hole ground state, we find that alloy fluctuations lead to strong wave function localization effects. While we still observe significant charge densities in both wells, the ground state wave function is preferentially localized in QW 1. However, we note also that, as the wells contain the same microscopic configuration, there is a second hole state which is almost energetically degenerate with the state presented in Fig. 5.3 (ii); this second state has a slightly higher probability density in QW 2 (not shown). We attribute the smaller energetic separation of the first two hole states, when compared to the electrons, to a reduced electronic coupling between the two wells due to the larger hole mass and stronger hole localization effects when compared to electrons.

In Random II the picture changes noticeably. Now that the two wells differ in their microscopic alloy configuration, the symmetry of the system is broken and the ground state for electrons and holes are localized entirely within one well, as $P(z_\alpha^k)$ clearly shows in Fig. 5.3 (iii).

Having discussed the electronic structure of the three different systems in the absence of the electrostatic built-in field, Fig. 5.4 displays isosurface plots of the electron (red) and hole (blue) ground state charge densities along with planar integrated probability density, $P(z_\alpha^k)$, in the presence of the field. The corresponding CBE and VBE profiles, within VCA, are shown in Fig. 5.2 (b). As Fig. 5.2 (b) reveals, the polarization potential leads to a significant tilt in the band edges; thus already in VCA the symmetry between the wells is broken by the built-in field. As a consequence the ground state for the electrons is always found in QW 2, while the hole ground states is found in QW 1. Comparing the electron and hole ground state charge densities from VCA, Random I and Random II, cf. Fig. 5.4, at least in terms of localization of these states along the growth direction, the systems are not very different. However, it is important to highlight that in-plane localization effects are not captured in VCA and that the alloy microstructure will still affect carrier localization effects *within* the plane.

Having seen the impact of the spontaneous and piezoelectric polarization field induced built-in potential on the carrier confinement, we briefly discuss how the band edge profile is modified when the field of the *p-i-n* junction is also present and the barrier width, L_b, between the wells is changed. Figure 5.5 shows the CBE and VBE profile of the four QW system discussed in Section 5.2.2 for the barrier width L_b of (a) L_b=3.1 nm and (b) $L_b = 5.2$ nm. The horizontal lines indicate the CBE minimum and the VBE maximum in the systems. In the system with $L_b = 3.1$ nm there is a clear difference in the CBE of the first (most left) QW and the last (most right) QW, thus a symmetry breaking between the wells in the MQW system is observed. In the case of $L_b = 5.2$ nm, the field of the *p-i-n* junction "realigns" the CBEs of the four QWs. We note that these calculations are carried out for the same doping profiles; changes in the band edge profile arise entirely from changes in the barrier width. Below we discuss the effect of these changes in the band edge profile for transport properties. However, first, we focus

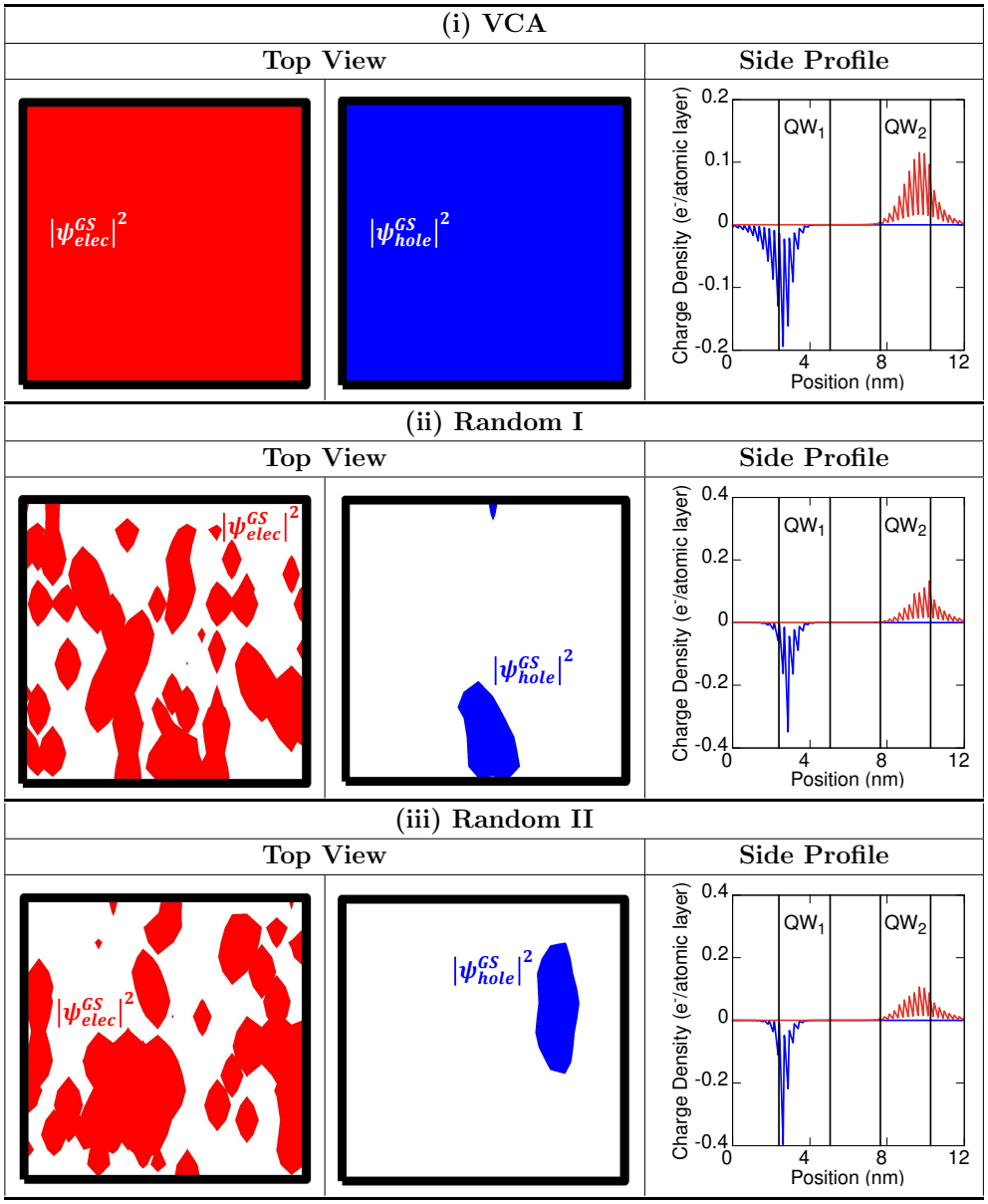

Figure 5.4: Top view (along the *c*-axis) of isosurface plots of (left) electron and (middle) hole charge densities for a (i) VCA, (ii) Random I and (iii) Random II system with the built-in polarization field included. The isosurfaces correspond to 40% of the respective maximum charge density values. The right panel of the figure shows the planar integrated charge density, $P(z^k_\alpha)$, along the supercell for both electrons and holes.

our attention on the impact of the different levels of randomness on the transmission properties of the two QW systems discussed above.

5.3.2 Impact of alloy fluctuations on transmission properties of (In,Ga)N MQWs

In order to understand the impact of the underlying alloy microstructure on ballistic electron and hole transport, we start with the 2 QW system discussed above. Since

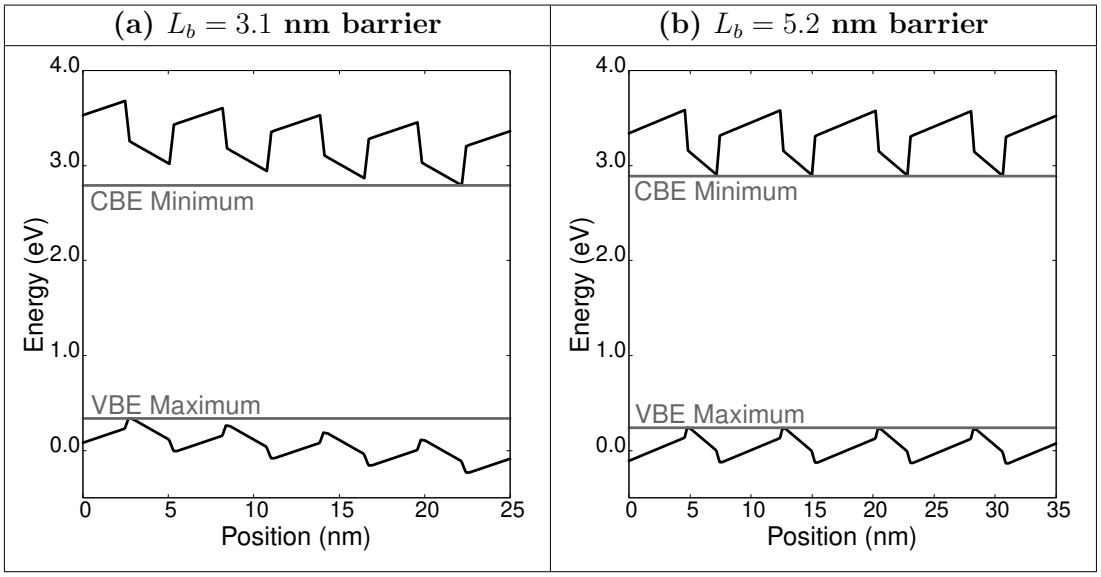

Figure 5.5: Conduction and valence band edges, in virtual crystal approximation, for the four $In_{0.12}Ga_{0.88}N$ multi quantum well system including a built-in field due to a *p-i-n* junction, spontaneous and piezoelectric polarization effects. Band edge profile for a barrier width (a) of $L_b = 3.1$ nm and (b) of $L_b = 5.2$ nm.

we have already seen that the intrinsic built-in field significantly affects the electronic structure of this system, we follow the same procedure as above and neglect this potential initially; its impact on the results will be discussed in a second step.

5.3.2.1 Absence of built-in field

Focusing on electrons/conduction band first, Fig. 5.6 (a) depicts the transmission spectrum of the two QW system in the absence of the built-in field when calculated within VCA (black) and Random I (blue). The results for Random I are averaged over 5 different random alloy configurations. In case of the VCA description (black), the transmission spectrum shows a doublet of peaks with transmission close to 1 below the GaN CBE of 3.45 eV. This doublet stems from the bonding/anti-bonding electron states in two QWs (see above). A similar situation is found for transmission peaks near the CBE of GaN (≈ 3.45 eV). The larger splitting in energetically higher lying peaks stems from the effect that near the GaN CBE the electronic states from the two QW interact more strongly, resulting in a larger splitting of bonding and anti-boding states when compared to the energetically lower lying (more strongly bound) electron states. Also, the broadening of the peaks is related to the confinement of the states. Above the GaN CBE (> 3.45 eV) there is a continuum of states which facilitate transmission. Turning to the results from the calculation within the Random I frame (blue), the spectrum is very similar to the VCA result. Figure 5.6 (a) also reveals that each microscopic configuration leads to transmission peaks at slightly different energetic positions. In general, this effect gives rise to a broadening of the energetic range over which transmission may be

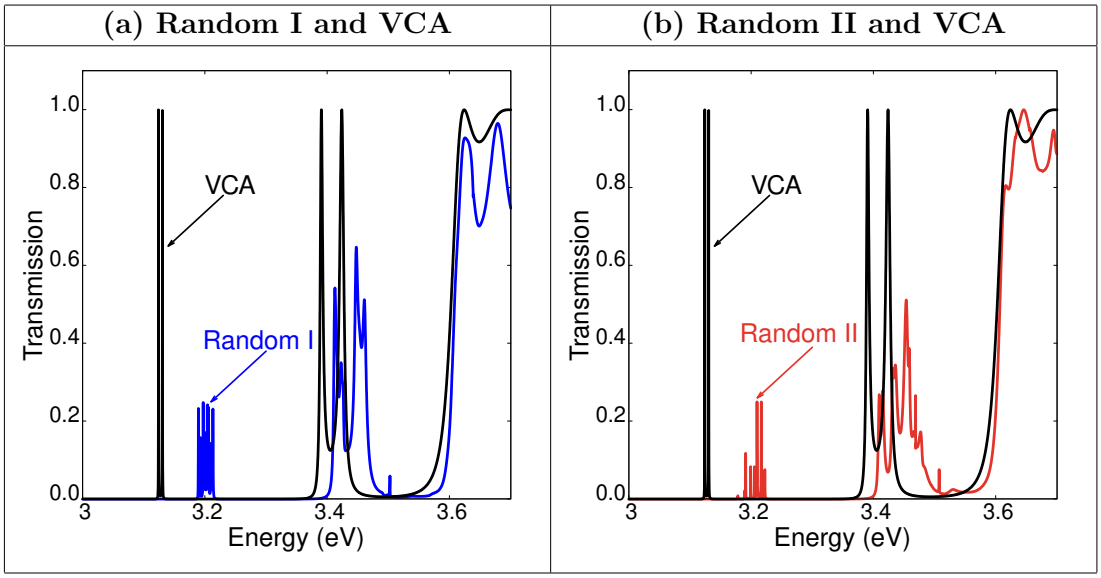

Figure 5.6: Electron transmission spectra through a two $In_{0.12}Ga_{0.88}N$/GaN multi quantum well system with well width of $L_w = 2.6$ nm and barrier width of $L_b = 2.6$ nm. The results are shown in absence of the built-in field. Virtual crystal approximation (VCA) results are given in black; random alloy system in blue and red, respectively, averaged over 5 microscopic configurations.

expected. Several things are important to note. First, the low transmission peak values at an energy of 3.2 eV in the Random I case result from averaging over the 5 different microscopic configurations and are *not* a result of the random alloy fluctuations in the well. For an individual configuration these peaks are sharp and they exhibit a transmission value of close to 1. This can be seen in Fig. 5.7 where the electron transmission spectrum of an arbitrary microscopic configuration is shown for Random I (blue). The same effect is seen at the energetically higher lying peaks, and the continuum above the GaN CBE. However, given that the peaks are sharp and their energies differ (slightly) between configurations, the averaging process reduces the heights of the peaks. This effect is less pronounced for higher lying peaks since these are broader and the variation in energy between different configurations is smaller. This analysis shows that, for electrons, the alloy fluctuations in the well do not lead to a (strong) reduction in the ballistic transport properties, at least when the alloy microstructure is the same in both wells.

We note also that for the VCA description, assumptions about the parameter averaging procedure (e.g. bowing parameters) has to be made. Therefore, usually a reference/benchmark system is required. Having now the random alloy system as a reference, by adjusting the VCA further, a good agreement between VCA and Random I may be achieved, given that the overall features of the transmission spectra are very similar.

So far we have assumed that the alloy microstructure in the two wells is the same.

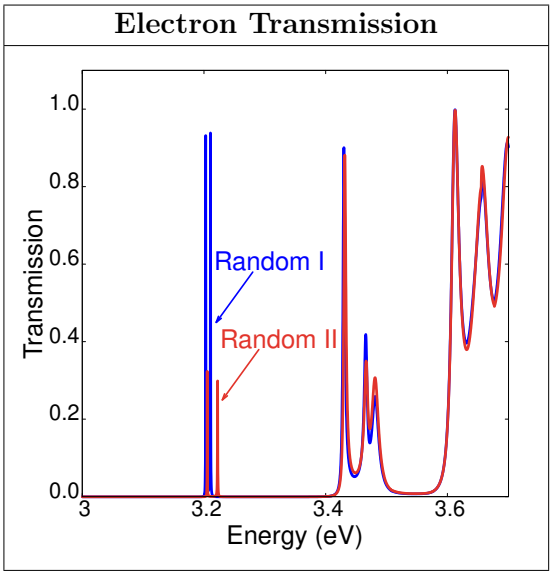

Figure 5.7: Comparison of the transmission properties of electrons for an arbitrary microscopic alloy configuration for Random I (blue) and Random II (red) in the $In_{0.12}Ga_{0.88}N$/GaN multi quantum well system with two wells; the well width $L_w = 2.6$ nm and the barrier width $L_b = 2.6$ nm. The calculations are performed in the absence of the built-in field. Random II differs from Random I by having a different microscopic alloy configuration in the second well, the alloy microstructure in the first well is identical in the two systems.

The question remains how the different random alloy configurations within the two wells will affect the transmission properties. Thus in the following we focus on the comparison between VCA and Random II.

Figure 5.6 (b) shows the transmission spectrum for the VCA (black) and the Random II (red) system. Overall, the spectrum within Random II is, at first glance, not very different from the spectrum calculated within Random I (cf. 5.6 (a)). Therefore the VCA spectrum also gives a good approximation of the Random II spectrum. However, now that the microscopic configuration differs between the two QWs, the symmetry between the wells is broken and the electronic states between the wells do not necessarily align energetically. As a result, the transmission of the lowest lying states is now indeed reduced. To see this clearly, Fig. 5.7 shows the transmission spectrum of an arbitrarily chosen microscopic configuration in Random II in comparison to the spectrum of Random I. While above the GaN CBE the two structures give basically the same spectrum, the transmission via bound QW states is noticeably reduced in the Random II case when compared to Random I. But, overall the electron transmission spectrum does not change dramatically between the two different random alloy assumptions and VCA gives a good description of the general features of the spectrum.

We now analyze the same situations for ballistic *hole* transport. Figure 5.8 (a) shows a comparison of the hole transmission spectra in VCA and Random I systems. The latter is again averaged over 5 different microscopic configurations. While for electrons, Ran-

dom I and VCA gave very similar results, the hole spectra reveal a drastically different picture. Since the VBE of the unstrained GaN barrier is chosen as the zero of energy for the considered structures, cf. Fig. 5.2 (a), the VCA calculation shows one doublet of transmission peaks stemming from bound hole states in the well. As in the electron calculation, this doublet originates from the bonding and anti-bonding states of the two QWs within VCA. By comparison, the Random I case reveals a high density of transmission channels close to the GaN band edge, which are not present in the VCA result. We note also that Random I gives rise to new transmission peaks energetically above the VCA QW related transmission peaks. As a result, a continuum based calculation neglecting alloy fluctuations would underestimate the ballistic hole transport.

We attribute the appearance of extra transmission channels in the Random I case to the alloy induced symmetry breaking effects. Given the strong hole localization discussed in the literature [41, 44, 232] and also above, a significant deviation from an ideal QW picture may already be expected. While in the VCA/ideal QW case all well states can be classified according to their in-plane $\mathbf{k}$-vector, $\mathbf{k}_{\|}$, this classification is no longer possible for the random alloy case. So, $\mathbf{k}_{\|}$-vector conservation for transmission is no longer required in the random alloy case. As a consequence, the random alloy calculations include extra channels which are available to contribute to transmission. A similar argument has recently been put forward for optical properties, where it has been argued that the absence of $\mathbf{k}_{||}$ as a good quantum number results in more optically allowed transitions when compared to a VCA description of an (In,Ga)N QW [58]. Overall, our analysis shows that the VCA gives a poor estimate of hole ballistic transport properties, in contrast to electrons.

The question remains how the result is changed when the randomness is different in the two wells, which is reflected in our system labeled as Random II. The outcome of this analysis is shown in Fig. 5.8 (b). For Random II the transmission close to the GaN VBE is very similar to the Random I case and therefore noticeably different from the VCA results. However, the transmission peaks at energies higher then the energetically highest doublet in VCA are basically missing in Random II, which presents a difference to the Random I data (cf. Fig. 5.8 (a)). We relate this effect to the symmetry breaking between the wells. Even though the average In content is the same, the difference in the alloy microstructure leads to different electronic structures in the wells, given the pronounced hole localization effects. As a consequence, the transmission probability involving energetically higher lying (more strongly bound QW) states is reduced in the Random II case when compared to its Random I counterpart. This can be seen in Fig. 5.9 where the transmission spectrum of Random I (blue) and Random II (red) of an arbitrarily chosen configuration is shown. Above 0.015 eV, most peaks in Random II are smaller when compared to Random I. By contrast, the states closer to 0 eV (unstrained GaN VBE) are more delocalized wave functions so that the electronic coupling between the wells is stronger and in turn a higher transmission probability is observed. Along

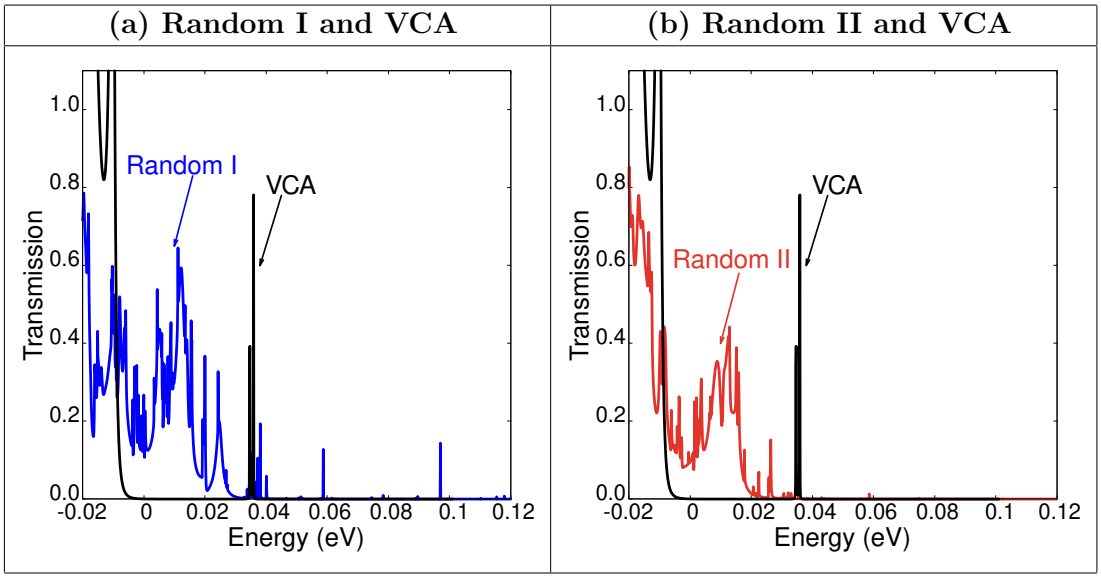

Figure 5.8: Hole transmission spectra through a two $In_{0.12}Ga_{0.88}N$/GaN multi quantum well system with well width of $L_w = 2.6$ nm and barrier width of $L_b = 2.6$ nm. The results are shown in the absence of the built-in field. Virtual crystal approximation (VCA) results are given in black; random alloy system in blue and red, respectively, averaged over 5 microscopic configurations.

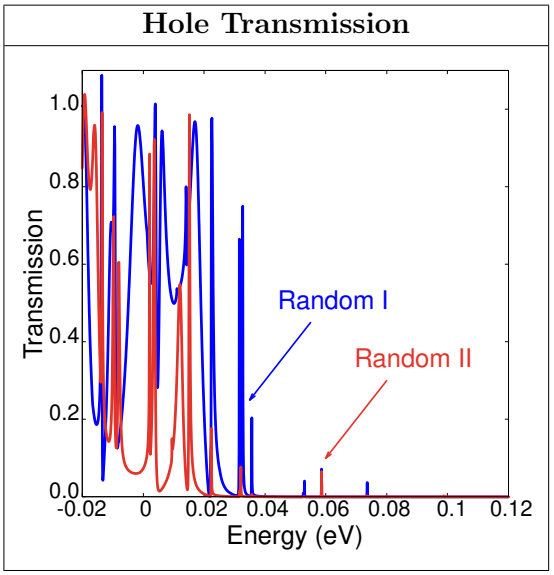

Figure 5.9: Comparison of the transmission properties of holes for an arbitrary microscopic alloy configuration for Random I (blue) and Random II (red) in the $In_{0.12}Ga_{0.88}N$/GaN multi quantum well system with two wells; the well width $L_w = 2.6$ nm and the barrier width $L_b = 2.6$ nm. The calculations are performed in the absence of the built-in field. Random II differs from Random I by having a different microscopic alloy configuration in the second well; the alloy microstructure in the first well is identical in the two systems.

with the breakdown of $\mathbf{k}_{\|}$ as a good quantum number, a larger number of transmission peaks is observed in Random I and II when compared to VCA.

Overall, our analysis shows that changing the randomness between the wells has a slight impact on the hole transmission spectrum. Introducing random alloy fluctuations in general is the dominant effect as seen above. But, in addition to the symmetry breaking of the random alloy fluctuations, the presence of the electrostatic built-in field will also have a strong impact. We study its impact on the electron and hole ballistic transport properties in the following section.

5.3.2.2 Impact of the built-in field

Including the polarization field results in a potential step across the QWs (cf Fig. 5.2 (b)), which modifies the GaN CBE and VBE profiles. Therefore, the energy at which states are present to contribute to the transmission through the two QWs is changed.

Before looking at the fine details, Fig. 5.10 (a) shows that for *electrons* the transmission spectrum obtained within VCA reflects the same behavior as the spectrum obtained from Random I. Also, when comparing the Random II result with the VCA data, as displayed in Fig. 5.10 (b), the spectra are very similar. We do not see a reduction in transmission peaks when the microscopic configurations are varied between the wells. Thus the transmission properties in this case are basically dominated by the electrostatic built-in field and not the random alloy fluctuations.

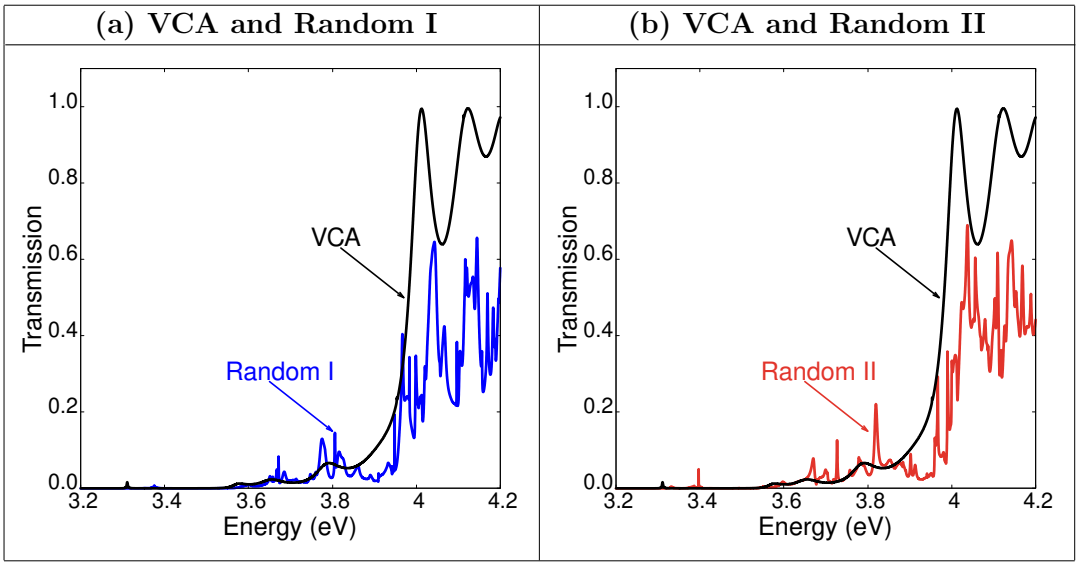

Figure 5.10: Electron transmission spectra through a two $In_{0.12}Ga_{0.88}N$/GaN multi quantum well system with well width of $L_w = 2.6$ nm and barrier width of $L_b = 2.6$ nm. The electrostatic built-in field is included in the calculations. Virtual crystal approximation (VCA) results are given in black, random alloy system in blue and red, respectively, averaged over 5 microscopic configurations.

The same is true for *holes*, as the calculated transmission spectra depicted in Fig. 5.11 reveal. Thus, when taking the electrostatic built-in field into account, the VCA provides

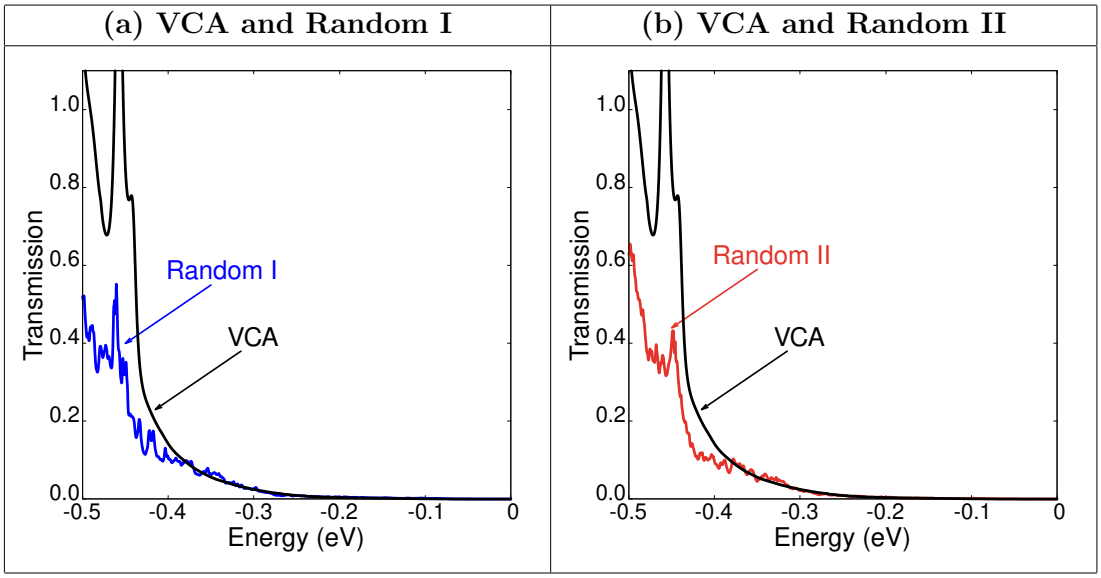

Figure 5.11: Hole transmission spectra through a two $In_{0.12}Ga_{0.88}N$/GaN multi quantum well system with well width of $L_w = 2.6$ nm and barrier width of $L_b = 2.6$ nm. The electrostatic built-in field is included in the calculations. Virtual crystal approximation (VCA) results are given in black, random alloy system in blue and red, respectively, averaged over 5 microscopic configurations.

a good description of ballistic transport properties for both electrons and holes. However, it is important to note that in the flat band condition (no field), as discussed in the previous section, the situation especially for the holes is different. As we have seen in Section 5.2, the symmetry breaking between the wells due to the built-in field also depends on the barrier width between the wells and the presence of the *p-i-n* junction induced field. Thus, we study in the following section how the presence of this external field in a device and changes in the barrier width affect the ballistic transport of electrons and holes in an (In,Ga)N MQW system.

5.3.3 Multi-quantum well system in a *p-i-n* junction

As already highlighted in Section 5.2, the built-in potential originating from the *p-i-n* junction affects the CBE and VBE profile of a (In,Ga)N/GaN MQW system. Also we have discussed that the barrier width L_b in conjunction with this field will affect the band edge profiles. In the following sections we analyze their combined impact on the ballistic transport properties of the MQW system introduced in Section 5.3.3.1. We start in Section 5.3.3.1 with the system with a barrier width of $L_b = 3.1$ nm before turning to the structure with $L_b = 5.2$ nm in Section 5.3.3.2. The width of the individual wells is kept constant at $L_w = 2.6$ nm. We reiterate that, as Random I is not a situation that is likely to be found in a real device, we only treat the systems using a VCA and Random II.

5.3.3.1 Barrier width $L_b = 3.1$ nm

The transmission spectrum calculated within VCA (black) and the Random II assumption (red) is shown in Fig. 5.12 for (a) electrons and (b) holes for the MQW system with four $In_{0.12}Ga_{0.88}N$ wells with a barrier width of $L_b = 3.1$ nm. The random alloy data is obtained as an average over the transmission spectra of 5 different random alloy configurations. Looking at the VCA results for electrons first, Fig. 5.12 (a), transmission is mainly found at higher energies (> 3.5 eV). Below 3.5 eV the VCA transmission probability is low. Examining the CBE profile depicted in Fig. 5.5 (a) indicates that in the VCA case, bound QW states do not contribute to the transmission through the MQW system. In VCA, a similar situation is found for the holes, as Fig. 5.12 (b) reveals. Here, the first peak in the VCA hole transmission spectrum is found at around -0.13 eV. Looking at the VBE profile depicted in Fig. 5.5 (a), in terms of the energy, mainly the fourth well (last well on the right in Fig. 5.5 (a)) presents a potential barrier for the transmission process. Energetically higher lying valence states (bound hole states) do not contribute to the transmission, given that due to their high effective mass, these wave functions are strongly localized within individual wells.

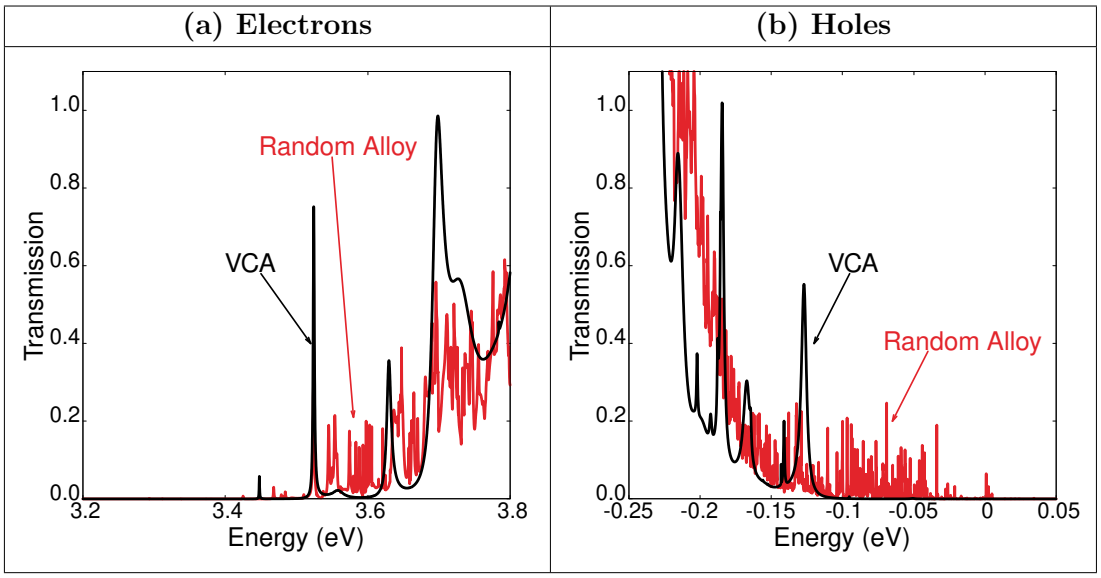

Figure 5.12: Transmission spectra of the four $In_{0.12}Ga_{0.88}N$/GaN multi quantum wells with well width of $L_w = 2.6$ nm and barrier width $L_b = 3.1$ nm calculated within virtual crystal approximation (black) and a random alloy description (Random II; red, averaged over 5 configurations). The calculations include spontaneous and piezoelectric built-in potentials as well as a field originating from a *p-i-n* junction.

Turning to the random alloy case, and focussing initially on the electron transmission spectrum (cf. Fig. 5.12 (a)), the calculated spectrum is very similar to the VCA case. This means one is also left with very low transmission probabilities below 3.5 eV; only for energies larger than 3.5 eV significant transmission is observed. The difference between the random alloy case (red) and the VCA result in this energy range is the

spectral broadening of the transmission. The VCA transmission is described by 2 distinct peaks before the onset of a continuum. By contrast, the random alloy calculation results in many peaks distributed across the same energy range (between 3.5 eV and 3.7 eV), before the continuum onset. These result from the differing microscopic configurations providing higher-probability transmission channels at different energies.

The situation is different for the holes. Figure 5.12 (b) shows, in addition to the VCA spectrum (black), also the hole transmission spectrum (red) of the Random II case. The comparison between VCA and Random II data reveal clearly that in the random alloy case an earlier onset (higher energies) of the transmission occurs. More specifically, we observe strong transmission peaks in the energy range from -0.1 eV to 0 eV in the random alloy calculation; VCA basically shows no peaks in this energy range. We again note that due to the averaging process, and the sharpness of the peaks, these peaks are a lower bound of the transmission in this energy range. In other words, a noticeable effect is observed due to the presence of random alloy fluctuations.

Overall, this investigation reveals that (i) the energetic alignment of the different wells in a MQW system becomes important for the transmission probability of the carriers, (ii) VCA gives a good description of the electron ballistic transport properties of the MQW system and (iii) that VCA underestimates the hole ballistic transport noticeably. Especially the last point is important. For efficient radiative recombination in an (In,Ga)N/GaN MQW system, the carriers ideally transfer easily between the wells so that when electrons are injected from the n-side and holes from the p-side of the device, all QWs in the MQW structure contribute to the light emission process. Therefore, the finding that the random alloy fluctuations introduce additional channels at lower energies would then facilitate a more efficient distribution of holes between the MQW system than expected from a VCA type calculation.

Overall alloying the GaN barrier with a small portion of In (e.g. 5%) could provide a pathway for improving hole transport in (In,Ga)N MQW systems and thus the carrier distribution in the different wells. Firstly, such an approach would reduce the effective barrier height, which results in weaker confinement of bound states and an increased leakage of carrier wave functions into the barrier. Secondly, (In,Ga)N barriers with low In content could also facilitate percolation transport between the wells. Here carriers can take a path through regions where the potential barrier is locally low. Similar effects have been observed for n-i-n transport studies containing AlGaN electron blocking layers [233]. However, the impact of alloying the barrier with small fractions of In on the ballistic hole transport between wells may be more subtle. In the absence of alloy disorder, $\mathbf{k}$ is a good quantum number in the GaN barrier, so that there is no scattering once the carrier enters the barrier. In the presence of alloy fluctuations, scattering is possible and the transmission probability should be reduced. However, while this may be true for individual transmission peaks, a large number of additional channels may be

made available. This is also reflected in our results above, which indicate that transmission above the GaN band edge is increased by alloy fluctuations. A similar feature has been observed in recent studies on the radiative recombination rates in (In,Ga)N/GaN QWs, where alloy fluctuations reduce the oscillator strength of individual transitions when compared to a VCA calculation. However, due to the breaking of the **k**-selection rules, the number of allowed transitions is increased, leading to an overall increase in the radiative recombination rate when compared to the VCA calculations [58]. We revisit the discussion of the potential impact of alloying the barrier material with In further below and present initial results in Appendix B.

Here, we have discussed the ballistic transport properties for a barrier width of $L_b = 3.1$ nm. As we have seen above, cf. Fig. 5.5, the barrier width will also affect the VBE and CBE profile. Additionally the electronic coupling between the wells, and therefore the ballistic transport, should also be affected by the barrier width. In the next section we analyze the impact of L_b on the transmission properties in more detail.

5.3.3.2 Barrier width $L_b = 5.2$ nm

Figure 5.13 (a) shows the electron transmission spectra in VCA (black) for the $In_{0.12}Ga_{0.88}N$/GaN MQW system introduced in Section 5.2.2 with a barrier width of $L_b = 5.2$ nm; the spectrum obtained within the random alloy description Random II is given in red. The depicted data for Random II is the average over 5 different random alloy configurations. Bearing in mind the band edges in Fig. 5.5 (b), and looking first at the VCA data, we mainly observe transmission peaks above 3.6 eV, which is the CBE of the barrier material. Basically the same behavior is observed in the random alloy case. Thus, similar to the smaller barrier width discussed above, for electron ballistic transport, VCA yields a good description of the system.

Figure 5.13 (b) depicts the transmission spectrum for holes in VCA (black) and Random II (red). When comparing the calculated spectra for VCA and random alloy description, we find that the random alloy fluctuations introduce “extra” transmission channels when compared to VCA data. We note also that for the chosen barrier width, the CBE and VBE of the different wells are almost perfectly aligned in the VCA case. This is obviously the best case scenario, but is probably not the norm when e.g. changing doping profile or the barrier width further. Even a slight shift in the energies between neighboring wells results in a sharp reduction of the VCA transmission peaks (not shown). For the random alloy system the situation is different. Here, alloy fluctuations already break the symmetry between wells intrinsically, thus aligning or not aligning the band edges is of secondary importance for the random alloy case. Bearing in mind the strong dependence of the VCA transmission on the alignment of the band edges, the random alloy fluctuations should still open additional transmission channels, given that **k**-conservation breaks down, and thus lead to an enhancement of

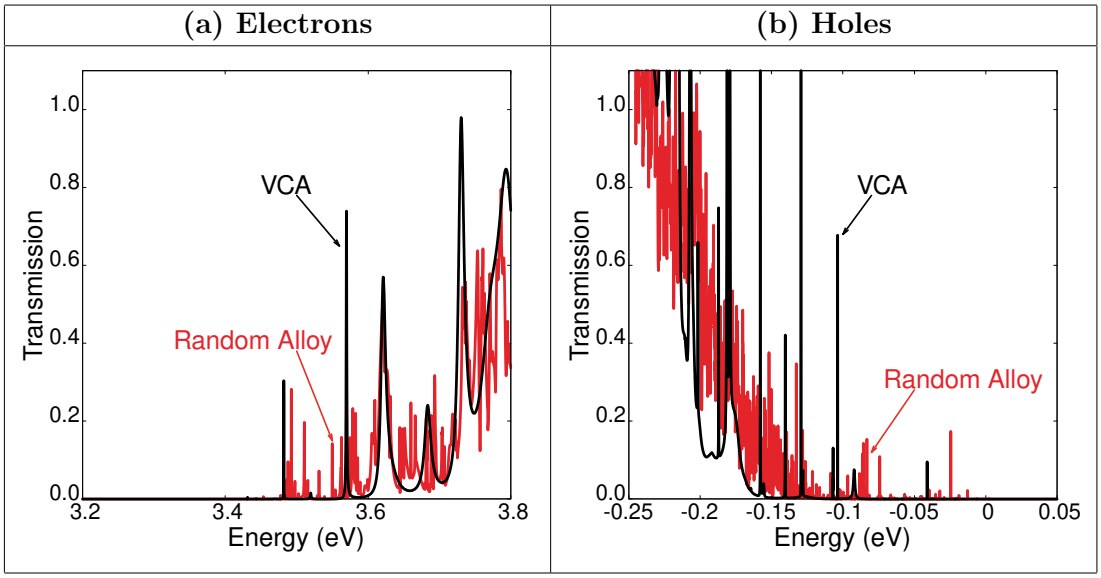

Figure 5.13: Transmission spectra of the four $In_{0.12}Ga_{0.88}N$/GaN multi quantum wells with well width of $L_w = 2.6$ nm and barrier width $L_b = 5.2$ nm calculated within virtual crystal approximation (black) and a random alloy description (Random II; red, averaged over 5 configurations). The calculations include spontaneous and piezoelectric built-in potentials as well as a field originating from a *p-i-n* junction.

the transmission. However, overall we can conclude that the wider barrier width suppresses ballistic transport compared to the narrower barrier width, given that electronic coupling between the QWs is reduced.

But, as discussed already above, alloying the barrier with In could provide a way forward to increase the transmission probability. Our calculations have shown that the hole transmission through the "extra" channels is sensitive to the state confinement, and the coupling between states in neighboring wells. Including In in the barrier would reduce the confinement of states within the wells, and could lead to a situation where hole ballistic transport is improved at wider barrier widths. In a recent experimental study, Marcinkevičius *et al.* analyzed such a situation [234]. Their data reveal indeed an increased hole transmission through an (In,Ga)N MQW system when 5% In was introduced in the GaN barrier. Our analysis indicates a potential mechanism underlying the experimentally observed increase in ballistic hole transport, which is supported by initial results presented in Appendix B. Further studies are required to shed more light on this question; this is beyond the scope of the present study, which is aimed at providing insight into the impact of alloy fluctuations within the well and how the level of randomness affects the carrier transport in (In,Ga)N/GaN MQW systems. Recent semi-classical (DD) studies have also observed that alloying the barrier region (using a random alloy description) near the QW leads to an increased carrier transport, in line with our expectations based on this study [210].

5.4 Conclusion

In this work we have presented an analysis of the ballistic transport properties of (In,Ga)N/GaN MQW systems by means of a combined atomistic TB-NEGF approach. We have paid special attention to the impact of (random) alloy fluctuations on both electron and hole ballistic transport. To investigate the impact of alloy disorder, results are compared to the outcome of calculations that utilize a virtual crystal approximation of the (In,Ga)N MQWs. Our data shows that for electrons the alloy microstructure is of secondary importance for their ballistic transport, while for hole transport the situation is different. We observe that for narrow GaN barrier width in an (In,Ga)N/GaN MQW system, the presence of the alloy fluctuations give rise to extra hole transmission channels when compared to a virtual crystal description of the same system. We attribute this effect to the situation that in the random alloy case, $\mathbf{k}_{\|}$-vector conservation is broken/relaxed and therefore the ballistic hole transport increases. Thus, a VCA description would underestimate the contribution from hole ballistic transport in general. However, for wider barrier width this effect is strongly reduced. Overall, our theoretical findings of significant ballistic hole transport for narrower barrier width, which decreases with increasing barrier width, is consistent with recent experimental studies [224].

Furthermore, the gained insight indicates a potential explanation for the recent experimental observation that alloying the GaN barrier region between the wells with small fractions of In (e.g. 5%) is beneficial for hole ballistic transport in (In,Ga)N MQW system. Based on our results, such an approach results in (i) the breakdown of $\mathbf{k}_{\|}$-vector conservation and (ii) a slight reduction in the barrier height between the wells.

The NEGF methods used in this chapter are numerically very demanding, so our study was focused only on the region close to QWs which could form the active region of an LED. This chapter has highlighted that a VCA description is *not* sufficient to describe hole transport, however new methods are needed to investigate how this will impact transport in, for example, a full LED structure. Therefore we focus next on a multi-scale, DD based description of transport which allows us to scale the simulations up to larger system sizes.

Chapter 6

Multiscale simulations of uni-polar charge transport in (In,Ga)N-based devices with random fluctuations

In Chapter 5 we saw that alloy fluctuations can have a significant impact on ballistic transport in (In,Ga)N-based devices. Due to the numerical demand of the NEGF method (even in the ballistic case) the simulations are basically limited to a very small region - in this case the area close to the QWs. Given this numerical burden the workhorse for transport calculations still remains largely DD. Thus, we now we employ the quantum corrected DD model which was derived in Section 4.2; this ensures that the impact of alloy fluctuations in the QW region ìs still included. We begin by applying the framework to uni-polar carrier transport in both the *n-i-n* (electron) and *p-i-p* (hole) case. This allows us to disentangle transport effects from other effects such as recombination. It also enables us to address each carrier individually, starting with uni-polar electron transport.

6.1 Uni-polar electron transport

As we highlighted in the prologue, III-nitride-based QW structures are at the heart of modern short wavelength LEDs [29,235]. Here, (In,Ga)N/GaN multi-QWs (MQWs) are used to realize devices operating in the visible part of the spectrum. We also previously stressed the different properties that nitride-based heterostructures have compared to other III-V material systems; namely the underlying wurtzite crystal structure, and the built-in polarization field. These features can be accounted for in 1-D simulations, however generally the predicted I-V curves of such simulations do not reflect experimental results [64, 218, 236]. It has recently been shown that this shortcoming in the simulation of (In,Ga)N-based LEDs [67] or uni-polar devices [218] is related to (i) treating

these systems as 1-D as well as (ii) the semi-classical nature of DD models.

Regarding (i), as previously stated, the theoretical and experimental studies have revealed that the electronic and optical properties of III-N-based heterostructures are strongly affected by alloy fluctuations and accompanying carrier localization, all of which is not fully reflected within a 1-D DD transport model [67, 70, 218]. Furthermore, (ii) the semi-classical nature of DD models neglects quantum mechanical effects, such as tunneling. Fortunately, such quantum effects can be included, to some extent, in DD simulations via LLT (discussed in Section 3.4) or the (nonlocal) effective potential method to smooth band edges [186, 237, 238]. Thus, to accurately guide the design of future III-N based LEDs, a fully 3-D, ideally atomistic, transport model which includes quantum mechanical effects for the *entire* device is required.

As mentioned previously, the numerical demand of the atomistic NEGF calculations of Chapter 5 is high. When extending simulations to full device calculations via the DD formalism the challenge is to transfer atomistic effects into a modified, quantum-corrected transport model. Previous work, targeting for instance (In,Ga)N LED or unipolar devices, tackled such a multi-scale problem in the following way: [67, 219] First, a random distribution of In and Ga atoms on either a cubic or a wurtzite grid is generated. Second, based on such a distribution, the local In content is determined by using averaging procedures on the underlying grid. Equipped with this information, continuum-based strain and built-in field calculations are performed which can then be used to generate an "energy landscape" (conduction and valence band edges/confining potential), mainly in the framework of a single-band EMA. This information can either be directly used for 3-D DD-based transport calculations or even coupled with LLT to account for quantum corrections. It is important to note that such an approach relies on (i) identifying an interpolation procedure for the local alloy content, (ii) the knowledge of how related material parameters change with composition locally and (iii) on assuming that bulk parameters can be used locally to obtain strain and built-in fields effects. Finally, it assumes that even when including random alloy fluctuations, the modified continuum-based single-band EMA describes the electronic structure of this complicated system accurately. Thus, overall "atomistic" aspects enter mainly at the In atom distribution level. However, it is difficult to judge how well local fluctuations in strain or built-in fields are captured in comparison to a fully atomistic approach (valence force field plus local polarization theory). Furthermore, consequences of alloy fluctuations for the electronic structure of the well and again how this compares to a fully atomistic description, e.g. TB, is not widely discussed or analyzed.

We discussed in Section 4.2.2.1 a framework to make just such a comparison. We extracted an energy landscape from TB which was used in single band EMA to calculate the electronic structure, and calibrated the model using TB such that the band gap and splitting between states provided a good comparison. In this work, we extend this

theoretical framework to study charge transport in III-N based devices. Details of the formalism have already been presented in Chapter 4. In general, we use the energy landscape calculated from our atomistic TB model in conjunction with LLT to generate a quantum-corrected energy landscape. This landscape presents the backbone of our DD simulation. For the active (In,Ga)N QW region we use a FEM mesh with as many nodes as atomic lattice sites, which we later enlarge to work in combination with a specialized FVM. In doing so, (*n*-doped) contact regions can be added to the system on a much coarser grid to model a full device. We highlight that the developed approach can be extended to investigate uni-polar hole transport (Section 6.2) or complete (In,Ga)N-based LED structures (*p*-*i*-*n* systems, e.g. Chapter 7).

The remainder of the section is organized as follows: We present the theoretical ingredients of our multi-scale model which were discussed in detail in Chapter 3 and Chapter 4, namely TB, LLT and DD. Our results for uni-polar transport in (In,Ga)N-based (single QW) SQW and MQW systems are detailed in Section 6.1.2. Finally, we summarize our framework and the results in Section 6.1.3.

6.1.1 Theoretical framework

In order to capture the effects of (random) alloy fluctuations on the CBE and VBE and ultimately on the electronic structure of the QW active region of a III-N device, we employ an atomistic TB model which has been discussed in detail in Section 3.2. An atomistic description of strain is found by relaxing the atomic coordinates using a VFF model. The (local) polarization potential is then calculated using a local polarization theory. These were discussed in detail in Section 3.3.

A key ingredient for DD transport calculations are the (local) CBEs and VBEs. This information can be extracted from our TB model by generating and diagonalizing a local Hamiltonian at each lattice site, following the procedure of Section 4.2.2.1. This forms a 3-D confining energy landscape on the wurtzite lattice sites which can include alloy fluctuations as well as atomistic strain and polarization effects. The local band edges need to be transferred to a mesh that allows us to perform the transport calculations. This is done by including coarse mesh regions, where alloy fluctuations are of secondary importance, to the atomistic region as detailed in Section 4.2.2.4. This allows us to generate a FVM mesh which can be used for DD calculations. Details of the system size used will be given later in Section 6.1.2.

In Section 4.2.2 we discussed the complication associated with a strongly fluctuating landscape coupled with DD equations. In order to address this issue we include a Gaussian softening of the band edge energies which were extracted from TB, following the approach in Section 4.2.2.

6.1.1.1 Smoothing by Gaussian averaging

In general, employing such a Gaussian averaging procedure comes at the cost of having to correctly determine the width, σ, a priori. To analyze the impact of the σ on the CBE profile, which ultimately will also impact the transport, Fig. 6.1 shows the profile of $E_c^\sigma - q\psi$ in a 3.1 nm wide $In_{0.1}GaN_{0.9}$/GaN SQW, comparing random alloy fluctuations with different Gaussian widths σ to a VCA. Here ψ denotes the electrostatic potential in the *n-i-n* device, including also piezoelectric and spontaneous polarization effects; q denotes the elementary charge; E_c^σ is the CBE energy when a Gaussian width of σ is used. At each plane along the *c*-direction, the full range of CBE values over the x-y plane is shown, which allows a clear visualization of the impact of the alloy fluctuations on the CBE. Several features are important. The most striking difference between the VCA and the smoothed random alloy (RA) CBE is that the potential barrier between GaN and (In,Ga)N QW material is significantly reduced. This feature is expected to reduce the turn-on voltage of the device and will be discussed in detail further below. Moreover, the barrier-well interface reduces further with increasing σ. However, the reduction between $\sigma = 0.6$ nm and $\sigma = 0.9$ nm is smaller than the reduction from $\sigma = 0.3$ nm to $\sigma = 0.6$ nm, even though the difference in σ values is the same ($\Delta\sigma = 0.3$ nm). We also note that while the average band edge energy in the well is basically unaffected by different σ values, the CBE fluctuations in the well noticeably reduce. Consequences of these effects on the current-voltage characteristics are discussed below.

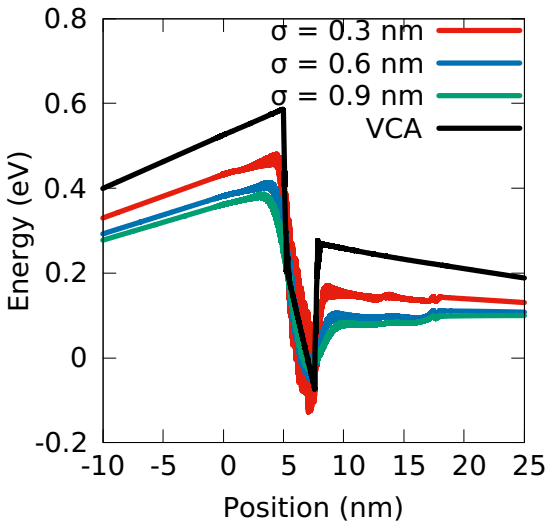

Figure 6.1: Randomly fluctuating, smoothed conduction band edge profile along the z-(c)-axis of an *n-i-n* $In_{0.1}Ga_{0.9}N$/GaN single quantum system at zero bias (more details given in the main text). The results are displayed in the *absence* of quantum corrections via LLT, but for three different Gaussian widths σ, namely σ =0.3 nm (red), σ =0.6 nm (blue) and σ =0.9 nm (green), as well as for a "standard" virtual crystal approximation (VCA, black).

6.1.1.2 Quantum corrections by localization landscape theory

Having determined the local band edges from atomistic TB theory, we can now also include quantum corrections using LLT [158]. These corrections are not limited to a calculation that accounts for random alloy fluctuations; LLT can also be used in conjunction with a VCA description. We note that many commercial software packages targeting transport properties of III-N devices also have the option to include quantum mechanical effects by solving Schrödinger's equation in the active region (QW region) of a device. However, such an approach is numerically extremely demanding even for a 1-D simulation, not to mention a full 3-D calculation, which is necessary in the presence of random fluctuations. As already discussed in detail in Section 3.4, when using LLT one avoids having to solve the Schrödinger equation, and thus a large eigenvalue problem since the landscape equation is:

$$H\,|u\rangle = 1\ . \tag{3.26 revisited}$$

Here we use it to extract an effective confining potential, W, via Eq. (3.27):

$$W_j = \frac{1}{u_j}\ . \tag{3.27 revisited}$$

Regarding the computational aspects, we numerically solve the LLT equation, Eq. (3.26), supplied with appropriate Dirichlet and Neumann boundary conditions on the atomistic FEM mesh via a standard FEM [239]. The Dirichlet conditions are applied on the left and right boundaries of the atomistic FEM mesh, and are implemented via a penalty technique [240]. The FEM discretization is implemented in `WIAS-pdelib` [223], using `PARDISO` as linear solver [241].

Since LLT basically replaces the Schrödinger equation, LLT provides also information about the energy spectrum and the wave functions [242]. Thus, the outcome of the LLT calculations can be directly compared to our TB data. For the SQW structures analyzed in Section 6.1.2, we find very good agreement between TB and LLT when applying a rigid band edge shift of 129 meV to the CBE in the QW region in the EMA description, in line with Ref. [4]. All this provides a feedback loop between our atomistic model, the obtained landscape and the resulting electronic structure. This benchmarking gives further confidence that the here established simulation framework for performing transport calculations captures alloy fluctuations accurately in a SQWs.

Examples for the resulting effective energy landscapes/confining potential energies $W - q\psi$ are given in Fig. 6.2. We observe that similar to the random alloy case *without* quantum corrections, cf. Fig. 6.1, the LLT treatment leads also to a reduction in the potential barrier between GaN material and (In,Ga)N QW. Therefore, the strongly fluctuating TB landscape is "softened", given that the carrier wave functions sample a wider "area" on this landscape, as one may expect from a quantum mechanical wave

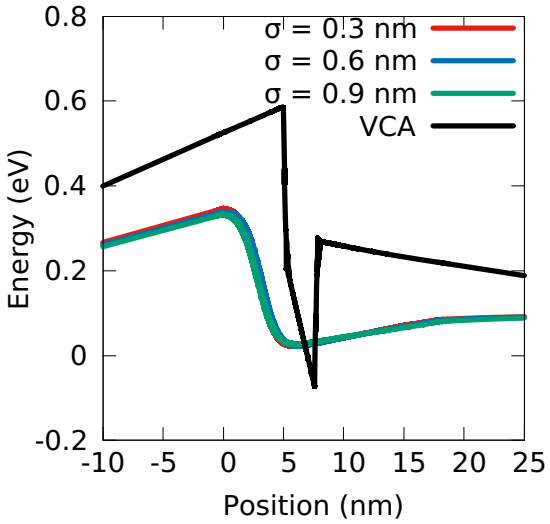

Figure 6.2: Randomly fluctuating, smoothed conduction band edge profile along the z- (c)-axis of an n-i-n $In_{0.1}Ga_{0.9}N$/GaN single quantum well system at zero bias (more details given in the main text). The results are displayed in the *presence* of quantum corrections via LLT, but for three different Gaussian widths σ, namely σ =0.3 nm (red), σ =0.6 nm (blue) and σ =0.9 nm (green), as well as a "standard" virtual crystal approximation (VCA, black).

function analysis. However, two additional aspects are important to note. As already highlighted above, LLT cannot only be combined with the random alloy system, it can also also be employed in a VCA type calculation. Thus, from a VCA plus LLT description it is also expected that the potential barrier between the GaN and the (In,Ga)N QW material is reduced. Therefore, including quantum corrections in VCA should also affect the turn-on voltage of a device when compared to a "standard" VCA calculation without quantum corrections. Secondly, as one can infer from Fig. 6.2, once LLT has been applied, increasing the Gaussian width σ for the CBE softening in the random alloy case has very little impact on the resulting band edge profile. Below we will analyze this aspect in greater detail when looking at the I-V curves of (In,Ga)N/GaN-based uni-polar devices.

6.1.1.3 Uni-polar drift-diffusion model

In previous sections, we have discussed the mesh generation and also how random alloy fluctuations and quantum corrections in the confining potential are treated. In this section, we focus our attention on the semi-classical van Roosbroeck system which models DD charge transport in semiconductors. This was introduced in Section 4.2.1.2.

As we are interested in uni-polar electron transport the van Roosbroeck system of equa-

tions (given in full in Eq. (4.42)) is reduced to

$$-\nabla(\varepsilon\nabla\psi(\mathbf{r})) = -q(n(\mathbf{r}) - N_D(\mathbf{r})) \ , \tag{6.1a}$$

$$\nabla \cdot \mathbf{j}_n(\mathbf{r}) = 0 \ , \tag{6.1b}$$

$$\mathbf{j}_n(\mathbf{r}) = -q\mu_n n(\mathbf{r})\nabla\varphi_n(\mathbf{r}) \ . \tag{6.1c}$$

The electrons are treated using Boltzmann statistics:

$$n(\mathbf{x}) = N_C \exp\left(\frac{q(\psi(\mathbf{x}) - \varphi_n(\mathbf{x})) - E_c^{dd}(\mathbf{x})}{k_B T}\right), \tag{6.2}$$

where k_B is the Boltzmann constant, T denotes the temperature, $E_c^{dd}(\mathbf{x})$ is the (position dependent) band edge energy used in the transport calculations and N_C is the effective density of states:

$$N_C = 2\left(\frac{m_e^* k_B T}{2\pi\hbar^2}\right)^{3/2} .$$

If simulating a real device and targeting a theory-experiment comparison the Boltzmann approximation may not be adequate, and Fermi-Dirac statistics may need to be applied at high enough bias values. However, for the purposes of this chapter, where a framework is being established and a comparison between a VCA and random alloy is being carried out, Boltzmann statistics are sufficient.

We note that we have different options for setting the band edge energy E_c^{dd} in the DD simulations. One may choose (smoothed) TB data $E_c^{dd} = E_c^{\sigma}$, VCA results $E_c^{dd} = E_c^{\mathrm{VCA}}$ or the outcome of LLT calculations $E_c^{dd} = W$. Equation (6.2) indicates that the electric potential, ψ, leads to a bending of the energy landscape, $E_c - q\psi$, and thus results in a nonlinear, self-consistent coupling to the carrier densities. In the following, we assume a globally constant temperature for carriers and the crystal lattice of $T = 300$ K. As Boltzmann statistics are being employed the electron flux can be correctly discretized by extending the local Scharfetter-Gummel flux approximation [215] to variable band edges (c.f. Eq. (4.47)). The physical parameters used in the DD simulations are listed in Table 6.1.

Table 6.1: Material parameters used in drift-diffusion simulations. Unless otherwise stated, all parameters are taken from Ref. [67]; † from [243].

Physical Quantity	Value		Units
m_e^* GaN	0.2		m_0
m_e^* InN	0.07		m_0
μ_n n-GaN	200		$cm^2/(V\,s)$
μ_n i-GaN	440	†	$cm^2/(V\,s)$
μ_n i-(In,Ga)N	300		$cm^2/(V\,s)$
ϵ_r^{GaN}	9.7	†	ϵ_0
ϵ_r^{InN}	15.3	†	ϵ_0
n-doping (GaN)	5×10^{10}		cm^{-3}

6.1.2 Results

In this section, we apply the developed framework to uni-polar, *n*-doped/intrinsic/*n*-doped (*n*-*i*-*n*), (In,Ga)N/GaN-based structures: We analyze the impact of random alloy fluctuations and quantum corrections introduced by LLT on the I-V curves of such systems. The results are compared with data obtained from a VCA description of the same structures. Special attention is paid to the impact of the Gaussian broadening width, σ, on the results. This analysis is carried out for both SQW systems, Section 6.1.2.1, as well as for MQW structures consisting of 3 wells, Section 6.1.2.2. For all these calculations the well width is 3.1 nm, the In content in the well is 10% and the barrier material is GaN. In the MQW system the width of the barrier between the wells is 8.0 nm. Figure 6.3 gives a schematic illustration of the system. Except for the VCA systems, all calculations make a random alloy assumption for the (In,Ga)N alloy forming the QW; any additional penetration of In atoms into the GaN barrier are not considered. The assumption of such an abrupt interface between (In,Ga)N and GaN is consistent with the experimental data in Ref. [40], at least for growth of (In,Ga)N on GaN. When capping an (In,Ga)N QW with GaN, penetration of In atoms into the GaN barrier may occur. However, recent experimental studies show that by a careful choice of the growth conditions this effect can be reduced [244]. Given that we are interested in establishing a general simulation framework, these In atom "bleeding" effects are of secondary important for the present study.

6.1.2.1 (In,Ga)N SQW system

In a first step and before looking at a full I-V curve of the $In_{0.1}Ga_{0.9}N$ SQW system, we focus our attention on the impact of random alloy fluctuations on the results. More specifically we will study the impact of the Gaussian width σ and thus the related smoothing of the energy landscape on the current. Figure 6.4 displays the current in the system at a fixed bias of 3 V for different σ values. The data are shown when including and when neglecting quantum corrections arising from LLT. The calculations have been performed for 5 different random alloy configurations in the QW, allowing us to also study the influence of the alloy microstructure on the current; the error bars indicate the standard deviation. One can infer from Fig. 6.4 that when neglecting LLT effects, the resulting current (strongly) depends on the width of the Gaussian function, at least for $\sigma < 0.6$ nm ($\approx 2a$, where a is the in-plane lattice constant of GaN). Above this threshold the dependence of the current I on σ is less pronounced. We will discuss the impact of σ on the full I-V curve further below, but noting here that σ may impact the results. In the literature the value of σ has for instance been estimated using atom probe tomography data, and a value of σ_{APT} = 0.6 nm has been assumed [67]. Turning now to the calculations including quantum corrections via LLT, Fig. 6.4 reveals that

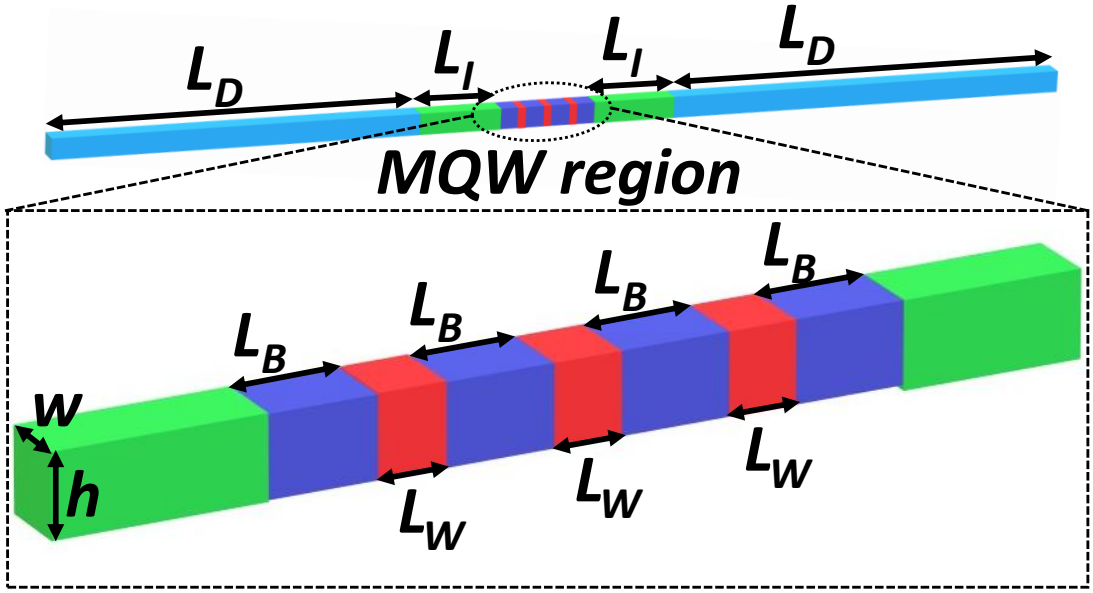

Figure 6.3: Schematic illustration of the simulation cell with 3 quantum wells (QWs) in the active region. The n-doped regions (light blue) have a doping density of $n = 5 \times 10^{18}$ cm^{-3} and a length of $L_D = 160$ nm. The intrinsic regions on the coarse mesh (green) have a length of $L_I = 40$ nm. The atomistic region, also assumed as intrinsic, contains regions of GaN barrier material (dark blue) with a length of $L_B = 8.0$ nm and $In_{0.1}Ga_{0.9}N$ QWs (red) with a length of $L_W = 3.1$ nm. The simulation cell has an in-plane dimension of $w \times h = 5.1 \times 4.4$ nm^2 along the entire system.

once these effects are taken into account, σ is of secondary importance for the obtained current I at the fixed bias of 3 V; this is at least the case for a SQW. We note however that this aspect may depend on the in-plane dimensions of the simulation cell and thus needs to be carefully investigated when performing calculations that include random alloy fluctuations in general. This observation agrees with our earlier conclusion that Gaussian smoothing does not affect the band edge profile, see Fig. 6.2, when including LLT effects in the calculations.

Having gained initial insight into the impact of the Gaussian width σ on the current I at a fixed voltage V, in a second step we focus our attention now on the full I-V curve of the SQW system. Figure 6.5 depicts the obtained results within the different approaches. Our reference point is again a "standard" VCA (black line) model, which neglects both alloy fluctuations and LLT effects. In addition, we present also the data of a combined VCA and LLT treatment. Finally, Fig. 6.5 displays results for the random alloy case for different σ values (red line: $\sigma = 0.3$ nm; blue line: $\sigma = 0.6$ nm) with and without LLT effects included in the calculations. Turning to the result in the absence of LLT first, it becomes clear that when accounting for random alloy fluctuations in the model, the turn on voltage is shifted to lower values in comparison to a standard VCA description. This is also consistent with previous literature results on uni-polar transport calculations of (In,Ga)N/GaN-based QW systems [218]. However, our calculations also reveal, and in line with Fig. 6.4, that the obtained current at a given voltage V de-

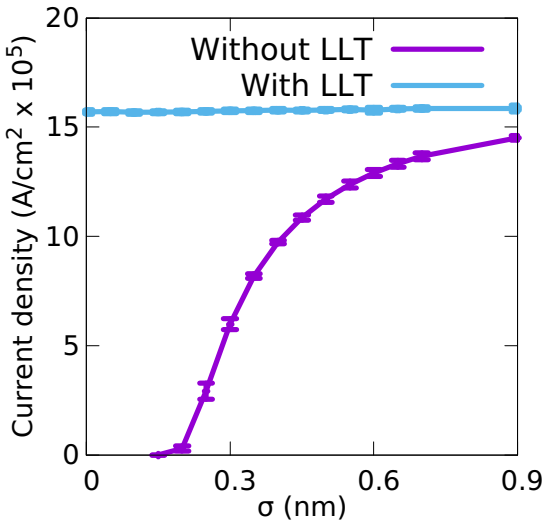

Figure 6.4: Current I at a bias of 3 V as a function of the Gaussian width, σ, without LLT (purple) and with LLT (blue) coerrections for an *n-i-n* system with a 3.1 nm wide $In_{0.1}Ga_{0.9}N$ single quantum well. The results are averaged over 5 different microscopic alloy configurations and errors bars are given by standard deviation.

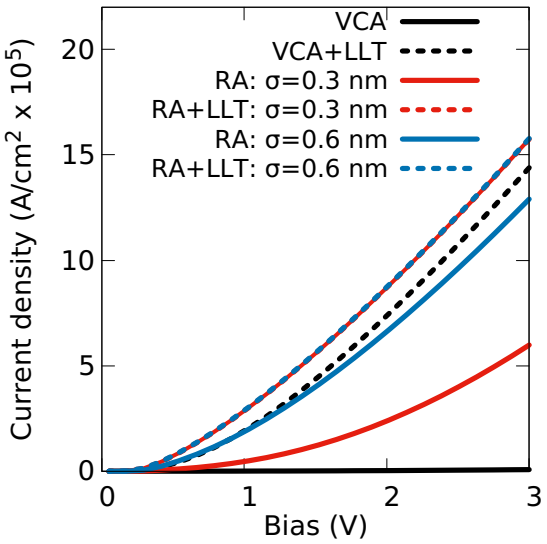

Figure 6.5: Current-voltage curves for an *n-i-n* $In_{0.1}Ga_{0.9}N$ single quantum well system, within virtual crystal approximation (VCA, black), random alloy (RA) with Gaussian widths of $\sigma = 0.3$ nm (red) and of $\sigma = 0.6$ nm (blue). Solid lines show results without quantum corrections, dashed lines denote results with quantum corrections included via localization landscape theory.

pends on the Gaussian width σ. As already indicated above, when neglecting quantum corrections via LLT, a further analysis is required to determine σ: if σ is too small, the resulting very strong fluctuations in the energy landscape within the well are beyond the applicability of a continuum-based DD model; if σ too large, the fluctuations in the energy landscape are completely removed as discussed in Section 6.1.1.1. So when neglecting LLT effects, care must be taken when choosing σ.

Next we turn and discuss the I-V curves when *including* effects arising from LLT (dashed lines in Fig. 6.5), both in the random alloy case but also in the VCA simulations. Looking at the calculations including random alloy fluctuations and LLT first, we observe that the Gaussian width σ is of secondary importance; this is again consistent with our findings in Fig. 6.2 and 6.4. We note also that when choosing a relatively large value of σ (e.g. 0.6 nm) the random alloy I-V curves with and without LLT (blue) do not differ significantly. We attribute this to the effect that both LLT and a relatively large Gaussian broadening soften the well-barrier interface and thus reduce the resistivity of the system. Furthermore, the fluctuations in the energy landscape within the QW are reduced, leading to a further decrease in the resistance of the QW region. We note that in the presented test system, the in-plane dimensions of the simulation cell are relatively small, and further tests on the impact of σ on the I-V curve may be required in future studies. However, this is beyond the scope of the present work, which introduces the general framework. Nevertheless, our results show that the calculations including random alloy fluctuations and LLT effects give the lowest turn-on voltage and highest current compared to all other models discussed here. However, and interestingly, we find also that the VCA plus LLT calculations give almost the same I-V curve as the quantum corrected random alloy simulations. This indicates that for a SQW, once LLT is included in the model, the VCA can provide a very good approximation of the I-V characteristics of the uni-polar *n-i-n* system in comparison to a full 3-D random alloy model; we saw a similar result in Chapter 5 using the fully quantum mechanical NEGF formalism. Furthermore, since the (3-D) VCA neglects any in-plane variation in the system, already a 1-D VCA simulation seems to lead to reliable results – as long as LLT is included. Having only to rely on a 1-D simulation would obviously reduce the computational cost immensely compared to a full 3-D calculation including alloy fluctuations. However, and as we will show in the following section, for a MQW system a 1-D VCA plus LLT calculation is no longer sufficient.

6.1.2.2 (In,Ga)N MQW system

Having discussed a SQW system in the previous section, we focus our attention now on a MQW system. Figure 6.6 shows the I-V curves for a MQW system consisting of three $In_{0.1}Ga_{0.9}N$/GaN QWs with a barrier width of $L_B = 8.0$ nm. Here, we followed the approach of the SQW and calculations have been performed using either a VCA treatment or account for random alloy fluctuations in the system. Again the simulations are carried out both with and without quantum corrections via LLT.

As in the SQW case, VCA calculations neglecting LLT effects show the highest turn-on voltage and lowest current at a fixed bias point when compared with all other data. When combining VCA and LLT, we find similar to the SQW case that the turn-on voltage is reduced and the current density is increased. However, and this is in *strong contrast* to the SQW data, cf. Fig. 6.5, in the MQW system the results from VCA plus LLT devi-

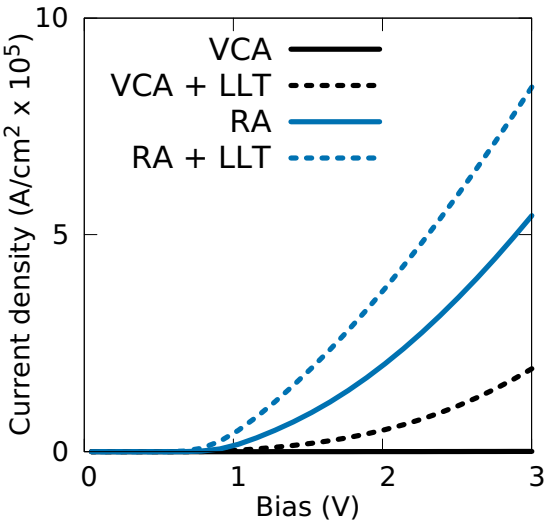

Figure 6.6: Current voltage curves for a three $In_{0.1}Ga_{0.9}N$ quantum well system, within virtual crystal approximation (VCA, black) and when random alloy (RA) fluctuations (Gaussian width of $\sigma = 0.6$nm) are included in the model (blue). Solid lines indicate results without quantum corrections, dashed lines show results with quantum corrections included via localization landscape theory.

ate noticeably from the outcome of calculations that accounted for both random alloy fluctuations and LLT, cf. Fig. 6.6. We also note that VCA plus LLT simulations show significant deviations (lower currents, higher turn-on voltages) from random alloy calculations that neglect LLT effects. Overall, we attribute the aspect that random alloy fluctuations seem to become more important in the MQW system to inherent features of LLT. As discussed for instance in detail in Section 3.4.3, as well as in Refs. [158,163], to predict the ground state energy of a QW, the reference energy, E_{ref}, has to be chosen appropriately. However, the choice of E_{ref} not only affects the prediction of the ground state energy of the system, it also affects the effective potential W, which is used in the DD transport calculations. If the QWs in a MQW system in a DD simulation are energetically aligned, e.g. CBEs of all wells forming the MQW have approximately the same energy for an applied bias, E_{ref} can be chosen as the bottom of the CBE. However, if there is a large difference in the CBEs of the different wells in the system, LLT may give a poorer approximation of W for the well where the CBE is energetically furthest away from the reference energy E_{ref}. This situation can be found when applying a bias V in an *n-i-n* system. As a result, the softening of the well-barrier interface along with an effective decrease of the QW depth (confinement energy), may be different for the different QWs in the MQW system. Obviously, for a SQW system this issue never arises. However, two important general aspects are to note. Firstly, the LLT treatment of MQWs may be further improved by partitioning the MQW system into different sub-regions in which LLT is then solved separately. This means one could calculate LLT in each region with its own reference energy and "stitch" the resulting effective potentials together. This approach will be discussed in detail in Section 6.2.1.2.1 where it has been applied

to uni-polar *hole* transport; the low effective *electron* mass compared to that of holes means this approach is much more challenging for electrons: reduced effective mass results in larger smoothing further into the barrier by LLT, making stitching regions together problematic, this is beyond the scope of the present work. Secondly, we note that in a *p-i-n* system, near the turn-on voltage, the QW band edges are expected to be energetically not too different. In that case, even without partitioning the system, LLT should provide a good approximation for biases near the turn-on voltage. This will be discussed further in Chapter 7.

In principle, the same difficulties with respect to E_{ref} apply here in the random alloy systems when including LLT in the calculations. However, and compared to the outcome of VCA plus LLT studies, our results show that for simulations including alloy fluctuations but neglecting LLT, larger currents are observed. As discussed above, the calculations taking random alloy fluctuations into account automatically include some softening of the well barrier interface. Combining LLT with random alloy fluctuations results in a further increase of the current and reduction of the turn-on voltage. We stress that standard 1-D VCA DD calculations presented in the literature on *n-i-n* (In,Ga)N QW systems, always predicted much higher turn-on voltages when compared to the experimental studies [218]. Thus, the here obtained results reveal and support again the origin of this discrepancy: standard 1-D VCA calculations neglect alloy fluctuations. Thus, even though E_{ref} still has to be treated carefully, the resulting energy landscape presents an improvement over VCA in terms of the predicted I-V characteristics.

While the above calculations have been performed at a fixed Gaussian width σ of $\sigma = 0.6$ nm, we still need to evaluate the impact of σ on the I-V characteristics. In the SQW case, cf. Fig. 6.4, the predicted current at a fixed voltage was virtually independent of σ once LLT was applied. Due to the difficulty of choosing E_{ref} in a MQW system, the current may now depend more strongly on the Gaussian width σ. However, our analysis reveals that after LLT has been applied at a fixed voltage of 3 V the obtained currents differ only by less than 8% from the mean over a σ range from 0 to 0.9 nm (not shown). The change due to different Gaussian widths σ is only a small correction compared to the change between e.g. VCA and random alloy fluctuation calculations, indicating again that a calculation including both random alloy fluctuations and LLT are robust against changes in σ. Random alloy calculations without including LLT follows a similar trend to that of the SQW shown in Fig. (6.4) (purple) where the result can strongly depend on the choice of σ, particularly for σ less than 0.6 nm.

6.1.3 Conclusions from studying uni-polar electron transport

In this section we applied the framework presented in Section 4.2 to uni-polar electron transport. This allows us to bridge the gap between atomistic TB theory and continuum-based DD calculations. The model also includes quantum corrections via

the localization landscape method, to address charge carrier transport in III-N based devices. Overall, we find that random alloy fluctuations and quantum corrections significantly impact the current voltage characteristics of uni-polar (In,Ga)N devices when compared to standard VCA studies, which are at the heart of most literature carrier transport solvers. In general and independent of SQW and MQW systems, the combination of quantum corrections and random alloy fluctuations lead to lower turn on voltages and higher currents when compared to a VCA. This effect is very important since literature studies on uni-polar carrier transport have revealed that "standard" 1-D continuum-based transport solvers, effectively corresponding to our virtual crystal results, give turn-voltages considerably larger than the experiment. Thus, our here predicted shift to lower voltages due to quantum corrections and alloy fluctuations indicates an improved description of experimental data. However, we note that the relative importance of quantum corrections and random alloy fluctuations varies between SQW and MQW systems. We find that in the SQW system, quantum corrections are extremely important. As a consequence, in the SQW, a combined virtual crystal approximation plus LLT treatment leads to almost the same current voltage curve as in a calculation that also includes alloy fluctuations. This indicates that for a SQW system, 1-D calculations including LLT may be sufficient; this reduces the computational demand significantly. However, our analysis also indicates that in a MQW system this finding may not hold, and alloy fluctuations and thus a full 3-D transport calculation is required. Therefore, our investigations highlight that for MQW systems both atomistic as well as quantum mechanical effects should be taken into account to achieve an accurate description of the I-V characteristics of uni-polar (In,Ga)N-based devices.

So far we have only studied uni-polar *electron* transport. Our fully quantum mechanical analysis in Chapter 5 highlighted that the response of electrons and holes to the random alloy microstructure differs significantly, so before turning to a full bi-polar transport problem we study in the following uni-polar *hole* transport to complement and compare with the electron transport.

6.2 Uni-polar hole transport

Our previous (NEGF and DD) simulation results have highlighted how the treatment of the alloy microstructure can affect carrier transport through (In,Ga)N-based quantum well systems. Having applied a DD framework to uni-polar electron transport, we turn our attention to holes. Recent work has investigated uni-polar hole transport through an *(Al,Ga)N barrier* [245]. The study showed the importance of considering alloy fluctuations for the theoretical description of the hole transport in such systems. However, a similar investigation for (In,Ga)N *quantum well* systems is missing. This stems in part from the fact that high quality p-doped-intrinsic-p-doped (p-i-p) systems are challenging to realise experimentally due to, e.g., high dopant activation energy [246], com-

pensation effect [247], memory effect [248], but also from the fact that the theoretical modeling of carrier localization in (In,Ga)N systems is a difficult task in itself [4, 219]. Moreover, given the difference in the material system ((Al,Ga)N vs (In,Ga)N) the results from Ref. [245] cannot necessarily be carried over to an (In,Ga)N/GaN structure. Therefore we focus in this chapter on uni-polar hole transport in (In,Ga)N QWs. Here, we apply our previously discussed multi-scale simulation framework to study uni-polar hole transport in (In,Ga)N SQW and MQW systems. We analyze in detail the impact of alloy and quantum corrections on the results.

This section is organized as follows: In Section 6.2.1 we outline the theoretical framework we use, with a particular focus on the implementation of LLT in a MQW (as discussed in Section 6.1.2.2). In Section 6.2.2 we present our results for uni-polar hole transport in (In,Ga)N/GaN SQW and MQW systems. Finally, Section 6.2.3 concludes this work.

6.2.1 Theoretical framework

The framework applied to the uni-polar hole transport systems is very similar to that presented for uni-polar electron transport in Section 6.1.1: The model builds on a TB model to include an atomistic description of the VBE energies extracted using a local Hamiltonian, which are embedded withing a sparser device mesh to describe p-doped GaN regions. The energies in the atomistic region are subjected to a Gaussian broadening with a width of σ in order to account for the spatial extent of the wave function, which does not only "see" valence band enedgies at a given lattice site but also beyond this.

6.2.1.1 Smoothing by Gaussian averaging

As seen in the discussion of uni-polar *electron* transport, when applying a Gaussian smoothing the averaging procedure depends on the width of the Gaussian, σ. Given that the Gaussian width σ is now effectively a free parameter, we will follow the same procedure as in Section 6.1 and study below the impact of σ on the effective energy landscape and the hole transport. Future studies may target evaluating σ values based on calculations of e.g. the density of states [159, 206] in (In,Ga)N-based QWs utilizing modified continuum models.

We follow a similar approach to that taken in the *n-i-n* study to understand the potential impact of σ on the results; Fig. 6.7 shows the VBE energy profile of an (In,Ga)N/GaN SQW with 10% In and a width of 3.1 nm for different values of σ ($\sigma = 0.1$ nm (purple), $\sigma = 0.3$ nm (green) and $\sigma = 0.5$ nm (blue)) at equilibrium (0 V). The VCA profile, which does not undergo broadening, is also depicted (black, dashed). Firstly, we note that when choosing a σ value smaller than the bond length of the material, d_0 (e.g. $\sigma = 0.1$ nm $< d_0^{\mathrm{GaN}}$ [91]), basically no averaging takes place. As a consequence, the

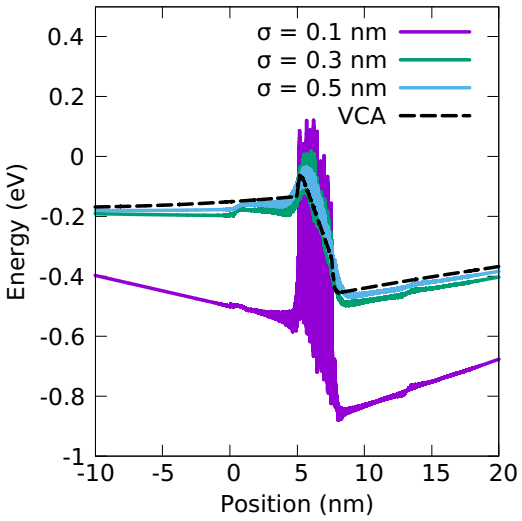

Figure 6.7: Comparison of valence band edge energies for an $In_{0.1}Ga_{0.9}N$ single quantum well of width 3.1 nm at a bias of 0 V (equilibrium solution) without quantum corrections for a VCA (black, dashed) and random alloy calculations using a Gaussian width, σ, of 0.1 nm (purple), 0.3 nm (green) and 0.5 nm (blue).

VBE energy exhibits very strong fluctuations due to the alloy fluctuations, see Fig. 6.7. We note that while the average QW "depth" (averaged over each atomic plane) does not differ significantly for different σ values, both the magnitude of the VBE energy fluctuations as well as the potential barrier between (In,Ga)N well and surrounding GaN is strongly impacted by the σ value. Thus, Fig. 6.7 gives already indications that carrier transport, e.g. I-V curves, may be strongly dependant on σ as we saw in the uni-polar electron systems in Section 6.1. We will discuss this in more detail below.

6.2.1.2 Quantum corrections by localization landscape theory

The framework of LLT has been introduced in detail both in the Chapter 3 and in Section 6.1. The procdure here is initially the same[1] as the *n-i-n* system in order to extract an effective landscape, W.

To provide first general insight into the impact of LLT corrections to the confining energy landscape for holes, Fig. 6.8 shows the effective potential W for the VBE of an $In_{0.1}Ga_{0.9}N$/GaN SQW system at equilibrium (0 V); the width of the well is 3.1 nm. The data are displayed for three different Gaussian broadening values σ, namely $\sigma = 0.1$ nm

[1] As the derivation of LLT requires that the Hamiltonian $\hat{H}$ is a positive definite operator [157], the landscape equation (Eq. (3.26)) is solved in the hole picture (where the hole ground state has the *lowest* energy on an absolute scale, and the hole effective mass is *positive*) rather than in the valence band picture (where the hole ground state has the *highest* valence band energy on an absolute scale, and the hole effective mass is *negative*). As such, the confining potential is described by $V = -E_v^{TB}$. The resulting effective landscape, W (Eq. (3.27)), is converted to the valence band picture (multiplication by -1) so that it can be used in transport calculations. *When displaying band edge profiles, we always use the valence band picture; if LLT has been applied, the obtained effective landscapes/potentials, W, have been transformed accordingly.*

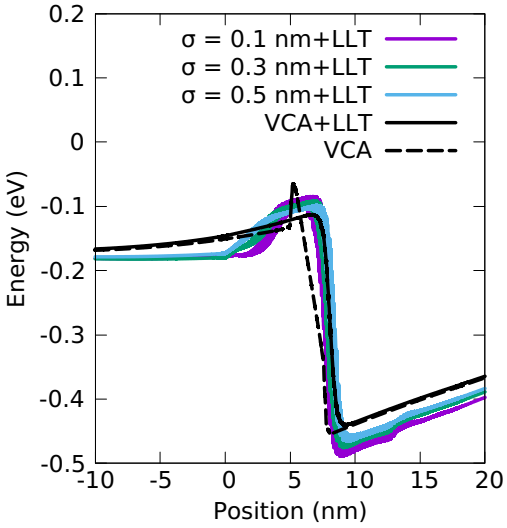

Figure 6.8: Comparison of valence band edge energies for a $In_{0.1}Ga_{0.9}N$ single quantum well of width 3.1 nm at 0 V *including* quantum corrections via LLT for a VCA (black, solid) and random alloy calculations using a Gaussian width of 0.1 nm (purple), 0.3 nm (green) and 0.5 nm (blue). The VCA result excluding quantum corrections is also shown (black, dashed).

(purple), $\sigma = 0.3$ nm (green) and $\sigma = 0.5$ nm (blue), as well as a LLT corrected VCA profile (black, solid). A "standard" VCA profile is also shown (black, dashed). This figure displays that once LLT is included in the calculations, the impact of σ on the band edge profile is significantly reduced. Looking at the VCA plus LLT results, one finds a very smooth confining band edge energy profile.The consequences of using a softened profile for carrier transport will be discussed below.

6.2.1.2.1 Subtleties of LLT for MQW structures

The drawbacks of LLT have already been discussed in Section 3.4.3. One key point mentioned is the change in energy landscape when the reference energy, E_{ref}, of the system is changed; ideally the reference energy should be chosen to maximize the contribution of the ground state ($|\psi_0\rangle$, with energy E_0) to the expansion of u (Eq. (3.28)):

$$|u\rangle = \sum_n \frac{\langle\psi_n|1\rangle}{E_n}|\psi_n\rangle \quad . \qquad \text{(3.28 revisited)}$$

While adjusting the reference energy of a SQW system is in principle a straightforward procedure, for a MQW system this becomes more involved. This was described briefly in Section 6.1, but here we focus more closely on the consequences, since the higher effective hole mass allows us to partition the system into different sub-systems as already mentioned in Section 6.1.2.2. To illustrate this in more detail, Fig. 6.9 shows a schematic of a 3 QW system. Here we assume a large energy difference between the VBE values of the different wells to highlight central aspects of LLT. If this structure

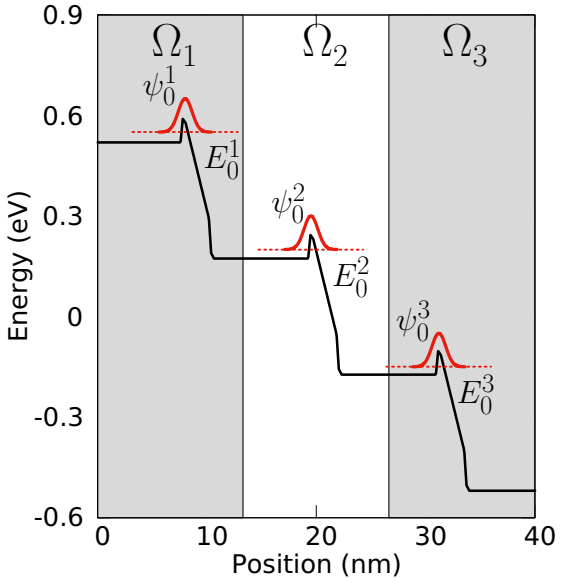

Figure 6.9: Schematic illustration of a potential band edge energy profile (black solid line) in a multi-quantum well with 3 quantum wells where the wells exhibit a large energy separation between their respective ground state energies E_0^i (red dashed line). The local hole ground state wave function in the ith localization region, Ω_i (marked by shading), are indicated by ψ_0^i (red, solid).

is treated as one single "localization" region Ω, and we choose the reference energy, E_{ref}, to be very close to E_0^1 (using the hole picture instead of the valence picture), u and consequently W will be dominated by the ground state wave function ψ_0^1, as $\frac{\langle\psi_0^1|1\rangle}{E_0^1}$ will dominate the series expansion in Eq. (3.28). Due to the larger energy separation between E_{ref} and E_0^2 and E_0^3, respectively, there will be basically no contribution from ψ_0^2 and ψ_0^3 to $W(\mathbf{x_i})$. As a consequence the effective potential W in the spatial region where ψ_0^2 (located in region Ω_2) and ψ_0^3 (located in region Ω_3) are localized is largely unaffected by LLT quantum corrections.

To circumvent this issues, one could in principle partition the system into multiple (here three) subregions $(\Omega_1, \Omega_2, \Omega_3)$ and solve LLT for each sub-system separately; for each subregion an individual E_{ref}^i can be chosen. In doing so, the wave functions ψ_0^i describe now the ground state wave function for each "localization" region Ω_i with its corresponding local ground state energy E_0^i. Now the series expansion of u in each region is dominated by the first term, and u obtained for each region Ω_i should give a very good description of the lowest state locally. As a consequence, the confining potential in each QW subregion Ω_i contains quantum corrections.

When using this approach of partitioning the system into different subregions, the remaining question is how to "connect" the local effective potentials W_i so that one obtains a global one, W. As we saw in the case of electrons, partitioning the system into different localization regions is difficult, as the low effective electron mass leads to a large "leaking" of the wave function into the barrier material. This makes it very

difficult to connect the individual effective potentials, W_i continuously. Holes, however, have a much higher effective mass, and partitioning the system is achievable if the separation between the wells in a MQW system is not too small. For the system under consideration (see Section 6.2.2) this is the case and the locally obtained effective landscapes return quickly to the band edge energy of the GaN barrier material; this guarantees that the interface between neighbouring localization regions is smooth and continuous when "stitching" the different W_i together to obtain W. A comparison of effective landscapes obtained with and without partitioning a MQW structure into different sub-regions is show in Appendix C.1. When analyzing hole carrier transport in a MQW system in Section 6.2.2.2, we will pay special attention to the above described partitioning of the system when including quantum corrections via LLT in the simulations.

We note also that similar considerations are usually required in "standard" coupled Schrödinger-Poisson simulations of MQW systems. Here, in principle two options are available: solve the Schrödinger equation for a large number of states over the full simulation cell. However, a full quantum mechanical treatment of the full simulation cell is numerically very demanding. Most often, the quantum mechanical description (i.e. solving the Schrödinger equation) of the system is restricted to spatial regions near the wells of a MQW structure with appropriate boundary conditions (e.g. wave functions decayed approximately to 0 in the barrier material). Such an approach is similar to the above described partitioning of the MQW in different localization regions in which LLT is solved.

6.2.1.3 Uni-polar drift-diffusion model

As discussed in Section 4.2.2.4, we transfer the atomistic VBE energy data, together with constant macroscopic VBE parameters for the doped regions, on to a FVM mesh. Following the discussion in the previous section, we may use for the atomistic VBE data either the valence band energy after Gaussian broadening, $E_v^\sigma(\mathbf{x}_i)$, or the effective confining potential extracted from LLT, $-W(\mathbf{x}_i)$; the multiplication of W by -1 is due to the change from the hole picture to the valence band picture. This atomistic data can either take the form of a VCA, where interpolated material parameters are used to describe an alloy, or it can contain fluctuations due to the underlying alloy microstructure. The DD model which describes charge transport through the device has already been introduced in Section 4.2.1.2. As we are considering steady-state uni-polar hole transport without any recombination processes the van Roosbroeck system is described by

$$-\nabla(\epsilon\nabla\psi(\mathbf{r})) = q(p(\mathbf{r}) - N_A(\mathbf{r})) \ , \tag{6.3a}$$

$$\nabla\cdot\mathbf{j}_p(\mathbf{r}) = 0 \ , \tag{6.3b}$$

$$\mathbf{j}_p(\mathbf{r}) = -q\mu_p p(\mathbf{r})\nabla\varphi_p(\mathbf{r}) \ . \tag{6.3c}$$

where ψ is the electrostatic potential, p is the hole density, N_A is the ionized acceptor density, $\mathbf{j}_p$ is the hole current, φ_p is the hole quasi-Fermi potential and q is the elementary charge. Hole densities are described using Boltzmann statistics:

$$p(\mathbf{x}) = N_V \exp\left(\frac{q(\varphi_p(\mathbf{x}) - \psi(\mathbf{x})) + E_v^{dd}(\mathbf{x})}{k_B T}\right), \tag{6.4}$$

where the effective density of states is given by

$$N_V = 2\left(\frac{m_h^* k_B T}{2\pi\hbar^2}\right)^{3/2} .$$

Above, m_h^* is the hole effective mass, k_B is the Boltzmann constant, T is the temperature and $\hbar$ is the reduced Planck's constant. The hole flux is discretized by the Scharfetter-Gummel approximation (Eq. (4.47)). Bias values are implemented via Dirichlet boundary conditions. In the here-studied systems the Boltzmann approximation is sufficient to describe carriers; this is outlined in more detail in Appendix C.2 where a comparison of Fermi-Dirac and Boltzmann statistics is carried out.

6.2.2 Results

In this section, we apply the framework described above to a p-doped-intrinsic-p-doped (p-i-p) system in both a SQW, Section 6.2.2.1, and a MQW, Section 6.2.2.2, setting. Our simulations are carried out within the `ddfermi` simulation tool [222], which is implemented within the `WIAS-pdelib` toolbox [223]. A schematic of the MQW system including the contact regions is shown in Fig. 6.10. Details about well and barrier widths, as well as the In content are given in the figure caption. The material parameters entering the DD calculations are summarized in Table 6.2; in all calculations the temperature T is set to $T = 300$ K. To study the influence of alloy fluctuations and quantum corrections on the carrier transport, the simulations have been performed for the different E_v^{dd} settings discussed in Section 6.2.1.3. Thus, we compare results from calculations including alloy fluctuations to results from VCA simulations; the simulations have been carried out in the absence and presence of LLT quantum corrections. In the case of the MQW, we also investigate how the I-V curves change when partitioning the MQW system to solve LLT locally (for each QW), see also discussion in Section 6.2.1.2.1.

6.2.2.1 (In,Ga)N SQW system

In the following we analyze the impact of random alloy fluctuations and quantum corrections on the I-V characteristics of a p-i-p (In,Ga)N SQW system; details of the structure and simulation cell are given in the caption of Fig. 6.10. In order to study the influence of the alloy microstructure on the results we have repeated these calculations

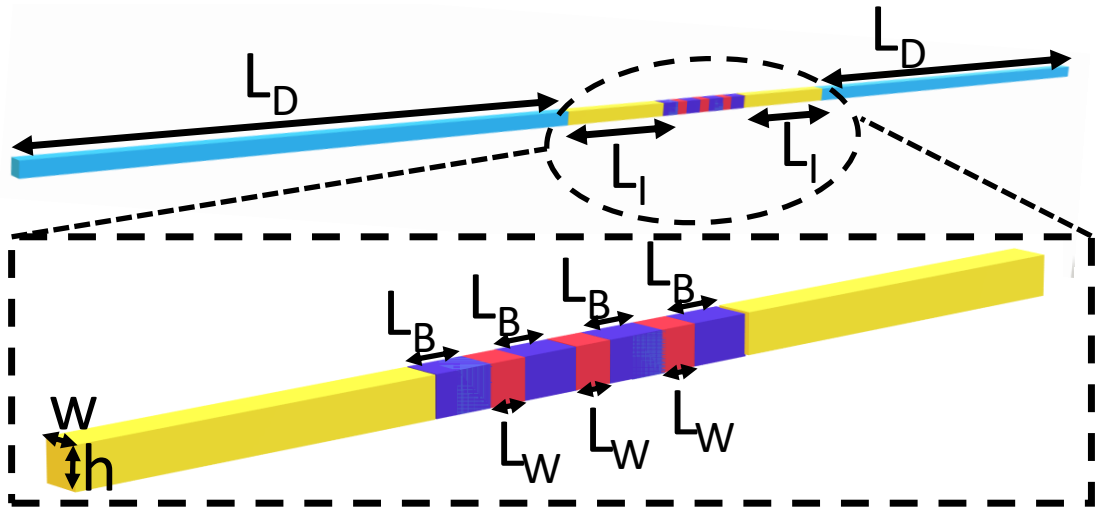

Figure 6.10: Schematic illustration of the simulation cell with three quantum wells (QWs) in the active region. The p-doped regions (light blue) have a doping density of 2×10^{19} cm^{-3} and a length of $L_D = 160$ nm. The intrinsic regions on the coarse mesh (yellow) have a length of $L_I = 40$ nm. The atomistic region, also assumed as intrinsic, contains regions of a GaN barrier material (dark blue) with a length of $L_B = 8.0$ nm and $In_{0.1}Ga_{0.9}N$ QWs (red) with a width of $L_W = 3.1$ nm. For a single QW calculation the atomistic region contains only one $In_{0.1}Ga_{0.9}N$ QW ($L_w = 3.1$ nm) and two GaN barrier regions. The simulation cell has an in-plane dimension of $w \times h = 5.1 \times 4.4$ nm^2 along the entire system.

Table 6.2: Material parameters used in the simulations. Unless otherwise specified, all parameters are taken from Ref. [67]; † Ref. [249].

Physical Quantity	Value	Units
m_h^* GaN	1.87	m_0
m_h^* InN	1.61	m_0
μ_h p−GaN	5	cm^2/(V s)
μ_h i−GaN	10 †	cm^2/(V s)
μ_h i−(In,Ga)N	10	cm^2/(V s)
ϵ_r^{GaN}	9.7	ϵ_0
ϵ_r^{InN}	15.3	ϵ_0
p−doping (GaN)	2×10^{19}	cm^{-3}

for 5 different microscopic configurations. Furthermore, the Gaussian broadening σ has been varied to study how σ affects the results. Before turning our attention to the full I-V curve of the system, and similar to our electron transport study above, Fig. 6.11 depicts the current in the SQW system at a fixed bias of 1.0 V for different σ values. As discussed in Section 6.1.1.1, when σ is increased, the Gaussian function softens the band edges and reduces the magnitude of the fluctuations. As a consequence, in the *absence* of quantum corrections, the current at 1.0 V increases with increasing σ and starts to converge for σ values larger than approximately 0.5 nm. For these large σ values the VBE becomes smooth and the current approaches that of a VCA

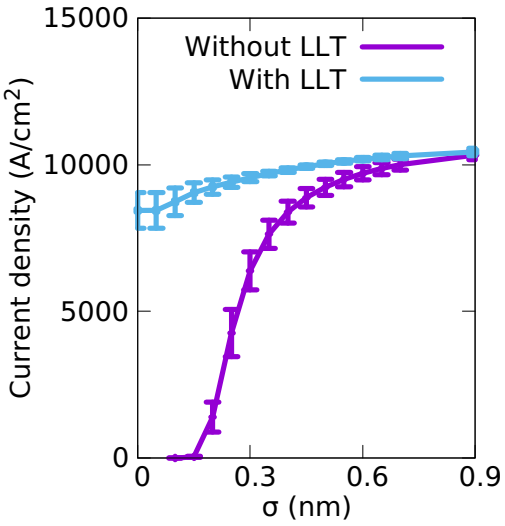

Figure 6.11: Impact of Gaussian width, σ, on the current in a single $In_{0.1}Ga_{0.9}N$/GaN quantum well system at a bias of 1.0 V. Results are obtained in the presence (blue) and absence (purple) of quantum corrections via LLT and are averaged over 5 different microscopic configurations. The errorbars show the standard deviation of the current over the 5 configurations.

without quantum corrections, as we will discuss further below. In addition, Fig. 6.11 also reveals that there is an abrupt increase in the current at around $\sigma = 0.2$ nm. We attribute this to the fact that if σ is small and below the bond length of e.g. GaN, the band edge profile entering the DD simulations exhibits strong (local) fluctuations which noticeably affect the carrier transport.

In the next step we turn our attention to the full I-V curves in the presence of alloy fluctuations but in the *absence* of LLT quantum corrections. Overall, the behavior discussed for the fixed bias of 1.0 V, Fig. 6.11, is also reflected in the full I-V curves, Fig. 6.12: for a Gaussian width of $\sigma = 0.1$ nm the current is extremely low, but increases with increasing σ. However, it is important to note that the here obtained results are in contrast to uni-polar *electron* transport, for instance discussed in Section 6.1. In the case of the electrons, the current always *exceeds* the VCA results, while we find here that in the hole case it *approaches* the VCA data. This means that for electron transport alloy fluctuations are beneficial, while they are detrimental for the hole transport in (In,Ga)N QWs. This result is consistent with the observation that alloy fluctuations lead to strong hole localization effects, while electron wave functions, due to their lower effective mass, are affected to a lesser extent by the alloy fluctuations [40,41].

To shed more light onto the influence of alloy fluctuations on the hole transport, Fig. 6.13 shows the charge density distribution in and around the (In,Ga)N SQW region for $\sigma = 0.1$ nm in the absence of any LLT quantum corrections and at a bias of 1.0 V. For comparison the VCA charge density distribution is also depicted (black, dashed) and the VCA charge density distribution including quantum corrections (black, solid).

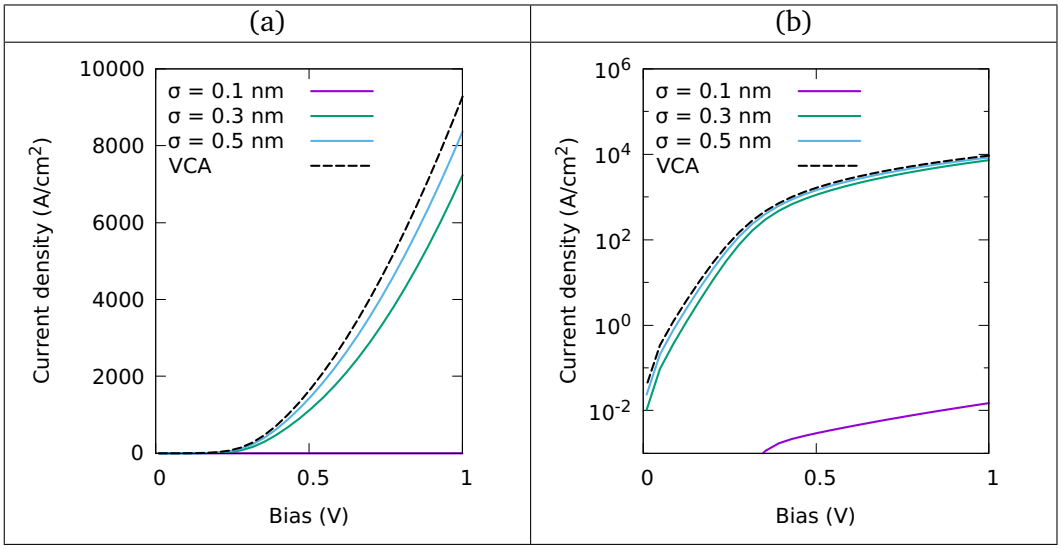

Figure 6.12: Comparison of current-voltage curves for a single $In_{0.1}Ga_{0.9}N$/GaN quantum well for VCA (black, dashed) and random alloy calculations using a Gaussian width of $\sigma = 0.1$ nm (purple), $\sigma = 0.3$ nm (green) and $\sigma = 0.5$ nm (blue) in the absence of quantum corrections. Results are shown on a linear scale (left) and log scale (right).

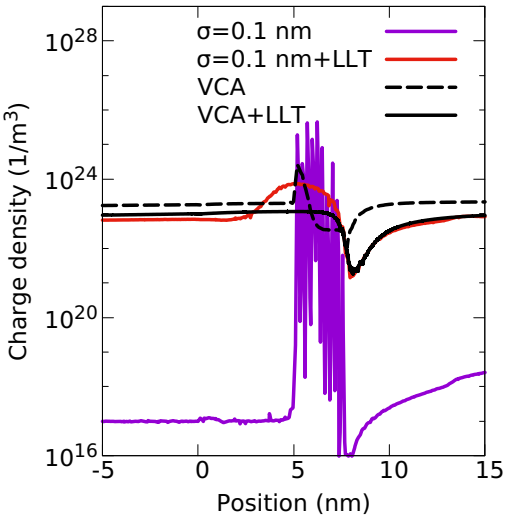

Figure 6.13: Carrier density distribution in and around a single $In_{0.1}Ga_{0.9}N$/GaN quantum well of width 3.1 nm at a bias of 1.0 V for calculations including random alloy fluctuations and using a Gaussian width of 0.1 nm. The results are shown in the absence (purple) and presence (red) of quantum corrections via LLT. For comparison VCA data (black, dashed), and VCA including LLT (black, solid) are also depicted.

We stress again that due to the small σ value, the alloy fluctuations lead to a strongly fluctuating VBE energy profile, which in turn results in strong hole localization effects. From Fig. 6.13 one can infer that due to the strong carrier localization effect, the carrier density is very high when compared to the VCA result in the QW region; the carrier density in the barrier material is depleted in the random alloy case compared to VCA. As a consequence, these carrier localization effects/the strong VBE fluctuations lead to

a strong VBE bending, originating from the coupling of the hole density and the quasi-Fermi level via Eq. (6.3c) and Eq. (6.4). Overall, and compared to the VCA result, this gives rise to a larger resistivity of the device. Thus for this small value of $\sigma = 0.1$ nm, the current through the device is very low, as seen in Fig. 6.12. We note that such a low broadening parameter can result in an underlying energy landscape which is not compatible with the DD framework (as σ is much smaller than the de Broglie wavelength), and this extreme depletion of the barriers may be physically unrealistic.

The situation changes with increasing σ as Fig. 6.14 shows. Here, the charge density distribution in and around the QW for both $\sigma = 0.3$ nm (green) and $\sigma = 0.5$ nm (blue) are similar to the VCA results (black, dashed). Furthermore, as the charge density distributions with increasing σ approaches the VCA profile, so does the resulting I-V curve, Fig. 6.12.

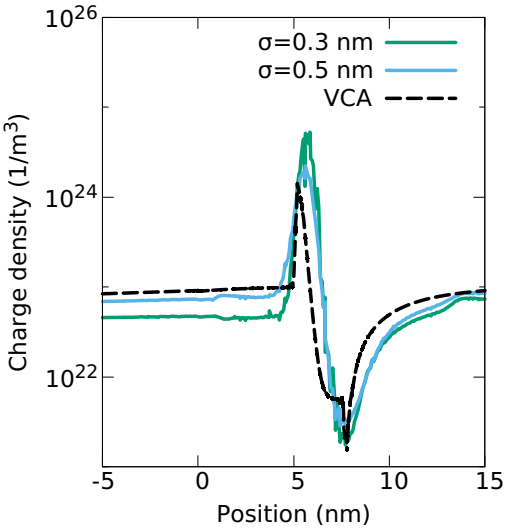

Figure 6.14: Carrier density distribution in and around a single $In_{0.1}Ga_{0.9}N$/GaN quantum well of width 3.1 nm at a bias of 1.0 V for a VCA (black, dashed) and random alloy calculations. The latter use Gaussian widths of $\sigma = 0.3$ nm (green) and $\sigma = 0.5$ nm (blue) and exclude quantum corrections.

Having discussed the impact of alloy fluctuations on the hole transport, we focus our attention now on the impact of quantum corrections on the results. Overall, we find that when including quantum corrections via LLT in the transport calculations, the Gaussian width σ influences the results to a much lesser extent. This can for instance been seen in Fig. 6.11, where the current is shown as a function of σ (light blue) at a fixed bias of 1.0 V. In contrast to the results without quantum corrections (purple), when including these corrections, the obtained current changes very little when increasing σ beyond 0.2 nm. We highlight also that even at the very low σ value of $\sigma = 0.1$ nm, the current is strongly increased when including quantum corrections. The origin of this becomes clear when looking again at the carrier density profile in and around the SQW, depicted in Fig. 6.13. As discussed above, in the absence of quantum corrections,

the strongly fluctuating energy landscape leads to a very large carrier density in the well and depletes the region surrounding the well. When accounting for quantum corrections, the carrier density profile including alloy fluctuations (red), even though the same σ value is used, is much smoother and approaches the VCA quickly in the barrier. This emphasizes again that quantum corrections soften the confining energy landscape and indicates also that once LLT corrections are taken into account, the importance of alloy microstructure is reduced. This is further supported by Fig. 6.11: the standard deviation (indicated by the error bars in the figure) is small relative to the current, at least for larger σ. The impact of the alloy microstructure is still visible for smaller σ values. We note here also that the magnitude of this effect may depend on the in-plane dimension of the simulation cell, especially when using small σ values. Thus careful studies are required to analyze this in more detail, including a further evaluation on the choice of the "correct" Gaussian width before LLT is applied. The impact of the in-plane dimension on hole transport in a SQW is further is further discussed in Appendix C.3.

When turning to the full I-V curve of the SQW system, Fig. 6.15, we find that the choice of σ is of secondary importance, at least for the system studied here. In addition to the random alloy calculations, Fig. 6.15 depicts also VCA results both in the presence (black, solid) and absence (black, dashed) of LLT quantum corrections. From this it is clear that in the case of a SQW, random alloy results do not differ strongly from the VCA data. Interestingly, these results are also well approximated by VCA simulations *excluding* quantum corrections. For the VCA, when there are no alloy fluctuations and the VBE is smooth, the combination of the small valence band offset as well as the high hole effective mass, results in similar profiles for the confining potentials of the VCA and quantum corrected VCA. Consequently the I-V curves do not differ significantly.

It should be noted that the above discussed results are different but also similar to uni-polar electron transport reported in Section 6.1. They are similar in the sense that once quantum corrections are taken into account, VCA and random alloy simulations give very similar results in terms of the I-V characteristics of SQW systems. However, a difference between electron and hole transport is that for uni-polar electron transport the current increases for larger σ values and exceeds the VCA result, for holes this is not the case. Our calculations also indicate that for holes, once LLT corrections are included, the current is not strongly dependent of σ; it should again be noted that this result may depend on the in-plane dimensions of the simulation cell. A larger in-plane cell may give rise to a larger extent of locally varying band edge energies. As a consequence carrier localization effects may be more pronounced. Thus the here presented results should be treated as "best" case scenario, since when carriers are "trapped" by alloy fluctuations they will increase the resistivity of the device. We conclude therefore that in general carrier localization effects in the well will have a detrimental effect on the hole transport, and the resulting currents will in general be smaller or equal to the VCA result, in contrast to electrons.

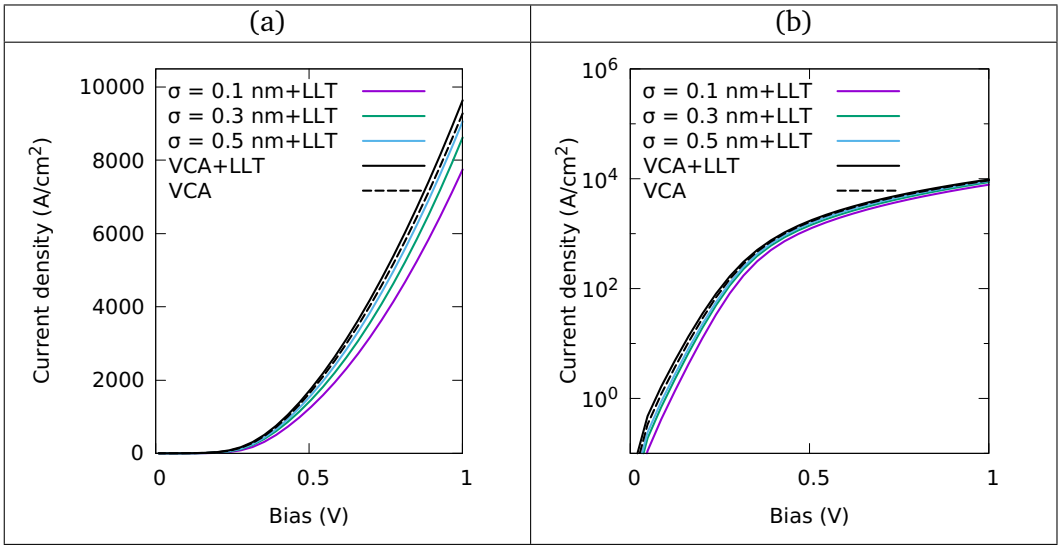

Figure 6.15: Including quantum corrections via LLT: Comparison of current-voltage curves for a single $In_{0.1}Ga_{0.9}N$/GaN quantum well of width 3.1 nm for a VCA (black, solid) and random alloy calculations; the random alloy simulations use Gaussian widths of $\sigma = 0.1$ nm (purple), $\sigma = 0.3$ nm (green) and $\sigma = 0.5$ nm (blue). Results are shown on a linear scale (left) and log scale (right).

But, the impact of carrier localization effects on the I-V curves may be more pronounced in MQWs, as the depletion of the carriers in the GaN barrier region may be amplified in such a system when compared to a SQW. In our previous study on uni-polar *electron* transport we have already seen that results from a SQW system cannot necessarily be carried over to MQWs. In general, gaining insight into hole transport in MQW systems is very important for understanding the carrier distribution in full (In,Ga)N-based MQW LED structures. Thus, we turn our attention in the next section to uni-polar hole transport in (In,Ga)N MQW structures.

6.2.2.2 (In,Ga)N MQW system

Similar to the SQW system discussed in the previous section, we start our analysis of the uni-polar hole transport in a (In,Ga)N/GaN MQW system by investigating the impact of the Gaussian width σ on the results. Figure 6.16 displays the current through the MQW system as a function of σ at a fixed bias of 1.0 V. Here we compare results from simulations that (i) exclude quantum corrections via LLT (purple), (ii) include quantum corrections via LLT but treating the entire MQW region as one localization region (green), and (iii) quantum corrections via LLT but solving the LLT equation for each well of the MQW system separately (red), as discussed in Section 6.2.1.2.1 (cf. Fig. 6.9).

Figure 6.16 shows that for all studied σ values, the calculation excluding LLT (purple line) exhibits the lowest current at a fixed voltage of 1.0 V. Also, the difference is largest at small σ values. In the case of the calculation without LLT corrections, the

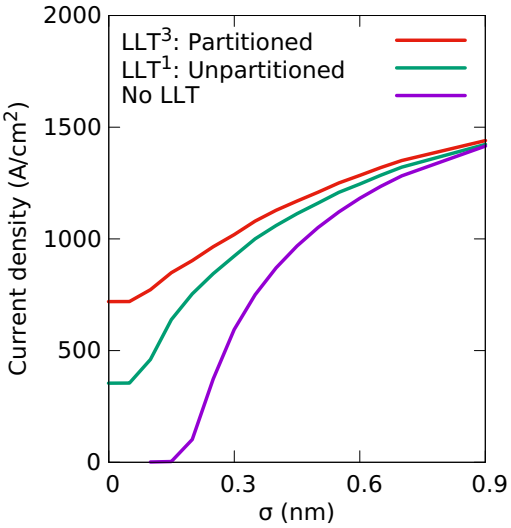

Figure 6.16: Impact of Gaussian width, σ, on the current in an $In_{0.1}Ga_{0.9}N$/GaN multi-quantum well system at 1.0 V. Results are shown (i) for a system including quantum corrections via LLT and partitioning the system into 3 localization regions each with a local reference energy (red), (ii) for a system including quantum corrections via LLT using a single (global) reference energy for the entire multi-quantum well region (green), and (iii) for a system excluding quantum corrections (purple).

VBE edge exhibits large local fluctuations. These fluctuations are intrinsically smoothed by the quantum corrections, and the resulting landscape (even for small σ values) exhibits significantly smaller fluctuations due to the alloy microstructure. The large VBE fluctuations increase the potential barrier and consequently increase the resistance in the *p-i-p* junction, thus leading to a smaller current. This is the same effect we have already seen in the SQW system, however, the result is more pronounced due to the combined influence of the 3 QWs in the MQW.

In a second step we discuss the results from the calculations including quantum corrections in more detail. Looking at the simulations using a global reference energy, i.e. the MQW system is treated as a single localization region (green), we find that the current drops a greater amount at low σ values compared the the outcome of the simulations using a local reference energy (where each well is treated as a separate localization region). More specifically, at the smallest considered σ value (no broadening), the current obtained from the model using a global reference energy is just over half the current using local reference energies. We attribute this drop to the combination of two factors. Firstly, given that the LLT model using a local reference energy also shows a slight drop in current with decreasing σ indicates that the strong fluctuations in the VBE energy still impact the current even though the LLT treatment softens this intrinsically. Secondly, when treating the MQW as a single localization region, a poorer description of the confining potential of the QW for which the VBE energy is furthest away from the global reference energy is expected in such an LLT treatment. As a

consequence, still larger fluctuations are present in the wells furthest away from the reference energy, especially for small σ values. All this will result in a higher resistivity of the MQW system and consequently a lower current at a fixed bias.

Having discussed the impact of Gaussian broadening and LLT quantum corrections on the current in a MQW system at a fixed bias, Fig. 6.17 depicts the full I-V curves. Here again results from calculations applying LLT, both using a single localization region (dashed), Ω, and sub-regions, Ω_i, for each QW (dotted), as well as results in the *absence* of quantum corrections (solid) are shown. This is displayed for both VCA (black) and random alloy calculations using a Gaussian width of 0.3 nm (green); to get first insight into the hole transport in a MQW structure we have restricted the calculations to one alloy configuration. Future studies can target analysing the statistics of different alloy microstructure configurations on the results. A value of $\sigma = 0.3$ nm has been chosen since it is large enough for the Gaussian averaging to including neighbouring sites but small enough to still capture effects due to carrier localization. Figure 6.17 reveals that in both VCA and random alloy calculations, quantum corrections increase the current similar to the situation in uni-polar electron transport (Section 6.1). Furthermore, when using a local reference energy for LLT, thus treating each QW as an individual localization region, Ω_i, the current increases further when compared to the LLT model employing a global reference energy. Our results also show that this effect is more pronounced for the random alloy case; partitioning the system in VCA impacts the I-V curve (black dashed and black dotted line) only slightly.

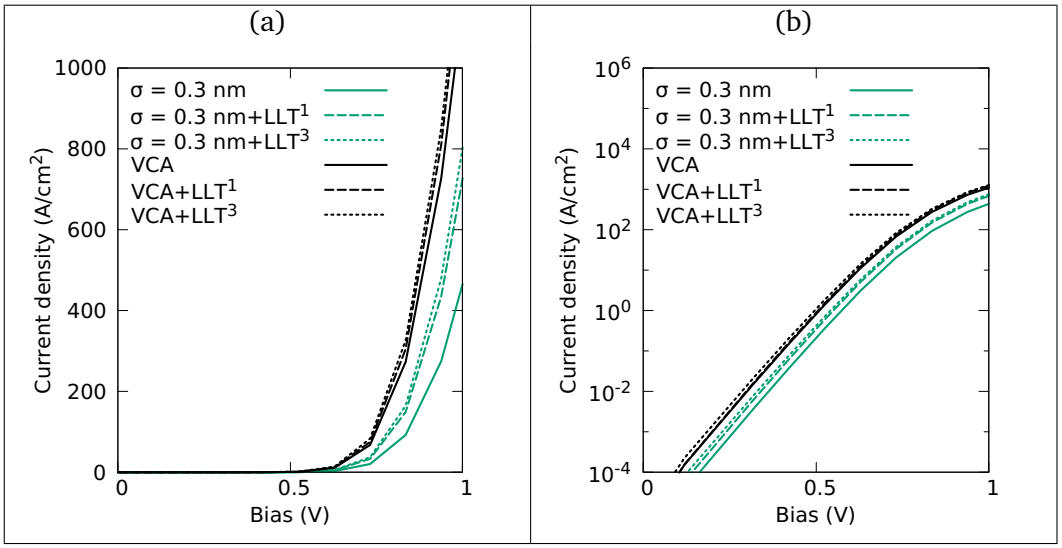

Figure 6.17: Comparison of current-voltage curves in a multi-quantum well $In_{0.1}Ga_{0.9}N$/GaN system for VCA (black) and random alloy calculations; the random alloy simulations use a Gaussian width of 0.3 nm (green). I-V curves are shown for calculations without any quantum corrections (solid), including quantum corrections when employing an un-partitioned (dashed, superscript '1') and partitioned multi-quantum well regions (dotted, superscript '3'). Results are shown on (a) a linear scale and (b) a log scale.

Overall our calculations reveal that in the MQW system and for the chosen σ value of $\sigma = 0.3$ nm, even when including LLT corrections, the random alloy calculations give a smaller current at fixed bias when compared to the VCA result. This finding is in contrast to the SQW system, where VCA and random alloy results give very similar results, see Fig. 6.15.

Furthermore, and again in contrast to the SQW structure, the magnitude of the difference in current between VCA and random alloy results will depend on the σ value, as Fig. 6.16 shows. We note that beyond σ, and as already mentioned above, the in-plane dimension of the simulation cell may impact the results as carrier localization effects due to *lateral* fluctuations in the (In,Ga)N wells can have a (detrimental) influence on the current. It should be noted that the LLT treatment builds on a single-band EMA; our previous studies indicate that such a model may underestimate hole localization effects [4], which in turn may lead to higher current.

Nevertheless, all these factors should only reduce the current further in the MQW system. Thus the VCA I-V curve should be regarded as a upper bound for the hole current in an (In,Ga)N MQW structure. This is in contrast to uni-polar electron transport, where alloy fluctuations and quantum corrections give rise to an *increase* in the current when compared to a VCA result (Section 6.1).

This result also appears to be in contrast to the results obtained in Chapter 5 studying hole transport through a MQW using the NEGF formalism. In that case the inclusion of alloy fluctuations introduced extra transmission channels not present in the VCA. However, recall that the extra channels were comprised of localized states which decayed quickly with increasing barrier width ($L_B > 3.1$ nm). Here we are studying a comparatively large barrier width ($L_B = 8.0$ nm) and the extra transmission channels are unlikely to play a significant role.

On top of this, in Chapter 5 the transmission was studied only through a prescribed well alignment (at equilibrium). In the DD case the transport equations are coupled with Poisson's equation and the well alignment is determined in a self-consistent manner. The states which are localized within the quantum wells, which are not contributing to transmission, do contribute an electric potential which in this case increases the barrier seen by holes.

Our NEGF results also indicated that alloying the barrier may lead to increased hole transport. This has not been considered in this study, however an alloyed barrier may lead to the presence of percolation paths, which requires further investigation. Overall, we conclude that alloy disorder in the QWs has a *detrimental* effect on *hole* transport (In,Ga)N MQWs in a *p-i-p* system. The degree to which this impacts the I-V curve requires further careful research into the description of the confining energy landscape.

6.2.3 Conclusions from studying uni-polar hole transport

In this section we applied the previously established TB-to-continuum framework to perform drift-diffusion calculations for *p-i-p* systems. The impact of alloy fluctuations was determined by comparing to a VCA, and quantum corrections were included via LLT. Our results showed that alloy fluctuations have a detrimental effect on hole transport through $In_{0.1}Ga_{0.9}N$/GaN QW systems, although the degree to which this impacts results depends on the treatment of the localization landscape, and the smoothing applied. For low Gaussian broadening values, σ, the alloy fluctuations reduce the current, due to the increased hole density localizing within the QWs and the resulting depletion of the barriers; this reduces the conductivity in the barrier regions. When the landscape is heavily smoothed (large σ) this effect is reduced, and the I-V curve approaches that of VCA (a smooth landscape).

6.3 Conclusions

In this chapter our newly developed drift-diffusion framework, which includes an atomistic description of the quantum well regions, is used to study electron and hole transport. This allowed us to investigate the impact that alloy fluctuations have on uni-polar carrier transport in the presence and absence of quantum corrections utilizing localization landscape theory. Our approach furthermore enables a feedback loop between atomistic theory and continuum models, since both operate on the same confining energy landscape. Current models in the literature mainly use modified continuum-based approaches that generate confining energy landscapes from locally averaged alloy contents and do not offer the option to compare the outcome of this with an atomistic model.

Our analysis reveals that alloy fluctuations *enhance* electron transport, but are *detrimental* for hole transport, in a uni-polar system. In both cases quantum corrections lead to an increase in current density at a given bias point.

Having now investigated the transport of electrons and holes separately, we are equipped with the tools needed to study a bi-polar system, where a MQW system is embedded in a *p-n* junction forming thus a *p-i-n* structure; this constitutes the backbone of modern LED structures.

Chapter 7

Impact of random alloy fluctuations on the carrier distribution in multi-colour (In,Ga)N/GaN quantum well systems

Chapter 6 highlighted that alloy fluctuations and quantum corrections influence transport properties of electrons and holes in uni-polar (In,Ga)N/GaN MQW systems. Specifically, quantum corrections are beneficial for electron and hole transport, whereas alloy fluctuations are beneficial for electrons, due to the softening of potential barriers, but they are detrimental for holes due to stronger hole localization effects. In the prologue we introduced (In,Ga)N as a candidate for efficient visible lighting applications. This requires the presence of both electrons and holes for radiative recombination. Therefore, our framework is extended to investigate the active region of (In,Ga)N-based MQW LED structures (*p*-*i*-*n* systems) and study how carriers distribute across the active region. In general, understanding the carrier distribution can help to guide maximizing the efficiency in an LED, since ideally the carriers shall be distributed evenly across the entire MQW region so that all QWs will contribute to emission [250]. However, previous experimental studies on carrier distribution in (In,Ga)N/GaN MQW systems have indicated that mainly the well closest to the *p*-doped contact side contributes to the light emission process [250–253]. These samples were specifically designed to gain insight into the carrier distribution inside the active region of an LED.

Overall, this has been attributed to a sequential filling of the QWs, resulting in a high hole density only in the *p*-side QW. To establish accurate carrier transport models the trends found in the experimental studies of Refs. [250–253] need to be captured. Previous theoretical studies have reproduced the experimentally observed behaviour, however this required (i) treating bound carriers in a quantum mechanical

picture, (ii) softening of the QW barrier interface to account for tunneling effects, (iii) distinguishing between continuum and bound carriers in the carrier transport model (multi-population model), and (iv) allowing for scattering between the different populations [69]. But, the impact of alloy disorder is basically neglected in this advanced but also complex carrier transport model.

In this chapter we show that when employing our quantum corrected 3-D simulation framework that accounts for random alloy fluctuations, the experimentally observed trends are captured, without introducing for instance a multi-population scheme. This highlights that our developed solver presents an ideal starting point for future device design studies.

To highlight clearly the impact that random alloy fluctuations have on the carrier distribution in the active region of an (In,Ga)N-based LED, we use as a reference point a VCA description which effectively can be described by a 1-D model. The benefit of this is twofold. Firstly, this enables us to compare directly the outcomes of our quantum corrected model with results from 1-D commercial software simulations; commercial software packages often employ a standard Schrödinger-Poisson-DD solver, which is numerically very costly and therefore unfeasible in large 3-D transport simulations. This motivates the need for an alternative implementation of quantum corrections. Secondly, and building on this benchmark, alloy fluctuations can be included in the calculations, revealing clearly their impact on the results. Our studies show, and when using the same input parameter set, only the model accounting for random alloy fluctuations produces trends that are consistent with the experimental data. The widely employed VCA yields results that are in contradiction with the experimental data, thus indicating that radiative recombination stems mainly from the well *furthest away* from the p-side. Overall, this highlights (i) that alloy fluctuations are essential to achieve an accurate description of the carrier transport and (ii) have to be taken into account when theoretically guiding the design of energy efficient III-N light emitters.

The chapter is organized as follows: In Section 7.1 we outline the model structure used for calculations and briefly summarise some of the literature experimental data from Ref. [251]. The theoretical framework which we use is summarized in Section 7.2. Our results are discussed in Section 7.3. Finally Section 7.4 presents our conclusions.

7.1 Model MQW structures and literature experimental findings

To investigate the carrier distribution in (In,Ga)N/GaN MQW systems we proceed similar to experimental studies in the literature [251, 253] and target MQW systems where one of the wells in the MQW stack has a slightly higher In content compared to the remaining wells. In our case, we study MQW systems with three (In,Ga)N/GaN wells.

Here two are $In_{0.1}Ga_{0.9}N$ ("shallow") wells and one is an $In_{0.125}Ga_{0.875}N$ ("deep") QW. These QWs are 3 nm wide and separated by 5 nm GaN barriers. The band edge profile of such a system along the transport (c-) direction, using a VCA, is shown in Fig. 7.1 at a current density of 50 A/cm^2.

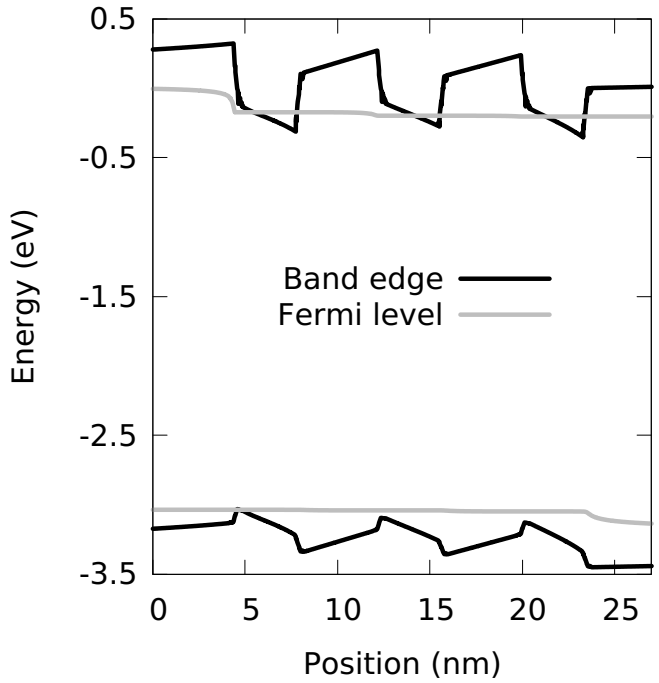

Figure 7.1: Conduction and valence band edges (black) along with the quasi-Fermi energies for electrons and holes (grey) in an (In,Ga)N/GaN multi-quantum well system described in virtual crystal approximation. The band edge profile and the quasi Fermi levels are shown at a current density of 50 A/cm^2. The leftmost (In,Ga)N quantum well contains 12.5% indium while the other two (In,Ga)N wells (centre and right) contain 10% indium.

In the following, we investigate the carrier transport properties in two settings: (i) on an atomistic level accounting for random alloy fluctuations and (ii) in the frame of a VCA thus neglecting alloy fluctuations. In the latter VCA case (ii), at a given z-position (along the *c*-direction), there is no variation in material properties within the growth plane (c-plane). This assumption is also made in the widely used 1-D transport simulations on (In,Ga)N MQWs.

To study the carrier distribution in MQW systems using the simulation settings (i) and (ii), we follow again the experimental approach e.g. presented in Ref. [251] and the deep QW is moved from the *n*-side (position 1 (*n*-side) in Fig. 7.2) to the *p*-side (position 3 (*p*-side) in Fig. 7.2). In the case of the random alloy structures, the same microscopic configuration is kept for each well and only the ordering is changed.

For each of these systems the ratio of radiative recombination from the shallow wells

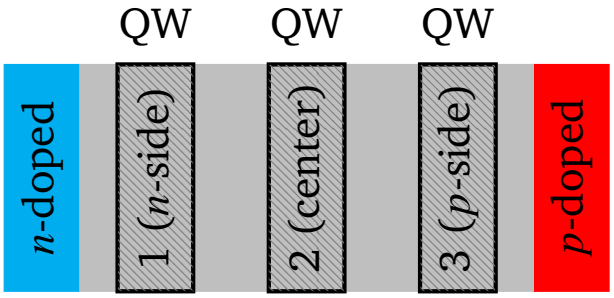

Figure 7.2: Schematic illustration of multi-quantum well system. The n-doped region is shown in cyan, the p-doped is in red and undoped regions are in grey. The quantum wells are numbered starting from the n-side.

to the deep well is calculated using:

$$\varrho = \frac{\mathcal{R}^{\mathrm{RAD}}_{\Omega_S}}{\mathcal{R}^{\mathrm{RAD}}_{\Omega_D}} \tag{7.1}$$

where

$$\mathcal{R}^{\mathrm{RAD}}_{\Omega_i} = \int_{\Omega_i} R^{\mathrm{RAD}}(\mathbf{r})\mathrm{dV} \ , \tag{7.2}$$

is the total radiative recombination from the region Ω_i. Here, Ω_D is the region containing the deep QW, Ω_S is the region containing the shallow wells (as there are two shallow QWs this is the union of the two shallow QW regions). The radiative recombination rate at position $\mathbf{r}$, $R^{\mathrm{RAD}}(\mathbf{r})$ is calculated via the ABC model as introduced in Section 4.2.1.3. Since we are studying a system with three QWs, an even distribution of carriers across the MQWs would result in a ratio of $\varrho = 2$. Previous experimental work on a similar system by Galler *et. al.* [251] found that ϱ *was small* (i.e. emission is dominated by the deep QW) *only when the deep well was closest to the p-doped side of the MQW system* (thus position 3 (p-side) in Fig. 7.2). The authors conclude that holes are responsible for this behavior, and argue that they are mainly found in the p-side QW and not in wells further away from the p-side. As a consequence, the overall emission from the (In,Ga)N/GaN MQW system is dominated by the emission from this well closest to the p-doped region. In line with Ref. [251], we calculate ϱ at a current density of 50 A/cm^2, which allows us to compare the here predicted trends with the trends found in the experimental studies. The theoretical framework employed to gain insight into ϱ is discussed in the following section.

7.2 Theoretical framework

In this section, we introduce the underlying (microscopic) theory of our multiscale simulations. Since the TB and DD approaches have already been discussed in detail in Chapter 3 and Chapter 4 , we here give only a brief summary, and highlight changes to the simulation framework.

7.2.1 Tight-binding energy landscape

The simulations build on the same TB model which was implemented in previous studies in this thesis that was introduced in detail in Chapter 3. As before, a potential energy landscape is extracted following the procedure in Section 4.2.2.1 by generating conduction and valence band energies at each lattice site including an atomistic description of the alloy microstructure, strain and polarization. The obtained 3-D confining energy landscape, after employing a Gaussian softening, forms the basis for our DD calculations.

In Chapter 6, while studying uni-polar transport, we have investigated and discussed in detail the influence of the Gaussian softening on transport calculations for electrons and holes. Here, we choose a Gaussian broadening on the order of the GaN lattice constant, $\sigma_{c,v} = a^{\mathrm{GaN}} = 0.3189$ nm, in all calculations. This value is large enough to average over a number of neighboring sites, while also small enough to retain fluctuations in the energy landscape.

To obtain an accurate description of carrier transport in (In,Ga)N-based LEDs, the DD equations, are often coupled with solving the Schrödinger equation to account for quantum corrections. As before, to reduce the numerical demand in our simulations we implement LLT, since we saw in Chapter 6 that it is important to include quantum corrections. From LLT we extract an effective confining potential for the conduction and valence band edge starting from the TB energy landscape. An example of the resulting quantum corrected energy landscape is given in Fig. 7.3 (a) and (b). Here, in-plane band edge profiles for a single atomic plane through an $In_{0.1}Ga_{0.9}N$ QW, after LLT has been applied, are shown. As Fig. 7.3 (a) reveals, the fluctuations in the VBE energy due to alloy fluctuations are of the order of 100 meV. In combination with the high effective hole mass, these fluctuations are large enough to give rise to strong carrier localization effects as seen in other studies already [40, 41, 254]. We therefore expect that, especially for holes, the inclusion of random alloy fluctuations in the simulation will impact the carrier distribution. Consequently recombination rates are also expected to be noticeably influenced.

The variation in the CBE energy is significantly smaller (order of 30 meV), as can be seen in Figure 7.3 (b). Since the effective electron mass is much lower in comparison with the holes, electron wave functions are less strongly perturbed by alloy fluctuations. The impact that these fluctuations in the band edge energies have on the radiative recombination is also seen in Fig. 7.3 (c); the radiative recombination is calculated with `ddfermi` as was described in Section 4.2.1.3. The correlation between the VBE maxima and regions of high radiative recombination can be clearly identified; similar spatial profiles can be seen for non-radiative (Auger) recombination (not shown).

In order to highlight the impact of random alloy fluctuations on carrier transport and the distribution of carriers across a MQW system, we compare our atomistic calcula-

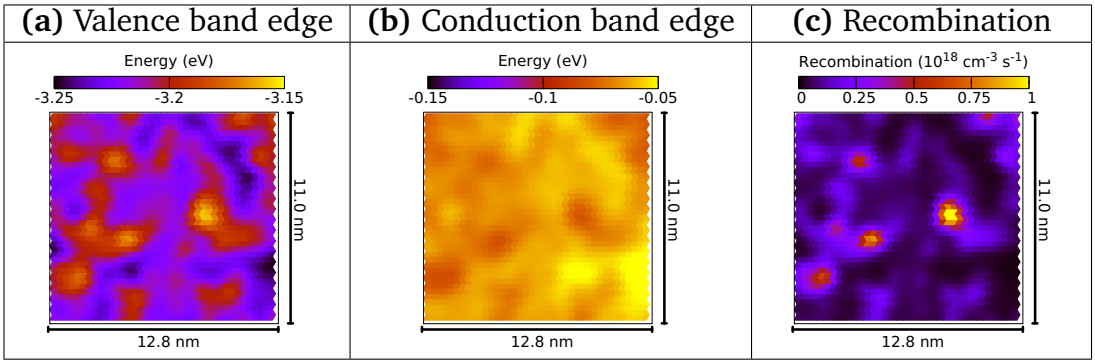

Figure 7.3: Profile of (a) valence band edge energy, (b) conduction band edge energy, and (c) radiative recombination rate in the growth plane (c-plane) of an $In_{0.1}Ga_{0.9}N$ quantum well; the current density is 50 A/cm^2 in all depicted figures. The slice displayed is the through the center well. The data are shown in all cases on a linear scale.

tions with the outcome of a VCA. The VCA description, without any Gaussian broadening, is similar to commercially available packages. However, and in contrast to commercial software packages, quantum corrections via LLT can also be taken into account in our VCA simulations, following the approach used for the random alloy case.

7.2.2 Device simulation

Having outlined above the generation of the energy landscape of the active region, e.g. the (In,Ga)N/GaN MQW system, a full device mesh, including the n- and p-doped regions, needs to be constructed on which the DD equations are solved. This is carried out following the procedure outlined in Section 4.2.2.4.

In order to capture the effects of carrier localization in the calculations, the in-plane dimensions of our 3-D simulation cell should be larger than the localization length of the holes, given that electrons are less strongly affected by alloy fluctuations [57]. In our atomistic calculations we use a system with in-plane dimensions of 12.8×11.0 nm^2. This is large enough to see the effects of hole localization as the in-plane hole localization length for $In_{0.1}Ga_{0.9}N$ QWs is of the order of 1 nm [44]. The in-plane dimensions can be seen in Fig. 7.3 (a) and (b) where a 2-D slice through the valence and conduction band edges of an $In_{0.1}Ga_{0.9}N$ QW are shown. In case of the VCA, given that there are no variations in material properties (band edge energies) within the growth plane (c-plane), a much smaller in-plane area is sufficient (1.3×1.1 nm^2), which reduces the numerical effort.

Equipped with the constructed mesh, we turn now to the DD simulations. To do so we build on the van Roosbroeck system of equations [199]. The system of equations was described in Eq. (4.42); unlike in previous sections we now use the full system of equations in steady-state and include for both electrons and holes. The electron and hole carrier densities are described statistically via the Fermi-Dirac distribution function,

and a temperature of $T = 300$ K has been used in all calculations. The recombination model used is the ABC model described in Section 4.2.1.3. We follow here the widely made assumption that the Shockley-Read-Hall, radiative and Auger recombination coefficients, A_0, B_0, and $C_{n,p}$, are constant across the (In,Ga)N MQW region [67, 210]. In the following we take a weighted average of parameters calculated in Ref. [205] for an electron and hole density of 3.8×10^{18} cm^{-3}, which is a good approximation for the average carrier densities in the QWs at a current density of 50 A/cm^2. As our active region consists of two $In_{0.1}Ga_{0.9}N$ QWs and one $In_{0.125}Ga_{0.875}N$ QW we evaluate the different recombination coefficients as follows:

$$R_i^{\text{eff}} = \frac{2 \times (R_i^{10\%}) + 0.5 \times (R_i^{15\%} + R_i^{10\%})}{3} \,. \tag{7.3}$$

Here, $R_i \in \{B_0, C_n, C_p\}$ are the radiative recombination, electron-electron-hole and hole-hole-electron Auger recombination coefficients, respectively. As there are no values for an $In_{0.125}Ga_{0.875}N$ QW in Ref. [205], a linear average of the coefficients in $In_{0.1}Ga_{0.9}N$ and $In_{0.15}Ga_{0.85}N$ wells has been used. A summary of the material parameters employed in all simulations is given in Table 7.1.

Table 7.1: Material parameters used in the different regions of the simulation supercell. Parameters denoted with † are taken from [67]; parameters denoted with ‡ are derived from [205] as described in the main text.

Parameter			Value in each region		
Name		**Units**	p-**GaN**	i-**InGaN**	n-**GaN**
Doping		cm^{-3}	5×10^{18}	1×10^{16}	5×10^{18}
μ_h	†	cm^2/Vs	5	10	23
μ_e	†	cm^2/Vs	32	300	200
τ_p	†	s	10	1×10^{-7}	7×10^{-10}
τ_n	†	s	6×10^{-10}	1×10^{-7}	10
B_0	‡	cm^3/s	2.8×10^{-11}	2.8×10^{-11}	2.8×10^{-11}
C_p	‡	cm^6/s	5.7×10^{-30}	5.7×10^{-30}	5.7×10^{-30}
C_n	‡	cm^6/s	1×10^{-31}	1×10^{-31}	1×10^{-31}

The numerical approximation of the van Roosbroeck system is again implemented (in 3-D) in `ddfermi` [222]. We employ the FVM described in Section 4.2.1.4 and the current is discretized using the SEDAN (excess chemical potential) approach [216, 217, 255] described in Eq. (4.48), which yields a thermodynamically consistent flux approximation in the sense of Ref. [103].

To simulate the devices under study, we also used the commercial software next**nano** [200], which relies on the simulation of a self-consistent Schrödinger-Poisson-DD system. Here we use next**nano** to simulate the carrier transport in the above discussed MQW systems within a 1-D approximation. In next**nano** we utilize the same parameter set as in the `ddfermi` simulations. Therefore, the obtained results can be directly compared to our 3-D VCA model. When including quantum corrections in

ddfermi, LLT is used. In next**nano** a self-consistent Schrödinger-Poisson-DD calculation is performed where a $\mathbf{k} \cdot \mathbf{p}$ Hamiltonian is used to calculate eigenstates across the full simulation domain. Following the ddfermi set up, in next**nano** we employ also a 1-band model for the calculation of the electron and hole densities.

7.3 Results

In this section we present the results of our study on the carrier distribution in the above described (In,Ga)N/GaN MQW systems. To understand the impact of the alloy microstructure on the carrier distribution, in Section 7.3.1 we start with standard 1-D calculations building on the commercial software package next**nano** [200]. We use this entirely continuum-based description of the QWs also to determine the impact (i) of an EBL and (ii) a self-consistent Schrodinger-Poisson-DD treatment on the transport properties. Moreover, and as already mentioned above, (ii) can also be used as a benchmark for our 3-D ddfermi solver. In Section 7.3.2 we then proceed to investigate the influence of random alloy fluctuations on the carrier distribution in the (In,Ga)N/GaN MQW stack.

7.3.1 Continuum-based simulations of the carrier transport in (In,Ga)N-based LEDs

To examine the impact of random alloy fluctuations on the carrier distribution in an (In,Ga)N/GaN MQW stack, we start with a 'standard' 1-D simulation approach that is widely applied in the literature. In a first step we begin with next**nano** calculations and as outlined above, compare the results to our ddfermi data.

7.3.1.1 nextnano simulations

To study how the presence of an EBL affects the ratio of radiative recombination ϱ, Eq. (7.1), the systems outlined in Section 7.1 are simulated with and without a 20 nm $Al_{0.15}Ga_{0.85}N$ EBL using next**nano**. The EBL is separated from the p-side QW (position 3 (p-side) in Fig. 7.2) by a 10 nm GaN barrier. Similar settings for an (Al,Ga)N EBL have been used in previous studies [67]. The next**nano** calculated ratio of radiative recombination ϱ, when varying the position of the deep QW in the MQW stack, are depicted in Fig. 7.4 (a). Turning first to the data without quantum corrections, we find that in the case of the employed 1-D VCA-like continuum-based description, *ϱ is small when the deep QW is at the n-side (position 1 (n-side) Fig. 7.2) and larger when the deep well is at the p-side (position 3 (p-side) Fig. 7.2)*. Thus, the 1-D model *predicts the opposite trend* when compared to experiment [251]. This trend is only slightly changed when including quantum corrections via a self-consistent Schrödinger-Poisson-DD model. In this case a much weaker dependence of the results on the position of the deep QW in the MQW stack is observed. However, even when including quantum

corrections, the next**nano** results for ϱ are not reflecting the experimentally observed behavior (see discussion above). Figure 7.4 (a) reveals also that qualitatively the results do not depend on the presence of the EBL, indicating that for the structures considered, this feature of an LED is of secondary importance for the aims of this study.

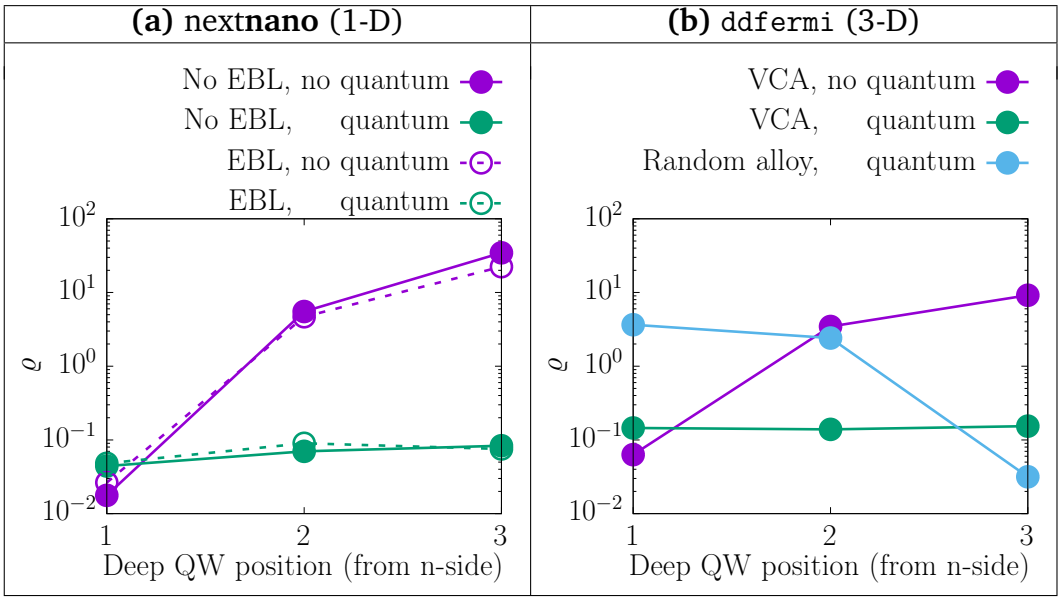

Figure 7.4: Ratio of radiative recombination ϱ, Eq. (7.1), from the shallow wells ($In_{0.1}Ga_{0.9}N$) to recombination from the deep well ($In_{0.1}Ga_{0.9}N$) calculated as a function of the position of the deep well in the multi-quantum well stack. Here ϱ is evaluated using (a) next**nano** excluding (purple) and including (green) quantum corrections via a self-consistent Schrödinger-Poisson-drift diffusion solver; results are shown when excluding (solid, filled circles) and including (dotted, open circles) an $Al_{0.15}Ga_{0.85}N$ blocking layer, and (b) `ddfermi` excluding (purple), including (green) quantum corrections via localization landscape theory (LLT) using a virtual crystal approximation (VCA) and a random alloy calculation including LLT-based quantum corrections (blue); these calculations neglect the AlGaN blocking layer.

7.3.1.2 `ddfermi` simulations

Since we are also able to use the atomistic framework in a VCA setting, we compare our `ddfermi` results, cf. Fig. 7.4 (b) (purple), with those from next**nano**, cf. Fig. 7.4 (a) (purple, solid). We focus on structures which neglect the EBL as we have found above that it does not impact results in a VCA. In both next**nano** and `ddfermi` a similar trend is found: the deep QW dominates recombination only when it is located at the *n*-side. This is illustrated further in Fig. 7.5 (a), which displays the contribution (in percent) to the radiative recombination rate from each QW (colours) in the MQW stack. The data are shown as a function of position of the deep QW in the MQW system. This confirms that it is always the QW which is closest to the *n*-doped side (position 1) that dominates the recombination process; the *n*-side QW contributes $\approx 95\%$ when the deep QW is at position 1, $\approx 70\%$ when the deep QW is at position 2 or 3. Again, we stress that this is the *opposite* trend to the experimental findings in Ref. [251].

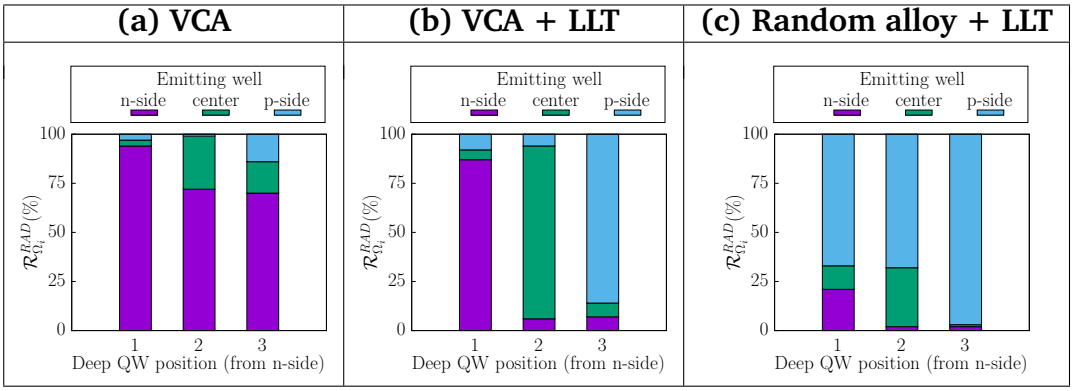

Figure 7.5: Contribution of each quantum well (n-side; centre; p-side) in the (In,Ga)N multi-quantum well system to the total radiative recombination $\mathcal{R}^{RAD}_{\Omega_i}$ for $i \in \{n\text{-side}, \text{center}, p\text{-side}\}$ as a percentage of the total radiative recombination from all 3 quantum wells for (a) virtual crystal approximation (VCA), (b) virtual crystal approximation with quantum corrections included via localization landscape theory (VCA + LLT) and (c) a random alloy calculation including localization landscape theory based quantum corrections (Random alloy + LLT). That data are shown as a function of the position of the deep quantum well (x-axis). Each bar contains the percentage recombination from the n-side quantum well (purple), the center quantum well (green) and the p-side quantum well (blue). Labelling is consistent with that introduced in Fig. 7.2.

To shed more light on this result, the upper row in Figure 7.6 depicts the average hole (black, solid), electron (black, dashed) and radiative recombination (red) rate along the c-axis when the deep QW ($In_{0.125}Ga_{0.875}N$ well) is (a) closest to the n-side (position 1), (b) in the centre of the MQW stack (position 2) and (c) closest to the p-side (position 3). Focusing on the VCA data, Figs. 7.6 (i) (a-c), we see the cause of the dominant recombination from the n-side QW: the hole density is always high in this region, independent of which well is closest to the n-side. In particular, the p-side QW fails to capture holes effectively and consistently has the lowest hole density. We note that a similar behavior is also found in the next**nano** calculations discussed in Sec. 7.3.1.1.

Given that our VCA `ddfermi` approach and next**nano** treat (In,Ga)N as a homogeneous alloy that can be described by averaged material parameters which do not vary throughout the wells (no alloy fluctuations included), it allows us also to compare the implemented methods for quantum corrections in DD simulations. Here, as discussed above, next**nano** builds on the widely used Schrödinger-Poisson-DD model while `ddfermi` utilizes the recently developed LLT method. It has been discussed and shown in the literature that the LLT method can produce results in good agreement with the solution of the Schrödinger equation in the case of a 1-D EMA [158, 163]. Looking at Fig. 7.4 (a) (green, solid) and Fig. 7.4 (b) (green) we see that the results from our in-house developed `ddfermi`-based 3-D model, which employs LLT (3-D, `ddfermi`), are very similar to the standard self-consistent 1-D Schrödinger-Poisson-DD calculation underlying next**nano**. This gives confidence that our LLT treatment is providing a comparable

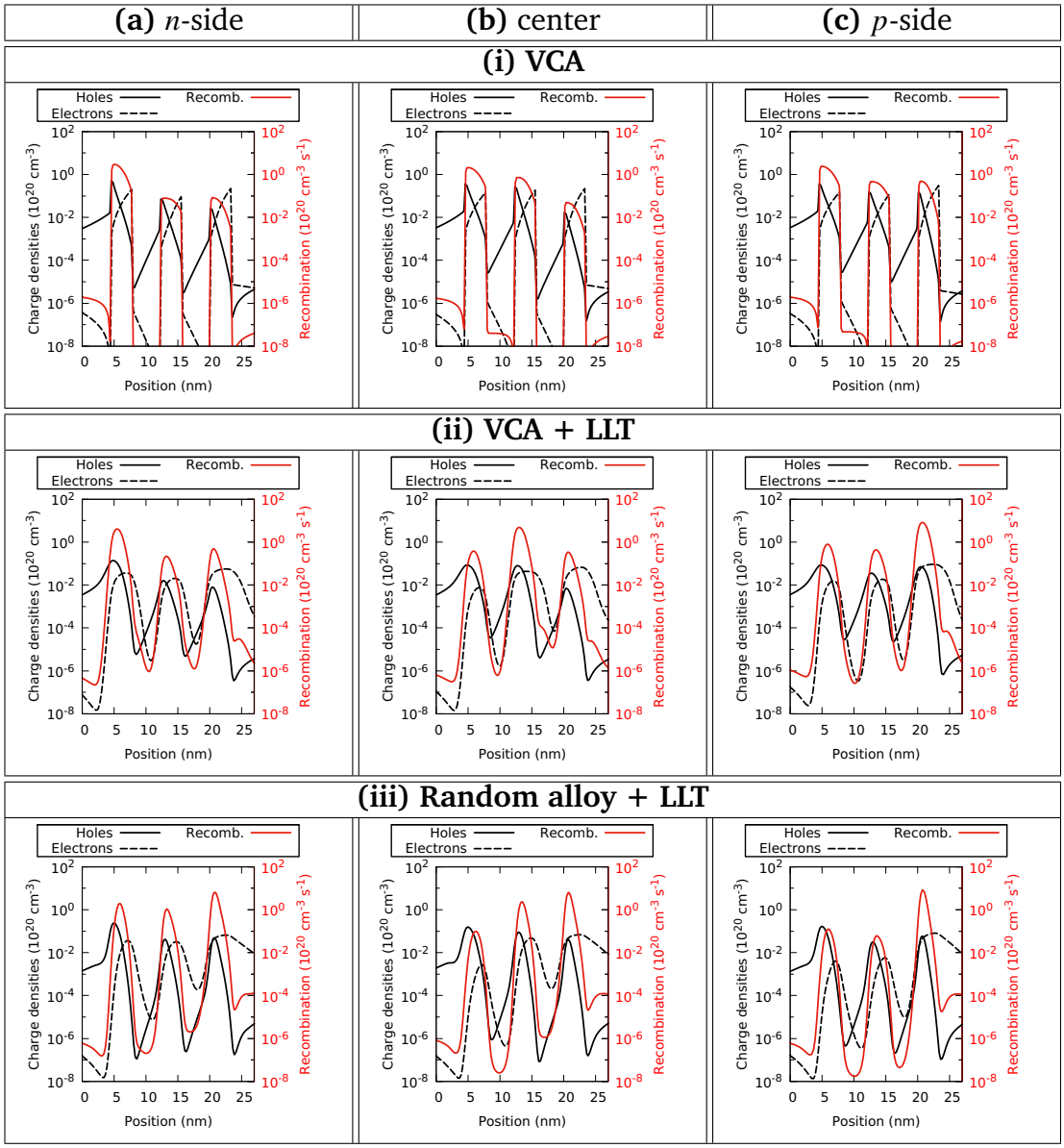

Figure 7.6: Hole density (black, solid), electron density (black, dashed), and radiative recombination rate (red, solid) averaged over each atomic plane along the transport direction. Results from calculations building on (i) a virtual crystal approximation (top), (ii) a virtual crystal including quantum corrections via localization landscape theory (LLT) (center) and a (iii) random alloy description including LLT-based quantum corrections (bottom); the deep well is located at (a) the *n*-side (left), (b) the center (middle) and (c) the *p*-side (right). The data are shown on a log scale.

description of the quantum corrections in the system.

Overall, Fig. 7.4 (a) reveals that when including quantum corrections in the VCA calculations, the position of the deep QW has little impact on the ratio of the relative radiative recombination, ϱ. From Fig. 7.5 (b) one can also gain more insight into this behavior and how quantum corrections impact the carrier distribution in the MQW stack. In the *absence* of quantum corrections but utilizing a VCA, Fig. 7.5 (a), the well

closest to the *n*-side dominates the relative radiative recombination ratio ϱ independent of the position of the deep well in MQW systems. When *including* quantum corrections this situation is now changed: the deep QW is now the dominant emitter independent of its position in the MQW stack.

This behavior becomes clear when analyzing the electron and hole densities as a function of the position of the deep well in the (In,Ga)N/GaN MQWs, as shown in Fig. 7.6 (ii). Looking at the electron densities first, we find that electrons preferentially occupy the well closest to the *p*-side. This effect is enhanced when the deep QW is closest to the *p*-side (cf. Fig. 7.6 (ii) (c)). In our previous study on uni-polar electron transport (Ref. [3] and Section 6.1), we have already seen that including quantum corrections leads to a softening of the potential barrier at the QW barrier interfaces. This in turn can lead to an increased electron current at a fixed bias point, when compared to a VCA system without LLT treatment, and thus the electrons can more easily 'overshoot' the wells in the MQW system. As a consequence, a lower electron density in the well closest to the *n*-side is observed. Turning to the hole density, the situation is different. Here, we find that holes preferentially populate the well closest to the *n*-side. Only when the deep QW is closest to the *p*-side, the hole density in this well is noticeably increased. However, when comparing the distribution of holes in the MQW as a function of the position of deep well in absence (Fig. 7.6 (i)) and presence (Fig. 7.6 (ii)) of quantum corrections, the results are not very different. This indicates that quantum corrections, at least when employing a VCA, are of secondary importance for the hole distribution. This finding is consistent with our previous results on uni-polar hole transport (Ref. [2] and Section 6.2), where we have discussed that due to the high effective hole mass and the small valence band offset, quantum corrections have a smaller impact on the hole transport when compared to electrons. As a consequence, the distribution of holes follows a similar pattern to that of the VCA where quantum corrections are neglected. Finally, when looking at the ratio of radiative recombination ϱ, it is important to note that this quantity is not only determined by having both large electron and hole densities in the same well but also by their spatial overlap. As one can infer from Fig. 7.6 (ii) (a-c), the largest radiative recombination rate is always observed in the deepest well. This indicates also that the spatial overlap of electron and hole densities largest in the deep QW regardless of its position across the MQW system. We stress again that even when including quantum corrections in the VCA calculations, the resulting trend in ϱ is not reflecting the trend observed in experimental studies [251].

7.3.2 Impact of random alloy fluctuations on the carrier transport in (In,Ga)N/GaN MQWs

In the last step, we move away from the VCA description of the system and include, in addition to quantum corrections, also random alloy fluctuations in the calculations. Figure 7.4 (b) (blue) shows that, and this time in line with the experimental results

by Galler *et. al* [251], the deep QW only contributes significantly to the radiative recombination when it is *closest to the p-side* (position 3). In fact, when including random alloy fluctuations in the calculations, the well closest to the *p*-side always has the largest contribution to total radiative recombination, as can be seen in Fig. 7.5 (c).

To understand this behavior, Fig. 7.6 (iii) depicts the electron and hole densities in the different wells as a function of the position of the deep well in the MQW systems. Looking at the electron density first, in comparison to the VCA calculations both including and excluding quantum corrections, random alloy fluctuations lead a reduction in electron density at the *n*-side QW. As discussed above and previously, quantum corrections can lead to increased electron transport, and including alloy fluctuations adds further to this effect due to the softening of the barrier at the well interfaces [3]. As a consequence, the electrons can more easily 'overshoot' the wells in the MQWs, which can also be seen in the increased electron density beyond the *p*-side QW when alloy fluctuations and quantum corrections are included. However, in comparison to the VCA result including quantum corrections, the electron density in the *p*-side well is only slightly affected by alloy fluctuations.

In contrast, hole densities in the *p*-side QW are more dramatically changed by alloy fluctuations. As Figs. 7.6 (ii) and 7.6 (iii) show, in comparison to the VCA description, alloy fluctuations lead to an *increase* in the hole density in the *p-side QW* (position 3) even when the deep QW is closest to the *n*-side (position 1) or in the centre (position 2) of the MQW system. While the smoothing of the well barrier interface can increase hole transport, as in the case of electrons, there are now also alloy disorder induced localization effects to contend with. As discussed in our previous work, these localization effects are *detrimental* to hole transport (Ref. [2] and Section 6.2) and result in an increased hole density in the *p*-side QW. As a consequence, the well closest to the *p*-side dominates radiative recombination

We note that there is still a reasonable hole density present in the *n*-side QW (Fig. 7.6 (iii) (a-c)). In general, the distribution of carriers will also depend on the GaN barrier width and a 5 nm barrier is narrow enough to allow for some hole transport across the MQW [253]; a similar dependence of hole transmission on the barrier width was seen in the NEGF study in Chapter 5. Thus we expect that increasing the barrier width will mainly lead to a reduction of the hole density in the well furthest away from the *p*-side, but should to a lesser extent affect the hole density in the well closest to the *p*-side. Therefore, even for a larger barrier width than the here considered 5 nm, we expect that the recombination will still be dominated by the *p*-side QW.

We note that based on the VCA results we did not consider the EBL in the atomistic calculations. In general the EBL needs to be treated with an atomistic resolution. Previous studies of (Al,Ga)N barriers in uni-polar device settings have found that the impact of these barriers is lower than what is expected from a 1-D simulation for both

electrons [256] and holes [245]. Thus given that our VCA calculations show that the presence of the EBL is of secondary importance for our study, we expect a similar conclusion when treating the EBL with alloy fluctuations. Therefore, it is unlikely that the EBL impacts the here presented result.

7.4 Conclusions

In this chapter we apply a 3-D quantum corrected multiscale simulation framework to gain insight into the impact of random alloy fluctuations on the electron and hole distribution across the active region of an (In,Ga)N/GaN LED. To study the spatial distribution of carriers we have followed literature experimental studies [251] and analyzed the radiative recombination ratio in a multi-quantum well system, where one of the wells in the system has a higher indium content (deeper well) and its position is varied within the stack.

The here considered MQW systems are not only of interest for a comparison with experiment, they provide also the ideal opportunity to benchmark and validate results from our in-house developed 3-D multiscale simulation framework against commercially available software packages. To do so we treat the QWs in a VCA, to mimic the 1-D simulation widely used in the literature for (In,Ga)N QWs and implemented in the commercial software package next**nano**. In addition, this study allows us also to compare the different schemes to account for quantum corrections (localization landscape theory vs. Schrödinger-Poisson-DD simulations) in the simulations. Overall, this analysis showed very good agreement between results obtained from our in-house software and next**nano**, when neglecting random alloy fluctuation.

Equipped with this benchmarked model, our analysis reveals that including (random) alloy fluctuations in the calculations is vital for reproducing trends seen in experiment. More specifically, when using the widely employed VCA, the hole density in the well closest to the p-doped region of the device is significantly reduced compared to our atomistic random alloy calculation. As a consequence, and in contrast to the experiment, in VCA the well closest to the p-side contributes very little to the radiative recombination process, an effect that can be reduced by accounting for quantum corrections. While this leads to enhanced radiative recombination from the well closest to the p-side, at least when this well is the deep well, it still does not reflect the trends observed in the experimental studies. However, when including random alloy fluctuations and quantum corrections in our 3-D simulation framework, these effects lead to an increase in the hole density in the well closest to the p-side. Consequently, this well dominates the radiative recombination process in line with the experimental data. We note that in addition to quantum corrections and alloy fluctuations no further ingredients are required (e.g. multi-population model) to explain the experimentally observed trends. Therefore, our calculations highlight that alloy fluctuations are a key ingredient in sim-

ulations guiding the design of III-N based devices. Thus, the here developed model presents an ideal starting point for future calculations of (In,Ga)N-based LED structures.

Part IV

Summary, conclusion and outlook

Chapter 8

Summary and conclusions

In this thesis a theoretical study of carrier transport was carried out, with a particular focus on (In,Ga)N/GaN quantum wells due to their technological importance for visible lighting applications. Atomistic and fully quantum mechanical simulations were used to analyse ballistic transport. Furthermore, in order to investigate device behaviour, a new framework was developed and established to include alloy fluctuations and quantum corrections in a multi-scale semi-classical transport simulation. Such a formalism is not limited to (In,Ga)N-based LEDs, but can be extended to other material systems.

All calculations were built on an atomistic, sp^3 nearest neighbour tight-binding model. This was employed to describe systems (i) as a random alloy, in order to capture the atomistic nature of the underlying alloy microstructure, and (ii) as a virtual crystal which acts as a continuum-based description. The implementation of a random alloy microstructure, setting (i), is not widely utilized in literature transport calculations, and often only a virtual crystal approximation is used. The work in this thesis targeted exactly the impact of random alloy fluctuations, which cause carrier localization effects due to the alloy microstructure.

To analyse the impact of the alloy microstructure on ballistic transport, the tight-binding model was coupled with the non-equilibrium Green's function (NEGF) solver, OMEN. This allowed a fully atomistic, quantum mechanical description of ballistic transport through (In,Ga)N/GaN multi-quantum wells which has not been addressed in the literature. Results were compared with those from a virtual crystal approximation, which neglects the alloy fluctuations, so the influence of the alloy microstructure could be deduced.

Our results showed that the treatment of the alloy microstructure is of secondary importance for describing *electron* transport in a fully quantum mechanical framework: The virtual crystal approximation gave the same general features as the random distribution of atoms in terms of transmission peaks, however the random alloy description introduced a broadening of these peaks due to the variation of the alloy microstruc-

tures between different regions of a device. In contrast to this, *hole* transmission was strongly influenced by disorder in the alloy microstructure. The breakdown of the translational symmetry modified the hole states significantly when a random alloy was used. As a result, the transmission through states near the band edge (perturbed by the alloy fluctuations) is drastically different between the two schemes, and a virtual crystal approximation might underestimate hole transport. However, the extra transmission channels are sensitive to barrier width, and quickly decay as the well separation is increased; this observation is backed up by previous literature experimental results. Initial investigations into the impact of alloying the barrier between quantum wells were also performed, which offer a first insight into experimental findings that alloying the barrier increases ballistic transport.

The numerical demand of the fully quantum mechanical non-equilibrium Green's function approach means that it is not suitable for full device simulation, especially when such a model is used to guide the design of, e.g. LEDs where several parameters (well width, barrier width, etc.) have to be varied. Thus, due to the numerical constraints of a fully atomistic and quantum mechanical formalism, a 3-D multi-scale framework to study carrier transport in a semi-classical context was developed. To achieve this, a method of extracting an energy landscape directly from the atomistic tight-binding model was developed and implemented. This was then included in drift-diffusion calculations to provide an atomistic description of (In,Ga)N quantum wells (including local strain and polarization effects calculated with atomistic theories). Quantum corrections have also been included in the energy landscape using the recently formulated localization landscape theory.

To decouple transport properties from recombination aspects, we first applied the framework to uni-polar transport systems. Starting with uni-polar electron transport, without including quantum corrections, the virtual crystal approximation results in a lower current at a given bias point compared to a random alloy. This is attributed to the reduction of potential barriers caused by the alloy microstructure. Previous experimental and simulation results indicate that the virtual crystal approximation underestimates the electron current in an *n-i-n* system, and thus our approach that accounts for alloy fluctuations corrects the current-voltage curve (at least qualitatively) towards experimental data.

Including quantum corrections causes an increase in current for both the virtual crystal and random alloys. Overall, when quantum corrections are considered in a single quantum well system we find that the virtual crystal provides a good approximation for a random alloy system. This is the same result which we saw using the fully atomistic and quantum mechanical non-equilibrium Green's function formalism. In a multi-quantum well system the situation becomes more involved. In this case the random alloy treatment including quantum corrections results in a higher current than the virtual crystal

approximation. We conclude and show that this is attributed to subtleties in the localization landscape theory rather than a physical effect.

Turning to hole transport, *p-i-p* system have been studied using the drift-diffusion framework. Here we observed that alloy fluctuations are *detrimental* to hole transport, particularly in the absence of quantum corrections. When quantum corrections are included this effect is reduced, but still present. The decrease in current is attributed to carrier localization capturing holes in the quantum well region so they do not contribute to carrier transport. This effect is neglected in a virtual crystal approximation.

The current is also reduced through a multi-quantum well system when a random alloy microstructure is considered. Unlike in the case of electrons, this difference between a single quantum well and multi-quantum well is not due to difficulties in implementing quantum corrections. This is demonstrated by partitioning the system into different sub-regions, and applying quantum corrections in each region individually, an approach which was not possible in the *n-i-n* system due to the lower electron effective mass.

The difference between the drift-diffusion results for holes in a uni-polar system and the ballistic hole transport results using non-equilibrium Green's function formalism is attributed to two factors. First, a wide barrier is used in the drift-diffusion formalism, so localized states do not contribute strongly to transport. On top of this, the localized holes within the quantum wells will contribute an electric potential that is determined self-consistently; such a self-consistent approach due to its numerical expense is not taken into account in the ballistic transport simulation.

Having ascertained the influence that that alloy microstructure has on the transport of electrons and holes in uni-polar systems, we extended our analysis to a *p-i-n* structure, similar to a setup found in an LED. Here we used the developed multi-scale drift-diffusion framework to study the distribution of carriers across a multi-colour quantum well system. Similar structures have been studied experimentally in the literature, and the conclusion was that holes could not distribute beyond the first quantum well on the *p*-side. Using a virtual crystal description with the here developed theoretical framework, and a commercial software package that has been used to validate our developed model, this trend was not predicted excluding or including quantum corrections. However, by using the same simulation parameters, but changing only the confining energy landscape to include alloy fluctuations and quantum corrections, the trend seen in the experiment is reproduced by our multi-scale model. This is attributed to the fact that fluctuations in the alloy microstructure results in holes becoming localized more strongly in the *p*-side well, an effect neglected in 1-D simulations. Our calculations highlight that alloy fluctuations are a key ingredient in simulations guiding the design of III-N based devices, and the here developed model presents an ideal starting point for future calculations.

Overall, we have seen throughout this thesis that the specific treatment of the alloy

microstructure will impact transport simulations in (In,Ga)N/GaN quantum well systems. In the case of electrons, a virtual crystal approximation might suffice if quantum corrections are included, however the strong localization of holes means that transport properties are noticeably varied depending on the treatment of the alloy microstructure.

Chapter 9

Outlook

In its present form, the drift-diffusion framework described in this thesis is the ideal starting point to study many systems. For example, the model could be used to research the impact of indium penetration into GaN barriers, or the influence of graded alloy composition and alloyed barrier material in a multi-scale setting. Such studies could be tailored to analyse specific devices in collaboration with experimental groups. A theory-experiment comparison could also be used to find an empirical value for the width of the Gaussian broadening function, σ. This could involve, for example, a study of the width of the EL emission spectra, whose observed broadened profile is attributed to localization effects.

To progress the drift-diffusion model further several aspects could be earmarked for further study. The energy landscape derived from tight-binding, including atomistic descriptions of strain and polarization, has been used to calculate the electronic structure. This allowed for a direct comparison with the tight-binding electronic structure as the two approaches operate on the same alloy microstructure. No direct study on importance of the atomistic description of strain and polarization effects has been carried out. This could be achieved by first generating a random distribution of atoms which is used for tight-binding. This distribution can be converted into a composition map on the wurtzite mesh by (for example) getting the average alloy content over a local tetrahedron. Strain could be calculated using a linear elasticity theory, and polarization by solving Poisson's equation via a continuum approach, using the composition map as input. The resulting strain and polarization profiles could be compared, as well as the calculated electronic structures using tight-binding and e.g. a single band effective mass approximation. Thus a solid evaluation could be made on the effectiveness of continuum-based approaches when applied to systems which call for an atomistic treatment.

The question also remains about how fine the mesh in the drift-diffusion calculations needs to be. In the current setup there is a node for every atom in the active region.

After quantum corrections have been applied, the strong fluctuations initially present in the energy landscape are much reduced, and possibly the full atomistic resolution is not required. The required mesh density may depend on the effective mass of the carriers, and is therefore likely limited by the behaviour of the holes in both (In,Ga)N and (Al,Ga)N systems. The impact that coarse-graining the mesh after quantum corrections have been applied has on transport properties such as current-voltage curves could be investigated. This could enable simulations on larger supercells to further study percolation transport, or permit a quicker simulation of systems which would allow for a more efficient systematic study of device parameters.

In Chapter 7 the impact of an (Al,Ga)N electron blocking layer was discussed. It was touched on that ideally the blocking layer would be treated as a random alloy. This is a feature which could be targeted in future studies using the here established tight-binding to drift-diffusion framework, particularly because (as already mentioned) 1-D simulations fail to accurately described transport properties of these structures. If such a question is being addressed careful attention would have to be paid to treatment of the quantum corrections using localization landscape theory. Localization landscape theory is well suited to describing localized states in a given region, and provides a good description in an energy range close to the energy of the ground state. As a result, localization landscape theory is not necessarily well adapted for a quantum barrier: As the blocking layer is a barrier for electrons, the conduction band edge sits energetically *above* the band edge of the (GaN) material which hosts the quantum wells. As such, the height of the barrier may not be accurately described, and this may be exacerbated by the presence of polarization fields.

In order to investigate this, a 1-D virtual crystal approximation of the barrier without including transport could first be constructed. As this is a numerically accessible problem this could be used to calculate the wave functions using the Schrödinger equation as well as the localization landscape. This would provide a good initial insight into the accuracy of localization landscape theory when applied to such a barrier before advancing to the more complex situation of a 3-D random alloy including self-consistent drift-diffusion and Poisson equations.

Not only could the blocking layer be treated as (Al,Ga)N, the active region could also be composed of these alloys. This allows for the simulation of *p-i-n* diodes which can target UV emission. Unlike the (In,Ga)N/GaN structures investigated in this thesis, the barrier material in these systems is also an alloy, such that the active region is composed of $Al_xGa_{1-x}N/Al_yGa_{1-y}N$. Current work is ongoing on the importance for transport of the alloy microstructure in the barrier and the well regions respectively.

As was discussed in Section 3.4.3, the localization landscape theory is currently applied to a single band Hamiltonian. As the orbital character of the AlN and GaN valence band edge differs (p_z vs $p_{x,y}$) the polarization of the emitted light depends on the

composition of the alloy in the active region. Studies targeting questions around the light polarization in (Al,Ga)N may therefore require multi-band descriptions of the valence band edge. Applying quantum corrections to this description requires further development of the localization landscape theory, and could be the focus of upcoming research as this would be an important element in 3-D models of (Al,Ga)N/(Al,Ga)N systems including quantum corrections. A multi-band localization landscape theory could also be applied directly to the sp^3 tight-binding Hamiltonian solving the equation $\hat{H}^{\mathrm{TB}}|u\rangle = 1$, without the extra step of generating an energy landscape and subsequently a $\mathbf{k}\cdot\mathbf{p}$ Hamiltonian.

We have seen in Chapter 7 that the carrier density in a multi-quantum well system is influenced by the description of the alloy microstructure. To populate a well, the carriers either can tunnel into the well, as we saw in the ballistic transport simulations in Chapter 5, or can be scattered from a different (higher energy) state into the wells. The scattering is considered implicitly in the drift-diffusion framework in the mobilities chosen, however a fully quantum mechanical description of this scattering mechanism was not considered in this thesis. Including scattering in the NEGF formalism could confirm, or provide further insight into, the impact that the alloy microstructure has on the hole distribution across a multi-quantum well structure. Electron-phonon coupling drastically increases the numerical demand of the NEGF formalism further, which would provide a technical challenge for such a study; however it may result in new insight into the behaviour of carriers in (In,Ga)N QW systems.

Overall, the work contained in this thesis has provided new physical insights into III-N based quantum well structures and in order to do this a new framework was developed to connect an atomistic tight-binding model to a multi-scale, quantum corrected, drift-diffusion model. This has also opened up new avenues for a variety of studies. These could be the start point for research projects focusing on either the numerical or physical aspects of the simulation methods.

"But since it falls unto my lot
That I should rise and you should not,
I gently rise and softly call
Good night and joy be to you all."

Excerpt from *The Parting Glass*

Part V

Appendix

Appendix A

Covariance of momentum distribution and its relation to temperature

In Section 4.2.1 we used the result that the integral of $\mathbf{kk}$ was related to the carrier temperature. Here we look at this in a little more detail, though we start with the assumption the average momentum is $\mathbf{0}$ (the same result holds if the average momentum is finite, once you shift your coordinate system so the origin sits at $\overline{\mathbf{k}}$). Here we shall consider a 3-D system, with momentum coordinates (k_x, k_y, k_z). We shall also focus on a single position, $\mathbf{r_0}$ with coordinates (x_0, y_0, z_0), and time t_0. Our distribution function over $\mathbf{k}$-space is therefore $f(\mathbf{k}, \mathbf{r}_0, t_0)$. The elements of the covariance matrix of this function is given by

$$C_{ij}[\mathbf{k}; \mathbf{r}_0, t_0] = \frac{\int_{k_x}\int_{k_y}\int_{k_z} f(\mathbf{k}, \mathbf{r}_0, t_0) k_i k_j \mathrm{d}k_x \mathrm{d}k_y \mathrm{d}k_z}{\int_{k_x}\int_{k_y}\int_{k_z} f(\mathbf{k}, \mathbf{r}_0, t_0) \mathrm{d}k_x \mathrm{d}k_y \mathrm{d}k_z} \ , \tag{A.1}$$

where $i, j \in \{x, y, z\}$. We note the denominator is simply $n(\mathbf{r}_0, t_0)$, so we focus on the numerator of the ij entry of $\mathbf{C}[\mathbf{k}; \mathbf{r}_0, t_0]$, C_{ij}^{NUM}. Here we shall assume that our distribution function, f, is an even function in all k-components around the mean value, $\overline{\mathbf{k}}$ which can be separated into the product of functions of k_x, k_y and k_z,

$$f(\mathbf{k}, \mathbf{r}_0, t_0) = f_x(k_x, \mathbf{r}_0, t_0) \cdot f_y(k_y, \mathbf{r}_0, t_0) \cdot f_z(k_z, \mathbf{r}_0, t_0) \ .$$

Physically here we are assuming that the distribution of momenta is due to the random motion of particles, and there is no tendency to skew the momenta to higher or lower values in any direction, so assuming a distribution function similar to, for example, a Gaussian (as is done in Ref. [192]) seems a reasonable choice to make.

There are only two cases for us to consider, the diagonal entries of C ($i = j$) and the off-

diagonal entries ($i \neq j$). Let us first look at the off-diagonal case, and take the example of $i = x$ and $j = y$. Because of our assumption about f, The numerator of Eq. (A.1) becomes

$$C_{xy}^{\mathrm{NUM}} = \int_{k_x} \overbrace{k_x f_x(k_x, \mathbf{r}_0, t_0)}^{\text{odd function}} \mathrm{d}k_x \cdot \int_{k_y} \overbrace{k_y f_y(k_y, \mathbf{r}_0, t_0)}^{\text{odd function}} \mathrm{d}k_y \cdot \int_{k_z} \overbrace{f_z(k_z, \mathbf{r}_0, t_0)}^{\text{even function}} \mathrm{d}k_z \ .$$

Parity considerations help us out greatly here: k_i is an odd function around $\overline{k_i}$, whereas f_x, f_y and f_z are assumed to be even. Therefore the off-diagonal elements will be zero under these assumptions, as they include the integrals of an odd function over an interval centered on $\overline{\mathbf{k}}$.

Returning now to the diagonal elements, we take C_{xx} as a test case (note here we are looking at the full expression, not just the numerator):

$$C_{xx} = \frac{\int_{k_x} \overbrace{k_x^2 f_x(k_x, \mathbf{r}_0, t_0)}^{\text{even function}} \mathrm{d}k_x \cdot \int_{k_y} \overbrace{f_y(k_y, \mathbf{r}_0, t_0)}^{\text{even function}} \mathrm{d}k_y \cdot \int_{k_z} \overbrace{f_z(k_z, \mathbf{r}_0, t_0)}^{\text{even function}} \mathrm{d}k_z}{\int_{k_x} f_x(k_x, \mathbf{r}_0, t_0)\mathrm{d}k_x \cdot \int_{k_y} f_y(k_y, \mathbf{r}_0, t_0)\mathrm{d}k_y \cdot \int_{k_z} f_z(k_z, \mathbf{r}_0, t_0)\mathrm{d}k_z} \ .$$

As all the integrands are even functions we are going to have a non-zero result. Simplifying this, we see that the C_{xx} entry is the k_x^2 expectation value, which is related to the kinetic energy associated with the random motion around the average k_x value,

$$C_{xx} = \frac{\int_{k_x} k_x^2 f_x(k_x, \mathbf{r}_0, t_0)\mathrm{d}k_x}{\int_{k_x} f_x(k_x, \mathbf{r}_0, t_0)\mathrm{d}k_x} = \overline{k_x^2} \ .$$

If we consider our assumption about f again it is also reasonable to assume that the characteristic width of the distributions is the same in all k-directions, so $\overline{k_x^2} = \overline{k_y^2} = \overline{k_z^2} = \overline{k^2}$. Now the covariance matrix a diagonal matrix which is proportional to the identity:

$$\mathbf{C}[\mathbf{k}; \mathbf{r_0}, t_0] = \overline{k^2}(\mathbf{r}_0, t_0)\mathbb{1}_3$$

where $\overline{k^2}$ is the is the average k-squared value, and therefore related to the the average kinetic energy associated with the random motion, as the kinetic energy is $\frac{\hbar^2 k^2}{2m^*}$.

We associate this random kinetic energy with the average temperature [191]:

$$\frac{1}{2}k_B T = \frac{\hbar^2 \overline{k^2}}{2m^*} \implies T\mathbb{1}_3 = \frac{\hbar^2}{m^* k_B}\mathbf{C}[\mathbf{k}; \mathbf{r}_0, t_0] \ .$$

This is the result used in Eq. (4.28), though here we have only considered the temperature at the lattice site $\mathbf{r}_0$. In general this can vary across the entire device so each lattice site would have it's own associated temperature tensor which is, under the assumptions made here, proportional to the 3×3 identity matrix, $\mathbb{1}_3$. In the main text

we make the assumption that the temperature is also constant across the entire device, so that the full temperature tensor is also proportional to the identity matrix (of dimensions suitable to describe the full device).

Appendix B

NEGF: Alloyed Barrier Material

As discussed in Chapter 5, alloying the barrier material could provide a pathway to enhance the ballistic transport in InGaN MQW systems. To analyze the potential impact of In in the barrier on the transmission spectrum for electrons and holes, we focus in the following on a 2 QW $In_{0.12}Ga_{0.88}N$ system. The system is generated in the Random II setting, where the microscopic configuration between the QWs differs.

We compare an $In_{0.12}Ga_{0.88}N$/GaN system to an $In_{0.12}Ga_{0.88}N$/$In_{0.05}Ga_{0.95}N$ system. The barrier is also treated as a random alloy which differs between each region of $In_{0.05}Ga_{0.95}N$. Here the barrier and the well width are both 2.6 nm. The QW configuration is kept fixed, so only the barrier material is changed for this comparison. We only consider one microscopic configuration in each case, so no averaging is done to obtain the results.

For the sake of simplified discussion, we neglect strain and polarization fields. When alloying the GaN barrier with 5% In, the CBE is shifted downwards from 3.45 eV (pure GaN) to approximately 3.36 eV ($In_{0.05}Ga_{0.95}N$) in the barrier region of the MQW system. Also the VBE of the barrier material changes: for pure GaN barriers, the VBE is chosen to be at 0 eV; in the case of 5% In in the barrier region, the VBE then shifts to approximately 0.03 eV.

Figure B.1 (a) shows the electron transmission spectrum of the system with the pure GaN barrier (black) along with the spectrum obtained for an $In_{0.12}Ga_{0.88}N$/$In_{0.05}Ga_{0.95}N$ MQW structure (blue). With pure GaN barriers, transmission through the electron ground states (transmission peaks around 3 eV) is weak, while in case of the $In_{0.05}Ga_{0.95}N$ barrier, the ground state transmission is strongly enhanced. The effect of enhanced QW ground state transmission is accompanied by a slight red shift of the transmission peaks. We attribute both effects (red shift, enhanced transmission) to changes in carrier confinement in case of the alloyed barrier when compared to the pure GaN system. Similar effects are observed for the excited QW states at approximately 3.2 eV.

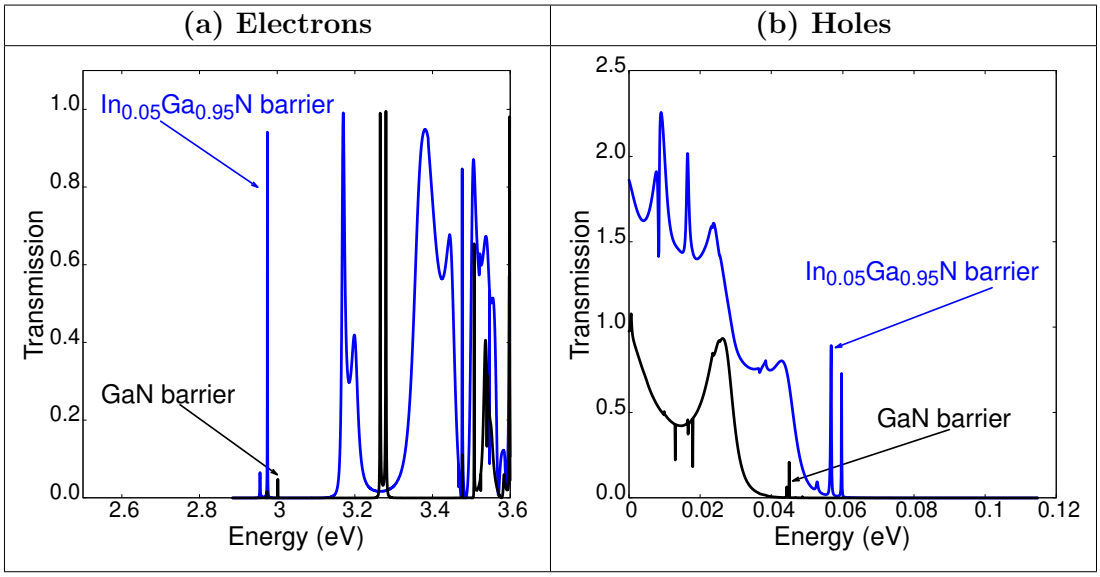

Figure B.1: Transmission spectra of a 2 $In_{0.12}Ga_{0.88}N$ QW system with GaN (black) and $In_{0.05}Ga_{0.95}N$ (blue) barriers for (a) electrons and (b) holes. The microscopic configuration differs between the QWs but is kept the same for the pure GaN and the InGaN barrier. Thus only the barrier material differs between the two systems. Strain and built-in fields are not considered. The barrier and well width are $L_b = L_w = 2.6$ nm.

Figure B.1 (b) depicts the results for the hole transmission. Our calculations show that the $In_{0.05}Ga_{0.95}N$ barrier significantly increase the ballistic hole transport facilitated by QW confined states near energies of 0.06 eV. Also, and in comparison with the pure GaN barriers, transmission in the energy range of 0.03 eV to 0.05 eV is also increased significantly. We attribute this effect again to the reduction in the carrier confinement when comparing pure GaN and $In_{0.05}Ga_{0.95}N$ barriers.

Overall, these initial studies indicate that using InGaN barriers with low In content are beneficial for increasing the ballistic transport in InGaN MQW systems, and thus potentially enabling an improved distribution of carriers between the different QWs in a MQW structure. This finding may explain the experimental observation made in the work by Marcinkevičius *et al.* [224]. To shed further light on the influence of InGaN barriers on the transport properties of InGaN MQWs, future studies may target a variety of different questions. For instance, the question remains if there is a critical barrier In content at which alloy scattering will have a detrimental effect on the ballistic transport. Furthermore, we have followed here the experimental work of Ref. [224] and kept the In content in the well constant while increasing the In content in the barrier. As discussed above, this will reduce the carrier confinement. To disentangle effects arising from alloy fluctuations in the barrier and the barrier height (carrier confinement), investigations may be performed in which the relative band offset difference is kept constant, e.g. comparing transport properties of an $In_{0.12}Ga_{0.88}N$/GaN MQW system to the properties of an $In_{0.17}Ga_{0.05}N/In_{0.05}Ga_{0.95}N$ MQW structure. Such a detailed

and extensive analysis can be targeted in future investigations, which may focus on the impact of alloy fluctuations in the barrier material on the ballistic carrier transport. However, this is beyond of the scope of the present study, where our main aim is to understand the impact of alloy fluctuations within the well on transport properties.

Appendix C

Uni-polar hole transport

C.1 Effective confining potential in MQW structure: Partitioned vs Unpartitioned LLT

In this appendix we provide further insight into the question how the effective confining potential, W, obtained from LLT is modified when partitioning the MQW into subregions, i.e. different "localization" regions. As discussed in Section 3.4.3, the choice of the reference energy E_{ref} for a given localization region can impact the resulting quantum corrected effective landscape. As a test case we use the system discussed in Section 6.2.1.2.1 which exhibits a large potential difference between the QWs (as shown in Fig. 6.9) forming the MQW. For demonstrative purposes we neglect any effects due to the presence of a *p-i-p* junction and we assume a capacitor-like potential profile with a potential drop across each QW of 0.35 V. Figure C.1 reveals the impact that partitioning the MQW into different subregions has on the effective band edge. The starting point is the "standard" VCA description of the system without quantum corrections (purple). Here, each QW exhibits the same VBE profile. Treating the MQW system as a single localization region within LLT, the resulting band edge profile (green) reveals that the band edge of the first QW (leftmost in Fig. C.1) is smoothed significantly. However, the two other wells forming the MQW system, which are energetically far from the global reference energy chosen, undergo noticeably smaller corrections. As discussed in Sec. 6.2.1.2.1, this stems from the fact that the contributions from (localized) states in these QWs contribute only weakly to the series expansion of u (Eq. (3.28)). However, Fig. C.1 also reveals that when the system is partitioned into 3 sub-regions, and each localization region (QW region) is described by an individual reference energy which is close the *local* ground state energy, the resulting effective landscape (red, dashed) is significantly softened in all three wells of the MQW system. In doing so, one assures that quantum corrections in all 3 QWs are properly treated. Figure C.1 also confirms that the landscape is not only smoothed but also continuous between each localization

region, which is important to construct a global effective landscape that can be used for transport calculations.

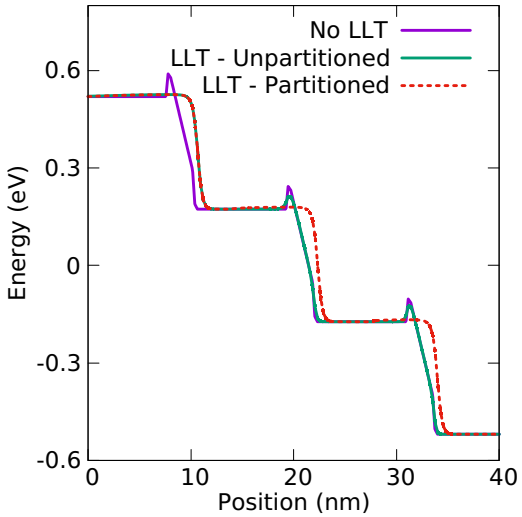

Figure C.1: Valence band edge profile in virtual crystal approximation for a fictive (In,Ga)N/GaN multi-quantum well system in the absence of LLT (purple) and presence of LLT quantum corrections. When including LLT two scenarios are considered (i) using a single reference energy (green) and (ii) separate reference energies for each quantum well region (red, dashed).

C.2 Comparison of impact of distribution function on results

The results presented in Section 6.2.2 rely on the Boltzmann approximation for free carrier density. In this appendix we briefly discuss how and if the results are affected by employing Fermi-Dirac statistics instead of Boltzmann. Overall, we find that in the case of the here studied uni-polar hole transport, the resulting I-V curves are basically unaffected when changing the distribution function from Boltzmann to Fermi-Dirac. This is illustrated in Fig. C.2 (a) for a SQW.

To shed more light onto this finding, we have also investigated how the Fermi-level changes when using Fermi-Dirac instead of Boltzmann. The resulting Fermi-levels (green) for the two distribution functions are depicted in Fig. C.2 (b) (Boltzmann) and Fig. C.2 (c) (Fermi-Dirac). In addition to the Fermi-level, the valence band edge (purple) is also given. The data are plotted at 0.5 V, for a relatively low Gaussian width of $\sigma = 0.2$ nm and when excluding LLT. Comparing the Fig. C.2 (b) (Boltzmann) and Fig. C.2 (c) (Fermi-Dirac), one observes that choosing Fermi-Dirac statistics only very weakly affects the Fermi-level inside the well; in the barrier it is basically unchanged. This explains our finding that both distribution functions give basically the same I-V curve. Above we used a calculation without LLT and a relatively low σ value ($\sigma = 0.2$ nm), so that differences between Boltzmann and Fermi-Dirac will be further

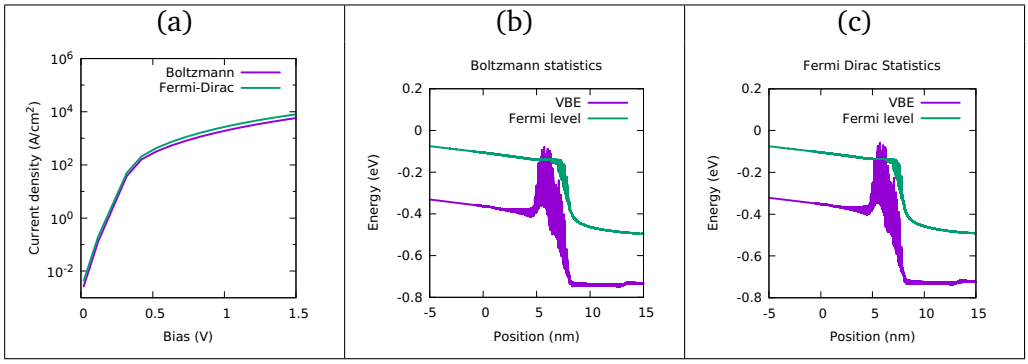

Figure C.2: Impact of distribution function for a random alloy system using a Gaussian width of $\sigma = 0.2$ nm on the I-V curve, the valence band edge and Fermi-level in the (In,Ga)N/GaN SQW described in Section 6.2. Left: I-V curves for Boltzmann system (purple) and Fermi-Dirac system (green). Center: Valence band edge (purple) and Fermi level (green) at 0.5 V using Boltzmann statistics. Right: Valence band edge (purple) and Fermi level (green) at 0.5 V using Fermi-Dirac statistics.

reduced when using a larger broadening (larger σ value) and/or when including LLT in the calculations, since both contributions will result in a smoother energy landscape (not shown).

C.3 Study of the in-plane dimensions on current density

In Sec. 6.2.2.2 we have already highlighted that the results may depend on the in-plane dimension of the simulation cell. Here, we extend this discussion. Figure C.3 depicts the current density for an in-plane slice through the an $In_{0.1}Ga_{0.9}N$ SQW for two different applied voltages, namely 0.5 V (left column) and 3.0 V (right column); for the Gaussian broadening we have used $\sigma = 0.2$ nm. The upper row displays the data in the absence of LLT corrections, while the lower row depicts the results in the presence of LLT corrections.

Looking at the results *without* LLT, one can clearly see that that current density strongly fluctuates within the plane. This means that in *the absence* of quantum corrections via LLT, the simulation cell is large enough to resolve the alloy fluctuations and potentially connected percolation paths. In Section 6.2 we have compared I-V curves without LLT but in the presence of alloy fluctuations to VCA results, obtained also in the absence of LLT. We observed that the turn on voltage/knee voltage for the hole transport is higher and the current is lower in the alloy case when compared to the VCA. Therefore, the observed fluctuations in the current density, and thus potential percolation paths, are *not* beneficial for the hole transport. Given that we resolve the variation in the current density already for the present simulation cell size, one could expect that the observed results will not change dramatically when increasing the in-plane dimension of the simulation cell.

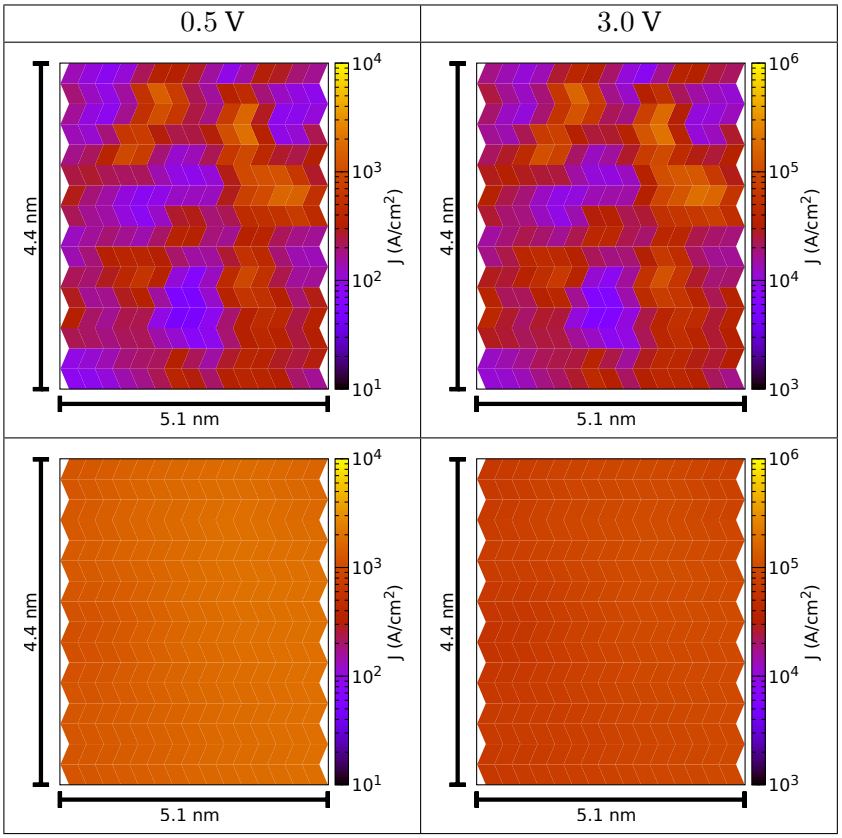

Figure C.3: Current density within a slice of a (In,Ga)N SQW at 0.5 V (left) and 3.0 V (right) using a Gaussian broadening of 0.2 nm without LLT (top) and with LLT (bottom). The total current density is shown using the colour scale on a log scale.

However, when including LLT in the calculations, the alloy fluctuations are "washed out" for the given cell size as the lower row of Fig. C.3 shows. Here, the current density indeed behaves more like the VCA case. But, if the in-plane dimension of the simulation cell is increased, the softening of the energy landscape will be reduced, as the likelihood of regions with locally high/low indium content increases. Thus we can expect to recover an in-plane current density profile with regions of high and low current, similar to the calculation neglecting quantum corrections, but on a larger scale. As a consequence, with increasing simulation cell size and even with LLT, it is expected that one finds a situation more similar to the results in the absence of LLT, thus the upper row in Fig. C.3. Therefore, it is expected that in case of LLT and random alloy fluctuations, the current density decreases with increasing in-plane dimension. As such, our conclusion in the paper that the VCA I-V curve presents an upper limit for the hole transport, should still hold even when increasing the in-plane dimensions of the simulation cell.

Part VI

Bibliography

References

[1] M. O'Donovan, P. Farrell, J. Moatti, T. Streckenbach, T. Koprucki, and S. Schulz, "Impact of random alloy fluctuations on the carrier distribution in multi-color (In,Ga)N/GaN quantum well systems," 2022.

[2] M. O'Donovan, P. Farrell, T. Streckenbach, T. Koprucki, and S. Schulz, "Multi-scale simulations of uni-polar hole transport in (In,Ga)N quantum well systems," *Optical and Quantum Electronics*, vol. 54, p. 405, 2022.

[3] M. O'Donovan, D. Chaudhuri, T. Streckenbach, P. Farrell, S. Schulz, and T. Koprucki, "From atomistic tight-binding theory to macroscale drift–diffusion: Multiscale modeling and numerical simulation of uni-polar charge transport in (In,Ga)N devices with random fluctuations," *Journal of Applied Physics*, vol. 130, no. 6, p. 065702, 2021.

[4] D. Chaudhuri, M. O'Donovan, T. Streckenbach, S. K. P. O. Marquardt, P. Farrell, T. Koprucki, and S. Schulz, "Multiscale simulations of the electronic structure of III-nitride quantum wells with varied indium content: Connecting atomistic and continuum-based models," *J. Appl. Phys.*, vol. 129, p. 073104, 2021.

[5] M. O'Donovan, M. Luisier, E. P. O'Reilly, and S. Schulz, "Impact of random alloy fluctuations on inter-well transport in InGaN/GaN multi-quantum well systems: an atomistic non-equilibrium Green's function study," *J. Phys.: Condens. Matter*, vol. 33, p. 045302, 2021.

[6] H. J. Round, "A note on carborundum," *Electrical World*, no. 49, p. 309, 1907.

[7] H. F. Ivey, "Electroluminescence seen in 1907," *Science*, vol. 164, no. 3886, p. 1342, 1969.

[8] O. Lossev, "CII. Luminous carborundum detector and detection effect and oscillations with crystals," *The London, Edinburgh, and Dublin Philosophical Magazine and Journal of Science*, vol. 6, no. 39, p. 1024, 1928.

[9] D. MacIsaac, G. Kanner, and G. Anderson, "Basic physics of the incandescent lamp (lightbulb)," *The Physics Teacher*, vol. 37, no. 9, p. 520, 1999.

[10] N. Zheludev, "The life and times of the LED — a 100-year history," *Nature Photonics*, vol. 1, 2007.

[11] K. Y. Cheng, *III–V Compound Semiconductors and Devices*. Springer Cham, 2020.

[12] M. Riordan and L. Hoddeson, "The origins of the pn junction," *IEEE Spectrum*, vol. 34, no. 6, p. 46, 1997.

[13] N. W. Ashcroft and N. D. Mermin, *Solid State Physics*. Thomson Learning, 1976.

[14] K. Lehovec, C. A. Accardo, and E. Jamgochian, "Injected Light Emission of Silicon Carbide Crystals," *Phys. Rev.*, vol. 83, p. 603, 1951.

[15] G. L. Harris, *Properties of silicon carbide*. No. 13, Iet, 1995.

[16] F. M. Steranka, "Chapter 3: AlGaAs Red Light-Emitting Diodes," vol. 48 of *Semiconductors and Semimetals*, p. 65, Elsevier, 1997.

[17] K. Katayama, H. Matsubara, F. Nakanishi, T. Nakamura, H. Doi, A. Saegusa, T. Mitsui, T. Matsuoka, M. Irikura, T. Takebe, S. Nishine, and T. Shirakawa, "ZnSe-based white LEDs," *Journal of Crystal Growth*, vol. 214-215, p. 1064, 2000.

[18] Z. I. Alferov, "Nobel Lecture: The double heterostructure concept and its applications in physics, electronics, and technology," *Reviews of modern physics*, vol. 73, no. 3, p. 767, 2001.

[19] O. Shchekin and M. G. Craford, "History of solid-state light sources," in *Handbook of Advanced Lighting Technology*, Springer Cham, 2017.

[20] S. den Uijl and H. J. de Vries, "Pushing technological progress by strategic manoeuvring: the triumph of Blu-ray over HD-DVD," *Business History*, vol. 55, no. 8, p. 1361, 2013.

[21] M. Shur and R. Zukauskas, "Solid-State Lighting: Toward Superior Illumination," *Proceedings of the IEEE*, vol. 93, no. 10, p. 1691, 2005.

[22] J. Wu, W. Walukiewicz, W. Shan, K. M. Yu, J. W. Ager, S. X. Li, E. E. Haller, H. Lu, and W. J. Schaff, "Temperature dependence of the fundamental band gap of InN," *Journal of Applied Physics*, vol. 94, no. 7, p. 4457, 2003.

[23] J. Y. Tsao, S. Chowdhury, M. A. Hollis, D. Jena, N. M. Johnson, K. A. Jones, R. J. Kaplar, S. Rajan, C. G. Van de Walle, E. Bellotti, C. L. Chua, R. Collazo, M. E. Coltrin, J. A. Cooper, K. R. Evans, S. Graham, T. A. Grotjohn, E. R. Heller, M. Higashiwaki, M. S. Islam, P. W. Juodawlkis, M. A. Khan, A. D. Koehler, J. H. Leach, U. K. Mishra, R. J. Nemanich, R. C. N. Pilawa-Podgurski, J. B. Shealy, Z. Sitar, M. J. Tadjer, A. F. Witulski, M. Wraback, and J. A. Simmons, "Ultrawide-

Bandgap Semiconductors: Research Opportunities and Challenges," *Advanced Electronic Materials*, vol. 4, no. 1, p. 1600501, 2018.

[24] I. Vurgaftman and J. R. Meyer, "Band parameters for nitrogen-containing semiconductors," *Journal of Applied Physics*, vol. 94, no. 6, p. 3675, 2003.

[25] I. Vurgaftman, J. R. Meyer, and L. R. Ram-Mohan, "Band parameters for III–V compound semiconductors and their alloys," *Journal of Applied Physics*, vol. 89, no. 11, p. 5815, 2001.

[26] H. Karzel, W. Potzel, M. Köfferlein, W. Schiessl, M. Steiner, U. Hiller, G. M. Kalvius, D. W. Mitchell, T. P. Das, P. Blaha, K. Schwarz, and M. P. Pasternak, "Lattice dynamics and hyperfine interactions in ZnO and ZnSe at high external pressures," *Phys. Rev. B*, vol. 53, p. 11425, 1996.

[27] J. Piprek, *Semiconductor optoelectronic devices: introduction to physics and simulation*. Elsevier, 2013.

[28] S. Nakamura, "Nobel Lecture: Background story of the invention of efficient blue InGaN light emitting diodes," *Rev. Mod. Phys.*, vol. 87, p. 1139, 2015.

[29] C. J. Humphreys, "Solid-State Lighting, The nature of carrier localisation in polar and nonpolar InGaN/GaN quantum wells," *MRS Bulletin*, vol. 33, no. 4, p. 459, 2008.

[30] S. Nakamura, "InGaN/AlGaN blue-light-emitting diodes," *Journal of Vacuum Science & Technology A*, vol. 13, no. 3, p. 705, 1995.

[31] T. Mukai, H. Narimatsu, and S. Nakamura, "Amber InGaN-Based Light-Emitting Diodes Operable at High Ambient Temperatures," *Japanese Journal of Applied Physics*, vol. 37, no. 5A, p. L479, 1998.

[32] J. Park, J. H. Choi, K. Kong, J. H. Han, N. Kim, E. Lee, D. Kim, J. Kim, D. Chung, S. Jun, M. Kim, E. Yoon, J. Shin, and S. Hwang, "Electrically driven mid-submicrometre pixelation of InGaN micro-light-emitting diode displays for augmented-reality glasses," *Nature Photonics*, vol. 15, p. 449, 2021.

[33] Z. Wang, S. Zhu, X. Shan, Z. Yuan, X. Cui, and P. Tian, "Full-color micro-LED display based on a single chip with two types of InGaN/GaN MQWs," *Opt. Lett.*, vol. 46, no. 17, p. 4358, 2021.

[34] X. Ren, Z. Wang, W. E. I. Sha, and W. C. H. Choy, "Exploring the Way To Approach the Efficiency Limit of Perovskite Solar Cells by Drift-Diffusion Model," *ACS Photonics*, vol. 4, no. 4, p. 934, 2017.

[35] W. Tress, K. Leo, and M. Riede, "Optimum mobility, contact properties, and open-circuit voltage of organic solar cells: A drift-diffusion simulation study," *Phys. Rev. B*, vol. 85, p. 155201, 2012.

[36] H. Amano, M. Kito, K. Hiramatsu, and I. Akasaki, "P-type conduction in mg-doped gan treated with low-energy electron beam irradiation (leebi)," *Japanese Journal of Applied Physics*, vol. 28, no. 12A, p. L2112, 1989.

[37] S. Nakamura, T. Mukai, M. S. M. Senoh, and N. I. N. Iwasa, "Thermal annealing effects on p-type mg-doped gan films," *Japanese Journal of Applied Physics*, vol. 31, no. 2B, p. L139, 1992.

[38] "Nobel prize 2014 press release." URL: www.nobelprize.org/prizes/physics/2014/press-release/. Accessed 2022-11-08.

[39] S. Chichibu, T. Azuhata, T. Sota, and S. Nakamura, "Spontaneous emission of localized excitons in ingan single and multiquantum well structures," *Applied Physics Letters*, vol. 69, no. 27, p. 4188, 1996.

[40] D. Watson-Parris, M. J. Godfrey, P. Dawson, R. A. Oliver, M. J. Galtrey, M. J. Kappers, and C. J. Humphreys, "Carrier localization mechanisms in $In_xGa_{1-x}N$/GaN quantum wells," *Phys. Rev. B*, vol. 83, p. 115321, 2011.

[41] S. Schulz, M. A. Caro, C. Coughlan, and E. P. O'Reilly, "Atomistic analysis of the impact of alloy and well-width fluctuations on the electronic and optical properties of InGaN/GaN quantum wells," *Physical Review B*, vol. 91, p. 035439, 2015.

[42] S. F. Chichibu, K. Wada, J. Müllhäuser, O. Brandt, K. H. Ploog, T. Mizutani, A. Setoguchi, R. Nakai, M. Sugiyama, H. Nakanishi, K. Korii, T. Deguchi, T. Sota, and S. Nakamura, "Evidence of localization effects in InGaN single-quantum-well ultraviolet light-emitting diodes," *Applied Physics Letters*, vol. 76, no. 13, p. 1671, 2000.

[43] C. Frankerl, F. Nippert, M. P. Hoffmann, H. Wang, C. Brandl, H.-J. Lugauer, R. Zeisel, A. Hoffmann, and M. J. Davies, "Strongly localized carriers in Al-rich AlGaN/AlN single quantum wells grown on sapphire substrates," *Journal of Applied Physics*, vol. 127, no. 9, p. 095701, 2020.

[44] D. S. P. Tanner, P. Dawson, M. J. Kappers, R. A. Oliver, and S. Schulz, "Polar $(\mathrm{In},\mathrm{Ga})\mathrm{N}/\mathrm{GaN}$ Quantum Wells: Revisiting the Impact of Carrier Localization on the "Green Gap" Problem," *Phys. Rev. Applied*, vol. 13, p. 044068, 2020.

[45] W. Hahn, J.-M. Lentali, P. Polovodov, N. Young, S. Nakamura, J. S. Speck, C. Weisbuch, M. Filoche, Y.-R. Wu, M. Piccardo, F. Maroun, L. Martinelli, Y. Lassailly, and J. Peretti, "Evidence of nanoscale anderson localization induced by intrinsic compositional disorder in ingan/gan quantum wells by scanning tunneling luminescence spectroscopy," *Phys. Rev. B*, vol. 98, p. 045305, 2018.

[46] Y.-H. Cho, G. H. Gainer, A. J. Fischer, J. J. Song, S. Keller, U. K. Mishra, and S. P. DenBaars, ""S-shaped" temperature-dependent emission shift and carrier dy-

namics in InGaN/GaN multiple quantum wells," *Applied Physics Letters*, vol. 73, no. 10, p. 1370, 1998.

[47] F. Wang, Z. Ji, Q. Wang, X. Wang, S. Qu, X. Xu, Y. Lv, and Z. Feng, "Green and blue emissions in phase-separated InGaN quantum wells," *Journal of Applied Physics*, vol. 114, no. 16, p. 163525, 2013.

[48] M. Usman, M. Munsif, U. Mushtaq, A.-R. Anwar, and N. Muhammad, "Green gap in GaN-based light-emitting diodes: in perspective," *Critical Reviews in Solid State and Materials Sciences*, vol. 46, no. 5, p. 450, 2021.

[49] F. C.-P. Massabuau, M. J. Davies, F. Oehler, S. K. Pamenter, E. J. Thrush, M. J. Kappers, A. Kovács, T. Williams, M. A. Hopkins, C. J. Humphreys, P. Dawson, R. E. Dunin-Borkowski, J. Etheridge, D. W. E. Allsopp, and R. A. Oliver, "The impact of trench defects in ingan/gan light emitting diodes and implications for the "green gap" problem," *Applied Physics Letters*, vol. 105, no. 11, p. 112110, 2014.

[50] T. Langer, A. Kruse, F. A. Ketzer, A. Schwiegel, L. Hoffmann, H. Jönen, H. Bremers, U. Rossow, and A. Hangleiter, "Origin of the "green gap": Increasing non-radiative recombination in indium-rich GaInN/GaN quantum well structures," *physica status solidi c*, vol. 8, no. 7, p. 2170, 2011.

[51] J. Piprek, "How to decide between competing efficiency droop models for GaN-based light-emitting diodes," *Applied Physics Letters*, vol. 107, no. 3, p. 031101, 2015.

[52] J.-R. Chen, Y.-C. Wu, S.-C. Ling, T. ko, T.-c. Lu, H.-C. Kuo, Y.-K. Kuo, and S.-C. Wang, "Investigation of wavelength-dependent efficiency droop in InGaN light-emitting diodes," *Applied Physics B*, vol. 98, p. 779, 2010.

[53] E. Kioupakis, P. Rinke, K. T. Delaney, and C. G. Van de Walle, "Indirect Auger recombination as a cause of efficiency droop in nitride light-emitting diodes," *Applied Physics Letters*, vol. 98, no. 16, p. 161107, 2011.

[54] D. S. Meyaard, G.-B. Lin, J. Cho, E. Fred Schubert, H. Shim, S.-H. Han, M.-H. Kim, C. Sone, and Y. Sun Kim, "Identifying the cause of the efficiency droop in gainn light-emitting diodes by correlating the onset of high injection with the onset of the efficiency droop," *Applied Physics Letters*, vol. 102, no. 25, p. 251114, 2013.

[55] A. David and C. Weisbuch, "Excitons in a disordered medium: A numerical study in ingan quantum wells," *Phys. Rev. Research*, vol. 4, p. 043004, 2022.

[56] M. Auf der Maur, A. Pecchia, G. Penazzi, W. Rodrigues, and A. Di Carlo, "Efficiency Drop in Green $\mathrm{InGaN/GaN}$ Light Emitting Diodes: The Role of Random Alloy Fluctuations," *Phys. Rev. Lett.*, vol. 116, p. 027401, 2016.

[57] D. S. P. Tanner, M. A. Caro, E. P. O'Reilly, and S. Schulz, "Random alloy fluctuations and structural inhomogeneities in c-plane $In_xGa_{1-x}N$ quantum wells: theory of ground and excited electron and hole states," *RSC Adv.*, vol. 6, p. 64513, 2016.

[58] C. M. Jones, C.-H. Teng, Q. Yan, P.-C. Ku, and E. Kioupakis, "Impact of carrier localization on recombination in InGaN quantum wells and the efficiency of nitride light-emitting diodes: Insights from theory and numerical simulations," *Applied Physics Letters*, vol. 111, no. 11, p. 113501, 2017.

[59] N. Roccato, F. Piva, C. D. Santi, R. Brescancin, K. Mukherjee, M. Buffolo, C. Haller, J.-F. Carlin, N. Grandjean, M. Vallone, A. Tibaldi, F. Bertazzi, M. Goano, G. Verzellesi, G. Meneghesso, E. Zanoni, and M. Meneghini, "Modeling the electrical characteristics of InGaN/GaN LED structures based on experimentally-measured defect characteristics," *Journal of Physics D: Applied Physics*, vol. 54, no. 42, p. 425105, 2021.

[60] D. S. Sizov, R. Bhat, A. Zakharian, K. Song, D. E. Allen, S. Coleman, and C. Zah, "Carrier Transport in InGaN MQWs of Aquamarine- and Green-Laser Diodes," *IEEE Journal of Selected Topics in Quantum Electronics*, vol. 17, no. 5, p. 1390, 2011.

[61] C. S. Xia, Z. M. Simon Li, Y. Sheng, L. W. Cheng, W. D. Hu, and W. Lu, "Simulation of InGaN/GaN light-emitting diodes with a non-local quantum well transport model," *Optical and Quantum Electronics*, vol. 45, p. 597, 2013.

[62] Y.-K. Kuo, J.-Y. Chang, M.-C. Tsai, and S.-H. Yen, "Advantages of blue InGaN multiple-quantum well light-emitting diodes with InGaN barriers," *Applied Physics Letters*, vol. 95, no. 1, p. 011116, 2009.

[63] C. H. Wang, S. P. Chang, P. H. Ku, J. C. Li, Y. P. Lan, C. C. Lin, H. C. Yang, H. C. Kuo, T. C. Lu, S. C. Wang, and C. Y. Chang, "Hole transport improvement in InGaN/GaN light-emitting diodes by graded-composition multiple quantum barriers," *Applied Physics Letters*, vol. 99, no. 17, p. 171106, 2011.

[64] P. McBride, Q. Yan, and C. Van de Walle, "Effects of In profile on simulations of InGaN/GaN multi-quantum-well light-emitting diodes," *Applied Physics Letters*, vol. 105, p. 083507, 2014.

[65] Y. C. Chow, C. Lynsky, F. Wu, S. Nakamura, S. P. DenBaars, C. Weisbuch, and J. S. Speck, "Reduction of efficiency droop in c-plane InGaN/GaN light-emitting diodes using a thick single quantum well with doped barriers," *Applied Physics Letters*, vol. 119, no. 22, p. 221102, 2021.

[66] C. Sheng Xia, Z. M. Simon Li, W. Lu, Z. Hua Zhang, Y. Sheng, and L. Wen Cheng, "Droop improvement in blue InGaN/GaN multiple quantum well light-emitting

diodes with indium graded last barrier," *Applied Physics Letters*, vol. 99, no. 23, p. 233501, 2011.

[67] C.-K. Li, M. Piccardo, L.-S. Lu, S. Mayboroda, L. Martinelli, J. Peretti, J. Speck, C. Weisbuch, M. Filoche, and Y.-R. Wu, "Localization landscape theory of disorder in semiconductors. III. Application to carrier transport and recombination in light emitting diodes," *Physical Review B*, vol. 95, p. 144206, 2017.

[68] F. Römer, M. Guttmann, T. Wernicke, M. Kneissl, and B. Witzigmann, "Effect of Inhomogeneous Broadening in Ultraviolet III-Nitride Light-Emitting Diodes," *Materials*, vol. 14, no. 24, 2021.

[69] F. Römer and B. Witzigmann, "Luminescence distribution in the multi-quantum well region of III-nitride light emitting diodes," in *Light-Emitting Diodes: Materials, Devices, and Applications for Solid State Lighting XXI* (J. K. Kim, M. R. Krames, L.-W. Tu, and M. Strassburg, eds.), vol. 10124, p. 101240Y, International Society for Optics and Photonics, SPIE, 2017.

[70] T.-J. Yang, R. Shivaraman, J. S. Speck, and Y.-R. Wu, "The influence of random indium alloy fluctuations in indium gallium nitride quantum wells on the device behavior," *Journal of Applied Physics*, vol. 116, no. 11, p. 113104, 2014.

[71] Q.-H. Pham, J.-C. Chen, and H.-B. Nguyen, "Three-Dimensional Numerical Study on the Efficiency Droop in InGaN/GaN Light-Emitting Diodes," *IEEE Photonics Journal*, vol. 11, no. 1, p. 1, 2019.

[72] M. Brozel, "Gallium Arsenide," in *Springer Handbook of Electronic and Photonic Materials* (S. Kasap and P. Capper, eds.), ch. 23, p. 499, Springer US, 2007.

[73] J. S. Galsin, "Chapter 1 - Crystal Structure of Solids," in *Solid State Physics* (J. S. Galsin, ed.), p. 1, Academic Press, 2019.

[74] S. Schulz, *Electronic and Optical Properties of Quantum Dots: A Tight-Binding Approach*. PhD thesis, University of Bremen, 2007.

[75] A. Kobayashi, O. F. Sankey, S. M. Volz, and J. D. Dow, "Semiempirical tight-binding band structures of wurtzite semiconductors: AlN, CdS, CdSe, ZnS, and ZnO," *Phys. Rev. B*, vol. 28, p. 935, 1983.

[76] T. Hanada, "Basic Properties of ZnO, GaN, and Related Materials," in *Oxide and Nitride Semiconductors* (T. Yao and S.-K. Hong, eds.), vol. 12, ch. 1, p. 1, Springer Berlin, Heidelberg., 1 ed., 2009.

[77] F. Tang, T. Zhu, F. Oehler, W. Y. Fu, J. T. Griffiths, F. C.-P. Massabuau, M. J. Kappers, T. L. Martin, P. A. J. Bagot, M. P. Moody, and R. A. Oliver, "Indium clustering in a-plane InGaN quantum wells as evidenced by atom probe tomography," *Applied Physics Letters*, vol. 106, no. 7, p. 072104, 2015.

[78] F. Wu, Y.-D. Lin, A. Chakraborty, H. Ohta, S. P. DenBaars, S. Nakamura, and J. S. Speck, "Stacking fault formation in the long wavelength InGaN/GaN multiple quantum wells grown on m-plane GaN," *Applied Physics Letters*, vol. 96, no. 23, p. 231912, 2010.

[79] Y. Zhao, Q. Yan, C.-Y. Huang, S.-C. Huang, P. Shan Hsu, S. Tanaka, C.-C. Pan, Y. Kawaguchi, K. Fujito, C. G. Van de Walle, J. S. Speck, S. P. DenBaars, S. Nakamura, and D. Feezell, "Indium incorporation and emission properties of nonpolar and semipolar InGaN quantum wells," *Applied Physics Letters*, vol. 100, no. 20, p. 201108, 2012.

[80] M. Ueno, M. Yoshida, A. Onodera, O. Shimomura, and K. Takemura, "Stability of the wurtzite-type structure under high pressure: GaN and InN," *Phys. Rev. B*, vol. 49, p. 14, Jan 1994.

[81] P. Phillips, *Advanced Solid State Physics*. Cambridge University Press, 2 ed., 2012.

[82] M. Born and R. Oppenheimer, "Zur Quantentheorie der Molekeln," *Annalen der Physik*, vol. 389, no. 20, p. 457, 1927.

[83] S. M. Girvin and K. Yang, *Modern Condensed Matter Physics*. Cambridge University Press, 1 ed., 2019.

[84] F. Bloch, "Über die Quantenmechanik der Elektronen in Kristallgittern," *Z. Physik*, vol. 52, p. 555, 1929.

[85] S. Schulz and E. P. O'Reilly, "Electronic Band Structure," in *Handbook of Optoelectronic Device Modeling and Simulation* (J. Piprek, ed.), vol. 1, ch. 1, p. 3, CRC Press, 2017.

[86] P. G. Moses and C. G. Van de Walle, "Band bowing and band alignment in InGaN alloys," *Applied Physics Letters*, vol. 96, no. 2, p. 021908, 2010.

[87] M. Asif Khan, J. N. Kuznia, D. T. Olson, T. George, and W. T. Pike, "GaN/AlN digital alloy short-period superlattices by switched atomic layer metalorganic chemical vapor deposition," *Applied Physics Letters*, vol. 63, no. 25, p. 3470, 1993.

[88] W. Sun, C.-K. Tan, and N. Tansu, "III-Nitride Digital Alloy: Electronics and Optoelectronics Properties of the InN/GaN Ultra-Short Period Superlattice Nanostructures ," *Scientific Reports*, vol. 7, 2017.

[89] A. Bonfiglio, M. Lomascolo, G. Traetta, R. Cingolani, A. Di Carlo, F. Della Sala, P. Lugli, A. Botchkarev, and H. Morkoc, "Well-width dependence of the ground level emission of GaN/AlGaN quantum wells," *Journal of Applied Physics*, vol. 87, no. 5, p. 2289, 2000.

[90] C. Weisbuch, "Review—on the search for efficient solid state light emitters: Past, present, future," *ECS Journal of Solid State Science and Technology*, vol. 9, no. 1, p. 016022, 2020.

[91] D. S. P. Tanner, *A study of the elastic and electronic properties of III-nitride semiconductors*. PhD thesis, University College Cork, 2017.

[92] Q. Yan, P. Rinke, A. Janotti, M. Scheffler, and C. G. Van de Walle, "Effects of strain on the band structure of group-III nitrides," *Phys. Rev. B*, vol. 90, p. 125118, 2014.

[93] C. E. Dreyer, A. Janotti, and C. G. Van de Walle, "Effects of strain on the electron effective mass in GaN and AlN," *Applied Physics Letters*, vol. 102, no. 14, p. 142105, 2013.

[94] V. Fiorentini, F. Bernardini, F. Della Sala, A. Di Carlo, and P. Lugli, "Effects of macroscopic polarization in III-V nitride multiple quantum wells," *Phys. Rev. B*, vol. 60, p. 8849, 1999.

[95] A. Schliwa, G. Hönig, and D. Bimberg, "Electronic Properties of III-V Quantum Dots," in *Multi-Band Effective Mass Approximations: Advanced Mathematical Models and Numerical Techniques* (M. Ehrhardt and T. Koprucki, eds.), p. 57, Cham: Springer International Publishing, 2014.

[96] M. A. Caro, S. Schulz, and E. P. O'Reilly, "Theory of local electric polarization and its relation to internal strain: Impact on the polarization potential and electronic properties of group-III nitrides," *Physical Review B*, vol. 88, p. 214103, 2013.

[97] S. K. Patra and S. Schulz, "Electrostatic built-in fields in wurtzite III-N nanostructures: Impact of growth plane on second-order piezoelectricity," *Phys. Rev. B*, vol. 96, p. 155307, 2017.

[98] D. J. Griffiths, *Introduction to electrodynamics*. Prentice Hall, 3 ed., 1999.

[99] J.-H. Ryou, P. D. Yoder, J. Liu, Z. Lochner, H. Kim, S. Choi, H. J. Kim, and R. D. Dupuis, "Control of Quantum-Confined Stark Effect in InGaN-Based Quantum Wells," *IEEE Journal of Selected Topics in Quantum Electronics*, vol. 15, no. 4, p. 1080, 2009.

[100] S. M. Sze and K. K. Ng, *Physics of Semiconductor Devices*. Wiley, 3rd ed., 2006. ISBN: 978-0-471-14323-9.

[101] M. T. Thompson, "Review of Diode Physics and the Ideal (and Later, Nonideal) Diode," in *Intuitive Analog Circuit Design (Second Edition)* (M. T. Thompson, ed.), ch. 3, p. 53, Boston: Newnes, second edition ed., 2014.

[102] E. F. Schubert, *Light-Emitting Diodes*. Cambridge University Press, 2 ed., 2006.

[103] P. Farrell, N. Rotundo, D. H. Doan, M. Kantner, J. Fuhrmann, and T. Koprucki, "Mathematical Methods: Drift-Diffusion Models," in *Handbook of Optoelectronic Device Modeling and Simulation* (J. Piprek, ed.), vol. 2, ch. 50, p. 733, CRC Press, 2017.

[104] D. S. Sholl and J. A. Steckel, *Density Functional Theory*. John Wiley & Sons, Ltd, 2009.

[105] D. Bagayoko, "Understanding density functional theory (DFT) and completing it in practice," *AIP Advances*, vol. 4, no. 12, p. 127104, 2014.

[106] P. P. Ingole, G. B. Markad, D. Saraf, L. Tatikondewar, O. Nene, A. Kshirsagar, and S. K. Haram, "Band Gap Bowing at Nanoscale: Investigation of CdSxSe1–x Alloy Quantum Dots through Cyclic Voltammetry and Density Functional Theory," *The Journal of Physical Chemistry C*, vol. 117, no. 14, p. 7376, 2013.

[107] A. Puzder, A. J. Williamson, F. m. c. Gygi, and G. Galli, "Self-Healing of CdSe Nanocrystals: First-Principles Calculations," *Phys. Rev. Lett.*, vol. 92, p. 217401, 2004.

[108] W. Kohn and L. J. Sham, "Self-consistent equations including exchange and correlation effects," *Phys. Rev.*, vol. 140, p. A1133, 1965.

[109] A. Afzalian, E. Akhoundi, G. Gaddemane, R. Duflou, and M. Houssa, "Advanced DFT–NEGF Transport Techniques for Novel 2-D Material and Device Exploration Including HfS 2/WSe 2 van der Waals Heterojunction TFET and WTe 2/WS 2 Metal/Semiconductor Contact," *IEEE Transactions on Electron Devices*, vol. 68, no. 11, p. 5372, 2021.

[110] M. Kaur, R. S. Sawhney, and D. Engles, "Proliferating miller indices of C20 fullerene device under DFT-NEGF regime," *Journal of Molecular Graphics and Modelling*, vol. 71, p. 184, 2017.

[111] J. Maassen, M. Harb, V. Michaud-Rioux, Y. Zhu, and H. Guo, "Quantum Transport Modeling From First Principles," *Proceedings of the IEEE*, vol. 101, no. 2, p. 518, 2013.

[112] E. O. Kane, "Chapter 3 the k•p method," in *Semiconductors and Semimetals* (R. Willardson and A. C. Beer, eds.), vol. 1 of *Semiconductors and Semimetals*, p. 75, Elsevier, 1966.

[113] G. Bester and A. Zunger, "Cylindrically shaped zinc-blende semiconductor quantum dots do not have cylindrical symmetry: Atomistic symmetry, atomic relaxation, and piezoelectric effects," *Phys. Rev. B*, vol. 71, p. 045318, 2005.

[114] S. L. Chuang and C. S. Chang, "k·p method for strained wurtzite semiconductors," *Phys. Rev. B*, vol. 54, p. 2491, 1996.

[115] F. M. Fernández, *Perturbation theory in quantum mechanics*. CRC Press, 2001.

[116] D. J. Dugdale, S. Brand, and R. A. Abram, "Direct calculation of $\mathbf{k} \cdot \mathbf{p}$ parameters for wurtzite AlN, GaN, and InN," *Phys. Rev. B*, vol. 61, p. 12933, 2000.

[117] P. Löwdin, "A Note on the Quantum Mechanical Perturbation Theory," *Journal of Chemical Physics*, vol. 19, no. 11, p. 1396, 1951.

[118] S. L. Chuang, *Physics of optoelectronic devices*. John Wiley and Sons, 1 ed., 1995.

[119] E. Dimakis, U. Jahn, M. Ramsteiner, A. Tahraoui, J. Grandal, X. Kong, O. Marquardt, A. Trampert, H. Riechert, and L. Geelhaar, "Coaxial Multishell (In,Ga)As/GaAs Nanowires for Near-Infrared Emission on Si Substrates," *Nano Letters*, vol. 14, no. 5, p. 2604, 2014. PMID: 24678901.

[120] J. C. Slater and G. F. Koster, "Simplified LCAO method for the periodic potential problem," *Physical Review*, vol. 94, no. 6, p. 1498, 1954.

[121] D. J. Chadi and M. L. Cohen, "Tight-binding calculations of the valence bands of diamond and zincblende crystals," *physica status solidi (b)*, vol. 68, no. 1, p. 405, 1975.

[122] S. Schulz, S. Schumacher, and G. Czycholl, "Tight-binding model for semiconductor quantum dots with a wurtzite crystal structure: From one-particle properties to Coulomb correlations and optical spectra," *Phys. Rev. B*, vol. 73, p. 245327, 2006.

[123] M. Luisier, A. Schenk, W. Fichtner, and G. Klimeck, "Atomistic simulation of nanowires in the $sp^3d^5s^*$ tight-binding formalism: From boundary conditions to strain calculations," *Physical Review B*, vol. 74, p. 205323, 2006.

[124] D. W. Jenkins and J. D. Dow, "Electronic structures and doping of InN, $\mathrm{In_xGa_{1-x}N}$, and $\mathrm{In_xAl_{1-x}N}$," *Phys. Rev. B*, vol. 39, p. 3317, 1989.

[125] T. Yang, S. Nakajima, and S. Sakai, "Electronic structures of wurtzite GaN, InN and their alloy $ga_{1-x}in_xn$ calculated by the tight-binding method," *Japanese Journal of Applied Physics*, vol. 34, no. Part 1, No. 11, p. 5912, 1995.

[126] E. Abate and M. Asdente, "Tight-Binding Calculation of $3d$ Bands of Fe with and without Spin-Orbit Coupling," *Phys. Rev.*, vol. 140, p. A1303, 1965.

[127] P. Löwdin, "On the Non-Orthogonality Problem Connected with the Use of Atomic Wave Functions in the Theory of Molecules and Crystals," *The Journal of Chemical Physics*, vol. 18, no. 3, p. 365, 1950.

[128] W. M. C. Foulkes and R. Haydock, "Tight-binding models and density-functional theory," *Phys. Rev. B*, vol. 39, p. 12520, 1989.

[129] D. Porezag, T. Frauenheim, T. Köhler, G. Seifert, and R. Kaschner, "Construction of tight-binding-like potentials on the basis of density-functional theory: Application to carbon," *Phys. Rev. B*, vol. 51, p. 12947, 1995.

[130] G. Seifert, "Tight-Binding Density Functional Theory: An Approximate Kohn–Sham DFT Scheme," *The Journal of Physical Chemistry A*, vol. 111, p. 5609, 2007.

[131] J.-M. Jancu, R. Scholz, F. Beltram, and F. Bassani, "Empirical spds^* tight-binding calculation for cubic semiconductors: General method and material parameters," *Phys. Rev. B*, vol. 57, p. 6493, 1998.

[132] P. Vogl, H. P. Hjalmarson, and J. D. Dow, "A semi-empirical tight-binding theory of the electronic structure of semiconductors," *Journal of Physics and Chemistry of Solids*, vol. 44, no. 5, p. 36, 1983.

[133] E. P. O. Reilly, A. Lindsay, S. Tomi, and M. Kamal-Saadi, "Tight-binding and k·p models for the electronic structure of Ga(In)NAs and related alloys," *Semiconductor Science and Technology*, vol. 17, no. 8, p. 870, 2002.

[134] Z. Q. Li and W. Pötz, "Electronic density of states of semiconductor alloys from lattice-mismatched isovalent binary constituents," *Phys. Rev. B*, vol. 46, p. 2109, 1992.

[135] T. B. Boykin, N. Kharche, G. Klimeck, and M. Korkusinski, "Approximate bandstructures of semiconductor alloys from tight-binding supercell calculations," *Journal of Physics: Condensed Matter*, vol. 19, no. 3, p. 036203, 2007.

[136] J. Wu, W. Walukiewicz, K. M. Yu, J. W. Ager, E. E. Haller, H. Lu, and W. J. Schaff, "Small band gap bowing in $In_{1-x}Ga_xN$ alloys," *Applied Physics Letters*, vol. 80, no. 25, p. 4741, 2002.

[137] M. Feneberg, R. A. R. Leute, B. Neuschl, K. Thonke, and M. Bickermann, "High-excitation and high-resolution photoluminescence spectra of bulk AlN," *Phys. Rev. B*, vol. 82, p. 075208, 2010.

[138] M. A. Caro, S. Schulz, S. B. Healy, and E. P. O'Reilly, "Built-in field control in alloyed c-plane III-N quantum dots and wells," *J. Appl. Phys.*, vol. 109, p. 084110, 2011.

[139] M. Povolotskyi, M. Auf der Maur, and A. Di Carlo, "Strain effects in freestanding three-dimensional nitride nanostructures," *physica status solidi (c)*, vol. 2, no. 11, p. 3891, 2005.

[140] F. H. Stillinger and T. A. Weber, "Computer simulation of local order in condensed phases of silicon," *Phys. Rev. B*, vol. 31, p. 5262, 1985.

[141] J. E. Jones and S. Chapman, "On the determination of molecular fields.—I. From the variation of the viscosity of a gas with temperature," *Proceedings of the Royal Society of London. Series A, Containing Papers of a Mathematical and Physical Character*, vol. 106, no. 738, p. 441, 1924.

[142] M. J. P. Musgrave and J. A. Pople, "A general valence force field for diamond," *Proceedings of the Royal Society of London. Series A. Mathematical and Physical Sciences*, vol. 268, no. 1335, p. 474, 1962.

[143] P. N. Keating, "Effect of invariance requirements on the elastic strain energy of crystals with application to the diamond structure," *Phys. Rev.*, vol. 145, p. 637, 1966.

[144] T. Takayama, M. Yuri, K. Itoh, and J. S. Harris, "Theoretical predictions of unstable two-phase regions in wurtzite group-III-nitride-based ternary and quaternary material systems using modified valence force field model," *Journal of Applied Physics*, vol. 90, no. 5, p. 2358, 2001.

[145] O. Landré, D. Camacho, C. Bougerol, Y. M. Niquet, V. Favre-Nicolin, G. Renaud, H. Renevier, and B. Daudin, "Elastic strain relaxation in GaN/AlN nanowire superlattice," *Phys. Rev. B*, vol. 81, p. 153306, 2010.

[146] D. S. P. Tanner, M. A. Caro, S. Schulz, and E. P. O'Reilly, "Fully analytic valence force field model for the elastic and inner elastic properties of diamond and zincblende crystals," *Phys. Rev. B*, vol. 100, p. 094112, 2019.

[147] R. M. Martin, "Elastic properties of ZnS structure semiconductors," *Phys. Rev. B*, vol. 1, p. 4005, 1970.

[148] M. A. Caro, S. Schulz, and E. P. O'Reilly, "Hybrid functional study of the elastic and structural properties of wurtzite and zinc-blende group-III nitrides," *Phys. Rev. B*, vol. 86, p. 014117, 2012.

[149] A. P. Thompson, H. M. Aktulga, R. Berger, D. S. Bolintineanu, W. M. Brown, P. S. Crozier, P. J. in 't Veld, A. Kohlmeyer, S. G. Moore, T. D. Nguyen, R. Shan, M. J. Stevens, J. Tranchida, C. Trott, and S. J. Plimpton, "LAMMPS - a flexible simulation tool for particle-based materials modeling at the atomic, meso, and continuum scales," *Comp. Phys. Comm.*, vol. 271, p. 108171, 2022.

[150] C. Pryor, J. Kim, L. W. Wang, A. J. Williamson, and A. Zunger, "Comparison of two methods for describing the strain profiles in quantum dots," *Journal of Applied Physics*, vol. 83, no. 5, p. 2548, 1998.

[151] R. Benchamekh, S. Schulz, and E. P. O'Reilly, "Theoretical analysis of influence of random alloy fluctuations on the optoelectronic properties of site-controlled (111)-oriented ingaas/gaas quantum dots," *Phys. Rev. B*, vol. 94, p. 125308, 2016.

[152] Y. M. Niquet, D. Rideau, C. Tavernier, H. Jaouen, and X. Blase, "Onsite matrix elements of the tight-binding Hamiltonian of a strained crystal: Application to silicon, germanium, and their alloys," *Phys. Rev. B*, vol. 79, p. 245201, 2009.

[153] T. B. Boykin, G. Klimeck, R. C. Bowen, and F. Oyafuso, "Diagonal parameter shifts due to nearest-neighbor displacements in empirical tight-binding theory," *Phys. Rev. B*, vol. 66, p. 125207, 2002.

[154] M. Winkelnkemper, A. Schliwa, and D. Bimberg, "Interrelation of structural and electronic properties in $\mathrm{In}_x\mathrm{Ga}_{1-x}\mathrm{N}/\mathrm{GaN}$ quantum dots using an eight-band $\mathbf{k}\bullet\mathbf{p}$ model," *Phys. Rev. B*, vol. 74, p. 155322, 2006.

[155] Q. Yan, P. Rinke, M. Scheffler, and C. G. Van de Walle, "Strain effects in group-III nitrides: Deformation potentials for AlN, GaN, and InN," *Applied Physics Letters*, vol. 95, no. 12, p. 121111, 2009.

[156] M. A. C. Bayo, *Theory of elasticity and electric polarization effects in the group-III nitrides*. PhD thesis, University College Cork, 2013.

[157] M. Filoche and S. Mayboroda, "Universal mechanism for Anderson and weak localization," *Proceedings of the National Academy of Sciences*, vol. 109, no. 37, p. 14761, 2012.

[158] M. Filoche, M. Piccardo, Y.-R. Wu, C.-K. Li, C. Weisbuch, and S. Mayboroda, "Localization landscape theory of disorder in semiconductors. I. Theory and modeling," *Phys. Rev. B*, vol. 95, p. 144204, 2017.

[159] M. Piccardo, C.-K. Li, Y.-R. Wu, J. S. Speck, B. Bonef, R. M. Farrell, M. Filoche, L. Martinelli, J. Peretti, and C. Weisbuch, "Localization landscape theory of disorder in semiconductors. II. Urbach tails of disordered quantum well layers," *Phys. Rev. B*, vol. 95, p. 144205, 2017.

[160] E. N. Economou, *Green's functions in Quantum Physics*. Springer, Berlin, Heidelberg, 3 ed., 2006.

[161] B. N. Datta, "Chapter 2 - A review of some basic concepts and results from theoretical linear algebra," in *Numerical Methods for Linear Control Systems* (B. N. Datta, ed.), p. 19, San Diego: Academic Press, 2004.

[162] N. Aronszajn and K. T. Smith, "Characterization of Positive Reproducing Kernels. Applications to Green's Functions," *American Journal of Mathematics*, vol. 79, no. 3, p. 611, 1957.

[163] D. Chaudhuri, J. C. Kelleher, M. R. O'Brien, E. P. O'Reilly, and S. Schulz, "Electronic structure of semiconductor nanostructures: A modified localization landscape theory," *Phys. Rev. B*, vol. 101, p. 035430, 2020.

[164] J.-P. Banon, P. Pelletier, C. Weisbuch, S. Mayboroda, and M. Filoche, "Wigner-Weyl description of light absorption in disordered semiconductor alloys using the localization landscape theory," *Phys. Rev. B*, vol. 105, p. 125422, 2022.

[165] W. Wang and S. Zhang, "The exponential decay of eigenfunctions for tight-binding Hamiltonians via landscape and dual landscape functions," *Annales Henri Poincaré*, vol. 22, p. 1429, 2021.

[166] D. Arnold, M. Filoche, S. Mayboroda, W. Wang, and S. Zhang, "The Landscape Law for Tight Binding Hamiltonians," *Communications in Mathematical Physics*, 2022.

[167] P. Rinke, M. Winkelnkemper, A. Qteish, D. Bimberg, J. Neugebauer, and M. Scheffler, "Consistent set of band parameters for the group-III nitrides AlN, GaN, and InN," *Phys. Rev. B*, vol. 77, p. 075202, 2008.

[168] J.-M. Jancu, F. Bassani, F. D. Sala, and R. Scholz, "Transferable tight-binding parametrization for the group-III nitrides," *Applied Physics Letters*, vol. 81, no. 25, p. 4838, 2002.

[169] S. Schulz, M. A. Caro, L.-T. Tan, P. J. Parbrook, R. W. Martin, and E. P. O'Reilly, "Composition-Dependent Band Gap and Band-Edge Bowing in AlInN: A Combined Theoretical and Experimental Study," *Applied Physics Express*, vol. 6, no. 12, p. 121001, 2013.

[170] J. E. Northrup, C. L. Chua, Z. Yang, T. Wunderer, M. Kneissl, N. M. Johnson, and T. Kolbe, "Effect of strain and barrier composition on the polarization of light emission from AlGaN/AlN quantum wells," *Applied Physics Letters*, vol. 100, no. 2, p. 021101, 2012.

[171] J. Schwinger, "Brownian Motion of a Quantum Oscillator," *Journal of Mathematical Physics*, vol. 2, no. 3, p. 407, 1961.

[172] S. Fujita, "Partial self-energy parts of Kadanoff-Baym," *Physica*, vol. 30, no. 4, p. 848, 1964.

[173] L. V. Keldysh *et al.*, "Diagram technique for nonequilibrium processes," *Sov. Phys. JETP*, vol. 20, no. 4, p. 1018, 1965.

[174] S. Datta, *Lessons from Nanoelectronics*. World Scientific, 2nd ed., 2018.

[175] S. Datta, *Electronic Transport in Mesoscopic Systems*. Cambridge University Press, 1997.

[176] M. L. Sancho, J. L. Sancho, J. L. Sancho, and J. Rubio, "Highly convergent schemes for the calculation of bulk and surface Green functions," *Journal of Physics F: Metal Physics*, vol. 15, no. 4, p. 851, 1985.

[177] R. Venugopal, M. Paulsson, S. Goasguen, S. Datta, and M. S. Lundstrom, "A simple quantum mechanical treatment of scattering in nanoscale transistors," *Journal of Applied Physics*, vol. 93, no. 9, p. 5613, 2003.

[178] W. Lee, N. Jean, and S. Sanvito, "Exploring the limits of the self-consistent Born approximation for inelastic electronic transport," *Phys. Rev. B*, vol. 79, p. 085120, 2009.

[179] M. Luisier and G. Klimeck, "Atomistic full-band simulations of silicon nanowire transistors: Effects of electron-phonon scattering," *Phys. Rev. B*, vol. 80, p. 155430, 2009.

[180] S. Souma and M. Ogawa, "Impact of electron–phonon scattering on the strain-induced current-blocking effect in graphene field-effect transistors," *Journal of Applied Physics*, vol. 127, no. 9, p. 094304, 2020.

[181] R. Lake, G. Klimeck, R. C. Bowen, and D. Jovanovic, "Single and multiband modeling of quantum electron transport through layered semiconductor devices," *Journal of Applied Physics*, vol. 81, no. 12, p. 7845, 1997.

[182] M. A. der Maur, "Multiscale approaches for the simulation of InGaN/GaN LEDs," *Journal of Computational Electronics*, vol. 14, p. 398, 2015.

[183] A. Martinez, M. Aldegunde, N. Seoane, A. R. Brown, J. R. Barker, and A. Asenov, "Quantum-transport study on the impact of channel length and cross sections on variability induced by random discrete dopants in narrow gate-all-around silicon nanowire transistors," *IEEE Transactions on Electron Devices*, vol. 58, no. 8, p. 2209, 2011.

[184] R. Bertoncini, A. M. Kriman, and D. K. Ferry, "Airy-coordinate technique for nonequilibrium Green's-function approach to high-field quantum transport," *Phys. Rev. B*, vol. 41, p. 1390, 1990.

[185] A. Shedbalkar and B. Witzigmann, "Non equilibrium Green's function quantum transport for green multi-quantum well nitride light emitting diodes," *Optical and Quantum Electronics*, vol. 50, no. 67, 2018.

[186] F. Roemer and B. Witzigmann, "Signature of the ideality factor in III-nitride multi quantum well light emitting diodes," *Optical and Quantum Electronics*, vol. 50, no. 11, p. 1, 2018.

[187] D. Jiménez, "Drift-diffusion model for single layer transition metal dichalcogenide field-effect transistors," *Applied Physics Letters*, vol. 101, no. 24, p. 243501, 2012.

[188] M. Z. Szymański, D. Tu, and R. Forchheimer, "2-D Drift-Diffusion Simulation of Organic Electrochemical Transistors," *IEEE Transactions on Electron Devices*, vol. 64, no. 12, p. 5114, 2017.

[189] C. Cercignani and E. Gabetta, eds., *Transport Phenomona and Kinetic Theory*. Birkhäuser Boston, MA, 2007.

[190] G. Dimarco, R. Loubère, J. Narski, and T. Rey, "An efficient numerical method for solving the Boltzmann equation in multidimensions," *Journal of Computational Physics*, vol. 353, p. 46, 2018.

[191] M. Auf der Maur, *A Multiscale Simulation Environment for Electronic and Optoelectronic Devices*. PhD thesis, University of Rome *Tor Vergata*, 2008.

[192] F. Bertazzi, M. Goana, G. Ghione, A. Tibaldi, P. Debernardi, and E. Bellotti, "Electron Transport," in *Handbook of Optoelectronic Device Modeling and Simulation* (J. Piprek, ed.), vol. 1, ch. 50, p. 35, CRC Press, 2017.

[193] J. Uffink, "Compendium of the foundations of classical statistical physics," in *Philosophy of Physics: A volume in Handbook of the Philosophy of Science* (J. Butterfield and J. Earman, eds.), vol. 1B, ch. 1, p. 923, Elsevier B.V., 1 ed., 2007.

[194] Carlo Jacoboni, Paolo Lugli, *The Monte Carlo Method for Semiconductor Device Simulation*. Springer Vienna, 1 ed., 1989.

[195] W. Hackbusch, *Tensor Spaces and Numerical Tensor Calculus*. Springer Cham, 2 ed., 2019.

[196] J. Honerkamp, *Statistical Physics: An Advanced Approach with Applications*. Springer-Verlag Berlin Heidelberg, 2002.

[197] H.-T. Shen, C. Weisbuch, J. S. Speck, and Y.-R. Wu, "Three-Dimensional Modeling of Minority-Carrier Lateral Diffusion Length Including Random Alloy Fluctuations in $(\mathrm{In},\mathrm{Ga})\mathrm{N}$ and $(\mathrm{Al},\mathrm{Ga})\mathrm{N}$ Single Quantum Wells," *Phys. Rev. Applied*, vol. 16, p. 024054, 2021.

[198] K. Huang, *Statistical mechanics*. Wiley, New York, 1963.

[199] W. van Roosbroeck, "Theory of the Flow of Electrons and Holes in Germanium and Other Semiconductors," *Bell System Technical Journal*, vol. 29, no. 4, p. 560, 1950.

[200] S. Birner, T. Zibold, T. Andlauer, T. Kubis, M. Sabathil, A. Trellakis, and P. Vogl, "nextnano: General Purpose 3-D Simulations," *IEEE Transactions on Electron Devices*, vol. 54, no. 9, p. 2137, 2007.

[201] "Silvaco, inc. Atlas User Manual (Santa Clara: Silvaco Inc.).," 2012.

[202] S. Karpov, "ABC-model for interpretation of internal quantum efficiency and its droop in III-nitride LEDs: a review.," *Optical and Quantum Electronics*, vol. 47, p. 1293, 2015.

[203] J. Piprek, "Efficiency droop in nitride-based light-emitting diodes," *physica status solidi (a)*, vol. 207, no. 10, p. 2217, 2010.

[204] D. Matsakis, A. Coster, B. Laster, and R. Sime, "A renaming proposal: "The Auger–Meitner effect"," *Physics Today*, vol. 72, no. 9, p. 10, 2019.

[205] J. M. McMahon, E. Kioupakis, and S. Schulz, "Atomistic analysis of Auger recombination in c-plane (In,Ga)N/GaN quantum wells: Temperature-dependent competition between radiative and nonradiative recombination," *Phys. Rev. B*, vol. 105, p. 195307, 2022.

[206] J. M. McMahon, D. S. P. Tanner, E. Kioupakis, and S. Schulz, "Atomistic analysis of radiative recombination rate, Stokes shift and density of states in c-plane InGaN/GaN qunatum wells," *Appl. Phys. Lett.*, vol. 116, p. 181104, 2020.

[207] E. Kioupakis, Q. Yan, D. Steiauf, and C. G. Van de Walle, "Temperature and carrier-density dependence of Auger and radiative recombination in nitride optoelectronic devices," *New Journal of Physics*, vol. 15, no. 12, p. 125006, 2013.

[208] A. David, N. G. Young, C. A. Hurni, and M. D. Craven, "Quantum Efficiency of III-Nitride Emitters: Evidence for Defect-Assisted Nonradiative Recombination and its Effect on the Green Gap," *Phys. Rev. Applied*, vol. 11, p. 031001, 2019.

[209] A. David, N. G. Young, C. Lund, and M. D. Craven, "Review—The Physics of Recombinations in III-Nitride Emitters," *ECS Journal of Solid State Science and Technology*, vol. 9, no. 1, p. 016021, 2019.

[210] C. Lynsky, G. Lheureux, B. Bonef, K. S. Qwah, R. C. White, S. P. DenBaars, S. Nakamura, Y.-R. Wu, C. Weisbuch, and J. S. Speck, "Improved Vertical Carrier Transport for Green III-Nitride LEDs Using $(\mathrm{In,Ga})\mathrm{N}$ Alloy Quantum Barriers," *Phys. Rev. Applied*, vol. 17, p. 054048, 2022.

[211] A. Deinega and S. John, "Finite difference discretization of semiconductor drift-diffusion equations for nanowire solar cells," *Computer Physics Communications*, vol. 183, no. 10, p. 2128, 2012.

[212] R. J. L. Veque, *Numerical Methods for Conservation Laws*. Springer Basel AG, 2 ed., 1992.

[213] J. Shewchuk, "Triangle: A two-dimensional quality mesh generator and Delaunay triangulator." URL: http://www.cs.cmu.edu/q̃uake/triangle.html. Accessed 2015-12-01.

[214] H. Si, K. Gärtner, and J. Fuhrmann, "Boundary conforming Delaunay mesh generation," *Computational Mathematics and Mathematical Physics*, vol. 50, p. 38, 2010.

[215] D. L. Scharfetter and H. K. Gummel, "Large-signal analysis of a silicon Read diode oscillator," *IEEE Transactions on Electron Devices*, vol. 16, no. 1, p. 64, 1969.

[216] D. Abdel, P. Farrell, and J. Fuhrmann, "Assessing the quality of the excess chemical potential flux scheme for degenerate semiconductor device simulation," *Optical and Quantum Electronics*, vol. 53, 2021.

[217] C. Cancès, C. Chainais-Hillairet, J. Fuhrmann, and B. Gaudeul, "A numerical-analysis-focused comparison of several finite volume schemes for a unipolar degenerate drift-diffusion model," *IMA Journal of Numerical Analysis*, vol. 41, no. 1, p. 271, 2020.

[218] D. Browne, B. Mazumder, Y.-R. Wu, and J. Speck, "Electron transport in unipolar InGaN/GaN multiple quantum well structures grown by NH_3 molecular beam epitaxy," *Journal of Applied Physics*, vol. 117, p. 185703, 2015.

[219] A. Di Vito, A. Pecchia, A. Di Carlo, and M. Auf Der Maur, "Simulating random alloy effects in III-nitride light emitting diodes," *J. Appl. Phys.*, vol. 128, p. 041102, 2020.

[220] H. Si, "TetGen, a Delaunay-Based Quality Tetrahedral Mesh Generator," *ACM Transactions on Mathematical Software*, vol. 41, p. 1, 2015.

[221] H. Si, "TetGen version 1.5." URL: http://tetgen.org/. Accessed 2015-12-01.

[222] D. H. Doan, P. Farrell, J. Fuhrmann, M. Kantner, T. Koprucki, and N. Rotundo, "ddfermi – a drift-diffusion simulation tool," ddfermi – a drift-diffusion simulation tool, Weierstrass Institute (WIAS), doi: `http://doi.org/10.20347/WIAS.SOFTWARE.DDFERMI`, 2020.

[223] J. Fuhrmann, T. Streckenbach, *et al.*, "pdelib: A finite volume and finite element toolbox for PDEs. [Software].," pdelib: a finite volume and finite element toolbox for pdes. [software]. version: 2.4.20190405, Weierstrass Institute (WIAS), `http://pdelib.org`, 2019.

[224] S. Marcinkevičius, R. Yapparov, L. Y. Kuritzky, Y.-R. Wu, S. Nakamura, and J. S. Speck, "Low-temperature carrier transport across InGaN multiple quantum wells: Evidence of ballistic hole transport," *Physical Review B*, vol. 101, p. 075305, 2020.

[225] U. Özgür, X. Ni, X. Li, J. Lee, S. Liu, S. Okur, V. Avrutin, A. Matulionis, and H. Morkoç, "Ballistic transport in InGaN-based LEDs: Impact on efficiency," *Semiconductor Science and Technology*, vol. 26, p. 014022, 2010.

[226] C.-Y. Tsai, C.-H. Chen, T.-L. Sung, C.-Y. Tsai, and J. M. Rorison, "Theoretical modeling of nonequilibrium optical phonons and electron energy relaxation in GaN," *Journal of Applied Physics*, vol. 85, no. 3, p. 1475, 1999.

[227] Y. Huang, Z. Liu, X. Yi, Y. Guo, S. Wu, G. Yuan, J. Wang, G. Wang, and J. Li, "Overshoot effects of electron on efficiency droop in InGaN/GaN MQW light-emitting diodes," *AIP Advances*, vol. 6, no. 4, p. 045219, 2016.

[228] N. Kharch, M. Luisier, T. B. Boykin, and G. Klimeck, "Electronic structure and transmission characteristics of SiGe nanowires," *Journal of Computational Electronics*, vol. 7, p. 350, 2008.

[229] T. B. Boykin, M. Luisier, A. Schenk, N. Kharche, and G. Klimeck, "The Electronic Structure and Transmission Characteristics of Disordered AlGaAs Nanowires," *IEEE Transactions on Nanotechnology*, vol. 6, no. 1, p. 43, 2007.

[230] C. Haller, J.-F. Carlin, G. Jacopin, D. Martin, R. Butté, and N. Grandjean, "Burying non-radiative defects in InGaN underlayer to increase InGaN/GaN quantum well efficiency," *Applied Physics Letters*, vol. 111, no. 26, p. 262101, 2017.

[231] T.-J. Y. Y.-R. Wu, C.K. Wu, "Influence of Random InGaN Alloy Fluctuations on GaN-Based Light-Emitting Diodes," in *Handbook of Optoelectronic Device Modelling and Simulation* (J. Piprek, ed.), ch. 18, p. 559, CRC Press, 2017.

[232] P. Dawson, S. Schulz, R. A. Oliver, M. J. Kappers, and C. J. Humphreys, "The nature of carrier localisation in polar and nonpolar InGaN/GaN quantum wells," *Journal of Applied Physics*, vol. 119, no. 18, p. 181505, 2016.

[233] D. N. Nath, Z. C. Yang, C.-Y. Lee, P. S. Park, Y.-R. Wu, and S. Rajan, "Unipolar vertical transport in GaN/AlGaN/GaN heterostructures," *Applied Physics Letters*, vol. 103, no. 2, p. 022102, 2013.

[234] S. Marcinkevičius, R. Yapparov, L. Y. Kuritzky, Y.-R. Wu, S. Nakamura, S. P. DenBaars, and J. S. Speck, "Interwell carrier transport in InGaN/(In)GaN multiple quantum wells," *Applied Physics Letters*, vol. 114, no. 15, p. 151103, 2019.

[235] M. Kneissl, T.-Y. Seong, J. Han, and H. Amano, "The emergence and prospects of deep-ultraviolet light-emitting diode technologies," *Nat. Photonics*, vol. 13, p. 233, 2019.

[236] K. Bulashevich, O. Khokhlev, I. Evstratov, and S. Karpov, "Simulation of light-emitting diodes for new physics understanding and device design," in *Light-Emitting Diodes: Materials, Devices, and Applications for Solid State Lighting XVI*

(K. P. Streubel, H. Jeon, L.-W. Tu, and N. Linder, eds.), p. 152, International Society for Optics and Photonics, SPIE, 2012.

[237] D. Ferry, S. Ramey, L. Shifren, and R. Akis, "The effective potential in device modeling: the good, the bad and the ugly," *Journal of Computational Electronics*, vol. 1, p. 59, 2002.

[238] D. A. Zakheim, A. S. Pavluchenko, D. A. Bauman, K. A. Bulashevich, O. V. Khokhlev, and S. Y. Karpov, "Efficiency droop suppression in InGaN-based blue LEDs: Experiment and numerical modelling," *physica status solidi (a)*, vol. 209, no. 3, p. 456, 2012.

[239] D. Braess, *Finite Elemente*. Springer Berlin Heidelberg, 1997.

[240] J. W. Barrett and C. M. Elliott, "Finite element approximation of the Dirichlet problem using the boundary penalty method," *Numerische Mathematik*, vol. 49, no. 4, p. 343, 1986.

[241] O. Schenk, "PARDISO version 5.0.0." URL: http://www.pardiso-project.org. Accessed 2016-02-22.

[242] D. N. Arnold, G. David, M. Filoche, D. Jerison, and A. Mayboroda, "Computing spectra without solving eigenvalue problems," *SIAM J. SCI. COMPUT.*, vol. 41, p. B69, 2019.

[243] M. Ilegems and H. Montgomery, "Electrical properties of n-type vapor-grown gallium nitride," *Journal of Physics and Chemistry of Solids*, vol. 34, no. 5, p. 885, 1973.

[244] F. Massabuau, N. Piot, M. Frentrup, X. Wang, Q. Avenas, M. Kappers, C. Humphreys, and R. Oliver, "X-ray reflectivity method for the characterization of InGaN/GaN quantum well interface," *physica status solidi (b)*, vol. 254, no. 8, p. 1600664, 2017.

[245] K. S. Qwah, M. Monavarian, G. Lheureux, J. Wang, Y.-R. Wu, and J. S. Speck, "Theoretical and experimental investigations of vertical hole transport through unipolar AlGaN structures: Impacts of random alloy disorder," *Applied Physics Letters*, vol. 117, no. 2, p. 022107, 2020.

[246] P. Kozodoy, H. Xing, S. P. DenBaars, U. K. Mishra, A. Saxler, R. Perrin, S. Elhamri, and W. C. Mitchel, "Heavy doping effects in Mg-doped GaN," *Journal of Applied Physics*, vol. 87, no. 4, p. 1832, 2000.

[247] D. Iida, K. Tamura, M. Iwaya, S. Kamiyama, H. Amano, and I. Akasaki, "Compensation effect of Mg-doped a- and c-plane GaN films grown by metalorganic vapor phase epitaxy," *Journal of Crystal Growth*, vol. 312, no. 21, p. 3131, 2010.

[248] Y. Ohba and A. Hatano, "A study on strong memory effects for Mg doping in GaN metalorganic chemical vapor deposition," *Journal of Crystal Growth*, vol. 145, no. 1, p. 214, 1994.

[249] C.-K. Li, M. Rosmeulen, E. Simoen, and Y.-R. Wu, "Study on the Optimization for Current Spreading Effect of Lateral GaN/InGaN LEDs," *IEEE Transactions on Electron Devices*, vol. 61, no. 2, p. 511, 2014.

[250] J. H. Zhu, S. M. Zhang, H. Wang, D. G. Zhao, J. J. Zhu, Z. S. Liu, D. S. Jiang, Y. X. Qiu, and H. Yang, "The investigation on carrier distribution in InGaN/GaN multiple quantum well layers," *Journal of Applied Physics*, vol. 109, no. 9, p. 093117, 2011.

[251] B. Galler, A. Laubsch, A. Wojcik, H. Lugauer, A. Gomez-Iglesias, M. Sabathil, and B. Hahn, "Investigation of the carrier distribution in InGaN-based multi-quantum-well structures," *physica status solidi c*, vol. 8, no. 7, p. 2372, 2011.

[252] A. David, M. J. Grundmann, J. F. Kaeding, N. F. Gardner, T. G. Mihopoulos, and M. R. Krames, "Carrier distribution in (0001)InGaN/GaN multiple quantum well light-emitting diodes," *Applied Physics Letters*, vol. 92, no. 5, p. 053502, 2008.

[253] J. P. Liu, J.-H. Ryou, R. D. Dupuis, J. Han, G. D. Shen, and H. B. Wang, "Barrier effect on hole transport and carrier distribution in InGaN/GaN multiple quantum well visible light-emitting diodes," *Applied Physics Letters*, vol. 93, no. 2, p. 021102, 2008.

[254] A. Di Vito, A. Pecchia, A. Di Carlo, and M. Auf Der Maur, "Characterization of non-uniform InGaN alloys: spatial localization of carriers and optical properties," *Japanese Journal of Applied Physics*, vol. 58, no. SC, p. SCCC03, 2019.

[255] Z. Yu and R. Dutton, "SEDAN III – A one-dimensional device simulator." `www-tcad.stanford.edu/tcad/programs/sedan3.html`, 1988.

[256] D. A. Browne, M. N. Fireman, B. Mazumder, L. Y. Kuritzky, Y.-R. Wu, and J. S. Speck, "Vertical transport through AlGaN barriers in heterostructures grown by ammonia molecular beam epitaxy and metalorganic chemical vapor deposition," *Semiconductor Science and Technology*, vol. 32, no. 2, p. 025010, 2017.